## Vibrational and Thermodynamic Properties of Energetic Materials: A Density Functional Theory study

A Thesis submitted to University of Hyderabad for the award of the degree of

Doctor of Philosophy in Physics

by

Bushnagar Adivaiah (15ACPA12)



ACRHEM, School of Physics
University of Hyderabad
Hyderabad-500 046
January 2022

#### Declaration

I, Bushnagar Adivaiah hereby declare that this thesis entitled Vibrational and Thermodynamic Properties of Energetic Materials: A Density Functional Theory study submitted by me under the supervision of Dr. G. S. Vaitheeswaran, ACRHEM, School of physics, University of Hyderabad, Hyderabad, India, is a bonafide research work which is also free from plagiarism. I also declare that it has not been submitted previously in part or in full to this University or any other University or Institution for the award of any degree or diploma. I hereby agree that my thesis can be deposited in Shodhganga/INFLIBNET.

A report on plagiarism statistics from the University Librarian is enclosed.

Date 27/01/2022

Bushnagar Adivaiah Reg. No: 15ACPA12.

Dr. G. S. Vaitheeswaran,

Thesis Supervisor,

ACRHEM, School of Physics,

G. Vaithers war

University of Hyderabad.

Dr. G.S. Vaitheeswaran
Associate Professor
School of Physics
University of Hyderabad
Hyderabad-500 046 (TS) INDIA

#### Certificate

This is to certify that the thesis entitled Vibrational and Thermodynamic Properties of Energetic Materials: A Density Functional Theory study being submitted to the University of Hyderabad by Bushnagar Adivaiah (Reg. No. 15ACPA12), for the award of the degree of Doctor of Philosophy in Physics, is a record of bonafide work carried out by him under my supervision and is free of plagiarism. The matter embodied in this report has not been submitted to any other University or Institution for the award of any degree or diploma.

The student has passed the following courses towards the fulfilment of course work requirement for PhD.

S.No.	Course Code	Year	Name of the course	Credits	Pass/Fail
1	PY801	2015	Advanced Quantum Mechanics	04	Pass
2	PY804	2015	Advanced Electromagnetic Theory	04	Pass
3	PY801	2016	Research Methodology	04	Pass
4	PY804	2016	Advanced Mathematical Methods	04	Pass

Dr. G.S. Vaitheeswaran
Associate Professor
School of Physics
University of Hyderabad
Hyderabad-500 046. (TS) INDIA

Dr. G. S. Vaitheeswaran, Thesis Supervisor, ACRHEM, School of Physics, University of Hyderabad.

Director, ACRHEM,

University of Hyderabad.

Director ACRHEM

Dean,

School of Physics, University of Hyderabad.

DEAN
School of Physics
University of Hyderabad
vderabad-500 046, INDIA

#### A word of Gratitude

I wish to express my personal gratitude to everyone who has made this thesis a reality. First, I am ever thankful to my research guide, **Dr. G. S. Vaitheeswaran**, School of Physics, University of Hyderabad for his motivation, suggestions, and guidance throughout the course of my research.

I wish to convey my heartfelt thanks to my doctoral committee members **Prof. Ashok Chatterjee**, School of Physics and **Dr. G. Manoj kumar**, ACRHEM, University of Hyderabad for their suggestions and valuable inputs towards the completion of my doctoral research work.

I am very much thankful to the director **Dr. V. Kameswara Rao** of **ACRHEM**, University of Hyderabad and Dean **Prof. K C James Raju**, School of Physics, University of Hyderabad for administrative support.

I express my sincere thanks to Honorary Professor Sunandana C S, Prof. Hari kumar E, Prof. Chaturvedi S, Prof. Anantha Lakshmi P, Prof. Nageswara Rao S V S, Dr. Ashok V, Dr. Venkataiah G, Dr. Venugopal Rao S, for their encouragement and support. I extend my gratitude to faculty members of SoP and faculty members of ACRHEM for their contribution in my academic career.

I would like to thank the Defence Research and Development Organization (DRDO), Ministry of Defence, Govt. of India through **ACRHEM** for their financial support and **CMSD**, University of Hyderabad for providing me the computational facilities.

I am grateful to all my group members and friends, Dr. Atahar Parveen, Dr. Appalakondaiah S, Narsimha Rao E, Dr. Yedukondalu N, Dr. Moses Abraham B,Prathap Kumar J, Mondal.S, Dr. Jyothirmai V, Supratik Mukherjee, and Aiswarya T, Dr. Krishnakanth K, Srinivas V, Souvik Roy, Rama krishna, Dr. Bharathi M S S, Sini N S, and Dr. Pani Sri for their contribution throughout this project.

Finally, I am indebted to and thank all my family members and friends who have helped me to achieve this accomplishment through their support.

Bushnagar Adivaiah

## Contents

Co	nten	t <mark>s</mark>	i
Lis	t of f	igures	iii
Lis	t of t	ables .	v
1	Intro	oduction	1
	1.1	Density functional theory (DFT)	5
	1.2	Lattice dynamic study in energetic materials	6
	1.3	Outline of the thesis	7
2	The	oretical background	17
	2.1	Introduction to the many body Hamiltonian	17
	2.2	Born-Oppenheimer approximation	18
	2.3	Hartree-Fock Approximation	19
	2.4	Thomas-Fermi Theory	20
	2.5	Density functional theory	21
	2.6	Exchange-correlation functionals	23
	2.7	van der Waals (vdW) in DFT	24
	2.8	Pseudopotentials method	25
		2.8.0.1 Norm-conserving pseudopotentials	27
		2.8.0.2 Ultra-soft pseudopotentials	27
	2.9	Density Functional Perturbation Theory (DFPT)	28
	2.10	Thermodynamic properties using Quasi-Harmonic approximation	31
3	Alka	lline-earth metal salts	37
	3.1	Introduction	38
	3.2	Materials and methods	43
		3.2.1 Crystal structure	43
		3.2.2 Computational methods	44
	3.3	Results and discussion	45

ii CONTENTS

		3.3.1 Unit cell optimization	45
		3.3.2 Mechanical properties	49
		3.3.3 Born effective charge analysis	54
		3.3.4 Infrared spectra	59
		3.3.5 Phonon dispersion and Phonon density of states	72
		3.3.6 Thermodynamic properties	75
	3.4	Conclusions	79
4	Initi	ator and improvised explosives	87
	4.1	Introduction	88
	4.2	Computational methods	91
	4.3	Results and discussion	92
		4.3.1 Crystal structure and Unit cell optimization	92
		4.3.2 Born effective charge analysis	94
		4.3.3 Infrared spectra	100
		4.3.4 Phonon dispersion	108
		4.3.5 Thermodynamic properties	116
	4.4	Conclusions	118
	4.5	References	119
5		h-Performance Insensitive Energetic Material (MAD-X1)	125
	5.1	Introduction	126
	5.2	Materials and methods	128
		5.2.1 Crystal structure	128
		5.2.2 Computational details	128
	5.3	Results and discussion	129
		5.3.1 Zone center IR spectra	129
		5.3.2 Phonon dispersion	135
		5.3.3 Thermodynamic properties	137
	5.4	Conclusions	140
6	Con	clusions	145
<u> </u>	6.1	Summary	146
	6.2	Future scope	149
Lic	at of I	Publications and Scientific activities	150
			150
Sir	nilari	ty index	152

## List of Figures

2.1	DFT Algorithm	23
2.2	Schematic illustration of the concept behind the pseudopotential	
	approach. The dashed lines show the all-electron wavefunction and ionic potential; while the corresponding pseudo wavefunction given by the pseudopotential is plotted in solid lines. All quantities are represented as a function of distance, r, from the atomic nucleus. The point beyond which the all-electron and pseudo-electron values become identical is designated as cutoff radius.	26
3.1	Crystal structure of M(NO <sub>3</sub> ) <sub>2</sub> , the cation local atomic site arrange-	
	ment in the respective nitrate crystal structures showing the six nitrate groups and associated 6 + 6 coordinated oxygen atomic shells, and a cuboctahedron with eight triangular faces and six square faces.	42
3.2	Crystal structure of Orthorhombic Sr(N <sub>3</sub> ) <sub>2</sub> (top) along (a) x-y-z	
	and (b) z-y-x axes. Monoclinic $Ba(N_3)_2$ (bottom) along (c) x-y-z and (d) z-y-x axes. Blue color represents N atoms, and green color represents $Sr/Ba$ atoms.	44
3.3	Density functional perturbation theory-calculated infrared spec-	
	tra of (a) $Sr(NO_3)_2$ , $Ba(NO_3)_2$ , $Sr(N_3)_2$ and $Ba(N_3)_2$ in the 0 – 2100 cm <sup>-1</sup> wavenumber range.	61
3.4	Normal modes (cm <sup>-1</sup> ) behind the most intense maxima in the infrared spectra of $Sr(NO_3)_2$ and $Ba(NO_3)_2$	65
3.5	Normal modes (cm <sup>-1</sup> ) behind the most intense maxima in the in-	
	frared spectra of $Sr(N_3)_2$	69
3.6	Normal modes (cm <sup>-1</sup> ) behind the most intense maxima in the infrared spectra of $Ba(N_3)_2$	70
3.7	(Phonon dispersion curves for Sr(NO <sub>3</sub> ) <sub>2</sub> , Ba(NO <sub>3</sub> ) <sub>2</sub> , Sr(N <sub>3</sub> ) <sub>2</sub> and	
	$Ba(N_3)_2$ wavenumber range over the 0–200 cm <sup>-1</sup>	73

3.8	Phonon partial density of states (PDOS) for (a) Sr(NO <sub>3</sub> ) <sub>2</sub> and Ba(NO	$()_3)_2$
	(b) $Sr(N_3)_2$ and $Ba(N_3)_2$	74
3.9	Density functional theory-calculated thermodynamic properties,	
	$Sr(NO_3)_2$ , $Ba(NO_3)_2$ , $Sr(N_3)_2$ and $Ba(N_3)_2$	76
3.10	Density functional theory-calculated specific heat (top) and De-	
	by etemperature (bottom) for (a) $Sr(NO_3)_2$ , $Ba(NO_3)_2$ , $Sr(N_3)_2$	
	and $Ba(N_3)_2$	78
4.1	Unit cell of the cyanuric triazide crystal.	91
4.2	Unit cell (a), crystal structure (b), and single molecule (c) of urea	
	nitrate	93
4.3	Calculated infrared spectra of $C_3N_{12}$ at the optimized equilibrium	
	volume in the 0 – 900 cm <sup>-1</sup> range (fig(a)) and $900 - 2100 \text{ cm}^{-1}$ (fig(b))	).100
4.4	Normal modes of C <sub>3</sub> N <sub>12</sub> corresponding to the calculated IR ab-	
	sorption lines at 67, 514, 670, 775, 1184, 1317, 1467 and 1957 $\mathrm{cm}^{-1}$	
	with their respective assignments.	101
4.5	Calculated infrared spectra of Urea nitrate at the optimized equi-	
	librium volume in the 0-900 cm <sup>-1</sup> range	102
4.6	Calculated infrared spectra of Urea nitrate at the optimized equi-	
	librium volume in the 900-1800 cm $^{-1}$ range	103
4 <b>.</b> 7	Calculated infrared spectra of Urea nitrate at the optimized equi-	
	librium volume in the 2100-3600 cm $^{-1}$ range	104
4.8	Normal modes of UN corresponding to the calculated IR absorp-	
	tion lines at 176, 531, 1260, 1653, 2602 and 3288 cm <sup>-1</sup> with their	
	respective assignments	105
4.9	Phonon dispersion curves for C <sub>3</sub> N <sub>12</sub> crystal (a) 0-2100 cm <sup>-1</sup> (b)	
	Close-up showing the 0-300 cm $^{-1}$ wavenumber range	111
4.10	Phonon partial density of states (PDOS) for the C <sub>3</sub> N <sub>12</sub> crystal (a)	
	(a) $0-2100 \text{ cm}^{-1}$ (b) Close-up showing the $0-300 \text{ cm}^{-1}$ wavenumber	110
	range.	112
4.11	Phonon dispersion curves for Urea nitrate crystal (a) 0-3600 cm <sup>-1</sup>	443
	(b) Close-up showing the 0-300 cm <sup>-1</sup> wavenumber range	113
4.12		
	tal (a) $0-3600 \text{ cm}^{-1}$ (b) Close-up showing the $0-300 \text{ cm}^{-1}$ wavenum-	11/
4.42	ber range.	114
4.13	Calculated (a) temperature times entropy, enthalpy, and free en-	
	ergy of the cyanuric triazide crystal for temperature of up to 1000	115
	K and (b) Heat capacity curves for the cyanuric triazide crystal	113

LIST OF FIGURES v

4.14	Calculated (a) temperature times entropy, enthalpy, and free en-	
	ergy of the urea nitrate crystal for temperature of up to 1000 K	
	and (b) Heat capacity curves for the cyanuric triazide crystal	117
	77 1 11 1 1 1 1 1 1 1 1 1 7 7 7 7 1 7 7 7 1	
5.1	Unit cell and single molecule of the MAD-XI crystal. Here, Blue	
	color represents N atoms, red color O atoms, white color H atoms,	
	and gray represents C atoms	127
5.2	Calculated infrared spectra of MAD-XI at the optimized equilib-	
	rium volume in the 0-900 cm <sup>-1</sup> range (fig(a)), $900-1800 \text{ cm}^{-1}$	
	(fig(b)), and 2800-3400 cm <sup>-1</sup> ((fig(c))	130
5.3	Normal modes of MAD-XI corresponding to the calculated IR	
	absorption lines at 486.59, 735.59, 1245.73, 1641.86, 2866.87, and	
	3191.49 cm <sup>-1</sup> with their respective assignments	131
5.4	(a) Phonon dispersion curves, (b) Phonon partial density of states	
	(PDOS) for the MAD-X1 crystal	136
5.5	Calculated (a) temperature times entropy, enthalpy, and free en-	
	ergy (b) Heat capacity of the MAD-XI crystal for temperature of	
	up to 1000 K for the MAD-XI crystal).	138
5.6	Calculated Debye temperature curves of the MAD-XI crystal for	
	temperature of up to 1000 K for the MAD-XI crystal	139

## List of Tables

3.1	Calculated and experimental lattice constants with error percent-	
	age in parentheses of $M(NO_3)_2$ (M = Sr, Ba)	46
3.2	Calculated and experimental (in parentheses) [47] atomic coordi-	
	nates of $Sr(NO_3)_2$ and $Ba(NO_3)_2$ . The WP values are calculated	
	using van der Waals (vdW) functional	46
3.3	Calculated and experimental (in parentheses) [47] bond distances	
	(Å) and bond angles (degrees) between the $M^{2+}$ cation and the near-	
	est oxygen atoms for $M(NO_3)_2$ (M = Sr, Ba)	48
3.4	Calculated and experimental lattice constants with error percent-	
	ages in parentheses of $M(N_3)_2$ (M = Sr, Ba)	48
3.5	Calculated atomic coordinates of Sr(N <sub>3</sub> ) <sub>2</sub> and Ba(N <sub>3</sub> ) <sub>2</sub> . The WP	
	values are calculated using van der Waals (vdW) functional	49
3.6	Calculated and experimental (in parentheses) [50, 51] bond dis-	
	tances (Å) and bond angles (degrees) between the $M^{2+}$ cation and	
	the nearest oxygen atoms for $M(N_3)_2$ (M = Sr, Ba)	49
3.7	Calculated and experimental (in parentheses) components of the	
	elastic tensor $C_{ij}$ , Young's modulus (E), bulk modulus (B), shear	
	modulus (G), compressibility (K), anisotropy (A), Poison's ratio	
	$(\sigma)$ , $B/G$ ratio, longitudinal $(V_l)$ , transverse $(V_t)$ , and average $(V_m)$	
	sound velocities, and Debye temperature $(\Theta_D)$ of $M(NO_3)_2$ $(M =$	
	<u>Sr, Ba</u> )	50
3.8	Elastic constants $C_{ij}$ (GPa) of $Sr(N_3)_2$ and $Ba(N_3)_2$ . Previously re-	
	ported $M(N_3)_2$ values are shown for comparison	52
3.9	Calculated components of the bulk modulus (B), shear modulus	
	(G), Young's modulus (E) of $Sr(N_3)_2$ and $Ba(N_3)_2$ . Previously re-	
	ported $M(N_3)_2$ values are shown for comparison	53
3.10	Calculated BEC's of $Sr(N_3)_2$ . Actual ionic charges are $Sr = +2$ , N	
	= -3.	55
3.11	Calculated BEC's of Ba( $N_3$ ) <sub>2</sub> . Actual ionic charges are Ba = +2,	
	N = -3.	55

3.12	Percentage of deviations of BEC's all inquivalent atoms are along	
	xx, yy, zz directions.	56
3.13	Calculated BEC's of $Sr(NO_3)_2$ . Actual ionic charges are $Sr = +2$ ,	
	$O = -2, N = -3, \dots$	58
3.14	Calculated BEC's of Ba( $NO_3$ ) <sub>2</sub> . Actual ionic charges are Ba = +2,	
	O = -2, N = -3.	59
3.15	Percentage of deviations of BEC's all inquivalent atoms are shown	
	along xx, yy, zz directions	60
3.16	Calculated infrared frequencies (0-300 cm <sup>-1</sup> ) with symmetry as-	
	signment for $Sr(NO_3)_2$	62
3.17	Calculated and Experimental frequency (cm <sup>-1</sup> ) [12] of Infrared	
	frequencies (700-1500 cm $^{-1}$ ) with symmetry assignment for Sr(NO <sub>3</sub>	) <sub>2</sub> . 63
3.18	Calculated and Experimental frequency (cm <sup>-1</sup> ) [12] of Infrared	
	frequencies (700-1500 cm $^{-1}$ ) with symmetry assignment for Ba(NO)	$(3)_2$ . 63
3.19	Calculated infrared frequencies (0-300 cm <sup>-1</sup> ) with symmetry as-	
	signment for Ba(NO <sub>3</sub> ) <sub>2</sub>	64
3.20	Calculated infrared frequencies (0-2000 cm <sup>-1</sup> ) with symmetry as-	
	signment for $Sr(N_3)_2$	67
3.21	Calculated frequency and Experimental frequency (cm <sup>-1</sup> ) of In-	
	frared frequencies (0-2000 cm <sup>-1</sup> ) with symmetry assignment for	
	$Ba(N_3)_2$ .	68
4.1	Lattice parameters(Å) and unit cell volume (Å <sup>3</sup> ) of the $C_3N_{12}$ crys-	
	tal unit cell as calculated at the LDA, GGA, GGA+G06 and ex-	
	perimental values [18] with error percentage	90
4.2	Lattice parameters( $\mathring{A}$ ) and unit cell volume ( $\mathring{A}^3$ ) of the urea nitrate	
	crystal unit cell as calculated at the LDA, GGA, GGA+G06 and	
	experimental values [38] with error percentage	92
4.3	Calculated BEC's of $C_3N_{12}$ . Actual ionic charges are $C = +4$ , $N$	
	= -3	95
4.4	Percentage deviations of BEC's for C <sub>3</sub> N <sub>12</sub> along the xx, yy, zz	
	directions	96
4.5	Calculated BEC's of UN. Actual ionic charges are $C = +4$ , $H =$	
	+1, N = -3, O = -2.	98
4.6	Percentage deviations of BEC's for UN along the xx, yy, zz direc-	
	tions	99
4.7	Calculated normal modes infrared frequencies (0-670 cm <sup>-1</sup> ) with	
	symmetry assignment for the cyanuric triazide crystal using the	
	DFT GGA+G06 approach	103

LIST OF TABLES ix

4.8	Calculated normal modes infrared frequencies (670-2000 cm <sup>-1</sup> )	
	with symmetry assignment for the cyanuric triazide crystal using	
	the DFT GGA+G06 approach.	104
4.9	Calculated normal modes infrared frequencies (0-200 cm <sup>-1</sup> ) with	
	symmetry assignment for the UN crystal using the DFT GGA+G06	
	approach	107
4.10	Calculated normal modes infrared frequencies (200-750 cm <sup>-1</sup> ) with	
	symmetry assignment for the UN crystal using the DFT GGA+G06	
	approach	109
4.11	Calculated normal modes infrared frequencies (1250-3450 cm <sup>-1</sup> )	
	with symmetry assignment for the UN crystal using the DFT	
	GGA+G06 approach	110
5.1	Lattice parameters(Å) and unit cell volume (Å <sup>3</sup> ) of the MAD-XI	
	crystal calculated at the LDA, GGA, GGA + OBS and experi-	
	mental values [12] with error percentage.	129
5.2	Calculated normal modes infrared frequencies (0-400 cm <sup>-1</sup> ) with	
	symmetry assignment for the MAD-XI crystal using the DFT GGA	
	+ OBS approach.	132
5.3	Calculated normal modes infrared frequencies (400-1200 cm <sup>-1</sup> )	
	with symmetry assignment for the MAD-XI crystal using the DFT	
	GGA + OBS approach	133
5.4	Calculated normal modes infrared frequencies (1200-3400 cm <sup>-1</sup> )	
	with symmetry assignment for the MAD-XI crystal using the DFT	
	GGA + OBS approach	134

# Chapter 1

### Introduction

The history of explosives, riddled as it is with controversies, traces back its roots to China during the seventh century. Gun powders are believed to be used by the Chinese not only as explosives, but also as propellants and fireworks [1, 2]. The black powder, which was a mixture of charcoal, sulphur, and potassium nitrate, was the prototype for latter class of explosives that were developed using nitrocellulose (NC) and nitro-glycerine (NG) [3, 4]. These new types of explosives would burn slowly in a controlled manner, giving out large volumes of gas that were powerful enough to propel a projectile. This property allowed them to be used as propellants. High explosives were subsequently developed following this, and were mostly used as explosive fillings for bombs, shells and warheads. Some well-known high explosives are picric acid, trinitrotoluene (TNT), pentaerythritol tetranitrate (PETN), cyclotrymethylene trinitrramine (RDX), cyclotetramethylene tetranitramine (HMX), etc. [5–7]. They differed from the previous models in the sense that they were more powerful but relatively insensitive to various stimuli such as heat, impact friction and, spark. High explosives were further developed to meet military needs with specialized functions such as for illumination, delay, smoke, sound and incendiary, etc. [6, 7]. These effects were achieved through the formulations based on fuels, oxidizers, binders along, with additives. In fact, the addition of these specialized effects came to form a separate category known as pyrotechnics. All three types of explosives viz. explosives, propellants, and pyrotechnics, were initially developed independently until the early 1990s [1, 2]. However, this gave rise to various misuse and unethical usage. The need to control the research of explosives was also accompanied by a need to camouflage its nomenclature. Thus, the research for such a sensitive matter came to be termed as 'high energy materials'. It is within this context that the study of high energy materials (HEMs) or energetic materials (Ems) came to encompass explosives, propellants and pyrotechnics.

Energetic materials have been extensively used in huge amounts in mixtures for military and civil purposes (e.g., aerospace propellants, mining engineering, and pyrotechnic technology) [9, 10, 47]. Pyrotechnics: Pyrotechnic mixtures, which are typically made up of finely divided metallic or nonmetallic fuels and oxidizers, are used to produce smoke, noise, color, and sparks or flames by combustion [11]. The fact that nowadays, smoke is also used for camouflaging, signaling, and special effects [12] makes the study of pyrotechnics more significant. Besides their extensive use in fireworks, pyrotechnics are also predominantly used in technological applications such as matches, fire extinguishers, airbags and propellants, all kinds of flares, military countermeasures (acoustic and optical decoy devices), and igniters [12, 13]. There are several ways of classification of explosives and, one of them is the nature of bonds present in an explosive. On the basis of this classification, below we can see some of the compounds.

Azides (-N = N = N-): Azides are substances containing the N<sub>3</sub> group. They exist as inorganic salts, organic compounds, organo-metals, or complexes. The inorganic azides are prominent category of compounds for a number of reasons. These materials has empirical significance as an explosives, gas generators, industrial chemicals, and photographic materials at low temperature. The azide group is linear and symmetrical with, an average N-N separation being 1.18. Typically, the contrast in the bonding of azides leads to large variations in the observed stability and decomposition. Most of the solid inorganic azides decompose to give simple product of the anion and nitrogen [14]. This decomposition can occur by heat, shock, light, or ionization radiation. In the case of heavy metal azides, the reaction is highly exothermic and shows low sensitivity.

The alkali and alkaline earth metal azides are more stable [15], which are not sensitive to impact [16]. Among the inorganic metal azides, strontium azide and barium azide are well-known for their explosive properties such as detonation or deflagration. Sr(N<sub>3</sub>)<sub>2</sub> and Ba(N<sub>3</sub>)<sub>2</sub> undergo photochemical decomposition into metal atoms and nitrogen when they are exposed to ultra-violet light [17–19]. The decomposition of strontium azide, barium azide and calcium azide differ

from those for the Alkali metal azides in a markedly smaller fraction of nitrogen evolving as free atoms, and alkaline metal azides have larger lattice energies than alkali azides [20].

The decomposition reactions of strontium and barium azides [14] are as follows:

$$Sr(N_3)_2 \rightarrow Sr + 0.4N + 2.8N_2$$
 (1.1)

$$Ba(N_3)_2 \rightarrow Ba + 0.6N + 7.7N_2$$
 (1.2)

The series of inorganic azides such as KN<sub>3</sub>, TlN<sub>3</sub>, AgN<sub>3</sub>, CuN<sub>3</sub> plays significant role in determining the explosive sensitivity of the compound. Unfortunately, metal azides such as silver azide, lead azide, and thallous azide suffer from instability, sensitivity, or toxicity [21]. Lead azide  $(Pb(N_3)_2)$  was used as primary explosive for many years [17] but, use of Pb primaries has led to environmental pollution due to toxic Pb decomposition after detonation. One of the modern and principal trends in the development of energetic materials is to search for the so-called green primary explosives. A variety of organic azides exists and has been described in scientific literature. However, only some of them have the characteristics of primary explosives. The nitrogen-rich compounds are potential candidates for high energy density because of its high nitrogen content and good thermal stability [22]. Apart from this, these composites are environmentally safe with molecular nitrogen as their main combustion or detonation outcome. One of the representatives of such green primary explosives is cyanuric triazide (CTA) [23], which has distinctive properties based on thermal decomposition reactions; they do not pose health risks to personnel and cause much less pollution to the environment, but it has no practical use because of very high sensitivity towards external stimuli [24-29]. However, efforts have been made recently addressing its use as explosive material [24]. Cyanuric triazide is an effective initiator in explosives, synthesized and structurally characterized recently [30, 31]. It is a quite interesting compound, since it contains only carbon and nitrogen, three carbon and twelve nitrogen in each molecules. The compound is highly friction sensitive, it has sharp melting point under 400 K but it explodes upon heating above 500 K giving nitrogen and carbon in the form of graphite [25].

The decomposition reaction of cyanuric triazide has been reported previously [25]:

$$C_3N_3(N_3)_3 \rightarrow 3C + 6N_2$$
 (1.3)

Nitrates (-ONO<sub>2</sub>): The nitrates of alkali and alkaline earth metals are salts well known for their application in pyrotechnics because of their high oxygen content, high decomposition temperatures, and favorable thermodynamic properties [11, 32]. Nitrates are powerful oxidizing agents and decompose at elevated temperature to give oxygen as one of the major products. Sr(NO<sub>3</sub>)<sub>2</sub>, an alkaline earth metal nitrate, is one such interesting compound that could be used in pyrotechnic compositions as a coloring and oxidizing agent [33] because of its high thermal stability and the nature of its thermal decomposition [11]. The oxygen balance in strontium nitrate is 37.7%, and the material decomposes in a strongly endothermic manner into SrO, N<sub>2</sub>, and O<sub>2</sub>. It is widely used in pyrotechnics such as firework signal flares and tracer ammunition because strontium compounds burn with a brilliant red flame and no other material has been found to be better in these applications [34]. In green light-emitting pyrotechnic formulations, Ba(NO<sub>3</sub>)<sub>2</sub> is mostly used as both the colorant and the oxidant [11].

The decomposition reaction of barium nitrate and strontium nitrate has been reported previously [11]:

$$Sr(NO_3)_2 \rightarrow SrO + NO + NO_2 + O_2$$
 (1.4)

$$Ba(NO_3)_2 \rightarrow BaO + 2NO + 1.5O_2$$
 (1.5)

By differing the chemical nature of either or both ions an energetic material can be modify to fit specific requirements. The environmental impact and toxicity is the prime in the design of energetic materials. Thus, organic nitrates are typically biodegradable and produce environmentally relatively good combustion products, are of prime interest. Urea nitrate is a siginficant improvised explosive with a representative layered super molecular structure [35, 36]. The urea nitrate find make use of fertilizers, and most of that urea (85%) ends up as fertilizer, with

a little amount utilized for resins and plastics and a small percentage utilized in cattle feed. For long time, urea nitrate has been utilized by terrorists to make improvised explosives [37, 38]. It was put in service of the bombing of the World Trade Center (February 1993) and in many car bombings in Palestine [39].

Nitrogen-rich trizole (-C-N-): Energetic materials (explosives, propellants and pyrotechnics) are utilized broadly for both civilian and, military applications [40-42]; therefore, it is necessary to explore and understand the behavior of these materials. Insensitive high explosives (IHE) have high detonation properties, which means that they have high density, high detonation velocity, and excellent security properties. The last aspect also ensures that the response to external exigencies such as friction, shock, impact, heat, etc. [40, 41, 43] are met with amiable responses. This makes insensitive high explosives (IHE) highly favored for research. The Nitrogen-rich azole derivatives shows great interest to make use in newer primary and secondary explosives considering their high heats of formation, high density, improved thermal stability, and low sensitivities toward external stimuli [12, 44-48]. Recently, various favorable high-nitrogen-containing energetic materials have been synthesized that show great applications as insensitive high-performance explosives, such as 4-amino-3,5-dinitropyrazole (ADNP), 2,6-diamino-3,5-dinitropyrazine-N-oxide (LLM-105), dihydroxylammonium 5,5'bistetrazole-1,1'-diolate (TKX-50), and 5,5'-dinitro-2H,2H'-3,3'-bi-1,2,4-triazole (DNBT) and dihydroxylammonium 5,5'-bis(3-nitro-1,2,4-triazolate-1 N-oxide) (MAD-X1)[44, 49-51]. The energetic material MAD-XI is one of the most widely used military explosives and thus has been subject to large number of studies [50–52].

#### 1.1 Density functional theory (DFT)

Density functional theory as a quantum-many body technique is abundantly used for studying electronic structure of atoms, molecules and solids. Over the last years, this approach has rapidly grown as the revolutionary of quantum mechanical theory that is used consistently by large numbers of researchers in chemistry, physics, materials science and other disciplines. In case of solving Schrödinger equation, particle wave function is considered as the crucial ingredient which re-

quires  $N^3$  parameters. On the other hand, mathematically, a functional is denoted as follows: y = F[f(x)]. Here, the f(x) function becomes the input for the functional, that is, a function of a function. The energy of the material is a functional of the electron density. Hence, the electron density function is always dependent on three variables (x,y,z).

Electron density =  $\rho$  (x,y,z)

Energy =  $F[\rho(x,y,z)]$ 

So in practical terms, DFT can be said to reduce the  $N^3$ , dimensional problem to three dimensional [53-56].

In the 1960s, Hohenberg and Kohn [57, 58] were successful in developing the Thomas-Fermi theorem to make a definite version of the theory. Further, in 1965 Kohn and Sham were improved to make a practical version of the density functional theory [59].

The expression of electron densities and their correlations for KS theory is as shown below:

$$E_{DFT}[\rho] = T[\rho] + E_{ne}[\rho] + J[\rho] + E_{XC}[\rho]$$
 (1.6)

where E is the energy,  $E_{ne}$  is the nuclear-electron attraction (Coulomb) energy, T is the kinetic energy of the electrons, J is the electron-electron repulsive (Coulomb) energy, and  $E_{xc}$  is the electron exchange-correlation energy.

#### 1.2 Lattice dynamic study in energetic materials

The study of lattice dynamics of energetic materials are pivotal, from which we can know the spectroscopic and thermodynamic properties of a crystal [60–62]. The elucidation of vibrational features (normal mode assignments) has a crucial aid from density functional theory that gives a quantum-mechanical interpretation of the electronic energies and forces involved.

Perturbation theory allows to acquiring the normal vibrational modes by evaluating the derivatives of the Kohn-Sham energy concerning atomic displacements. The linear response method gives a systematic analytical way to calculate the sec-

ond derivative of the total energy regarding a given perturbation [63, 64].

The phonon's properties can be calculated by using an harmonic approximation, whose representation of the lattice vibrations, according to Ref. [65] gives

$$D_{\mu\nu}(R - R') = \left[\frac{\partial^2 E}{\partial u_{\mu}(R)\partial u_{\nu}(R')}\right]_{\nu=0}$$
(1.7)

where E is the total energy in the harmonic approximation and u is the displacement of a given atom. The atomic displacement is expressed in the form of plane waves, i.e.

$$u(R,t) = \epsilon e^{[i(k.R - \omega(k)t)]}$$
(1.8)

the polarization vector of each mode ( $\epsilon$ ) is an eigenvector (with a 3N dimension) of the eigenvalue problem:

$$M\omega(\mathbf{k})^2 \epsilon = D(\mathbf{k})\epsilon \tag{1.9}$$

The phonon density of states for a specified band n is interpreted as

$$N_n(\omega) = \int \frac{d\mathbf{k}}{4\pi^3} \delta \left[ \omega - \omega_n(\mathbf{k}) \right]$$
 (1.10)

where  $\omega_n(k)$  represents the dispersion of a specified band, the integral is computed over the first Brillouin zone.

#### 1.3 Outline of the thesis

The primary objective of the thesis is to provide a clear picture of vibrational and thermodynamic properties of energetic materials, which helps in fundamental understanding and possible insights about atomic lattice behavior of energetic materials. In the present thesis, theoretical approach to demonstrate the structure-property correlations of alkaline-earth metal nitrates; M (NO<sub>3</sub>)<sub>2</sub> (M = Sr, Ba), alkaline earth metal azides; M (N<sub>3</sub>)<sub>2</sub> (M = Sr, Ba), effective initiating explosive cyanuric triazide;  $C_3N_{12}$ , improvised explosive urea nitrate;((NH<sub>2</sub>)COHNO<sub>3</sub>) and nitrogen-rich triazole MAD-X1; dihydroxylammonium 5,5'-bis(3-nitro-1,2,4-

triazolate-1 N-oxide). The investigations include structure stability, Infrared (IR) spectroscopy to understand the vibrational properties. A brief comparison with results of metal nitrate, metal azide, an organic nitrate and, organic azide crystals are also accompanied in order to understand the difference in energetic performances of the metal azide  $M(N_3)_2$  (M = Sr, Ba) crystals when compared to metal nitrate M (NO<sub>3</sub>)<sub>2</sub> (M = Sr, Ba) crystals. In addition, to predict reliable mechanical stability and dynamical stability, elastic and thermodynamic properties obtained by using the linear-response approach implemented in the density functional perturbation theory.

Chapter 1 deals with the brief introduction of alkaline-earth metal azides; M  $(N_3)_2$  (M = Sr, Ba), alkaline-earth metal nitrates; M  $(NO_3)_2$  (M = Sr, Ba), cyanuric triazide;  $C_3N_{12}$ , urea nitrate; ((NH<sub>2</sub>)COHNO<sub>3</sub>) and MAD-X1; dihydroxylammonium 5,5'-bis(3-nitro-1,2,4-triazolate-1 N-oxide).

Chapter 2 provides a short description of Density Functional Theory (DFT) that derives properties of a molecule based on a determination of the electron density of the molecule. DFT is a successful theory to calculate the electron structure of atoms, molecules, and solids. Its goal is the quantitative understanding of material properties from the fundamental laws of quantum mechanics. In addition, the linear-response method within density functional perturbation theory (DFPT) for computing, the phonon properties were described in detail.

In Chapter 3 we have investigated the structural, elastic, vibrational, and thermodynamic properties of  $M(NO_3)_2$  and  $M(N_3)_2$  using an ab initio approach. We found that the van der Waals correction predicts the structural parameters, which are in fair agreement with the experimental values. The elastic constants and phonon spectra of  $M(NO_3)_2$  and  $M(N_3)_2$  confirm the mechanical and dynamical stabilities, while the calculated B/G ratio suggests that the materials are ductile. The phonon modes, their dispersion, and the symmetry and the IR spectra of the crystals were computed. The calculated normal mode frequencies were classified according to irreducible representations for both IR-active and Raman-active modes. IR spectra of  $Sr(NO_3)_2$ ,  $Ba(NO_3)_2$ ,  $Sr(N_3)_2$  and  $Ba(N_3)_2$  were analyzed in close comparison with results of lattice dynamical calculations. The zone-center low-frequency modes are different for  $Sr(NO_3)_2$  and  $Ba(NO_3)_2$ , and this

was predicted for the first time. The contributions of strontium and barium are much larger than those of nitrogen and oxygen atoms in the low-frequency region whereas the high-frequency zone-center modes are relatively the same for both materials as most of the vibrational modes here are due to the nitrate (NO<sub>3</sub>) group, owing to the covalent bonding among nitrogen and oxygen atoms. The vibrations of the azide (N<sub>3</sub>) group exhibits high intensity infrared absorption bands in the ranges of 1900–2100 cm<sup>-1</sup>. A comparison with the work of metal nitrates reveals that the nitrates are shifted towards the smaller wavenumbers than metal azides. Most of the calculated vibrational modes are in satisfactory agreement with the earlier reported experimental data. It has been seen that the calculated phonon dispersion curves of M(NO<sub>3</sub>)<sub>2</sub> and M(N<sub>3</sub>)<sub>2</sub> do not show any imaginary modes, hence both the materials are dynamically stable. The acoustic and first optical branches for M(NO<sub>3</sub>)<sub>2</sub> and M(N<sub>3</sub>)<sub>2</sub> are overlapping, which clearly indicates that both materials possess favorable conditions for thermal transport. Also, as the thermal behavior of these materials could play a key role in the growth of sustainable smoke compositions, the thermodynamic properties, such as entropy, Debye temperature, heat capacity, and enthalpy, at different temperatures ranging from 5 to 1000 K were described.

Chapter 4 the structural, vibrational, and thermodynamic properties of the cyanuric triazide and urea nitrate crystal are investigated through density functional theory (DFT) simulations within the dispersion corrected generalized gradient approximations Grimme (DFT-D2) and Tkatchenko and Scheffler (DFT-TS) by considering the norm-conserving pseudopotentials. Infrared spectra, Born effective charges are computed through the linear response method using the density functional perturbation theory (DFPT). Phonon dispersion curves and phonon density of states are obtained within the harmonic approximation. The calculated thermodynamic properties show that the Debye temperature, specific heat at constant volume, enthalpy, enthalpy, and entropy values increase as a function of temperature, while the free energy falls off as the temperature increases. The vibrational and thermodynamic properties reveal, C<sub>3</sub>N<sub>12</sub> is an effective initiating explosive, and urea nitrate is an improvised explosive.

In chapter 5, the vibrational and thermodynamic properties of MAD-X1 crys-

tal presented by using density functional theory within the GGA-PW91 + OBS approximation. The calculated lattice parameters are compared with the experimental values. The vibrational modes assignments are described in a detailed way. The high-frequency region shows symmetric and asymmetric stretching N-H, O-H bonds. We have presented the phonon dispersion and partial phonon density of states for MAD-X1 crystalline solid by using DFPT. Our results shows the absence of imaginary phonon frequencies in the Brillouin zone, which reveals the dynamical stability of MAD-X1 crystalline solid. The individual atomic contribution in the vibrational modes are displayed in the partial phonon density of states. The thermodynamic properties such as enthalpy (E), entropy (S), free energy (F), heat capacity ( $C_V$ ), and the Debye temperature ( $\Theta_D$ ) were presented in detail. We believe that this work will encourage experimental attempts to reveal the behavior of bis 1,2,4-triazoles and N-oxide derivatives.

Finally, in **chapter 6** presented the conclusion of thesis and future scope.

#### References

- [1] M. B. Talawar, R. Sivabalan, T. Mukundan, H. Muthurajan, A. K. Sikder, B. R. Gandhe and A. S. Rao, J. Hazard. Mater., 161, 589 (2009).
- [2] M. B. Talawar, J. P. Agrawal, M. Anniyappan, D. S. Wani, M. K. Bansode and G. M. J. Gore, Hazard. Mater., **B137**, 1074 (2006).
- [3] D. M. Badgujar, M. B. Talawar, S. N. Asthana and P. P. J. Mahulikar, Hazard. Mater., 151, 289 (2008).
- [4] D. Schmitt, P. Eyerer and P. Elsner, Propellants, Explos. Pyrotech., 22, 109 (1997).
- [5] A. A. Dippold and T.M. Klapötke, J. Am. Chem. Soc., 135, 9931 (2013).
- [6] R. Meyer, J. Kohler and A. Homburg, Explosives, *Wiley-VCH*; *Verlag GmbH*, *Weinheim*, (2007).
- [7] S. Meyers and E. S. J. Shanley, Hazard. Mater., 23, 183 (1990).
- [8] J. Zhang, L.A. Mitchell, D.A. Parrish, J.N.M. Shreeve, J. Am. Chem Soc. 137 (2015) 10532–10535.
- [9] Q. Zhang, J.N.M. Shreeve, Angew. Chem. Int. Ed. 52 (2013) 8792-8794.
- [10] J. Zhang, S. Dharavath, L.A. Mitchell, D.A. Parrish, J.N.M. Shreeve, J. Am. Chem. Soc. 138 (2016) 7500–7503.
- [11] G.H. Seyed, E. Abbas, J. Therm. Anal. Calorim. 101 (2010) 1111-1119.
- [12] T.M. Klapötke, G. Steinhauser, Angew. Chem. Int. Ed. 47 (2008) 3330–3347.
- [13] K.O. Brauer, Handbook of Pyrotechnics, Chemical Publishing Co., New York, 1974.
- [14] C. Michael, Propellants Explos. Pyrotech. 37(2012) 639-646.
- [15] C. E. Hathaway, P. temple, J. Phys. Rev. B, 3 (1971) 3497–3502.

12 REFERENCES

- [16] P. Gray, T. C. Waddington, Trans. Faraday Soc., 53 (1957) 901–908.
- [17] H. D. Fair, R. F. Walker, Eds. In Energetic Materials, Plenum Press, New York, 1977.
- [18] F. P. Bowden, A. D. Yoffe, Angew. Chem., 71 (1959) 752–752.
- [19] B.L. Evans, A.D. Yoffe, P. Gray, Chem. Rev., 59 (1959) 515–568.
- [20] H. Zhu, X. Han, P. Zhu, X. Wu, Y. Chen, L. Miaoran, L. Xuefeng, Q. Cui, J. Phys. Chem. C, 120 (2016) 12423–12428.
- [21] M. V. Huynh, M.D. Coburn, T.J. Meyer, M. Wetzler, Proc. Natl. Acad. Sci. U S A. 103 (2006) 10322–10327.
- [22] D. Kumar, A.J. Elias, Resonance 24 (2019) 1253-1271.
- [23] B.Adivaiah, G. Vaitheeswaran, J. Phys. Chem. Solids., 8 (2018) 9388.
- [24] L.M. Foroughi, R.A. Wiscons, D.R. Du Bois, A.J. Matzger, Chem. Commun. 56 (2020) 2111-2114.
- [25] G.G. Edward, Chem. Mater. 12 (2000) 3906–3912.
- [26] E. Kroke, M. Schwarz, Adv. Mater. 11 (1999) 158-161.
- [27] R. Meyer, Explosives, VCH, New York, (1987) 70.
- [28] D. Laniel, L.E. Downie, J.S. Smith, D. Savard, M. Murugesu, S. Desgreniers, J. Chem. Phys. 141 (2014) 234506(1–10).
- [29] L.E. Downie, Pathways to Recovering Single-Bonded Nitrogen at Ambient Conditions: High Pressure Studies of Molecular and Ionic Azides, Canada, 2010.
- [30] E. Ott, E. Ohse, E. Ber, Dtsch. Chem. Ges. 54 (1921) 179.
- [31] E. Kessenich, T.M. Klapötke, J. Knizek, H. Noth, A. Schulz, Eur. J. Inorg. Chem. 1998 (1998) 2013–2016.

- [32] J. Akhavan, The Chemistry of Explosives, Royal Society of Chemistry, London, 2004.
- [33] G. Johann, T.M. Klapötke, J.J. Sabatini, RSC Adv. 54 (2018) 821-824.
- [34] J.A. Conkling, M. Chris, Chromatogr. Sci. Ser. 75 (2012) 79–80.
- [35] T.P. Forbes, S.T. Krauss, G. Gillen, Trends Anal. Chem. 131 (2020) 116023.
- [36] S. Li, Q. Li, K.Wang, M.Zhou, X. Huang, J. Liu, Ke. Yang, B. Liu, T.Cui, G. Zou, Bo. Zou, J. Phys. Chem. C, 2013, 117, 152159.
- [37] R. I. Hiyoshi and J. Nakamura, Explosion Properties of Urea Nitrate and its Analysis, Proc. 6th Int. Symp. Anal. Det. Expl. Prague, CZ, 1998, paper 15.
- [38] R. I. Hiyoshi and J. Nakamura, Explosion Properties of Urea Nitrate, Kayaku Gakkaishi, 61 (2000) 120-123.
- [39] D. Price, "Contrasting Patterns in the Behavior of High Explosives", Eleventh Symp. (Int) Combustion, The Combustion Institute, Pittsburgh, PA, pp. 693-702, 1967.
- [40] J.P. Agrawal, Prog. Energy Combust. Sci., 24 (1998), p. 1
- [41] J. Akhavan, The chemistry of explosives. Gmbridge, UK: R. Soc. Chem., 2011.
- [42] D. Bedrova, G. D. Smith, and T. D. Sewell. 2000, J. Chem. Phys., 112 (2000) 7203–7208.
- [43] P. Pagoria, Propellants, Explosives, Pyrotechnics, 2016 Wiley Online Library.
- [44] A. A. Dippold, T. M. Klapötke, Chem. Eur. J., 18 (2012) 16742–16753.
- [45] Fischer, N.; Klapötke, T. M.; Reymann, M.; Stierstorfer, Eur. J. Inorg. Chem. 2013, 12, 2167–2180.

14 REFERENCES

[46] Dachs, M.; Dippold, A. A.; Gaar, J.; Holler, M.; Klapötke, T. M., Z. Anorg. Allg. Chem. 2013, 639, 2171–2180.

- [47] Zhang, Y.; Parrish, D. A.; Shreeve, J. M., J. Mater. Chem. A 2013, 1, 585–593.
- [48] Klapötke, T. M.; Piercey, D. G.; Stierstorfer, Eur. J. Inorg. Chem. 2013, 9, 1509–1517.
- [49] Singh, R. P.; Verma, R. D.; Meshri, D. T.; Shreeve, J. M., Angew. Chem., Int. Ed. 2006, 45, 3584–3601.
- [50] J. C. Bennion, J. A. Ciezak-Jenkins, T. A. Jenkins, Propellants Explos. Pyrotech., 44 (2019) 1263–1269.
- [51] Fischer, N.; Fischer, D.; Klapötke, T. M.; Piercey, D. G.; Stierstorfer, J., J. Mater. Chem. 2012, 22, 20418–20422.
- [52] Dippold, A. A.; Klapötke, T. M., J. Am. Chem. Soc. 2013, 135, 9931-9938.
- [53] P. W. Atkins and R. S. Friedman, *Molecular Quantum Mechanics*, Oxford University Press, Oxford (1997).
- [54] F. Jensen, *Introduction to Computational Chemistry*, Wiley, Chichester (1999).
- [55] T. Helgaker, P. Jørgensen and J. Olsen, *Molecular Electronic–Structure Theory*, Wiley, Chichester (2000).
- [56] W. Koch and M. C. Holthausen, A Chemists's Guide to Density Functional Theory, Wiley-VCH (2001).
- [57] P. Hohenberg and W. Kohn, Phys. Rev., 136 (1964) B864–B871.
- [58] W. Kohn. Rev. Mod. Phys., 71 (1999) 1253–1266.
- [59] W. Kohn and L. Sham, Phys. Rev., 140 (1965) A1133-A1138.

- [60] Z. Wu, K. Rajiv K., N. Aiichiro, P. Vashishta, J.Chem.Phy. 134 (2011) 204509(1-10).
- [61] J.J. Haycraft, L.L. Stevens, C.J. Eckhardta, J.Appl.Phys. 100 (2006) 053508(1-9).
- [62] Z. Sheng-Hai, Q. Han, Z. Wei, C. Ying-Meng, J. Xu-Yang, W. Yu-Hang, L. Fu-Sheng, T. Bin, L. Qi-Jun, J.Mol.Model 25 (2019) 182(1–16).
- [63] E.L.Albuquerque, D.R.Tilley, Solid State Commun. 26 (1998) 317-821.
- [64] C.A.Barboz, E.L.Albuquerque, C.Chesmana V.N.Freire, Phys. Lett. A, 255 (1998) 478–482.
- [65] S. Baroni, S. de Gironcoli, A. dal Corso, P. Giannozzi, Rev. Mod. Phys. 73 (2001) 515.

## Theoretical background

This chapter gives a brief introduction to the basic theory and computational details involved in this thesis. The Density Functional Theory (DFT) formalism along with exchange-correlational functionals was also presented [1-3]. The density functional perturbation (DFPT) theory which is used to compute reliable vibrational properties, were explained in detail. Finally, the thermodynamic properties (i.e., enthalpy, entropy, heat capacity, and Debye temperature) within the Quasi-Harmonic Approximation were described.

#### 2.1 Introduction to the many body Hamiltonian

The wave function of a particle is known to provide all the information regarding that system. This wave function can be obtained by solving the well known Schrödinger equation.

$$H\psi = E\psi \tag{2.1}$$

Here H is hamiltonian operator and it can be described as

$$H = \frac{\hat{p}^2}{2m} + V(x) \tag{2.2}$$

The Hamiltonian operator for a system can be expressed as

$$H = -\sum_{i} \frac{\hbar^{2} \nabla_{i}^{2}}{2M_{i}} + \frac{1}{2} \sum_{i,j} \frac{Z^{2} e^{2}}{|R_{i} - R_{j}|} - \sum_{k} \frac{\hbar^{2} \nabla_{k}^{2}}{2m_{k}} + \frac{1}{2} \sum_{k,l} \frac{e^{2}}{|r_{k} - r_{l}|} - \sum_{k,i} \frac{Z e^{2}}{|r_{k} - R_{i}|}$$

$$(2.3)$$

Here, the first term corresponds to the kinetic energy of the nuclei  $(T_N)$ , whereas the second term represents coulomb repulsive term between the nuclei  $(V_{NN})$ , the third term is the kinetic energy terms of the electrons, the fourth term coulomb repulsive interactions between the electrons and the last term is the coulomb attractive interaction between the electrons and the nuclei  $(V_{Ne})$ . As this equation involves a combination of different interactions, the complex nature of this Hamiltonian is quite evident. To reduce this complexity, different approximations are being considered. Among this Born-Oppenheimer approximation is the first one that will simplify the above Hamiltonian.

#### 2.2 Born-Oppenheimer approximation

According to Born-Oppenheimer approximation[4], above Hamiltonian can be formulated by decoupling the nuclear and electronic motions.

$$H = -\sum_{k} \frac{\hbar^{2} \nabla_{k}^{2}}{2m_{k}} + \frac{1}{2} \sum_{k,l}^{N} \frac{e^{2}}{|r_{k} - r_{l}|} - \sum_{k,i} \frac{Ze^{2}}{|r_{k} - R_{i}|}$$
(2.4)

With this simplification, the set of equations are now separable. Though, this approximation reduced the complex nature of this Hamiltonian in terms of electronic coordinates only still the complexity is present due to the electron-electron interaction present in the system.

The complexity of electron-electron interaction can be reduced by considering the Hartree approximation, where the many electronic systems is considered to constitute non-interacting electrons. This approximation provides the wave function of the system as the product of wave functions of constituent particles. The main drawback of this approximation is that it doesn't consider the antisymmetric nature of wave function. As a result, Hartree-Fock Approximation is coming into the picture.

#### 2.3 Hartree-Fock Approximation

In Hartree-Fock method [5], the wave function is described as a slater determinant of one-electron wave functions. The expression of wave function can be written as

$$\Psi(r_{1}\sigma_{1},...,r_{N}\sigma_{N}) = \frac{1}{\sqrt{N!}} \begin{pmatrix}
\psi_{1}(r_{1}\sigma_{1}) & \psi_{1}(r_{2}\sigma_{2}) & . & . & \psi_{1}(r_{N}\sigma_{N}) \\
\psi_{2}(r_{1}\sigma_{1}) & \psi_{2}(r_{2}\sigma_{2}) & . & . & \psi_{2}(r_{N}\sigma_{N}) \\
. & . & . & . & . \\
. & . & . & . & . \\
\psi_{N}(r_{1}\sigma_{1}) & \psi_{N}(r_{2}\sigma_{2}) & . & . & \psi_{N}(r_{N}\sigma_{N})
\end{pmatrix} (2.5)$$

Here N represents the number of electrons in the system.

And the energy minimization of Hartree-Fork equation can be describes as

$$[-\frac{\hbar^2}{2m}\nabla^2 + V_{ext} + V_d(r_i)]\Psi_i(r_i) - \sum_j \int d' \frac{e^2}{|r - r'|} \Psi_j^*(r')\psi_i(r')\Psi_j(r)\delta_{\sigma_i\sigma_j} = \epsilon_i \Psi_i(r_i)$$
(2.6)

In the above equation, the slater determinant operator between electrons with the same spin is known as the exchange term. And the correlation interaction occurs due to antisymmetric nature of the wave function. The difference between the exact energy and the Hartree-Fock energy can be expressed as the correlation energy. However, the equations are still nonlinear and have to be solved self consistently by iteration.

#### 2.4 Thomas-Fermi Theory

In Thomas and Fermi model, the full electron density is considered as the fundamental variable of the many-body problem. The representation of total electronic energy can be expressed in terms of kinetic energy, electron-nucleus, and electron-electron interaction derived from homogeneous electron gas [8, 7].

$$E_{\alpha}[\rho] = \int \rho(r)\epsilon_{\alpha}[\rho(r)]dr \qquad (2.7)$$

Here  $\epsilon[\rho(r)]$  is the energy density of contribution  $\alpha$  (kinetic, exchange, correlation)

The electron density is corresponds to fermi energy  $(\epsilon_F)$  in the case of homogeneous gas, and the correlation is given by

$$\rho = \frac{1}{3\pi^2} \left(\frac{2m}{\hbar^2}\right)^{\frac{3}{2}} \epsilon_F^{\frac{3}{2}} \tag{2.8}$$

The kinetic energy is given by  $T = (\frac{3}{5})\rho\epsilon_F$ . Hence the kinetic energy density can be written as

$$t[\rho] = \frac{3}{5} \frac{\hbar^2}{2m} (3\pi^2)^{\frac{2}{3}} \rho^{\frac{2}{3}}$$
 (2.9)

The is the first time when the LDA kinetic energy as been obtain can found from this equation and the form is

$$T_{TF} = C_k \int \rho(r)^{\frac{5}{3}} dr, \qquad (2.10)$$

where the value of  $C_k = 2.871$  hartree (the atomic unit of energy).

The final form of the total energy expression regarding the thomas fermi model is as follows

$$E_{TFD}[\rho] = C_k \int \rho(r)^{\frac{5}{3}} dr + \int \rho(r) v_{ext}(r) dr + \frac{1}{2} \int \int \frac{\rho(r)\rho(r')}{|r - r'|} dr dr' \qquad (2.11)$$

where the exchange energy is not treated and can be considered using the Thomas-Fermi-Dirac model

#### 2.5 Density functional theory

At the same time as Thomas fermi model, a similar approach has been considered by Hohenberg and Kohn [8–10], which is the base of DFT. In DFT, the density relies upon the spatial coordinates of an individual electrons.

In the case of solving Schrödinger's equation, the particle wave function is considered as the crucial ingredient which requires  $N^3$  parameters. On the other hand, mathematically, a functional is denoted as follows: y = F[f(x)]. Here, the f(x) function becomes the input for the functional, that is, a function of a function. The energy of the material is a functional of the electron density. Hence, the electron density function is always dependent on three variables (x,y,z).

Electron density =  $\rho$  (x,y,z)

Energy =  $F[\rho(x,y,z)]$ 

So in practical terms, DFT can be said to reduce the  $N^3$ , dimensional problem to three dimensional [1-3], [10].

The density functional theory is based on the two theorems, which are as follows:

**Theorem-1:** For interacting particles of any system in an external potential  $V_{ext}(r)$ , the ground-state particle density,  $n_0(r)$ , uniquely determines the potential  $V_{ext}(r)$  (up to an additive constant).

**Theorem-2:** The electron density n(r) that minimizes the energy E[n(r)] of the overall functional is the true electron density corresponding to the full solution of the Schrödinger equation.

Based on Hohenberg-Kohn theorems[8-10]:

The ground state expectation value of an observable is a functional of  $n_0$ , which is also true for the ground state energy. The functional of  $n_0$  can be written as

$$E_0 = E[n_0] = \langle \Psi_0[n_0] | \hat{T} + \hat{V} + \hat{U} | \Psi_0[n_0] \rangle$$
 (2.12)

T[n] and U[n] are known as universal functionals and the V[n] is non-universal functional. The minimization of this functional

$$E[n] = T[n] + U[n] + \int V(r)n(r)d^{3}r$$
 (2.13)

with respect to  $n(\vec{r})$  will provide the ground state density  $n_0$  and all other ground state observable.

To solve the minimization problem firstly, we have to assume an energy functional, without electron-electron interaction energy term,

$$E_{s}[n] = \langle \Psi_{s}[n]|\hat{T} + \hat{V}_{s}|\Psi_{s}[n]\rangle \tag{2.14}$$

Where  $\hat{T}$  is the kinetic energy operator and  $\hat{V}_s$  is the external effective potential. Now we can solve the Kohn-Sham[11] equations of this auxiliary non-interacting a system where the equation is given as

$$\left[-\frac{\hbar^2}{2m}\nabla^2 + V_s(r)\right]\phi_i(r) = \epsilon_i\phi_i(r) \tag{2.15}$$

After solving this we will get  $\psi_i$  and from which we will be able to get the density  $n(\vec{r})$  of the original many body system

$$n_s(r) = \sum_{i}^{N} |\phi_i(r)|^2$$
 (2.16)

The equation below describes the effective single-particle potential  $V_s$ .

$$V_{s} = V_{Ext} + V_{H} + V_{XC}[n_{s}(r)]$$
 (2.17)

where

$$V_H = \int \frac{e^2 n_s(r')}{|r - r'|} d^3 r'$$
 (2.18)

corresponding to the electron-electron coulomb repulsion and  $V_{XC}[n_s(\vec{r})]$  is the exchange-correlation potential, which involves many-particle interactions. This Kohn-sham equation has to be solved iteratively in a self-consistent way. This self-consistent calculation will follow the algorithm shown below.

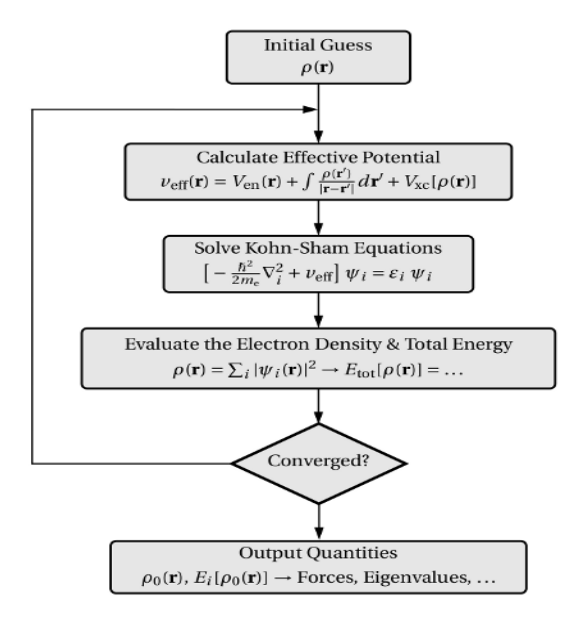


Figure 2.1: DFT Algorithm

# 2.6 Exchange-correlation functionals

The research direction of computational material science is advanced towards the use of approximations for  $E_{XC}$ . To get a sustainable and consistent analysis, we need an accurate approximation to the exchange-correlation energy ( $E_{XC}$ ) within the Kohn-Sham DFT. By comparing the theoretical results with experimental data, we can judge the accuracy of the approximations taken to construct the functional.

$$E_{xc}[n] = \int n(r)\epsilon_{xc}[n(r)]dr \qquad (2.19)$$

In the above equation,  $\epsilon_{xc}$  signifies the exchange-correlation energy per particle for a homogeneous electron gas that is evaluated at the local density denoted with n(r).

The expression of exchange energy of an electron in a homogeneous electron

gas of a particular density [12, 13].

$$\epsilon_x = -\frac{3}{4} \left(\frac{3n(r)}{\pi}\right)^{\frac{1}{3}} \tag{2.20}$$

However, the Local Density Approximation (LDA) will give significant error in computed energy differences, volume, elastic constants. So with years, the Generalized Gradient approximation (GGA) improved upon the LDA representations.

GGA mainly focused to introduce to the density gradient  $\nabla n(r)$ , considering for "non-locality" in realistic systems [14]. The generalized gradient approximation (GGA)  $E_{xc}$  as

$$E_{xc}^{GGA}[n] = \int f(n(r), \nabla n(r)) dr$$
 (2.21)

In the GGA functional, Perdew-Wang functional (PW91) and the Perdew-Burke-Ernzerhof functional (PBE) are most common functionals.

#### 2.7 van der Waals (vdW) in DFT

We also encounter another circumstance where DFT calculations give inappropriate results due to weak van der Waals (vdW) attractions that exist between atoms and molecules. We need high-level wave function-based methods and tools from quantum mechanics to calculate the strength of these interactions accurately and, also it should treat the electron correlation in a systematic way.

By following such approach ,the total energy of a system is the sum of the Kohn-Sham energy  $E_{KS}$  and the dispersion correction  $E_{disp}$ 

$$E_{DFT+D} = E_{KS} + E_{disp} (2.22)$$

 $E_{disp}$  is the sum of overall individual attractive atom pair contributions, which mainly depends on the dispersion coefficients and the inter-atomic distance.

The general formula for empirical dispersion corrections can be written as:

$$E_{disp} = -\sum_{AB} \sum_{n=6,8,10,\dots} \frac{C_n^{AB}}{R_{AB}^n} f_{damp}(R_{AB}, A, B), \qquad (2.23)$$

Here,  $C_n^{AB}$  describes the isotropic (averaged)  $n^{tb}$ -order dispersion coefficient for atom pair AB and  $R_{AB}$  as their internuclear distance. The first sum represents over all atom pairs in the system, The leading term of the expansion in the above equation with n = 6 expresses the correct asymptotic behavior of the potential, while the higher-order terms signify its shape at shorter distances. In addition, a damping function  $f_{damp}$  is used to avoid singularities at short distances.

According to literature, many energetic solids contains van der Waals (vdW) interactions [15–21]. The results can give a clear picture of the fact that GGA overestimates and LDA underestimates the crystal volumes by nearly ~30% when compared to experimental results. Grimme and co-workers developed empirical corrections such as DFT-D or DFT+E<sub>disp</sub> models. The corrections to PBE by Grimme (DFT-D2) [22] and Tkatchenko, Scheffler (DFT-TS) [23]. and, for PW91 the dispersion scheme proposed by Ortmann, Bechstedt, Schmidt (OBS) [24] is the most successful method. In this thesis, such successful methods are used to get an overall intrinsic description. The basic difference between DFT-TS and other vdW correction method is that the bond polarizability, as well as the chemical composition of the atoms, are considered in DFT-TS whereas, only chemical composition is considered in other methods.

### 2.8 Pseudopotentials method

The crucial point of concern in a solid material is that the wave function behaves peculiarly at various distances from the nuclei.

The atomic wavefunctions are the eigenstates of the atomic Hamiltonian, and the core and valence electronic wave functions are mutually orthogonal to each other. Around the nucleus, the core states are well localized, so we need a large basis to precisely illustrate the oscillations in the core regions. This needs an allelectron plane-wave calculation and hence increases the computational cost. We can eliminate such problem by treating the core and valence electrons differently.

The concept of Pseudopotential is related to replacing the effect of the core electrons with an effective potential. The electronic states of an atom categorized into:(1) Extended valence states which is mainly accountable for chemical bonding, (2) Localized and polarizable semi-core states that do not imply directly to chemical bonding and (3) Highly localized core states that do not take part in chemical bonding.

One such brief demonstration of the concept behind the pseudopotential approach is shown in figure 2.1.

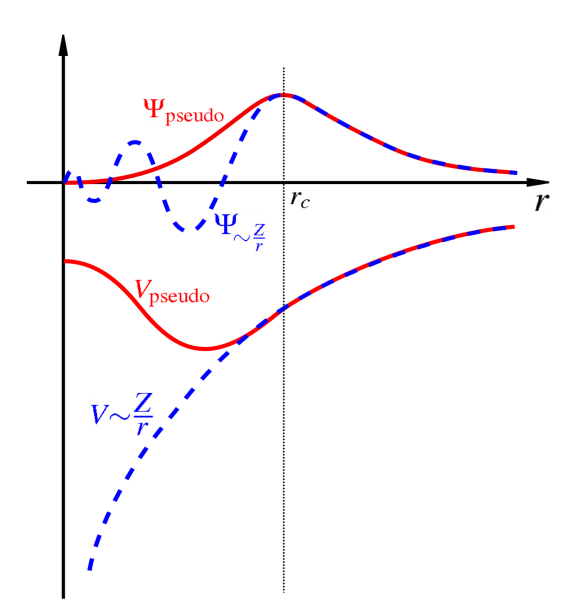


Figure 2.2: Schematic illustration of the concept behind the pseudopotential approach. The dashed lines show the all-electron wavefunction and ionic potential; while the corresponding pseudo wavefunction given by the pseudopotential is plotted in solid lines. All quantities are represented as a function of distance, r, from the atomic nucleus. The point beyond which the all-electron and pseudo-electron values become identical is designated as cutoff radius.

#### 2.8.0.1 Norm-conserving pseudopotentials

Pseudopotentials not only reduce the number of orbital but also basis sets, which intern reduces the computation time. However, the accuracy of pseudopotentials and transferability can be assessed by their potentiality to reproduce quantities from all–electron calculations over a wide range of various chemical compounds. Two properties, softness and transferability, are mainly related to the cutoff radius, and there is a competition between them. The higher the cutoff, the softer the pseudopotentials. But the low cutoffs give pseudopotentials with a promising transferability [25]. Therefore, the best smoothness and transferability can be achieved using norm-conserving pseudopotential (NCPP) developed by Hamann and co-workers. In this approach the norm of the psuedo-wave function and all electron wave function remains the same inside the cut-off radius.

The NCPP pseudo-potential needs a comparatively large number of plane waves for "semilocal" orbitals of elements. The reason behind that is about their substantial fraction inside the core region and their consequence to the bonding.

#### 2.8.0.2 Ultra-soft pseudopotentials

The basic requirement of pseudo-potentials is to create smooth pseudo wave functions with suitable reliability. We can obtain a much softer pseudo wave function with the minimum number of Fourier components. Hence it always requires large cutoff energy that remarkably increases the computational cost. In order to terminate this issue Vanderbilt [26] suggested a new modification for generating such pseudo-potentials. In this approach, they removed the norm-conservation constraint and considered the condition that the psudo wave function inside the core region must have the same density as the all-electron wave function. However, with such approach a much softer pseudo wave function can be achieved that employs only fewer plane-waves for calculations with similar accuracy; it's called ultra-soft pseudo-potentials. Such ultra-soft and norm-conserving pseudopotential methods are implemented through CAmbridge Series of Total Energy Package (CASTEP) [27] in the present thesis.

# 2.9 Density Functional Perturbation Theory (DFPT)

Linear response, or Density Functional Perturbation Theory (DFPT), is one of the preferred methods of ab initio calculation of lattice dynamics [28]. However, the applicability of the method extends over the study of vibrational properties. The linear response method provides an analytical way to compute the second derivative of the total energy with respect to a given perturbation. Depending on the nature of this perturbation, a number of properties can be calculated. For example, perturbation in the ionic positions gives the dynamical matrix and phonons, whereas perturbation in the magnetic field yields on NMR response. Similarly, one in the unit cell vectors gives us the elastic constants, while a perturbation in the electric field means its dielectric response. Likewise, other factors can be calculated in this manner [29].

Within the scope of the Born-Oppenheimer approximation, the properties of any system related to lattice dynamics are known to be determined using the Schrödinger equation of the form:

$$\left(-\sum_{I} \frac{\hbar^2}{2M_I} \frac{\partial^2}{\partial R_I^2} + E(R)\right) \Phi(R) = \epsilon \Phi(R), \tag{2.24}$$

Here, the nuclear coordinate and mass of the  $I^{th}$  nucleus are denoted by  $R_I$ ,  $M_I$ , respectively. E(R) represents the system clamped-ion energy and is also known as the Born-Oppenheimer surface energy. Practically, E(R) is the ground-state energy of an interacting electron system in the fixed nuclei field. The Hamiltonian of this system can be expressed as

$$H_{BO}(R) = -\frac{\hbar^2}{2m} \sum_{i} \frac{\partial^2}{\partial r_i^2} + \frac{e^2}{2} \sum_{i \neq j} \frac{1}{|r_i - r_j|} - \sum_{il} \frac{Z_l e^2}{|r_i - R_I|} + E_N(R), \qquad (2.25)$$

This  $H_{BO}(R)$  depends on R parametrically and acts onto the electronic variables.

The number of electrons associated with the  $I^{th}$  nucleus is denoted by  $Z_I$ , and e is known as an electronic charge. The last term represents the electrostatic

interaction between various nuclei:

$$E_N(R) = \frac{e^2}{2} \sum_{i \neq j} \frac{Z_I Z_J}{|R_I - R_J|}$$
 (2.26)

It is a well-known condition that all the forces on individual nuclei should vanish for obtaining any system's equilibrium geometry.

$$F_I = -\frac{\partial E(R)}{\partial R_I} = 0 (2.27)$$

In this context, the Hessian of E(n) is considered for obtaining the vibrational frequencies. The relevant equation can be expressed as:

$$det \left| \frac{1}{\sqrt{M_I M_I}} \frac{\partial^2 E(R)}{\partial R_I \partial R_J} - \omega^2 \right| = 0$$
 (2.28)

This leads to the importance of computation of the first and the second derivative of E(R). Use of the Hellmann-Feynman theorem in this connection is found to be very significant as this theorem states that the first eigenvalue derivative of a Hamiltonian,  $H_{\lambda}$ , which is dependent on a parameter  $\lambda$  can be written as the expectation value of the derivative of  $H_{\lambda}$ :

$$\frac{\partial E_{\lambda}}{\partial \lambda} = \left\langle \Psi_{\lambda} \left| \frac{\partial H_{\lambda}}{\partial \lambda} \right| \Psi_{\lambda} \right\rangle, \tag{2.29}$$

Here,  $\Psi_{\lambda}$  denotes the eigenfunction of  $H_{\lambda}$  associated to the  $E_{\lambda}$  eigenvalue:  $H_{\lambda}\Psi_{\lambda}=E_{\lambda}\Psi_{\lambda}$ . As the nuclear coordinates act as parameters according to the Born-Oppenheimer approximation, the force on the *I*th nucleus can be obtained using

$$F_{I} = -\frac{\partial E(R)}{\partial R_{I}} = -\left\langle \Psi(R) \left| \frac{\partial H_{BO}(R)}{\partial R_{I}} \right| \Psi(R) \right\rangle, \tag{2.30}$$

 $\Psi(r,R)$  denotes the ground-state electronic wave function of the Born-Oppenheimer Hamiltonian. This  $H_{BO}(R)$  is dependent on the parameter R through the electronion interaction. In this connection, the Hellmann-Feynman theorem states that

$$F_{I} = -\int n_{R}(r) \frac{\partial V_{R}(r)}{\partial R_{I}} dr - \frac{\partial E_{N}(R)}{\partial R_{I}}, \qquad (2.31)$$

Here, the interaction of electron and nucleus has been denoted using  $V_R(r)$ .

$$V_R(r) = -\sum_{il} \frac{Z_l e^2}{|r_i - R_I|},$$
 (2.32)

 $n_R(r)$  represents the electron charge density at the ground-state corresponding to the nuclear configuration R. The Hessian of E(R) can be obtained using the differentiation of the Hellmann-Feynman forces concerning nuclear coordinates,

$$\frac{\partial^2 E(R)}{\partial R_I \partial R_I} = -\frac{\partial F_I}{\partial R_I} = \int \frac{\partial n_R(r)}{\partial R_I} \frac{\partial V_R(r)}{\partial R_I} dr + \int n_R(r) \frac{\partial^2 V_R(r)}{\partial R_I \partial R_I} dr + \frac{\partial^2 E_N(R)}{\partial R_I \partial R_I}$$
(2.33)

This equation tells that the evaluation of the Hessian of E(R) requires the computation of the ground-state electron charge density  $n_R(r)$  along with its linear response for a nuclear distortion,  $\frac{\partial n_R(r)}{\partial R_I}$ . The Hessian matrix usually is called the interatomic force constants matrix.

DFT provides a crucial part that comes under elucidation of vibrational properties under normal mode assignments, which furnish a quantum-mechanical description of involved forces and electronic eigen-energies. One can acquire normal vibrational modes from the equations of the Kohn-Sham energy with regards to atomic displacement under perturbation [30, 31].

The phonon's properties can be calculated by using Quasi-Harmonic Approximation, whose interpretation of the lattice vibrations, according to Ref. [28] gives

$$D_{\mu\nu}(R - R') = \left[\frac{\partial^2 E}{\partial u_{\mu}(R)\partial u_{\nu}(R')}\right]_{u=0}$$
 (2.34)

where E is the total energy in the harmonic approximation and u is the displacement of a given atom.

Each atomic displacement is described as a plane waves, i.e.

$$u(R,t) = \epsilon e^{[i(k.R - \omega(k)t)]}$$
(2.35)

The eigenvector (with a 3N dimension)of the eigenvalue problem described below with respect to polarization vector of each mode  $\epsilon$ 

$$M\omega(\mathbf{k})^2\epsilon = D(\mathbf{k})\epsilon \tag{2.36}$$

The phonon density of states for a specified band n is described as

$$N_n(\omega) = \int \frac{d\mathbf{k}}{4\pi^3} \delta \left[ \omega - \omega_n(\mathbf{k}) \right]$$
 (2.37)

where  $\omega_n(k)$  represents the dispersion of a specified band and calculated over the first Brillouin zone.

# 2.10 Thermodynamic properties using Quasi-Harmonic approximation

The thermodynamic properties are highly related to the vibrational properties of a material. So the results of a calculation of phonon spectra can be used to compute the thermodynamic properties like enthalpy (H), free energy (F), the temperature times entropy (T× entropy) term, TS = U - F (U represents internal energy), and also the lattice heat capacity ( $C_V$ ) with temperature dependence. The calculations of H, F, TS, and  $C_V$  at finite temperatures can be done with the vibrational contribution to the thermodynamic properties as discussed below.

The temperature-reliant of the thermodynamic potentials can be expressed Ref. [28]. For the enthalpy H we have

$$H(T) = E_{tot} + E_{zp} + k_B T \int \frac{\hbar \omega}{e^{\frac{\hbar \omega}{k_B T}} - 1} N(\omega) d\omega$$
 (2.38)

where  $k_B$  is Boltzmann's constant,  $E_{zp}$  is the zero point vibrational energy,  $N(\omega)$  is the phonon density of states and  $\hbar$  is Planck's constant.

32 REFERENCES

The free energy (F) can be described with contribution of vibrational energy is

$$F(T) = E_{tot} + E_{zp} + k_B T \int \ln(1 - e^{-\frac{\hbar\omega}{k_B T}}) N(\omega) d\omega$$
 (2.39)

The temperature times the entropy term, TS = U-F, we have

$$TS(T) = k_B T \left[ \int \frac{\frac{\hbar \omega}{k_B T}}{e^{\frac{\hbar \omega}{k_B T}} - 1} N(\omega) d\omega - \int (1 - e^{-\frac{\hbar \omega}{k_B T}}) N(\omega) d\omega \right]$$
(2.40)

here, TS (T) being used instead of S(T) to emphasize the contribution of the thermodynamic potentials.

Also, the heat capacity  $C_V$ , with respect to T, has been determined at zero pressure. The contribution of lattice can be expressed for  $C_V$  is [28]

$$C_V(T) = k_B T \left[ \int \frac{\left(\frac{\hbar\omega}{k_B T}\right)^2 e^{\frac{\hbar\omega}{k_B T}}}{\left(e^{\frac{\hbar\omega}{k_B T}} - 1\right)^2} N(\omega) d\omega \right]$$
(2.41)

The heat capacity through the Debye model, as specified by [32]

$$C_V^{Debye}(T) = 9Nk_B \left(\frac{T}{\theta_D}\right)^3 \int_0^{x_D} \frac{x^4 e^x}{(e^x - 1)^2} dx$$
 (2.42)

Here N represents the number of atoms per cell.

#### References

- [1] P. W. Atkins and R. S. Friedman, *Molecular Quantum Mechanics*, Oxford University Press, Oxford (1997).
- [2] F. Jensen, *Introduction to Computational Chemistry*, Wiley, Chichester (1999).
- [3] T. Helgaker, P. Jørgensen and J. Olsen, *Molecular Electronic–Structure Theory*, Wiley, Chichester (2000).
- [4] M. Born and J. R. Oppenheimer, Am. J. Phys., 84 (1927) 457-484.

- [5] V. A. Fock, Z. Phys, 61 (1930) 126-148.
- [6] L. H. Thomas, Proc. Cambridge Phil. Soc., 23 (1927) 542-548.
- [7] E. Fermi, Z. Phys., 48, (1928) 73–78.
- [8] P. Hohenberg and W. Kohn, Phys. Rev., 136 (1964) B864-B871.
- [9] W. Kohn. Rev. Mod. Phys., 71 (1999) 1253–1266.
- [10] W. Koch and M. C. Holthausen, A Chemists's Guide to Density Functional Theory, Wiley-VCH (2001).
- [11] W. Kohn and L. Sham, Phys. Rev., 140 (1965) A1133-A1138.
- [12] F. Bloch, Z. Physik, 52 (1929) 555-600.
- [13] P. A. M. Dirac, Proc. Roy. Soc. Lond. A, 123 (1929) 714–733.
- [14] J. P. Perdew, M. Ernzerhof and K. Burke, J. Chem. Phys., 105 (1996) 9982-9985.
- [15] M. S. Miao, Z. A. Dreger, J. M. Winey and Y. M. Gupta, J. Phys. Chem. A, 112 (2008) 12228-12234.
- [16] J. J. Zhao and H. Liu, Comput. Mater. Sci., 42 (2008) 698–703.
- [17] S. Appalakondaiah, G. Vaitheeswaran and S. Lebegue, J. Chem. Phys., 140 (2014) 014105(1-7).
- [18] E. F. C. Byrd and B. M. Rice, J. Phys. Chem. C, 111 (2007) 2787–2796.
- [19] H. Liu, J. J. Zhao, J. G. Du, Z. Z. Gong, G. F. Ji and D. Q. Wei, Phys. Lett. A, 367 (2007) 383–388.
- [20] S. Appalakondaiah, G. Vaitheeswaran and S. Lebegue, J. Phys. Chem. A, 119 (2015) 6574–6581.
- [21] E. F. C. Byrd, G. E. Scuseria and C. F. Chabalowski, J. Phys. Chem. B, 108 (2004) 13100–13106.

34 REFERENCES

- [22] S. Grimme, J. Compu. Chem., 27 (2006) 1787-1799.
- [23] A. Tkatchenko and M. Scheffler, Phy. Rev. Lett., 102 (2009) 073005(1-4).
- [24] F. Ortmann, F. Bechstedt, W.G. Schmidt, Phys. Rev. B 73 (2006) 205101.
- [25] S. Goedecker and K. Maschke, Phys. Rev. A 45, (1992) 88-93.
- [26] D. Vanderbilt, Phys. Rev. B, 41, (1990) 7892–7895.
- [27] M. C. Payne, M. P. Teter, D. C. Allen, T. A. Arias and J. D. Joannopoulos, Rev. Mod. Phys., 64 (1992) 1045–1097.
- [28] S. Baroni, S. de Gironcoli, A. Corso, and P. Giannozzi Rev. Mod. Phys., 73 (2001) 515–562.
- [29] J.M. Henriques, C.A. Barboza, E.L. Albuquerque, U.L. Fulco, E. Moreira, J. Phys. Chem. solids, 76 (2015) 45-50.
- [30] E.L.Albuquerque, D.R.Tilley, Solid State Commun. 26 (1998) 317-821.
- [31] C.A.Barboz, E.L.Albuquerque, C.Chesmana V.N.Freire, Phys. Lett. A, 255 (1998) 478-482.
- [32] N.W. Ashcroft, N.D. Mermin, Solid State Physics, Saunders College, Philadelphia, 1976.
- [33] H. B. G. Casimir and B. Polder, Phys. Rev., 73 (1948) 360-372.
- [34] X. Chu and A. Dalgarno, J. Chem. Phys., 121 (2004) 4083-4088.
- [35] A. Tkatchenko, R. A. DiStasio, R. Car and M. Scheffler, Phy. Rev. Lett., 108 (2012) 236402(1-5).
- [36] P. E. Blöchl, Phys. Rev. B, 50 (1994) 17953–17979.
- [37] P. E. Blöchl, Phys. Rev. B, 41 (1990) 5414–5416.
- [38] J. Lehtomäki, I. Makkonen, M. A. Caro and A Harju, J. Chem. Phys., 141 (2014) 234102(1-7).

- [39] N. D. M. Hine, J. Phys.: Condens. Matter, 29 (2017) 024001(1-9).
- [40] G. Kresse and D. Joubert, Phys. Rev. B, 54 (1996) 11169-11186.
- [41] S. Baroni, S. D. Gironcoli, A. D. Corso and P. Giannozzi, Rev. Mod. Phys., 73 (2001) 515–562.
- [42] G.C. Strinati, in Encyclopedia of Condensed Matter Physics, 2005.

Chapter **2** 

# Lattice dynamics and thermodynamic properties of alkaline earth metal nitrates M $(NO_3)_2$ and metal azides M $(N_3)_2$ (M = Sr, Ba).

In this work, we have investigated the structural, elastic, vibrational, and thermodynamic properties of M(NO<sub>3</sub>)<sub>2</sub> and M(N<sub>3</sub>)<sub>2</sub> using an ab initio approach. We found that the van der Waals correction predicts the structural parameters, which are in fair agreement with the experimental values. The phonon modes, their dispersion, and the partial density of states were computed. The infrared spectrum of these compounds at ambient condition were studied, and critically evaluated in the light of previous experimental investigations. The elastic constants of M(NO<sub>3</sub>)<sub>2</sub> and M(N<sub>3</sub>)<sub>2</sub> confirm the mechanical stabilities, while the calculated B/G ratio suggests that the materials are ductile. Finally, as the thermal behavior of these materials could play a key role in the growth of sustainable smoke compositions, thermodynamic properties such as the entropy, Debye temperature, heat capacity, and enthalpy were calculated. The results revealed that the compounds are thermodynamically stable up to 750 K. This work demonstrates that Sr (NO<sub>3</sub>)<sub>2</sub> and Ba (NO<sub>3</sub>)<sub>2</sub> can be reliably used in pyrotechnics as they possess considerable thermal conductivity leading to a high burn rate. The results presented in this work could open a way to understand the lattice dynamics of materials of this type and could provide necessary input from the pyrotechnic applicability point of view, which would help experimental researchers in the future.

**B.** Adivaiah, E. Narsimha Rao, T. Atahar Parveen, G. Vaitheeswaran, "Lattice dynamics and thermodynamic properties of alkaline earth metal nitrates M  $(NO_3)_2$  (M = Sr, Ba): A first principles study", **J. Phys. Chem. Solids.**, 20, 29693 (2018).

**Bushnagar Adivaiah**, Elaprolu Narsimha Rao, G. Vaitheeswaran, "Structure-property correlation studies of alkaline-earth metal—azides M  $(N_3)_2$  (M = Sr, Ba) **J. Phys.: Condens. Matter.**, **31**, 475402 (2019).

#### 3.1 Introduction

The inorganic nitrates and azides of alkaline-earth metals are an important class of solid compounds for a number of reasons. These materials have empirical significance as an explosive, pyrotechnics, gas generators, industrial chemicals, and photographic materials. Nitrates are energetic materials, and this determines their wide range of applications. M (NO<sub>3</sub>)<sub>2</sub> are powerful oxidizing agents and decompose at elevated temperatures to give oxygen as one of the major products. The strontium nitrate and barium nitrate crystals M (NO<sub>3</sub>)<sub>2</sub> (M=Sr,Ba) studied display an isomorphous cubic structure with space group  $Pa\bar{3}$  (no. 205) and consist of four formula units per unit cell. Sr(NO<sub>3</sub>)<sub>2</sub>, an alkaline earth metal nitrate, is one such interesting compound that could be used in pyrotechnic compositions as a coloring and oxidizing agent [1] because of its high thermal stability and the nature of its thermal decomposition [2]. The oxygen balance in strontium nitrate is 37.7%, and the material decomposes in a strongly endothermic manner

into SrO,  $N_2$ , and  $O_2$ . It is widely used in pyrotechnics such as firework signal flares and tracer ammunition because strontium compounds burn with a brilliant red flame and no other material has been found to be better in these applications [3]. In green light-emitting pyrotechnic formulations,  $Ba(NO_3)_2$  is mostly used as both the colorant and the oxidant [2].

The decomposition reaction of barium nitrate and strontium nitrate has been reported previously [2]:

$$Sr(NO_3)_2 \rightarrow SrO + NO + NO_2 + O_2$$
 (3.1)

$$Ba(NO_3)_2 \rightarrow BaO + 2NO + 1.5O_2$$
 (3.2)

Recently many researchers have reported strontium and barium nitrates for use in advanced applications involving energetic materials [1, 4-9]. Many of them focused on the material applications from the aspect of environment-friendly pyrotechnic applications. These crystals are promising materials for optical flares and one of the best materials which provide the frequency shift of laser radiation in various spectrum regions via the Stimulated Raman scattering (SRS) technique. They are used as advanced materials for coupling SRS lasers inside resonators. Infrared (IR) spectroscopy study of alkaline earth metal nitrates are extremely important [10-17], and it is well confirmed that the vibrations lead to the interpretation of the optical and thermal properties. In spite of their importance, very few theoretical studies have been available in the literature so far. In results, we compare our theoretical results with the available experimental results [12] in a more precise manner. Our work allows a clear description and comparison of the basic yet technologically useful materials from the viewpoint of pyrotechnics. Among the divalent metal nitrates,  $Ba(NO_3)_2$  has been widely studied for a long time [10-15, 18], and experimental researchers demonstrated [15] that barium nitrate has a centrosymmetric crystal structure and belongs to the point group  $T_h^6$  (or Pa3). Barium nitrate crystals have been grown from aqueous solutions to achieve high optical quality for use as nonlinear optical elements for stimulated Raman scattering [19]. Also, several physical properties, such as ionic conductivity and dielectric properties, of barium nitrate have been studied by various experimentalists [20–23]. Two theoretical studies addressing the mechanical and vibrational properties of nitrates of alkaline earth metals were performed recently using the density functional theory (DFT) formalism [24, 25].

The azide group is linear and symmetrical, with an average N-N separation being 1.18 Å. Typically, the contrast in the bonding of azides leads to large variations in the observed stability and decomposition. Most of the solid inorganic azides decompose to give a simple product of the anion and nitrogen [26]. This decomposition can occur by heat, shock, light, or ionization radiation. In the case of heavy metal azides, the reaction is highly exothermic, and its shows low sensitivity. The alkali and alkaline earth metal azides are more stable [27], which are not sensitive to impact [29]. Among the inorganic metal azides, strontium azide and barium azide are well-known for their explosive properties such as detonation or deflagration. The calcium azide, strontium azide and barium azide are potential candidates to get polymer nitrogen [29]. Sr(N<sub>3</sub>)<sub>2</sub> and Ba(N<sub>3</sub>)<sub>2</sub> undergo photochemical decomposition into metal atoms and nitrogen when they are exposed to ultra-violet light [30–33]. The decomposition of strontium azide, barium azide, and calcium azide differ from those for the Alkali metal azides in a markedly smaller fraction of nitrogen evolving as free atoms and alkaline metal azides have larger lattice energies than alkali azides [34].

The decomposition reactions of strontium and barium azides [26] are as follows:

$$Sr(N_3)_2 \rightarrow Sr + 0.4N + 2.8N_2$$
 (3.3)

$$Ba(N_3)_2 \rightarrow Ba + 0.6N + 7.7N_2$$
 (3.4)

Numerous studies are available in the literature related to the structure-property correlations of alkaline metal azides and metal nitrates [2, 35-38]. The investigations include structure stability, electronic structure studies, Infrared (IR) and Raman spectroscopy to understand the vibrational properties [39-44]. A thorough study of alkaline metal azides, M(N<sub>3</sub>)<sub>2</sub> (M = Sr, Ba) suggests the feasibility of deciding microscopic properties and energetic behavior of metal azides. Also, the density functional theory (DFT) calculations at the LDA and GGA levels reported the structural, electronic, and optical properties[36, 45]. However, they did not assess the vibrational and thermodynamical properties of the alkaline-earth metal azide  $M(N_3)_2$  (M = Sr, Ba) crystals. It is our intention to fill this gap by introducing the results of DFT computations for both the metal azides of M(N<sub>3</sub>)<sub>2</sub>, predicting their mechanical stability, infrared spectra, phonon dispersion relations, and thermodynamic properties. A brief comparison with results for cubic metal nitrate  $M(NO_3)_2$  (M = Sr, Ba) crystals [46] is accompanied in order to understand the difference in energetic performances of the metal azide M(N<sub>3</sub>)<sub>2</sub> (M = Sr, Ba) crystals when compared to metal nitrate  $M(NO_3)_2$  (M = Sr, Ba)crystals.

In the present study keeping in mind the long-range intermolecular interactions, semi-empirical dispersion correction is incorporated to obtain the stability of the crystal structure and lattice dynamics for M(NO<sub>3</sub>)<sub>2</sub>, M(N<sub>3</sub>)<sub>2</sub> (M = Sr, Ba). Zone-center phonon spectra (IR) are calculated with the use of the density functional perturbation theory (DFPT) approach to obtain the vibrational properties. The calculated vibrational frequencies are reasonably consistent with the earlier reported experimental results. Unlike the experimental results of Brooker et al.[12], which failed to reveal a low-frequency band, we emphasize better precision of the low-frequency region, thereby unveiling the vibrational response of the materials. The vibrational nature of bonds in nitrate crystals was further explored by our obtaining a fundamental understanding of their thermodynamic behavior. The thermodynamic properties, such as enthalpy (*H*), entropy (*S*), De-

bye temperature ( $\Theta_D$ ), heat capacity ( $C_V$ ), coefficient of thermal expansion ( $\alpha$ ), and thermal conductivity (k), as a function of temperature over a wide range (5 K  $\leq T \leq$  750 K) are described in this chapter. The calculated results reveal that the materials under study are mechanically and dynamically stable. We believe that this work will pave the way for theoreticians and experimentalists to explore many more materials of this type.

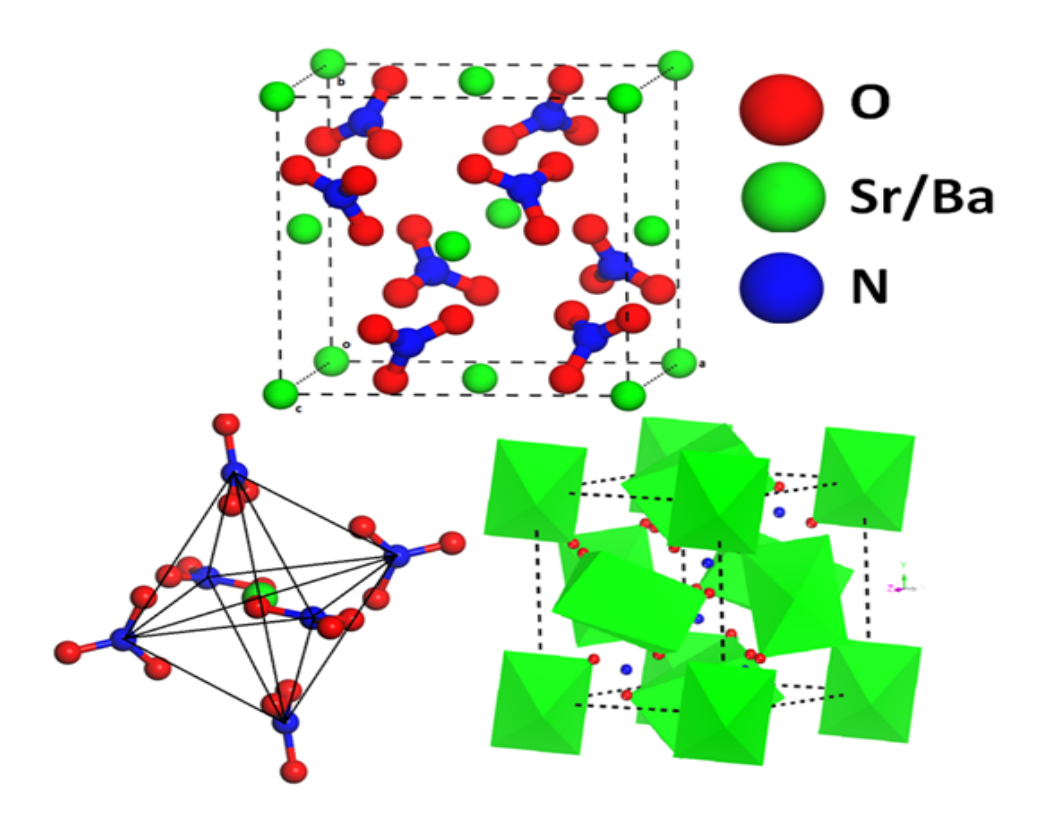


Figure 3.1: Crystal structure of  $M(NO_3)_2$ , the cation local atomic site arrangement in the respective nitrate crystal structures showing the six nitrate groups and associated 6 + 6 coordinated oxygen atomic shells, and a cuboctahedron with eight triangular faces and six square faces.

#### 3.2 Materials and methods

#### 3.2.1 Crystal structure

The strontium nitrate and barium nitrate crystals studied display an isomorphous cubic structure with space group  $Pa\overline{3}$  (no. 205) and consist of four formula units per unit cell [47]. The face-centered cubic Bravais lattice consists of arranged  $M^{2+}$  ions. The nitrate groups are located in each octahedral hole, and the center of symmetry relates the two nitrate groups [48, 49]. The neighboring cations are situated on the opposite side of the NO<sub>3</sub> pyramid with respect to the oxygen plane and the nitrate group (Figure 3.1). As there are eight nitrate ions in the primitive cell, 12 surrounding oxygen atoms build up a 6 + 6 cuboctahedron coordination at two different close coordination distances as shown in Figure 3.1. The alkaline–earth metal azides  $Sr(N_3)_2$  were first synthesized by Pringle [50], where as  $Ba(N_3)_2$  was synthesized by Choi [51]. Figure 3.2 shows the crystal structure of  $Sr(N_3)_2$  in face–centered orthorhombic structure(space group 'Fddd'(70)) with 2 formula units per primitive cell at ambient conditions.

The azide group is linear and symmetrical, with nitrogen-nitrogen distance being 1.194 Å, and the strontium-nitrogen separation is 2.63 Å and 2.77 Å. Whereas the Ba(N<sub>3</sub>)<sub>2</sub> crystal displays a monoclinic structure with space group ' $P2_1/m(11)$ ' and consists of two formula units per primitive cell. The Ba(N<sub>3</sub>)<sub>2</sub> possess similar C<sub>2b</sub> point group symmetry like (Li/Na)N<sub>3</sub>. All of the atoms in Ba(N<sub>3</sub>)<sub>2</sub> are located at '2e' wyckoff site. For Sr(N<sub>3</sub>)<sub>2</sub>, the Sr, N1, N2 atoms occupy '8a', '32h', '16e' wyckoff positions respectively. Whereas for (Li/Na)N<sub>3</sub> the metal atoms in both the crystals are located at '2a' wyckoff site, and sodium atoms are located at 2d, 4i position. The M(N<sub>3</sub>)<sub>2</sub> possess atomic wyckoff sites (Sr/Ba -'4a', N - '8c', O - '24d'), which is quite different than M(NO<sub>3</sub>)<sub>2</sub> [46]. This change in the atomic positions and number of atoms in the unit cells of (Li/Na)N<sub>3</sub> and Ba(N<sub>3</sub>)<sub>2</sub> leads to different energetic properties. It is also reported in the literature that, non bonding N-N distances are crucial in determining the structure-sensitivity correlations

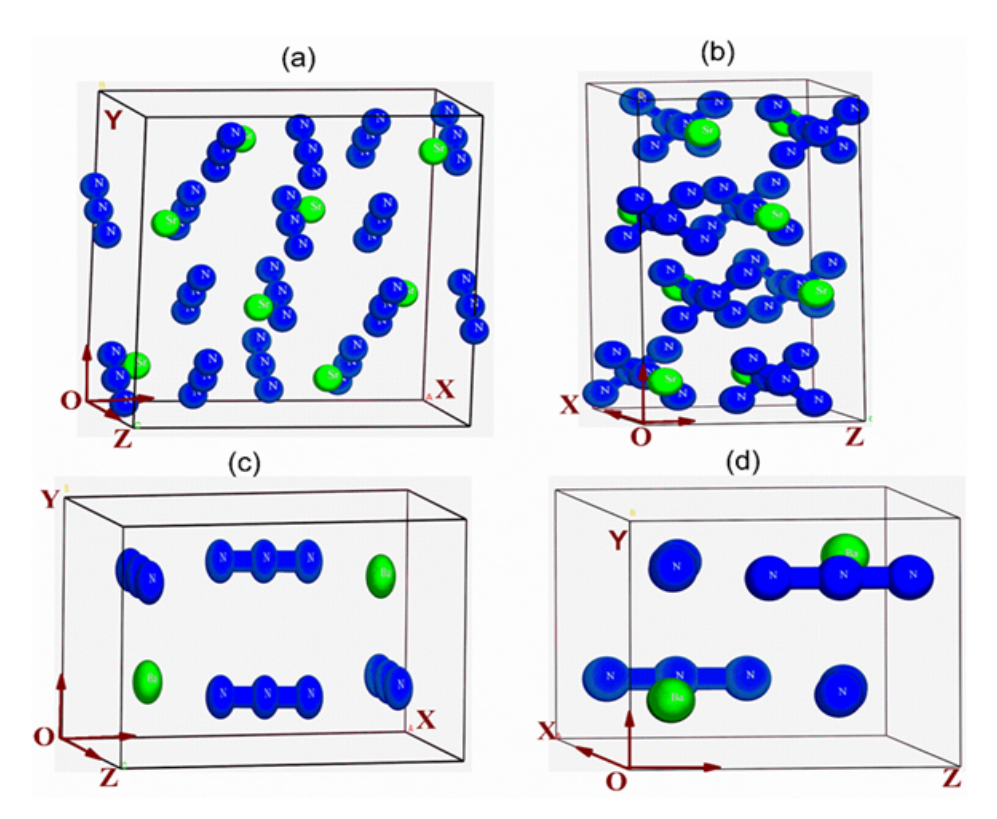


Figure 3.2: Crystal structure of Orthorhombic  $Sr(N_3)_2$  (top) along (a) x-y-z and (b) z-y-x axes. Monoclinic  $Ba(N_3)_2$  (bottom) along (c) x-y-z and (d) z-y-x axes. Blue color represents N atoms, and green color represents Sr/Ba atoms.

of these chosen classes of materials[52].

#### 3.2.2 Computational methods

Ab initio calculations were performed with the plane-wave pseudopotentials method within the framework of DFT as implemented in the Cambridge Serial Total Energy Package (CASTEP) code [53]. In keeping view of all the important bonded and non-bonded interactions of these layered materials, we have optimized the experimental crystal structures with different exchange–correlation functionals. As expected, the standard functionals like local density approximation (LDA) with CA-PZ method, generalized gradient approximation (GGA with PBE, PW91 functionals) generate large errors [54]. The Perdew-Burke-Ernzerhof (PBE) and

Perdew-Wang 1991 (PW91) exchange-correlation potentials [55, 56] within the generalized gradient approximation (GGA) were used along with the parameterfree dispersion correction scheme proposed by Grimme (G06) [57] and Ortmann, Bechstedt, Schmidt (OBS) [58] for Sr(NO<sub>3</sub>)<sub>2</sub> and Ba(NO<sub>3</sub>)<sub>2</sub> respectively. Similarly, we incorporated Tkatchenko-Scheffler [59] and Ortmann-Bechstedt-Schmidt [58] dispersion correction methods for  $Sr(N_3)_2$  and  $Ba(N_3)_2$  respectively. Unconstrained variable-cell geometry optimization of the M(NO<sub>3</sub>)<sub>2</sub> and M(N<sub>3</sub>)<sub>2</sub> crystal was performed with the Broyden-Fletcher-Goldfarb-Shanno algorithm [60]. The planewave energy cutoff was set as 975 eV for  $M(NO_3)_2$ , and for  $M(N_3)_2$  is 1100 eV. Integrations in the Brillouin zone were performed using k-points technique of Monkhorst-Pack[61] generated similar grids of  $6 \times 6 \times 6$ ,  $6 \times 6 \times 6$ ,  $7 \times 7 \times 7$  and  $3 \times 8 \times 6$  were chosen to perform reciprocal space integrations to determine wellconverged structures for  $Sr(NO_3)_2$ ,  $Ba(NO_3)_2$ ,  $Sr(N_3)_2$ , and  $Sr(N_3)_2$  respectively. Norm-conserving pseudopotentials [62] were used to describe the electronic cores: N,  $2s^2 2p^3$ ; O,  $2s^2 2p^4$ ; Sr,  $4s^2 4p^6 5s^2$ ; and Ba,  $5s^2 5p^6 6s^2$ . The convergence criteria for geometry optimization were as follows: total energy convergence in system  $5 \times 10^{-6}$  eV/atom, maximum ionic force 0.005 eV/Å maximum displacement  $0.5 \times 10^{-4}$  Å, and maximum stress component 0.02 GPa.

The phonon band structure and phonon density of states were calculated with use of the linear-response method within DFPT [63–66], and dynamical matrices were obtained at  $5 \times 5 \times 5$  q-points. Thereafter, to calculate the thermodynamic properties for the present  $M(NO_3)_2$  and  $M(N_3)_2$  materials, we used the quasi-harmonic approximation [67, 68].

# 3.3 Results and discussion

#### 3.3.1 Unit cell optimization

Before performing the calculations, we first examined the ability of the computational approaches to reproduce the experimental crystal structure of M(NO<sub>3</sub>)<sub>2</sub>

Table 3.1: Calculated and experimental lattice constants with error percentage in
parentheses of $M(NO_3)_2$ (M = Sr, Ba).

Compound	Method	a (Å)	$V(\mathring{ m A}^3)$
$Sr(NO_3)_2$	LDA	7.543 (3.08%)	429.27 (-8.8%)
	PBE	7.91 (1.6%)	495.05 (5.0%)
	PBE + G06	7.85 (0.8%)	483.77 (2.6%)
	Expt. <sup>a</sup>	7.78	471.15
$Ba(NO_3)_2$	LDA	7.87 (-2.95%)	488.98 (8.61%)
	PBE	8.26 (1.84%)	564.99 (5.59%)
	PW91	8.26 (1.84%)	564.26(5.4%)
	PW91 + OBS	8.17 (0.73%)	545.79 (2.0%)
	Expt. <sup>a</sup>	8.11	535.07

LDA, local density approximation; OBS, Ortmann-Bechstedt-Schmidt; PBE, Perdew-Burke-Ernzerhof; PW91, Perdew-Wang 1991.

<sup>a</sup>From [47].

Table 3.2: Calculated and experimental (in parentheses) [47] atomic coordinates of  $Sr(NO_3)_2$  and  $Ba(NO_3)_2$ . The WP values are calculated using van der Waals (vdW) functional.

Compound	Atom (WP)	x	у	Z
$Sr(NO_3)_2$	Sr (4a)	0.0 (0.0)	0.0 (0.0)	0.0 (0.0)
	N (8c)	0.343 (0.345)	0.343 (0.345)	0.343 (0.345)
	O (24d)	0.27081 (0.273)	0.283 (0.285)	0.474 (0.475)
$Ba(NO_3)_2$	Sr (4a)	0.0 (0.0)	0.0 (0.0)	0.0 (0.0)
	N (8c)	0.350 (0.351)	0.350 (0.351)	0.350 (0.351)
	O (24d)	0.284 (0.285)	0.289 (0.291)	0.477 (0.476)

WP, Wyckoff position.

and M(N<sub>3</sub>)<sub>2</sub>. Various DFT methods, the standard density functional local density approximation (CA-PZ), GGA (PW91), and GGA (PBE) and their corrected versions, were tested for calculation of the unit cell parameters. The calculated results are compared with the experimental values [47] in Table 3.1. As expected, the standard functionals generate large errors because they do not adequately account for the weak interactions in a molecular crystal. The calculated crystal volume is underestimated by 8.8% with the CA-PZ functional and is overestimated by 5.0% and 5.4% with the PW91 functional and the PBE functional, respectively. These discrepancies can, in principle, be reduced by inclusion of dispersion cor-

rections [54]. As seen in Table 3.1, the correction to CA-PZ did not improve the calculated results. However, corrections to the PW91 and PBE functionals provided significant improvements. The errors in the calculated volumes were reduced to -2.0% and -2.6% for PW91 + OBS, and PBE + G06, respectively. Our calculated structural details reveal that these methods reproduce the unit cell parameters very well [48]. In Tables 3.2 and 3.3 we present the atomic coordinates and the calculated bond lengths and bond angles of M(NO<sub>3</sub>)<sub>2</sub>, respectively; these are in good agreement with the earlier experimental results [48]. Similarly, the calculated crystal volume using (CA-PZ functional) is smaller then the experimental value by 5.8% for Sr(N<sub>3</sub>)<sub>2</sub>, and 7.78% for Ba(N<sub>3</sub>)<sub>2</sub> (Table 3.4). The PBE functional leads to results close to the one obtained using the PW91 functional. However, we have used OBS, TS corrections to the PW91 and PBE functionals. The results obtained using the PW91 + OBS and PBE + TS approach: 1.1% and 1.8% respectively. We further compared our structural optimization results with previously reported results [69] using Ultrasoft pseudopotentials.

In keeping view of all the important bonded and non-bonded interactions of these layered materials, we have optimized the experimental crystal structures with different exchange –correlation functional and the calculated structural parameters, bond lengths for M(N<sub>3</sub>)<sub>2</sub> are shown in Tables 3.5 and 3.6, together with experimental results obtained from Ref. [50, 51], for the sake of comparison. As expected, the standard functionals (like local density approximation (LDA) with CA-PZ method, generalized gradient approximation (GGA with PBE, PW91 functionals)) generate large errors because they do not adequately account for the weak interactions in a molecular crystal [54]. The calculated crystal volume using (CA-PZ, PBE/PW91 functionals) are deviated by (5.8%, 5.68%) for Sr(N<sub>3</sub>)<sub>2</sub>, (7.78%, 5.4%) for Ba(N<sub>3</sub>)<sub>2</sub>, respectively.

These discrepancies can, in principle, be reduced by inclusion of dispersion corrections [54] to the standard DFT functionals. The errors in the calculated volumes were reduced to 1.1% and 1.8% for PW91 + OBS, and PBE + TS, respec-

Table 3.3: Calculated and experimental (in parentheses) [47] bond distances (Å) and bond angles (degrees) between the  $M^{2+}$  cation and the nearest oxygen atoms for M(NO<sub>3</sub>)<sub>2</sub> (M = Sr, Ba).

	Type <sup>a</sup>	$Sr(NO_3)_2$	Ba(NO <sub>3</sub> ) <sub>2</sub>
M-O	m	2.73 (2.71)	2.894 (2.878)
M-O	n	2.86 (2.83)	2.95 (2.94)
M-M		5.55 (5.55)	5.779 (5.740)
N-O		1.269 (1.246)	1.271 (1.246)
O-O		2.198(2.159)	2.20 (2.15)
O-N-O (in angle)		120.00 (120.00)	120.00 (120.00)

<sup>&</sup>lt;sup>a</sup> Two different types (m, n) of M-O distance.

Table 3.4: Calculated and experimental lattice constants with error percentages in parentheses of  $M(N_3)_2$  (M = Sr, Ba).

Compound		a (Å)	b (Å)	c (Å)	$V(\mathring{A}^3)$
$Sr(N_3)_2$	LDA	11.325	11.413	6.0311	779.629 (5.81%)
	PBE	12.194	11.665	6.161	876.50 (-5.87%)
	PBE + TS	11.719	11.693	6.135	840.860(-1.8%)
	Expt. <sup>a</sup>	11.820	11.470	6.08	824.98
	Cal.c	11.842	11.650	6.1908	854.13
$Ba(N_3)_2$	LDA	9.363	4.245	5.352	210.424 (-8.4%)
	PBE	9.831	4.449	5.514	238.494(4.3%)
	PW91	9.759	4.441	5.541	237.496(3.9%)
	PW91 + OBS	9.69	4.39	5.48	230.72 (1.1%)
	Expt. <sup>b</sup>	9.590	4.390	5.420	224.88
	Cal.c	11.842	11.650	6.1908	854.13

LDA, local density approximation; OBS, Ortmann-Bechstedt-Schmidt; PBE, Perdew-Burke-Ernzerhof; PW91, Perdew-Wang 1991.

<sup>a</sup>From[50]. <sup>b</sup>From[51] <sup>c</sup>From[72]

Table 3.5: Calculated atomic coordinates of Sr(N<sub>3</sub>)<sub>2</sub> and Ba(N<sub>3</sub>)<sub>2</sub>. The WP values are calculated using van der Waals (vdW) functional.

Compound	Atom (WP)	X	Y	Z
$Sr(N_3)_2$	Sr (8a)	0.125	0.125	0.125
	N1 (32h)	0.00220	0.05937	0.7715
	N2 (16e)	-0.00389	0.125	0.625
$Ba(N_3)_2$	Ba (2e)	0.2822	0.000025	-0.1709
	N1 (2e)	-0.0825	0.000025	0.2263
	N2 (2e)	0.0411	0.000025	0.2579
	N3 (2e)	0.1642	0.000025	0.2904
	N4 (2e)	-0.3824	0.000025	0.4383
	N5 (2e)	-0.3921	0.000025	0.6483

WP, Wyckoff position.

Table 3.6: Calculated and experimental (in parentheses) [50, 51] bond distances (Å) and bond angles (degrees) between the  $M^{2+}$  cation and the nearest oxygen atoms for M(N<sub>3</sub>)<sub>2</sub> (M = Sr, Ba).

	$Sr(N_3)_2$	$Ba(N_3)_2$
N1-N2	1.194 (1.168)	1.199 (1.168)
N2-N3	1.194 (1.168)	1.194 (1.164)
N3-N4		1.203 (1.157)
N'2-N'3		1.185 (1.178)
N1-N2-N3	178.308 (172.9)	179.618
N'1-N'2-N'3		177.410
Mimimum Non-bond distance	3.246 (3.047)	3.258 (3.061)

tively. We further compared our structural optimization results with previously reported by Ramesh Babu et al. [69] using Ultrasoft pseudopotentials. All our calculated structural details with norm-conserving pseudopotentals along with previous Ultrasoft pseudopotentials reveal that dispersion corrected methods reproduce the unit cell parameters with better accuracy [50, 51].

#### 3.3.2 Mechanical properties

Elastic properties provide insight into the interatomic bonding forces as well as the dynamical behavior of the crystal. The structural stability and mechanical properties of M(NO<sub>3</sub>)<sub>2</sub> and M(N<sub>3</sub>)<sub>2</sub>, were extracted from our understanding of the elastic stiffness constants  $C_{ij}$ , which were determined using CASTEP code by using the finite-difference to calculate the Hessian matrix [70]. In the M(NO<sub>3</sub>)<sub>2</sub> materials, because of cubic symmetry, there are three independent elastic constants,  $C_{11}$ ,  $C_{12}$ , and  $C_{44}$ . The calculated elastic constants for Sr(NO<sub>3</sub>)<sub>2</sub> and Ba(NO<sub>3</sub>)<sub>2</sub> are shown in Table 3.7, and the results are compared with the available data in the literature [48]. In the case of cubic systems, the criterion for mechanical stability is that  $C_{ij}$  should fulfill the following conditions [54]:  $C_{11} - C_{12} > 0$ ,  $C_{11} + C_{12} > 0$ , and  $C_{44} > 0$ . The calculated elastic constants fulfill these conditions, thereby confirming the mechanical stability of the present nitrate crystals.

Table 3.7: Calculated and experimental (in parentheses) components of the elastic tensor  $C_{ij}$ , Young's modulus (E), bulk modulus (B), shear modulus (G), compressibility (K), anisotropy (A), Poison's ratio ( $\sigma$ ), B/G ratio, longitudinal ( $V_l$ ), transverse ( $V_t$ ), and average ( $V_m$ ) sound velocities, and Debye temperature ( $\Theta_D$ ) of M(NO<sub>3</sub>)<sub>2</sub> (M = Sr, Ba)

Property	$Sr(NO_3)_2$	Ba(NO <sub>3</sub> ) <sub>2</sub>
$C_{11}$ (GPa)	50.54 (43.48 <sup>a</sup> , 42.81 <sup>b</sup> )	39.67 (32.03 <sup>a</sup> , 29.21 <sup>b</sup> )
C <sub>44</sub> (GPa)	22.18 (17.94 <sup>a</sup> , 15.84 <sup>b</sup> )	15.12 (13.26 <sup>a</sup> , 12.82 <sup>b</sup> )
$C_{12}$ (GPa)	26.21 (28.11 <sup>a</sup> , 29.46 <sup>b</sup> )	25.30 (21.81 <sup>a</sup> , 20.57 <sup>b</sup> )
E (GPa)	44.78	29.930
B (GPa)	34.32 (33.23 <sup>a</sup> )	30.08 (25.22 <sup>a</sup> )
G (GPa)	17.42	11.21
K (GPa <sup>-1</sup> )	0.0291	0.037
A (GPa)	1.823 (2.3 <sup>a</sup> )	2.10 (2.59 <sup>a</sup> )
$\sigma$	0.2828	0.342
B/G	1.964	2.6826
$V_l$ (km/s)	4.450	3.767
$V_t$ (km/s)	2.449	1.8802
$V_m(\mathrm{km/s})$	2.729	2.109
$\Theta_D$ (K)	341	250
		[40]

<sup>a</sup>From [48], <sup>b</sup>From [49].

The elastic constants of single crystal  $Sr(N_3)_2$  and  $Ba(N_3)_2$  can be found in Table 3.8, and the results are compared with theoretical results [72]. For materials

with orthorhombic symmetry, there are nine independent elastic constants [73], whereas monoclinic systems have thirteen independent elastic constants [72].

The calculated elastic constants fulfils the corresponding mechanical stability criteria [74]. Therefore, the  $M(N_3)_2$  compounds are mechanically stable at ambient condition. The value of  $C_{22}$  is clearly higher for  $Sr(N_3)_2$  than for  $Ba(N_3)_2$ . Hence, one may conclude that  $Sr(N_3)_2$  is stiffest along the b-axis than  $Ba(N_3)_2$ , whereas  $Ba(N_3)_2$  is the stiffest across the c-axis. The value of  $C_{11}$  is smaller than the value of  $C_{33}$  for both the crystals, showing that the hardness of the material is smaller along the a-axis than that of c-axis. The  $C_{ij}$  values of  $Sr(N_3)_2$  are higher than the  $Ba(N_3)_2$ , indicating that strontium azide is stiffer than the barium azide. The complete set of independent elastic constants was used to compute other mechanical properties, such as bulk modulus, shear modulus, Poisson's ratio, Young's modulus, and elastic anisotropy, of the system, as shown in Table 3.9 following the Voigt approximation [54, 75, 76].

The bulk modulus (*B*) is inversely proportional to the lattice volume of the crystal [ $\overline{54}$ ]. The bulk modulus for strontium nitrate, which has a smaller volume than barium nitrate, was found to be 34.32 GPa, whereas for barium nitrate, it was 30.08 GPa. The calculated bulk moduli are consistent with earlier reported values [ $\overline{48}$ ] for both materials. The value of *B* can also be related to the material's hardness, the values confirming that strontium nitrate is harder than barium nitrate. The bulk modulus of  $Sr(N_3)_2(B_0 = 49.56 \text{ GPa})$  is greater than the  $Ba(N_3)_2(34.52 \text{ GPa})$ , which suggests that  $Ba(N_3)_2$  exists smaller stiffness compared to  $Sr(N_3)_2$ . Therefore,  $Ba(N_3)_2$  would be more sensitive to mechanical shock over  $Sr(N_3)_2$ . The bulk modulus of azide ion with alkaline metal atom display large difference on moving from Sr to  $Sr(N_3)_2$  and  $Sr(N_3)_2$ 0 ( $Sr(N_3)_2$ 1)  $Sr(N_3)_2$ 1.

Table 3.8: Elastic constants  $C_{ij}$  (GPa) of  $Sr(N_3)_2$  and  $Ba(N_3)_2$ . Previously reported  $M(N_3)_2$  values are shown for comparison.

System		$C_{11}$	$C_{22}$	$C_{33}$	$C_{4}$	$C_{55}$		$C_{12}$		$C_{15}$	$C_{23}$	$C_{25}$	$C_{25}$ $C_{35}$	$C_{46}$
$Sr(N_3)_2$	$Sr(N_3)_2$ This work	50.72	93.74	89.34	36.98	15.55		31.16			49.84			
	Other Theory $^{\mathrm{c}}$	43.1	89.1	7.67	44.8	8.9		34.4			55.8			
$Ba(N_3)_2$	This work	48.46	52.54	63.10	14.67	8.30	10.43	30.41	15.70	0.57	27.30	1.11	1.85	-1.15
	Other Theory $^{\mathrm{c}}$	48.4	44.2	62.9	14.4	10.3		22.4	15.6	1.4	25.3	4.0	-1.9	0.3
					$^{ m cFr}$	<sup>c</sup> From [72]	j							

Table 3.9: Calculated components of the bulk modulus (B), shear modulus (G), Young's modulus (E) of  $Sr(N_3)_2$  and  $Ba(N_3)_2$ . Previously reported  $M(N_3)_2$  values are shown for comparison

System	В	G	Е	-
$Sr(N_3)_2$	49.56 (48.9°)	24.01 (23.4°)	59.20 (57.1°)	<sup>c</sup> Ref.[72]
$Ba(N_3)_2$	34.52 (31.9°)	12.73 (13.1°)	30.85 (32.8°)	

The bulk modulus value of metal oxides SrO (116.1 GPa) and BaO (94.7 GPa) are very larger than metal azides/metal nitrates [24], which enables them as hard materials. Whereas the present studied compounds are highly compressible, which could be related to the electron transfer from the sp-valance bands of Sr and Ba to their empty d-band lying in close proximity to the sp-valence bands [76]. Fig. 3.1 clearly indicates that the compression of the crystal is basically due to the Sr(Ba)-O polyhedron as the bonds associated with nitrates are short and incompressible. As reported by Errandonea et al. [77], for such structural behavior, the bulk modulus of the crystal should be proportional to  $Z_i/d^3$ , where  $Z_i$  is the cationic formal charge and d is the mean value of the M-O bond distance (in angstroms). This proportionality leads to a proportionality constant of 375 for the present nitrates, thus allowing us to estimate the bulk modulus of isostructural nitrates such as Pb(NO<sub>3</sub>)<sub>2</sub>, Ca(NO<sub>3</sub>)<sub>2</sub>, and Mg(NO<sub>3</sub>)<sub>2</sub>; their respective bulk moduli are 34.42, 37.43, and 44.11 GPa. The calculated bulk moduli are consistent with earlier reported values of 29.56 GPa, 33.89 GPa [48], and 39.4 GPa [24], respectively. The proportionality relation between the bulk modulus and the bond distance leads to the conclusion that the family of cubic nitrates has bulk modulus in the range from 30 to 40 GPa. We also calculated the shear modulus (G), which is the relation between shear stress and shear strain [54]. The shear modulus (G) was found to be 20.48 GPa for strontium nitrate and 9.25 GPa for barium nitrate. The elastic shear strain, and surface penetration are proportional to hardness and they relate to a large shear modulus [54]. The shear modulus (G) was found to be 24.01 GPa for the strontium azide and 12.73 GPa for the

barium azide, which reveals that orthorhombic  $Sr(N_3)_2$  is more resistant surface penetration than the monoclinic barium azide, specifying that the first structure is stiffer. The Young's modulus (E) value represents the slope of the elastic region in a stress-strain curve. The smaller Young's modulus (E = 24.85 GPa) for  $Ba(NO_3)_2$  describes its greater receptiveness to physical changes than  $Sr(NO_3)_2$  (E = 46.74 GPa), which supports the aforementioned relative hardness of the materials. Strontium azide was found to have Young's modulus of 59.20 GPa, whereas for the barium azide, it was 30.85 GPa. The higher E value shows that strontium azide is more resistant to uniaxial tension-compression. Empirical information on the plastic properties of materials is described by the B/G ratio, which is larger than 1.75 for ductile materials and smaller than 1.75 for brittle materials, which puts both barium nitrate and strontium nitrate in the ductile category.

Information on interatomic forces in solids can be gleaned from Poisson's ratio  $(\sigma)$  as it involves the lateral and longitudinal strain in the elastic region [70]. Elastic anisotropy (A) results indicate that Ba(NO<sub>3</sub>)<sub>2</sub> (A = 2.1) is more anisotropic than Sr(NO<sub>3</sub>)<sub>2</sub> (A = 1.82). The experimental study of other mechanical properties of the same materials indicated that the calculated results are reliable (Table 3.7).

#### 3.3.3 Born effective charge analysis

The infrared absorption intensities are related to the dynamical matrix and Born effective charges, so we attempted to calculate the Born Effective Charges (BEC's) of each individual species. As the energetic properties of the studied metal azides are quite different from the metal nitrates, we tried to address the origin of variation in sensitivity by comparing the BEC differences for all the atoms in  $M(N_3)_2$ ,  $M(NO_3)_2$  materials. The obtained BEC and their deviations from their corresponding ionic charges using DFPT are presented in tables 3.10–3.15, respectively. It is clear from the results that all the calculated BEC values satisfy the acoustic sum rule within 0.0001 accuracy and hence converged. Among the nine BEC tensor components, the  $Z_{12}^*$ ,  $Z_{21}^*$ ,  $Z_{23}^*$ ,  $Z_{32}^*$  are found to be zero for Ba(NO<sub>3</sub>)<sub>2</sub>, whereas

all nonzero values are observed for  $M(N_3)_2$ ,  $M(NO_3)_2$ . All the BEC's of individual atoms in both crystal show considerable deviation from their ionic charges (Sr = +2; Ba = +2; N = -3; O = -2). In the case of  $M(N_3)_2$ , the 'Sr' atom charge deviation show an increasing trend from 'xx'  $\rightarrow$  yy  $\rightarrow$  zz, whereas the Ba atom display increment as follows:  $xx \rightarrow zz \rightarrow yy$ .

Table 3.10: Calculated BEC's of  $Sr(N_3)_2$ . Actual ionic charges are Sr = +2, N = -3.

Atom	$Z_{11}$	$Z_{12}$	$Z_{13}$	$Z_{21}$	$Z_{22}$	$Z_{23}$	$Z_{31}$	$Z_{32}$	$Z_{33}$
$N_1$	-0.52480	-0.12502	-0.07003	-0.15808	-1.39810	1.05905	-0.11753	0.94530	-1.90665
$N_2$	-0.52480	-0.12502	0.07003	-0.15808	-1.39810	-1.05905	0.11753	-0.94530	-1.90665
$N_3$	-0.52480	0.12502	-0.07003	0.15808	-1.39810	-1.05905	-0.11753	-0.94530	-1.90665
$N_4$	-0.52480	0.12502	0.07003	0.15808	-1.39810	1.05905	0.11753	0.94530	-1.90665
$N_5$	-0.52480	-0.12502	-0.07003	-0.15808	-1.39810	1.05905	-0.11753	0.94530	-1.90665
$N_6$	-0.52480	-0.12502	0.07003	-0.15808	-1.39810	-1.05905	0.11753	-0.94530	-1.90665
$N_7$	-0.52480	0.12502	-0.07003	0.15808	-1.39810	-1.05905	-0.11753	-0.94530	-1.90665
$N_8$	-0.52480	0.12502	0.07003	0.15808	-1.39810	1.05905	0.11753	0.94530	-1.90665
$N_9$	-0.08739	0.00000	-0.00000	0.00000	1.35661	-1.88428	-0.00000	-1.58686	2.16529
$N_{10}$	-0.08739	-0.00000	-0.00000	-0.00000	1.35661	1.88428	-0.00000	1.58686	2.16529
$N_{11}$	-0.08739	0.00000	-0.00000	0.00000	1.35661	-1.88428	-0.00000	-1.58686	2.16529
$N_{12}$	-0.08739	-0.00000	-0.00000	-0.00000	1.35661	1.88428	-0.00000	1.58686	2.16529
$Sr_1$	2.27400	0.00000	-0.00000	0.00000	2.87917	0.00000	-0.00000	0.00000	3.29602
Sr <sub>2</sub>	2.27400	0.00000	-0.00000	0.00000	2.87917	0.00000	-0.00000	0.00000	3.29602

Table 3.11: Calculated BEC's of  $Ba(N_3)_2$ . Actual ionic charges are Ba = +2, N = -3.

Atom	$Z_{11}$	$Z_{12}$	$Z_{13}$	$Z_{21}$	$Z_{22}$	$Z_{23}$	$Z_{31}$	$Z_{32}$	$Z_{33}$
$N_1$	3.02702	0.00000	-0.10582	0.00000	-0.13032	0.00000	0.13687	0.00000	-0.13953
$N_2$	-2.07751	0.00000	0.08422	0.00000	-0.31779	0.00000	-0.06303	0.00000	-0.84406
$N_3$	3.02702	0.00000	-0.10582	0.00000	-0.13032	0.00000	0.13687	0.00000	-0.13953
$N_4$	-2.07751	0.00000	0.08422	0.00000	-0.31779	0.00000	-0.06303	0.00000	-0.84406
$N_5$	-1.02455	0.00000	0.04911	0.00000	-0.74220	0.00000	0.28393	0.00000	-2.80884
$N_6$	0.00244	0.00000	-0.33339	0.00000	-0.13158	0.00000	-0.70947	0.00000	3.92358
$N_7$	-0.54617	0.00000	0.36971	0.00000	-0.66231	0.00000	0.52685	0.00000	-2.83093
$N_8$	-2.31805	0.00000	0.08691	0.00000	-0.74640	0.00000	-0.05044	0.00000	-0.37742
$N_9$	-1.02455	0.00000	0.04911	0.00000	-0.74220	0.00000	0.28393	0.00000	-2.80884
$N_{10}$	0.00244	0.00000	-0.33339	0.00000	-0.13158	0.00000	-0.70947	0.00000	3.92358
$N_{11}$	-0.54617	0.00000	0.36971	0.00000	-0.66231	0.00000	0.52685	0.00000	-2.83093
$N_{12}$	-2.31805	0.00000	0.08691	0.00000	-0.74640	0.00000	-0.05044	0.00000	-0.37742
$Ba_1$	2.93683	0.00000	-0.15075	0.00000	2.73061	0.00000	-0.12471	0.00000	3.07721
$Ba_2$	2.93683	0.00000	-0.15075	0.00000	2.73061	0.00000	-0.12471	0.00000	3.07721

The BEC show highly asymmetric nature for  $M(N_3)_2$  materials( $Z_{xx}^* \neq Z_{yy}^* \neq Z_{zz}^*$ ), which certainly confirms the presence of mixed ionic and covalent bond nature in the considered materials. The BEC deviations of different atoms in xx,

yy, zz directions show the following trend: (1) for  $Sr(N_3)_2$ :  $(N_9 = N_{10} = N_{11} = N_{12}) > (N_1 = N_2 = N_3 = N_4 = N_5 = N_6 = N_7 = N_8) > (Sr_1 = Sr_2)$ , whereas for  $Ba(N_3)_2$ , BEC deviations along zz direction are found to be larger than in xx, yy directions. (2) for  $Ba(N_3)_2$  (along zz direction):  $(N_6 = N_{10}) > (N_1 = N_3) > (N_8 = N_{12}) > (N_2 = N_4) > (N_5 = N_9) > (N_7 = N_{11}) > (Ba_1 = Ba_2)$ . Overall, in case of both azides, the nitrogen atoms show larger deviations than metal atoms ('Ba' show greater deviation than 'Sr') in all directions, and the BEC asymmetry is increased from strontium nitrate to barium nitrate. Hence, from BEC deviations, it can be concluded that the  $Sr(N_3)_2$  should be more stable than  $Ba(N_3)_2$ . Overall, the  $Ba(N_3)_2$  is found to be highly polarizable due to larger BEC deviations, hence optically active than  $Sr(N_3)_2$ . It is also clear from the minimum deviations of BEC's in different directions that the ionicity is increased from  $Sr(N_3)_2$  to  $Ba(N_3)_2$ . This clearly indicates that  $Ba(N_3)_2$  needs high activation energy to ignite than  $Sr(N_3)_2$ . This conclusion is in good agreement with the experimentally reported activation energies trend:  $Ba(N_3)_2$  (98 KJ/mol)  $> Sr(N_3)_2$  (84 KJ/mol)[71].

Table 3.12: Percentage of deviations of BEC's all inquivalent atoms are along xx, yy, zz directions.

$Sr(N_3)_2$				$Ba(N_3)_2$			
Atom	$Z_{11}$	$Z_{22}$	$Z_{33}$	Atom	$Z_{11}$	$Z_{22}$	$Z_{33}$
$N_1$	82.50	86.73	36.44	$N_1$	200.90	95.65	95.34
$N_2$	82.50	86.73	36.44	$N_2$	30.74	89.65	71.86
$N_3$	82.50	86.73	36.44	$N_3$	200.90	95.65	95.34
$N_4$	82.50	86.73	36.44	$N_4$	30.74	89.65	71.86
$N_5$	82.50	86.73	36.44	$N_5$	65.84	75.26	6.37
$N_6$	82.50	86.73	36.44	$N_6$	100.08	95.61	230.78
$N_7$	82.50	86.73	36.44	$N_7$	81.79	77.92	5.63
$N_8$	82.50	86.73	36.44	$N_8$	22.73	75.12	87.41
$N_9$	97.087	145.22	172.17	$N_9$	65.84	75.26	6.37
$N_{10}$	97.087	145.22	172.17	$N_{ m 10}$	100.08	95.61	230.78
$N_{11}$	97.087	145.22	172.17	$N_{11}$	81.79	77.92	5.63
$N_{12}$	97.087	145.22	172.17	$N_{12}$	22.73	75.12	87.41
$Sr_1$	-13.7	-43.95	-64.80	$Ba_1$	-46.84	-36.53	-53.86
Sr <sub>2</sub>	-13.7	-43.95	-64.80	$Ba_2$	-46.84	-36.53	-53.86

Similarly, in the case of M(NO<sub>3</sub>)<sub>2</sub> materials, the BEC show symmetric nature for nitrogen metal atoms (Sr, Ba) i.e.,  $Z_{xx}^* = Z_{yy}^* = Z_{zz}^*$ , whereas all the oxygen

atoms show slight asymmetric nature i.e.,  $Z_{xx}^* \neq Z_{yy}^* \neq Z_{zz}^*$ . It is also clear from the BEC deviations that, for all the Nitrogen atoms:  $Sr(NO_3)_2$  ( $Z_{xx}^* = Z_{yy}^* = Z_{zz}^*$ ) = Ba(NO<sub>3</sub>)<sub>2</sub> ( $Z_{xx}^* = Z_{yy}^* = Z_{zz}^*$ ). Interestingly, for oxygen atoms, Sr(NO<sub>3</sub>)<sub>2</sub> ( $Z_{yy}^*$ ) = Ba(NO<sub>3</sub>)<sub>2</sub> ( $Z_{yy}^*$ ), Sr(NO<sub>3</sub>)<sub>2</sub> ( $Z_{zz}^*$ ) = Ba(NO<sub>3</sub>)<sub>2</sub> ( $Z_{zz}^*$ ). This clearly indicates that these nitrates are nearly optical isotropic materials and slight optical anisotropy arises only due to oxygen atoms in xx direction. It is also clear from the BEC deviations of oxygen atoms  $Ba(NO_3)_2$   $(Z_{xx}^*) > Sr(NO_3)_2$   $(Z_{yy}^*)$  that  $Ba(NO_3)_2$  is only slightly more polarizable (optically active) than Sr(NO<sub>3</sub>)<sub>2</sub>. Hence M(NO<sub>3</sub>)<sub>2</sub> may found many technological applications like scintillating materials. The minimum values of BEC deviations of oxygen atoms clearly indicate that the ionicity is increased from barium nitrate to strontium nitrate. Therefore, Sr(NO<sub>3</sub>)<sub>2</sub> may need possess high activation energy than Ba(NO<sub>3</sub>)<sub>2</sub>. Our conclusions are well correlated with the experimentally reported activation energies trend: Sr(NO<sub>3</sub>)<sub>2</sub>  $(344.83 \text{ KJ/mol}) > \text{Ba(NO}_3)_2 (144.7 \text{ KJ/mol})[78]$ . Most importantly, we observed that the difference in the minimum BEC deviations of  $Sr(NO_3)_2$  ( $\sim$ 56) - Ba( $NO_3$ )<sub>2</sub> ( $\sim$ 165) (approximately 100) leads to an increase in the activation energy by 200 KJ/mole. The intensity of the peaks in the IR-spectra is directly proportional to BEC's [79] as follows:  $I_i = [\sum_{j,k} F^{\dagger}_{i,j} A_{j,k}]^2$ ; Here BEC tensor  $A_{i,j} = \frac{\partial^2 E}{\partial q_i \times \partial \mu_i}$ ; Here  $F_{i,j}^{l}$  is the eigenvector, E is the total energy,  $\mu$  is dipole moment, q is cartesian coordinate. As the BEC deviations are found to increase from Metal azides  $(Sr(N_3)_2 \rightarrow Ba(N_3)_2)$  to metal nitrates  $(Sr(NO_3)_2 \rightarrow Ba(NO_3)_2)$ , the intensities of the vibrational spectra also show a similar trend (see Figure 3.3). The IR-spectra's of nitrates are taken from our previous work[46] and plotted on top of the corresponding azide material just for comparison. Hence nitrates M(NO<sub>3</sub>)<sub>2</sub> (with high-intensity IR-peaks) will be more polarizable than azides and hence optically active. It is also clear from the BEC analysis that azides become sensitive to light mainly because of nitrogen atoms, whereas nitrates become light-sensitive mainly due to oxygen atoms. Moreover, the low BEC deviations of azides lead to different energy transfer mechanism to the lattice than optical isotropic nitrates. Hence, the explosive nature of the azides (detonate) and nitrates (deflagrate) will be different. These observations from our BEC analysis reveal the experimentally observed sensitivity differences of the studied materials. A further deep insight into the phonons, thermodynamic, optical isotropy, excited state properties, and sensitivity correlations may give an exact mechanism to understand the explosive nature (detonation and deflagration) between the azides and nitrates.

Table 3.13: Calculated BEC's of  $Sr(NO_3)_2$ . Actual ionic charges are Sr = +2, O = -2, N = -3.

Atom	$Z_{11}$	$Z_{12}$	$Z_{13}$	$Z_{21}$	$Z_{22}$	$Z_{23}$	$Z_{31}$	$Z_{32}$	$Z_{33}$
$N_1$	1.89202	-0.97303	-0.74065	-0.74065	1.89202	-0.97303	-0.97303	-0.74065	1.89202
$N_2$	1.89202	-0.97303	0.74065	-0.74065	1.89202	0.97303	0.97303	0.74065	1.89202
$N_3$	1.89202	0.97303	-0.74065	0.74065	1.89202	0.97303	-0.97303	0.74065	1.89202
$N_4$	1.89202	0.97303	0.74065	0.74065	1.89202	-0.97303	0.97303	-0.74065	1.89202
$N_5$	1.89202	-0.97303	-0.74065	-0.74065	1.89202	-0.97303	-0.97303	-0.74065	1.89202
$N_6$	1.89202	-0.97303	0.74065	-0.74065	1.89202	0.97303	0.97303	0.74065	1.89202
$N_7$	1.89202	0.97303	-0.74065	0.74065	1.89202	0.97303	-0.97303	0.74065	1.89202
$N_8$	1.89202	0.97303	0.74065	0.74065	1.89202	-0.97303	0.97303	-0.74065	1.89202
$O_1$	-0.96811	0.12138	0.53245	0.04539	-0.86090	0.46165	0.64132	0.37170	-1.32460
$O_2$	-0.96811	0.12138	-0.53245	0.04539	-0.86090	-0.46165	-0.64132	-0.37170	-1.32460
$O_3$	-0.96811	-0.12138	0.53245	-0.04539	-0.86090	-0.46165	0.64132	-0.37170	-1.32460
$O_4$	-0.96811	-0.12138	-0.53245	-0.04539	-0.86090	0.46165	-0.64132	0.37170	-1.32460
$O_5$	-1.32460	0.64132	0.37170	0.53245	-0.96811	0.12138	0.46165	0.04539	-0.86090
$O_6$	-1.32460	-0.64132	-0.37170	-0.53245	-0.96811	0.12138	-0.46165	0.04539	-0.86090
$O_7$	-1.32460	0.64132	-0.37170	0.53245	-0.96811	-0.12138	-0.46165	-0.04539	-0.86090
$O_8$	-1.32460	-0.64132	0.37170	-0.53245	-0.96811	-0.12138	0.46165	-0.04539	-0.86090
$O_9$	-0.86090	0.46165	0.04539	0.37170	-1.32460	0.64132	0.12138	0.53245	-0.96811
$O_{10}$	-0.86090	-0.46165	0.04539	-0.37170	-1.32460	-0.64132	0.12138	-0.53245	-0.96811
$O_{11}$	-0.86090	-0.46165	-0.04539	-0.37170	-1.32460	0.64132	-0.12138	0.53245	-0.96811
$O_{12}$	-0.86090	0.46165	-0.04539	0.37170	-1.32460	-0.64132	-0.12138	-0.53245	-0.96811
$O_{13}$	-0.96811	0.12138	0.53245	0.04539	-0.86090	0.46165	0.64132	0.37170	-1.32460
$O_{14}$	-0.96811	0.12138	-0.53245	0.04539	-0.86090	-0.46165	-0.64132	-0.37170	-1.32460
$O_{15}$	-0.96811	-0.12138	0.53245	-0.04539	-0.86090	-0.46165	0.64132	-0.37170	-1.32460
$O_{16}$	-0.96811	-0.12138	-0.53245	-0.04539	-0.86090	0.46165	-0.64132	0.37170	-1.32460
$O_{17}$	-1.32460	0.64132	0.37170	0.53245	-0.96811	0.12138	0.46165	0.04539	-0.86090
$O_{18}$	-1.32460	-0.64132	-0.37170	-0.53245	-0.96811	0.12138	-0.46165	0.04539	-0.86090
$O_{19}$	-1.32460	0.64132	-0.37170	0.53245	-0.96811	-0.12138	-0.46165	-0.04539	-0.86090
$O_{20}$	-1.32460	-0.64132	0.37170	-0.53245	-0.96811	-0.12138	0.46165	-0.04539	-0.86090
$O_{21}$	-0.86090	0.46165	0.04539	0.37170	-1.32460	0.64132	0.12138	0.53245	-0.96811
$O_{22}$	-0.86090	-0.46165	0.04539	-0.37170	-1.32460	-0.64132	0.12138	-0.53245	-0.96811
$O_{23}$	-0.86090	-0.46165	-0.04539	-0.37170	-1.32460	0.64132	-0.12138	0.53245	-0.96811
$O_{24}$	-0.86090	0.46165	-0.04539	0.37170	-1.32460	-0.64132	-0.12138	-0.53245	-0.96811
$Sr_1$	2.52320	-0.12941	-0.26488	-0.26488	2.52320	-0.12941	-0.12941	-0.26488	2.52320
$Sr_2$	2.52320	-0.12941	0.26488	-0.26488	2.52320	0.12941	0.12941	0.26488	2.52320
$Sr_3$	2.52320	0.12941	-0.26488	0.26488	2.52320	0.12941	-0.12941	0.26488	2.52320
Sr <sub>4</sub>	2.52320	0.12941	0.26488	0.26488	2.52320	-0.12941	0.12941	-0.26488	2.52320

Table 3.14: Calculated BEC's of Ba(NO<sub>3</sub>)<sub>2</sub>. Actual ionic charges are Ba = +2, O = -2, N = -3.

Atom	$Z_{11}$	$Z_{12}$	$Z_{13}$	$Z_{21}$	$Z_{22}$	$Z_{23}$	$Z_{31}$	$Z_{32}$	$Z_{33}$
$N_1$	1.87667	-0.94450	-0.75773	-0.75773	1.87667	-0.94450	-0.75773	-0.75773	1.87667
$N_2$	1.87667	-0.94450	0.75773	-0.75773	1.87667	0.94450	0.94450	0.75773	1.87667
$N_3$	1.87667	0.94450	-0.75773	0.75773	1.87667	0.94450	-0.94450	0.75773	1.87667
$N_4$	1.87667	0.94450	0.75773	0.75773	1.87667	-0.94450	0.94450	-0.75773	1.87667
$N_5$	1.87667	-0.94450	-0.75773	-0.75773	1.87667	-0.94450	-0.94450	-0.75773	1.87667
$N_6$	1.87667	-0.94450	0.75773	-0.75773	1.87667	0.94450	0.94450	0.75773	1.87667
$N_7$	1.87667	0.94450	-0.75773	0.75773	1.87667	0.94450	-0.94450	0.75773	1.87667
$N_8$	1.87667	0.94450	0.75773	0.75773	1.87667	-0.94450	0.94450	-0.75773	1.87667
$O_1$	-0.97833	0.14729	0.53080	0.08409	-0.91579	0.49824	0.60463	0.41497	-1.31574
$O_2$	-0.97833	0.14729	-0.53080	0.08409	-0.91579	-0.49824	-0.60463	-0.41497	-1.31574
$O_3$	-0.97833	-0.14729	0.53080	-0.08409	-0.91579	-0.49824	0.60463	-0.41497	-1.31574
$O_4$	-0.97833	-0.14729	-0.53080	-0.08409	-0.91579	0.49824	-0.60463	0.41497	-1.31574
$O_5$	-1.31574	0.60463	0.41497	0.53080	-0.97833	0.14729	0.49824	0.08409	-0.91579
$O_6$	-1.31574	-0.60463	-0.41497	-0.53080	-0.97833	0.14729	-0.49824	0.08409	-0.91579
$O_7$	-1.31574	0.60463	-0.41497	0.53080	-0.97833	-0.14729	-0.49824	-0.08409	-0.91579
$O_8$	-1.31574	-0.60463	0.41497	-0.53080	-0.97833	-0.14729	0.49824	-0.08409	-0.91579
$O_9$	-0.91579	0.49824	0.08409	0.41497	-1.31574	0.60463	0.14729	0.53080	-0.97833
$O_{10}$	-0.91579	-0.49824	0.08409	-0.41497	-1.31574	-0.60463	0.14729	-0.53080	-0.97833
$O_{11}$	-0.91579	-0.49824	-0.08409	-0.41497	-1.31574	0.60463	-0.14729	0.53080	-0.97833
$O_{12}$	-0.91579	0.49824	-0.08409	0.41497	-1.31574	-0.60463	-0.14729	-0.53080	-0.97833
$O_{13}$	-0.97833	0.14729	0.53080	0.08409	-0.91579	0.49824	0.60463	0.41497	-1.31574
$O_{14}$	-0.97833	0.14729	-0.53080	0.08409	-0.91579	-0.49824	-0.60463	-0.41497	-1.31574
$O_{15}$	-0.97833	-0.14729	0.53080	-0.08409	-0.91579	-0.49824	0.60463	-0.41497	-1.31574
$O_{16}$	-0.97833	-0.14729	-0.53080	-0.08409	-0.91579	0.49824	-0.60463	0.41497	-1.31574
$O_{17}$	-1.31574	0.60463	0.41497	0.53080	-0.97833	0.14729	0.49824	0.08409	-0.91579
$O_{18}$	-1.31574	-0.60463	-0.41497	-0.53080	-0.97833	0.14729	-0.49824	0.08409	-0.91579
$O_{19}$	-1.31574	0.60463	-0.41497	0.53080	-0.97833	-0.14729	-0.49824	-0.08409	-0.91579
$O_{20}$	-1.31574	-0.60463	0.41497	-0.53080	-0.97833	-0.14729	0.49824	-0.08409	-0.91579
$O_{21}$	-0.91579	0.49824	0.08409	0.41497	-1.31574	0.60463	0.14729	0.53080	-0.97833
$O_{22}$	-0.91579	-0.49824	0.08409	-0.41497	-1.31574	-0.60463	0.14729	-0.53080	-0.97833
$O_{23}$	-0.91579	-0.49824	-0.08409	-0.41497	-1.31574	0.60463	-0.14729	0.53080	-0.97833
$O_{24}$	-0.91579	0.49824	-0.08409	0.41497	-1.31574	-0.60463	-0.14729	-0.53080	-0.97833
$Ba_1$	2.66640	-0.10657	-0.28519	-0.28519	2.66640	-0.10657	-0.10657	-0.28519	2.66640
$Ba_2$	2.66640	-0.10657	0.28519	-0.28519	2.66640	0.10657	0.10657	0.28519	2.66640
Ba <sub>3</sub>	2.66640	0.10657	-0.28519	0.28519	2.66640	0.10657	-0.10657	0.28519	2.66640
Ba <sub>4</sub>	2.66640	0.10657	0.28519	0.28519	2.66640	-0.10657	0.10657	-0.28519	2.66640

# 3.3.4 Infrared spectra

**Nitrates:** Using the respective optimized crystal systems, we calculated the IR spectra using linear response theory [64, 80, 81] on the lines of Moreira et al. [80, 82] at the center of the Brillouin zone. The primitive unit cell of nitrates of the form  $M(NO_3)_2$  contains 36 atoms, and standard factor group analysis leads to 3 acoustic modes and 105 optical modes, among which 39 ( $T_u$ ) are IR active, 51 are Raman active, and 15 ( $A_u$ ) are silent. These optical modes of vibration can be

Table 3.15: Percentage of deviations of BEC's all inquivalent atoms are shown along xx, yy, zz directions.

Sr(NO <sub>3</sub> ) <sub>2</sub>				Ba(NO <sub>3</sub> ) <sub>2</sub>			
Atom	$Z_{11}$	$Z_{22}$	$Z_{33}$	Atom	$Z_{11}$	$Z_{22}$	$Z_{33}$
$N_1$	163.067	163.067	163.067	$N_1$	162.55	162.55	162.55
$N_2$	163.067	163.067	163.067	$N_2$	162.55	162.55	162.55
$N_3$	163.067	163.067	163.067	$N_3$	162.55	162.55	162.55
$N_4$	163.067	163.067	163.067	$N_4$	162.55	162.55	162.55
$N_5$	163.067	163.067	163.067	$N_5$	162.55	162.55	162.55
$N_6$	163.067	163.067	163.067	$N_6$	162.55	162.55	162.55
$N_7$	163.067	163.067	163.067	$N_7$	162.55	162.55	162.55
$N_8$	163.067	163.067	163.067	$N_8$	162.55	162.55	162.55
$O_1$	51.59	56.95	33.77	$O_1$	148.91	56.95	33.77
$O_2$	51.59	56.95	33.77	$O_2$	148.91	56.95	33.77
$O_3$	51.59	56.95	33.77	$O_3$	148.91	56.95	33.77
$O_4$	51.59	56.95	33.77	$O_4$	148.91	56.95	33.77
$O_5$	33.77	51.59	56.95	$O_5$	165.78	51.59	56.95
$O_6$	33.77	51.59	56.95	$O_6$	165.78	51.59	56.95
$O_7$	33.77	51.59	56.95	$O_7$	165.78	51.59	56.95
$O_8$	33.77	51.59	56.95	$O_8$	165.78	51.59	56.95
$O_9$	56.95	33.77	51.59	$O_9$	51.59	33.77	51.59
$O_{10}$	56.95	33.77	51.59	$O_{10}$	51.59	33.77	51.59
$O_{11}$	56.95	33.77	51.59	$O_{11}$	51.59	33.77	51.59
$O_{12}$	56.95	33.77	51.59	$O_{12}$	51.59	33.77	51.59
$O_{13}$	51.59	56.95	33.77	$O_{13}$	148.91	56.95	33.77
$O_{14}$	51.59	56.95	33.77	$O_{14}$	148.91	56.95	33.77
$O_{15}$	51.59	56.95	33.77	$O_{15}$	148.91	56.95	33.77
$O_{16}$	51.59	56.95	33.77	$O_{16}$	148.91	56.95	33.77
$O_{17}$	33.77	51.59	56.95	$O_{17}$	165.78	51.59	56.95
$O_{18}$	33.77	51.59	56.95	$O_{18}$	165.78	51.59	56.95
$O_{19}$	33.77	51.59	56.95	$O_{19}$	165.78	51.59	56.95
$O_{20}$	33.77	51.59	56.95	$O_{20}$	165.78	51.59	56.95
$O_{21}$	56.95	33.77	51.59	$O_{22}$	145.78	33.77	51.59
$O_{23}$	56.95	33.77	51.59	$O_{23}$	145.78	33.77	51.59
$O_{24}$	56.95	33.77	51.59	$O_{24}$	145.78	33.77	51.59
$Sr_1$	-26.16	-26.16	-26.16	$Ba_1$	-33.32	-33.32	-33.32
$Sr_2$	-26.16	-26.16	-26.16	$Ba_2$	-33.32	-33.32	-33.32
$Sr_3$	-26.16	-26.16	-26.16	$Ba_2$	-33.32	-33.32	-33.32
Sr <sub>4</sub>	-26.16	-26.16	-26.16	$Ba_2$	-33.32	-33.32	-33.32

further divided into 48 internal (stretching and bending of NO<sub>3</sub> group) modes and 57 external (lattice) modes. The irreducible representation of the phonon modes at the Brillouin zone center is  $\Gamma_{acoustic}=3T_u$ ,  $\Gamma_{IR}=12T_u$ ,  $\Gamma_{Raman}=4A_g+8E_g+12T_g$ ,  $\Gamma_{silent}=5A_u+10E_u$  for optical modes. Among these modes,  $T_u$  and  $T_g$  are triply degenerate and  $A_g$ ,  $E_g$ ,  $A_u$ , and  $E_u$  are nondegenerate modes. The  $T_u$  modes are IR active, and the  $A_g$ ,  $E_g$ , and  $T_g$  modes are Raman active. On the other hand, the  $A_u$  and  $E_u$  modes are neither IR active nor Raman active; hence they are called

silent modes.

The calculated IR bands and their vibrational assignments are depicted in Tables 3.16–3.19, and Figures 3.3 and 3.4 illustrate the simulated IR spectra and a few vibrational mode representations of M(NO<sub>3</sub>)<sub>2</sub>. The spectrum was divided into three parts to assist resolution of the peaks with different intensities:

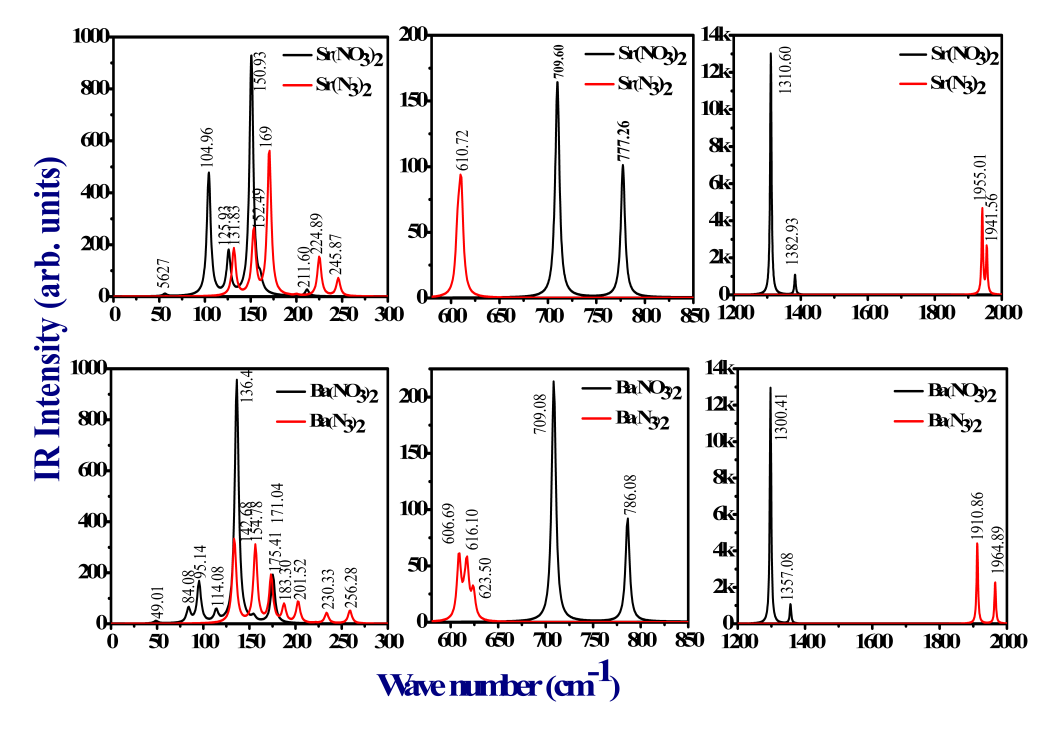


Figure 3.3: Density functional perturbation theory-calculated infrared spectra of (a)  $Sr(NO_3)_2$ ,  $Ba(NO_3)_2$ ,  $Sr(N_3)_2$  and  $Ba(N_3)_2$  in the 0-2100 cm<sup>-1</sup> wavenumber range.

- Low-frequency modes up to 300 cm<sup>-1</sup> are due to collective vibrations of anions and cations, and thus are attributed either to external (lattice) modes or to their mixture with low-frequency molecular vibrations.
- Intermediate modes (600-900 cm<sup>-1</sup>) are assigned to different distortions of the anion group and to the contributions from ONO<sub>2</sub> scissoring and bending vibrations.

• The highest-frequency modes (above 900 cm $^{-1}$ ) are due to the ONO<sub>2</sub> stretching vibrations.

Table 3.16: Calculated infrared frequencies (0-300  $\text{cm}^{-1}$ ) with symmetry assignment for  $Sr(NO_3)_2$ .

Mode number	Frequency (cm <sup>-1</sup> )	Symmetry	Mode	Assignment
M4-M6	56.27	$T_u$	IR	Sr, $NO_3^-$ trans.
M7	56.85	$A_{g}$	Raman	Sr, $NO_3^-$ trans.
M8-M9	66.86	$E_u$	Silent	Sr, $NO_3^-$ trans.
M10-M12	90.62	$T_{g}$	Raman	$NO_3^-$ rot.
M13	98.06	$A_u$	Silent	Sr trans., $NO_3^-$ rot.
M14-M16	104.17	$T_u$	IR	Sr trans., $NO_3^-$ rot.
M17-M19	104.46	$T_u$	IR	Sr trans., $NO_3^-$ rot.
M20-M22	107.99	$T_{ m g}$	R	$NO_3^-$ rot.
M23-M25	125.89	$T_u$	IR	Sr trans., $NO_3^-$ rot.
M26-M27	126.19	$E_{g}$	Raman	$NO_3^-$ trans.
M28-M29	138.89	$E_u$	Silent	$NO_3^-$ rotational
M30	144.35	$A_u$	Silent	Sr trans., $NO_3^-$ rot.
M31-M33	147.95	$T_{ m g}$	Raman	$NO_3^-$ rot.
M34-M36	150.77	$T_u$	IR	$NO_3^-$ trans.
M37-M39	160.50	$T_u$	IR	$NO_3^-$ trans.
M40	160.63	$A_u$	Silent	Sr trans., $NO_3^-$ rot.
M41-M43	164.30	$T_{g}$	Raman	$NO_3^-$ trans.
M44-M45	165.96	$E_u$	Silent	Sr, $NO_3^-$ trans.
M46-M48	166.86	$T_{ m g}$	Raman	$NO_3^-$ rot.
M49	174.88	$A_g^{\circ}$	Raman	Sr trans., $NO_3^-$ rot.
M50-M52	178.26	$T_u^{\circ}$	IR	$NO_3^-$ rot.
M53-M54	185.72	$E_{\mathrm{g}}$	Raman	$NO_3^-$ rot.
M55-M57	200.31	$T_{ m g}^{\circ}$	Raman	$NO_3^-$ rot.
M58-M60	211.60	$T_u^{\circ}$	IR	$NO_3^-$ rot.

Table 3.17: Calculated and Experimental frequency (cm<sup>-1</sup>) [12] of Infrared frequencies (700-1500 cm<sup>-1</sup>) with symmetry assignment for Sr(NO<sub>3</sub>)<sub>2</sub>.

Mode number	Cal.	Expt.	Sym.	Mode	Assignment
M61-M62	706.25		$E_u$	Silent	ONO <sub>2</sub> scissor.
M63-M65	707.26		$T_u$	IR	ONO <sub>2</sub> scissor.
M66-M67	708.08		$E_{g}$	Raman	$ONOO_2$ scissor.
M68-M70	709.79	738	$T_u$	IR	$ONO_2$ scissor.
M71-M73	710.03		$T_{\mathrm{g}}$	Raman	ONO <sub>2</sub> scissor.
M74-M76	713.23		$T_g$	Raman	ONO <sub>2</sub> scissor.
M77-M79	777.33		$T_u$	IR	ONO <sub>2</sub> bend.
M80	777.33		$A_u$	Silent	ONO <sub>2</sub> bend.
M81-M83	778.78		$T_{g}$	Raman	ONO <sub>2</sub> bend.
M84	777.95	814	$T_{g}$	Raman	ONO <sub>2</sub> bend.
M85-M87	1017.66	1055	$T_{g}$	Raman	ONO <sub>2</sub> symm. stretch.
M88-M90	11017.91		$T_u$	IR	ONO <sub>2</sub> symm. stretch.
M91-M92	1019.18		$A_{u}$	Silent	ONO <sub>2</sub> symm. stretch.
M93-M95	1310.61	1360	$T_u$	IR	ONO <sub>2</sub> asymm. stretch.
M96-M97	1322.05		$E_{g}$	Raman	ONO <sub>2</sub> asymm. stretch.
M98-M100	1354.905	1436	$T_g$	Raman	ONO <sub>2</sub> asymm. stretch.
M101-M102	1366.28	1474	$E_u^{\circ}$	Silent	ONO <sub>2</sub> asymm. stretch.
M103-M105	1373.62		$T_{g}$	Raman	ONO <sub>2</sub> asymm. stretch.
M106-M108	1382.82	1795	$T_u$	IR	ONO <sub>2</sub> asymm. stretch.

Table 3.18: Calculated and Experimental frequency (cm $^{-1}$ ) [12] of Infrared frequencies (700-1500 cm $^{-1}$ ) with symmetry assignment for Ba(NO<sub>3</sub>)<sub>2</sub>.

Mode number	Cal.	Expt.	Sym.	Mode	Assignment
M61-M62	707.32		$E_u$	Silent	ONO <sub>2</sub> scissor.
M63-M65	707.85		$T_u$	IR	ONO <sub>2</sub> scissor.
M66-M68	708.91		$T_u$	IR	$ONO_2$ scissor.
M69-M70	709.47	731	$E_{\rm g}$	Raman	ONO <sub>2</sub> scissor.
M71-M73	711.16		$T_g$	Raman	ONO <sub>2</sub> scissor.
M74-M76	713.62		$T_{g}$	Raman	$ONO_2$ scissor.
M77	785.49		$A_u$	Silent	ONO <sub>2</sub> bend.
M78-M80	786.16		$T_u$	IR	ONO <sub>2</sub> bend.
M81-M83	787.76		$T_{g}$	Raman	ONO <sub>2</sub> bend.
M84	788.76	817	$A_g$	Raman	ONO <sub>2</sub> bend.
M85-M87	1007.83		$T_{g}$	Raman	ONO <sub>2</sub> symm. stretch.
M88-M90	1007.94	1047	$T_u$	IR	ONO <sub>2</sub> symm. stretch.
M91	1008.53		$E_u$	Silent	ONO <sub>2</sub> symm. stretch.
M92	1009.12		$A_{g}$	Raman	ONO <sub>2</sub> symm. stretch.
M93-M95	1297.43	1345	$T_u$	IR	ONO <sub>2</sub> asymm. stretch.
M96-M97	1306.69		$E_{g}$	Raman	ONO <sub>2</sub> asymm. stretch.
M98-M100	1336.88	1415	$T_g$	Raman	ONO <sub>2</sub> asymm. stretch.
M101-M102	1342.54		$E_u$	Silent	ONO <sub>2</sub> asymm. stretch.
M103-M105	1352.92	1462	$T_{g}$	Raman	ONO <sub>2</sub> asymm. stretch.
M106-M108	1356.79	1780	$T_u$	IR	ONO <sub>2</sub> asymm. stretch.

Table 3.19: Calculated infrared frequencies (0-300 cm<sup>-1</sup>) with symmetry assignment for Ba(NO<sub>3</sub>)<sub>2</sub>.

Mode number         Frequency (cm $^{-1}$ )         Symmetry         Mode         Assignment           M4-M5         42.41 $E_u$ Silent         Ba, NO $_3^-$ trans.           M6-M8         49.01 $T_u$ IR         Ba, NO $_3^-$ trans.           M9         68.42 $A_g$ Raman         Ba, NO $_3^-$ trans.           M10-M12         81.49 $T_g$ Raman         NO $_3^-$ rot.           M13-M15         83.97 $T_u$ IR         Ba trans., NO $_3^-$ rot.           M16         84.72 $A_u$ Silent         Ba trans., NO $_3^-$ rot.           M17-M19         96.08 $T_u$ IR         Ba trans., NO $_3^-$ rot.           M20-M22         106.96 $T_g$ Raman         NO $_3^-$ rot.           M23-M24         110.37 $E_u$ Silent         Ba trans., NO $_3^-$ rot.           M25-M27         113.68 $T_u$ IR         NO $_3^-$ trans.           M28-M29         125.23 $E_g$ Raman         NO $_3^-$ rot.           M30         131.03 $A_u$ Silent         Ba trans., NO $_3^-$ rot.           M31-M33         135.10 $T_u$ IR </th <th></th> <th></th> <th></th> <th></th> <th></th>					
M6-M8         49.01 $T_u$ IR         Ba, NO $_3$ trans.           M9         68.42 $A_g$ Raman         Ba, NO $_3$ trans.           M10-M12         81.49 $T_g$ Raman         NO $_3$ rot.           M13-M15         83.97 $T_u$ IR         Ba trans., NO $_3$ rot.           M16         84.72 $A_u$ Silent         Ba trans., NO $_3$ rot.           M17-M19         96.08 $T_u$ IR         Ba trans., NO $_3$ rot.           M20-M22         106.96 $T_g$ Raman         NO $_3$ rot.           M23-M24         110.37 $E_u$ Silent         Ba trans., NO $_3$ rot.           M25-M27         113.68 $T_u$ IR         NO $_3$ trans.           M28-M29         125.23 $E_g$ Raman         NO $_3$ rot.           M30         131.03 $A_u$ Silent         Ba trans., NO $_3$ rot.           M31-M33         135.10 $T_u$ IR         NO $_3$ rot.           M34-M36         139.63 $T_g$ Raman         NO $_3$ trans.           M37-M39         152.79 $T_g$ Raman         NO $_3$ trans.	Mode number	Frequency (cm <sup>-1</sup> )	Symmetry	Mode	Assignment
M9         68.42 $A_g$ Raman         Ba, NO $_3^-$ trans.           M10-M12         81.49 $T_g$ Raman         NO $_3^-$ rot.           M13-M15         83.97 $T_u$ IR         Ba trans., NO $_3^-$ rot.           M16         84.72 $A_u$ Silent         Ba trans., NO $_3^-$ rot.           M17-M19         96.08 $T_u$ IR         Ba trans., NO $_3^-$ rot.           M20-M22         106.96 $T_g$ Raman         NO $_3^-$ rot.           M23-M24         110.37 $E_u$ Silent         Ba trans., NO $_3^-$ rot.           M25-M27         113.68 $T_u$ IR         NO $_3^-$ rot.           M28-M29         125.23 $E_g$ Raman         NO $_3^-$ rot.           M30         131.03 $A_u$ Silent         Ba trans., NO $_3^-$ rot.           M31-M33         135.10 $T_u$ IR         NO $_3^-$ rot.           M34-M36         139.63 $T_g$ Raman         NO $_3^-$ rot.           M37-M39         152.79 $T_g$ Raman         NO $_3^-$ trans.           M40-M43         154.60 $T_u$ IR         NO $_3^-$	M4-M5	42.41	$E_{u}$	Silent	Ba, $NO_3^-$ trans.
M10-M12         81.49 $T_g^{\epsilon}$ Raman $NO_3^-$ rot.           M13-M15         83.97 $T_u$ IR         Ba trans., $NO_3^-$ rot.           M16         84.72 $A_u$ Silent         Ba trans., $NO_3^-$ rot.           M17-M19         96.08 $T_u$ IR         Ba trans., $NO_3^-$ rot.           M20-M22         106.96 $T_g$ Raman $NO_3^-$ rot.           M23-M24         110.37 $E_u$ Silent         Ba trans., $NO_3^-$ rot.           M25-M27         113.68 $T_u$ IR $NO_3^-$ rot.           M28-M29         125.23 $E_g$ Raman $NO_3^-$ rot.           M30         131.03 $A_u$ Silent         Ba trans., $NO_3^-$ rot.           M31-M33         135.10 $T_u$ IR $NO_3^-$ rot.           M34-M36         139.63 $T_g$ Raman $NO_3^-$ rot.           M37-M39         152.79 $T_g$ Raman $NO_3^-$ trans.           M40-M43         154.60 $T_u$ IR $NO_3^-$ rotational           M44         155.45 $E_g$ Raman $NO$	M6-M8	49.01	$T_u$	IR	Ba, $NO_3^-$ trans.
M13-M15         83.97 $T_u$ IR         Ba trans., $NO_3^-$ rot.           M16         84.72 $A_u$ Silent         Ba trans., $NO_3^-$ rot.           M17-M19         96.08 $T_u$ IR         Ba trans., $NO_3^-$ rot.           M20-M22         106.96 $T_g$ Raman $NO_3^-$ rot.           M23-M24         110.37 $E_u$ Silent         Ba trans., $NO_3^-$ rot.           M25-M27         113.68 $T_u$ IR $NO_3^-$ rot.           M28-M29         125.23 $E_g$ Raman $NO_3^-$ rot.           M30         131.03 $A_u$ Silent         Ba trans., $NO_3^-$ rot.           M31-M33         135.10 $T_u$ IR $NO_3^-$ rot.           M34-M36         139.63 $T_g$ Raman $NO_3^-$ trans.           M37-M39         152.79 $T_g$ Raman $NO_3^-$ trans.           M40-M43         154.60 $T_u$ IR $NO_3^-$ trans.           M45-M46         155.68 $E_u$ Silent $NO_3^-$ trans.           M47-M49         175.78 $T_u$ IR $NO_$	M9	68.42	$A_{g}$	Raman	Ba, $NO_3^-$ trans.
M16         84.72 $A_u$ Silent         Ba trans., $NO_3^-$ rot.           M17-M19         96.08 $T_u$ IR         Ba trans., $NO_3^-$ rot.           M20-M22         106.96 $T_g$ Raman $NO_3^-$ rot.           M23-M24         110.37 $E_u$ Silent         Ba trans., $NO_3^-$ rot.           M25-M27         113.68 $T_u$ IR $NO_3^-$ trans.           M28-M29         125.23 $E_g$ Raman $NO_3^-$ rot.           M30         131.03 $A_u$ Silent         Ba trans., $NO_3^-$ rot.           M31-M33         135.10 $T_u$ IR $NO_3^-$ rot.           M34-M36         139.63 $T_g$ Raman $NO_3^-$ trans.           M37-M39         152.79 $T_g$ Raman $NO_3^-$ trans.           M40-M43         154.60 $T_u$ IR $NO_3^-$ trans.           M45-M46         155.45 $E_g$ Raman $NO_3^-$ trans.           M45-M46         155.68 $E_u$ Silent $NO_3^-$ rot.           M50-M52         176.31 $T_g$ Raman $NO_3^$	M10-M12	81.49	$T_{g}^{\circ}$	Raman	$NO_3^-$ rot.
M17-M19       96.08 $T_u$ IR       Ba trans., $NO_3^-$ rot.         M20-M22       106.96 $T_g$ Raman $NO_3^-$ rot.         M23-M24       110.37 $E_u$ Silent       Ba trans., $NO_3^-$ rot.         M25-M27       113.68 $T_u$ IR $NO_3^-$ trans.         M28-M29       125.23 $E_g$ Raman $NO_3^-$ rot.         M30       131.03 $A_u$ Silent       Ba trans., $NO_3^-$ rot.         M31-M33       135.10 $T_u$ IR $NO_3^-$ rot.         M34-M36       139.63 $T_g$ Raman $NO_3^-$ trans.         M37-M39       152.79 $T_g$ Raman $NO_3^-$ trans.         M40-M43       154.60 $T_u$ IR $NO_3^-$ rotational         M44       155.45 $E_g$ Raman $NO_3^-$ trans.         M45-M46       155.68 $E_u$ Silent $NO_3^-$ trans.         M47-M49       175.78 $T_u$ IR $NO_3^-$ rot.         M50-M52       176.31 $T_g$ Raman $NO_3^-$ rot.         M54-M56       203.72 $T_u$ IR $NO_3^-$ rot	M13-M15	83.97	$T_u$	IR	Ba trans., $NO_3^-$ rot.
M20-M22         106.96 $T_g$ Raman $NO_3^-$ rot.           M23-M24         110.37 $E_u$ Silent         Ba trans., $NO_3^-$ rot.           M25-M27         113.68 $T_u$ IR $NO_3^-$ trans.           M28-M29         125.23 $E_g$ Raman $NO_3^-$ rot.           M30         131.03 $A_u$ Silent         Ba trans., $NO_3^-$ rot.           M31-M33         135.10 $T_u$ IR $NO_3^-$ rot.           M34-M36         139.63 $T_g$ Raman $NO_3^-$ trans.           M37-M39         152.79 $T_g$ Raman $NO_3^-$ trans.           M40-M43         154.60 $T_u^-$ IR $NO_3^-$ rotational           M44         155.45 $E_g$ Raman $NO_3^-$ trans.           M45-M46         155.68 $E_u^-$ Silent $NO_3^-$ trans.           M47-M49         175.78 $T_u^-$ IR $NO_3^-$ rot.           M50-M52         176.31 $T_g^-$ Raman $NO_3^-$ rot.           M54-M56         203.72 $T_u^-$ IR $NO_3^-$ rot.<	M16	84.72	$A_u$	Silent	Ba trans., $NO_3^-$ rot.
M23-M24       110.37 $E_u$ Silent       Ba trans., $NO_3^-$ rot.         M25-M27       113.68 $T_u$ IR $NO_3^-$ trans.         M28-M29       125.23 $E_g$ Raman $NO_3^-$ rot.         M30       131.03 $A_u$ Silent       Ba trans., $NO_3^-$ rot.         M31-M33       135.10 $T_u$ IR $NO_3^-$ rot.         M34-M36       139.63 $T_g$ Raman $NO_3^-$ trans.         M37-M39       152.79 $T_g$ Raman $NO_3^-$ trans.         M40-M43       154.60 $T_u$ IR $NO_3^-$ rotational         M44       155.45 $E_g$ Raman $NO_3^-$ trans.         M45-M46       155.68 $E_u$ Silent $NO_3^-$ trans.         M47-M49       175.78 $T_u$ IR $NO_3^-$ rot.         M50-M52       176.31 $T_g$ Raman $NO_3^-$ rot.         M54-M56       203.72 $T_u$ IR $NO_3^-$ rot.         M57-M59       211.21 $T_g$ Raman $NO_3^-$ rot.	M17-M19	96.08	$T_u$	IR	Ba trans., $NO_3^-$ rot.
M25-M27       113.68 $T_u$ IR       NO $_3^-$ trans.         M28-M29       125.23 $E_g$ Raman       NO $_3^-$ rot.         M30       131.03 $A_u$ Silent       Ba trans., NO $_3^-$ rot.         M31-M33       135.10 $T_u$ IR       NO $_3^-$ rot.         M34-M36       139.63 $T_g$ Raman       NO $_3^-$ trans.         M37-M39       152.79 $T_g$ Raman       NO $_3^-$ trans.         M40-M43       154.60 $T_u$ IR       NO $_3^-$ rotational         M44       155.45 $E_g$ Raman       NO $_3^-$ trans.         M45-M46       155.68 $E_u$ Silent       NO $_3^-$ trans.         M47-M49       175.78 $T_u$ IR       NO $_3^-$ rot.         M50-M52       176.31 $T_g$ Raman       NO $_3^-$ rot.         M54-M56       203.72 $T_u$ IR       NO $_3^-$ rot.         M57-M59       211.21 $T_g$ Raman       NO $_3^-$ rot.	M20-M22	106.96	$T_{g}$	Raman	$NO_3^-$ rot.
M28-M29       125.23 $E_g$ Raman $NO_3^-$ rot.         M30       131.03 $A_u$ Silent       Ba trans., $NO_3^-$ rot.         M31-M33       135.10 $T_u$ IR $NO_3^-$ rot.         M34-M36       139.63 $T_g$ Raman $NO_3^-$ trans.         M37-M39       152.79 $T_g$ Raman $NO_3^-$ trans.         M40-M43       154.60 $T_u$ IR $NO_3^-$ rotational         M44       155.45 $E_g$ Raman $NO_3^-$ trans.         M45-M46       155.68 $E_u$ Silent $NO_3^-$ trans.         M47-M49       175.78 $T_u$ IR $NO_3^-$ rot.         M50-M52       176.31 $T_g$ Raman $NO_3^-$ rot.         M54-M56       203.72 $T_u$ IR $NO_3^-$ rot.         M57-M59       211.21 $T_g$ Raman $NO_3^-$ rot.	M23-M24	110.37	$E_u$	Silent	Ba trans., $NO_3^-$ rot.
M30       131.03 $A_u$ Silent       Ba trans., $NO_3^-$ rot.         M31-M33       135.10 $T_u$ IR $NO_3^-$ rot.         M34-M36       139.63 $T_g$ Raman $NO_3^-$ trans.         M37-M39       152.79 $T_g$ Raman $NO_3^-$ trans.         M40-M43       154.60 $T_u$ IR $NO_3^-$ rotational         M44       155.45 $E_g$ Raman $NO_3^-$ trans.         M45-M46       155.68 $E_u$ Silent $NO_3^-$ trans.         M47-M49       175.78 $T_u$ IR $NO_3^-$ rot.         M50-M52       176.31 $T_g$ Raman $NO_3^-$ rot.         M54-M56       203.72 $T_u$ IR $NO_3^-$ rot.         M57-M59       211.21 $T_g$ Raman $NO_3^-$ rot.	M25-M27	113.68	$T_u$	IR	$NO_3^-$ trans.
M31-M33       135.10 $T_u$ IR $NO_3^-$ rot.         M34-M36       139.63 $T_g$ Raman $NO_3^-$ trans.         M37-M39       152.79 $T_g$ Raman $NO_3^-$ trans.         M40-M43       154.60 $T_u$ IR $NO_3^-$ rotational         M44       155.45 $E_g$ Raman $NO_3^-$ trans.         M45-M46       155.68 $E_u$ Silent $NO_3^-$ trans.         M47-M49       175.78 $T_u$ IR $NO_3^-$ rot.         M50-M52       176.31 $T_g$ Raman $NO_3^-$ rot.         M54-M56       203.72 $T_u$ IR $NO_3^-$ rot.         M57-M59       211.21 $T_g$ Raman $NO_3^-$ rot.	M28-M29	125.23	$E_{g}$	Raman	$NO_3^-$ rot.
M34-M36       139.63 $T_g$ Raman $NO_3^-$ trans.         M37-M39       152.79 $T_g$ Raman $NO_3^-$ trans.         M40-M43       154.60 $T_u$ IR $NO_3^-$ rotational         M44       155.45 $E_g$ Raman $NO_3^-$ trans.         M45-M46       155.68 $E_u$ Silent $NO_3^-$ trans.         M47-M49       175.78 $T_u$ IR $NO_3^-$ rot.         M50-M52       176.31 $T_g$ Raman $NO_3^-$ rot.         M54-M56       203.72 $T_u$ IR $NO_3^-$ rot.         M57-M59       211.21 $T_g$ Raman $NO_3^-$ rot.	M30	131.03	$A_u^{\circ}$	Silent	Ba trans., $NO_3^-$ rot.
M44       155.45 $E_g$ Raman $NO_3^-$ trans.         M45-M46       155.68 $E_u$ Silent $NO_3^-$ trans.         M47-M49       175.78 $T_u$ IR $NO_3^-$ rot.         M50-M52       176.31 $T_g$ Raman $NO_3^-$ rot.         M54-M56       203.72 $T_u$ IR $NO_3^-$ rot.         M57-M59       211.21 $T_g$ Raman $NO_3^-$ rot.	M31-M33	135.10	$T_u$	IR	$NO_3^-$ rot.
M44       155.45 $E_g$ Raman $NO_3^-$ trans.         M45-M46       155.68 $E_u$ Silent $NO_3^-$ trans.         M47-M49       175.78 $T_u$ IR $NO_3^-$ rot.         M50-M52       176.31 $T_g$ Raman $NO_3^-$ rot.         M54-M56       203.72 $T_u$ IR $NO_3^-$ rot.         M57-M59       211.21 $T_g$ Raman $NO_3^-$ rot.	M34-M36	139.63	$T_{g}$	Raman	$NO_3^-$ trans.
M44       155.45 $E_g$ Raman $NO_3^-$ trans.         M45-M46       155.68 $E_u$ Silent $NO_3^-$ trans.         M47-M49       175.78 $T_u$ IR $NO_3^-$ rot.         M50-M52       176.31 $T_g$ Raman $NO_3^-$ rot.         M54-M56       203.72 $T_u$ IR $NO_3^-$ rot.         M57-M59       211.21 $T_g$ Raman $NO_3^-$ rot.	M37-M39	152.79	$T_{g}^{\circ}$	Raman	$NO_3^-$ trans.
M45-M46       155.68 $E_u$ Silent $NO_3^-$ trans.         M47-M49       175.78 $T_u$ IR $NO_3^-$ rot.         M50-M52       176.31 $T_g$ Raman $NO_3^-$ rot.         M54-M56       203.72 $T_u$ IR $NO_3^-$ rot.         M57-M59       211.21 $T_g$ Raman $NO_3^-$ rot.	M40-M43	154.60	$T_u$	IR	$NO_3^-$ rotational
M47-M49       175.78 $T_u$ IR $NO_3^-$ rot.         M50-M52       176.31 $T_g$ Raman $NO_3^-$ rot.         M54-M56       203.72 $T_u$ IR $NO_3^-$ rot.         M57-M59       211.21 $T_g$ Raman $NO_3^-$ rot.	M44	155.45	$E_{g}$	Raman	$NO_3^-$ trans.
M50-M52       176.31 $T_g$ Raman $NO_3^-$ rot.         M54-M56       203.72 $T_u$ IR $NO_3^-$ rot.         M57-M59       211.21 $T_g$ Raman $NO_3^-$ rot.	M45-M46	155.68	$E_u$	Silent	$NO_3^-$ trans.
M54-M56 203.72 $T_u$ IR NO $_3^-$ rot. M57-M59 211.21 $T_g$ Raman NO $_3^-$ rot.	M47-M49	175.78		IR	$NO_3^-$ rot.
M54-M56 203.72 $T_u$ IR NO $_3^-$ rot. M57-M59 211.21 $T_g$ Raman NO $_3^-$ rot.	M50-M52	176.31	$T_{ m g}$	Raman	$NO_3^-$ rot.
M57–M59 211.21 $T_g$ Raman $NO_3^-$ rot. M60 220.13 $T_g$ Raman $NO_3^-$ rot.	M54-M56	203.72	$T_u$	IR	$NO_3^-$ rot.
M60 220.13 $T_g$ Raman $NO_3^-$ rot.	M57-M59	211.21	$T_{g}$	Raman	$NO_3^-$ rot.
	M60	220.13	$T_{ m g}^{\circ}$	Raman	

Wavenumber range 0-300 cm<sup>-1</sup>: The IR spectrum of strontium nitrate (Figure 3.3) displays a set of broad absorption bands between 50 and 200 cm<sup>-1</sup> with four peaks worth emphasizing, and these absorptions are assigned to the lattice modes. The most intense maximum, which occurs at 150.93 cm<sup>-1</sup>, is due to the translational lattice mode of (M + NO<sub>3</sub>), followed by a secondary peak at 104.26 cm<sup>-1</sup>. Other translational lattice modes occur at 125.93 and 211.60 cm<sup>-1</sup>. However, for barium nitrate, there is a single IR absorption band with several peaks between 60 and 200 cm<sup>-1</sup>, with the most pronounced maximum at 136.41 cm<sup>-1</sup> (translational lattice mode), followed in intensity by peaks at 84.08, 95.41, 114.08,

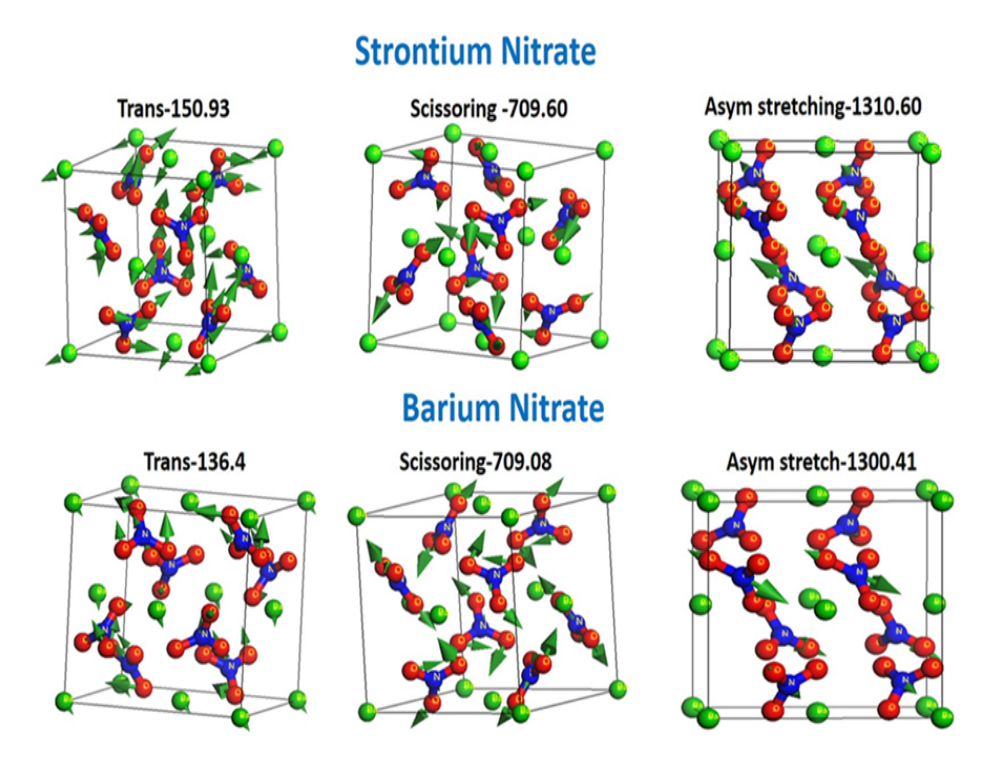


Figure 3.4: Normal modes (cm $^{-1}$ ) behind the most intense maxima in the infrared spectra of  $Sr(NO_3)_2$  and  $Ba(NO_3)_2$ .

and 175.41 cm<sup>-1</sup>. These peaks are due to the translational lattice mode of the barium atom and the rotational lattice mode of NO<sub>3</sub>. No experimental data are available for the low-frequency regions because of limitations of Fourier transform IR spectroscopy, a well-known experimental procedure for obtaining IR spectra. Our results in the low-frequency range are relevant in this aspect for the present divalent metal nitrates.

Wavenumber range 600-900 cm<sup>-1</sup>: For strontium nitrate, there are only two maxima, at 709.60 and 777.26 cm<sup>-1</sup>, which are due to scissoring motion and out-of-plane bending of the O-NO<sub>2</sub> group, respectively. Experimental work [12] suggests that there are two peaks in the IR spectrum of Sr(NO<sub>3</sub>)<sub>2</sub>, at 738 and 814 cm<sup>-1</sup>, respectively. Our results for the IR spectrum reveal similar peaks and satisfactorily match the experimental data. Also, in barium nitrate, an IR absorption

band occurs between 700 and 800 cm<sup>-1</sup>. The most intense absorption maximum occurs at 709.08 cm<sup>-1</sup> and is assigned to a scissoring motion of the O–NO<sub>2</sub> group, whereas a secondary maximum occurs at 786.08 cm<sup>-1</sup> (bending of the O–NO<sub>2</sub> group). The experimental values [12] for the two maxima are 731 and 817 cm<sup>-1</sup>, which are in good agreement with our results.

Wavenumber range 1200-1500 cm<sup>-1</sup>: As shown in Figure 3.3 the absorption lines for strontium nitrate occur at 1310.60 cm<sup>-1</sup> (most intense) and 1382.93 cm<sup>-1</sup>, and in the case of barium nitrate the peaks are at 1300.41 cm<sup>-1</sup> (most intense) and 1357.08 cm<sup>-1</sup>. The maxima in both materials are due to asymmetric stretching of the N-O bond. Brooker et al. [12] reported that the lowest-frequency absorption band occurs at 1360 cm<sup>-1</sup> for Sr(NO<sub>3</sub>)<sub>2</sub> and at 1345 cm<sup>-1</sup> for Ba(NO<sub>3</sub>)<sub>2</sub>, and our calculated frequencies are 1310 and 1297 cm<sup>-1</sup> for strontium nitrate and barium nitrate, respectively (Tables 3.6 and 3.8). The highest frequency as reported experimentally [12] for Sr(NO<sub>3</sub>)<sub>2</sub> is 1795 cm<sup>-1</sup>, whereas for Ba(NO<sub>3</sub>)<sub>2</sub> it is 1780 cm<sup>-1</sup>. We note a shift in the highest frequencies, 1382 and 1356 cm<sup>-1</sup> for strontium nitrate and barium nitrate, respectively (Tables 3.10 and 3.11). This shift in the frequency could be due to the anharmonic effects in the crystals [12]. As the phonon anharmonic interactions emerge from nonharmonic parts of the interatomic potential, they cannot be justified by the quasi-harmonic Debye model. A similar situation is seen for the higher-frequency modes of the azide ion in KN<sub>3</sub> [69].

Table 3.20: Calculated infrared frequencies (0-2000  $\text{cm}^{-1}$ ) with symmetry assignment for  $\text{Sr}(N_3)_2$ .

Mode number	Frequency (cm <sup>-1</sup> )	Symmetry	Mode	Assignment
M4	34.82	$B_1u$	IR	Sr, $N_3^-$ trans.
M5	47.27	$B_3g$	Raman	Sr, $N_3^-$ trans.
M6	105.14	$B_2g$	Raman	Sr, $N_3^-$ trans.
M7	105.82	$B_1g$	Raman	Sr, $N_3^-$ trans.
M8	128.48	$B_3u$	IR	Sr, $N_3^-$ trans.
M9	134.47	$B_3g$	Raman	Sr trans.
M10	141.23	$B_2u$	IR	Sr, $N_3^-$ trans.
M11	146.33	$A_{g}$	Raman	Sr, $N_3^-$ trans.
M12	147.62	$B_1g$	Raman	$N_3^-$ rot.
M13	147.70	$B_2u$	IR	$N_3^-$ rot.
M14	155.73	$B_2g$	Raman	$N_3^-$ rot.
M15	163.78	$B_1u$	IR	Sr, $N_3^-$ trans.
M16	176.46	$B_3g$	Raman	$N_3^-$ rot.
M17	186.94	$A_u$	silent	$N_3^-$ trans.
M18	187.79	$B_1g$	Raman	$N_3^-$ trans.
M19	193.29	$B_1u$	IR	$N_3^-$ rot.
M20	198.37	$A_{g}$	Raman	$N_3^-$ trans.
M21	193.29	$B_1 u$	IR	$N_3^-$ rot.
M22	210.27	$B_2u$	IR	$N_3^-$ rot.
M23	216.81	$B_2g$	Raman	$N_3^-$ rot.
M24	229.98	$B_1g$	Raman	$N_3^-$ rot.
M25	232.27	$B_3u$	IR	$N_3^-$ rot.
M26	280.28	$A_u$	silent	$N_3^-$ rot.
M27	601.00	$B_3g$	Raman	$N_3^-$ bend.
M28	603.80	$B_3u$	IR	$N_3^-$ bend.
M29	608.13	$B_1u$	IR	$N_3^-$ bend.
M30	608.87	$B_2u$	IR	$N_3^-$ bend.
M31	614.20	$A_{g}$	Raman	$N_3^-$ bend.
M32	617.13	$A_u^{\circ}$	silent	$N_3^-$ bend.
M33	622.65	$B_1g$	Raman	$N_3^-$ bend.
M34	623.77	$B_2g$	Raman	$N_3^-$ bend.
M35	1253.51	$B_3u$	IR	$N_3^-$ symm. stretch.
M36	1253.96	$A_u$	silent	$N_3^-$ symm. stretch.
M37	1258.57	$B_3g$	Raman	$N_3^-$ symm. stretch.
M38	1259.38	$A_{g}$	Raman	$N_3^-$ symm. stretch.
M39	1890.02	$B_1 g$	Raman	$N_3^-$ asymm. stretch.
M40	1936.96	$B_1g$	Raman	$N_3^-$ asymm. stretch.
M41	1945.57	$B_1u$	IR	$N_3^-$ asymm. stretch.
M42	1957.06	$B_2u$	IR	$N_3^-$ asymm. stretch.

Table 3.21: Calculated frequency and Experimental frequency (cm $^{-1}$ ) of Infrared frequencies (0-2000 cm $^{-1}$ ) with symmetry assignment for Ba(N<sub>3</sub>)<sub>2</sub>.

Mode number	Cal.	Expt.	Sym.	Mode	Assignment
M4	58.18	53	$B_{g}$	Raman	Sr, $N_3^-$ trans.
M5	67.40		$A_g$	Raman	Sr, $N_3^-$ trans.
M6	115.70	111	$A_g^{\circ}$	Raman	Sr, $N_3^-$ trans.
M7	127.87		$B_u^{\circ}$	IR	Sr, $N_3^-$ trans.
M8	142.68	136	$B_{u}$	IR	Sr, $N_3^-$ trans.
M9	147.93	140	$A_{g}$	Raman	Sr trans.
M10	154.78		$A_u^{\circ}$	IR	Sr, $N_3^-$ trans.
M11	163.12		$B_{ m g}$	Raman	Sr, $N_3^-$ trans.
M12	168.59	164	$A_u$	IR	$N_3^-$ rot.
M13	179.27		$A_{g}$	Raman	$N_3^-$ rot.
M14	189.90	185	$B_u^{\circ}$	IR	$N_3^-$ rot.
M15	194.59		$A_{g}$	Raman	Sr, $N_3^-$ rot.
M16	201.52	190	$B_u^{\circ}$	IR	$N_3^-$ rot.
M17	207.78	206	$B_{g}$	Raman	$N_3^-$ trans.
M18	209.16	208	$A_g$	Raman	$N_3^-$ trans.
M19	222.70		$A_g^{\circ}$	Raman	$N_3^-$ rot.
M20	225.69		$A_u$	IR	$N_3^-$ trans.
M21	227.27		$B_{g}$	Raman	$N_3^-$ rot.
M22	230.33		$A_u$	IR	$N_3^-$ rot.
M23	236.83		$A_{g}$	Raman	$N_3^-$ rot.
M24	252.67		$B_{g}^{\circ}$	Raman	$N_3^-$ rot.
M25	256.28		$B_{g}^{\circ}$	Raman	$N_3^-$ rot.
M26	256.40		$A_{u}$	IR	$N_3^-$ rot.
M27	606.69	604	$B_u$	IR	$N_3^-$ bend.
M28	611.66		$A_g$	Raman	$N_3^-$ bend.
M29	616.10		$A_u$	IR	$N_3^-$ bend.
M30	618.25		$A_{u}$	IR	$N_3^-$ bend.
M31	621.14	619	$B_{ m g}$	Raman	$N_3^-$ bend.
M32	622.45		$B_{ m g}^{\circ}$	Raman	$N_3^-$ bend.
M33	623.50	619	$B_u^{\circ}$	IR	$N_3^-$ bend.
M34	631.08		$A_{g}$	Raman	$N_3^-$ bending
M35	1231.78	1240	$B_u^{\circ}$	IR	$N_3^-$ symm. stretch.
M36	1233.68	1251	$A_{g}$	Raman	$N_3^-$ symm. stretch.
M37	1245.55	1263	$B_u^{\circ}$	IR	$N_3^-$ symm. stretch.
M38	1247.41	1272	$A_g$	Raman	$N_3^-$ symm. stretch.
M39	1866.44	1875	$A_g^{\circ}$	Raman	$N_3^-$ asymm. stretch.
M40	1898.85	1908	$A_g^{\circ}$	Raman	$N_3^-$ asymm. stretch.
M41	1910.86	2134	$B_u^{\circ}$	IR	$N_3^-$ asymm. stretch.
M42	1964.89	2150	$B_u$	IR	$N_3^-$ asymm. stretch.

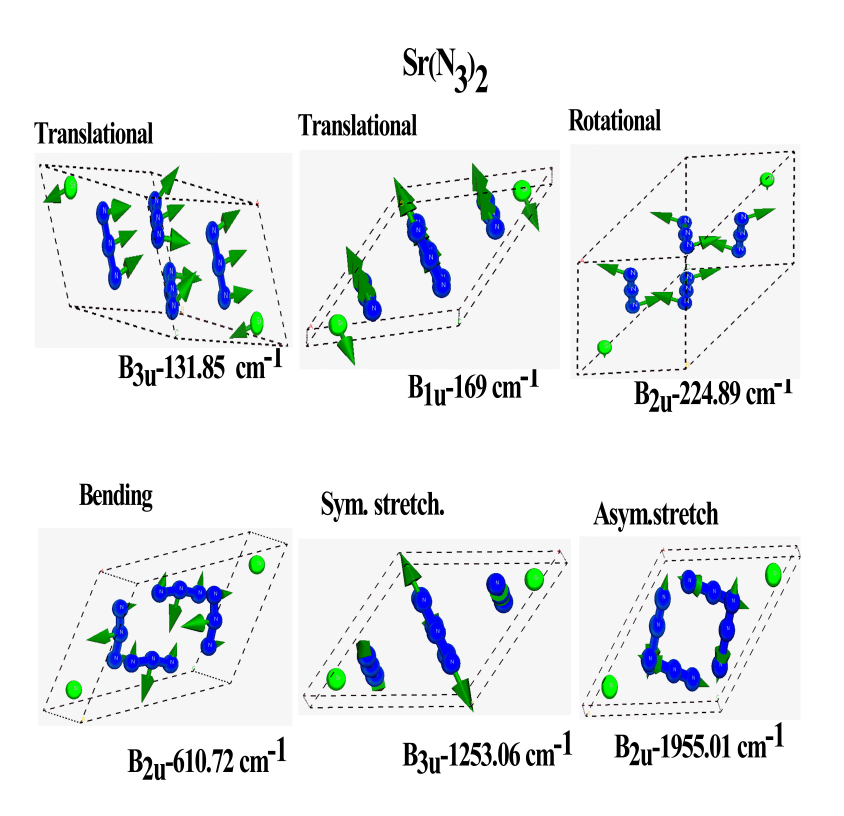


Figure 3.5: Normal modes (cm<sup>-1</sup>) behind the most intense maxima in the infrared spectra of  $Sr(N_3)_2$ .

**Azides:** The infrared spectra of  $Sr(N_3)_2$  and  $Ba(N_3)_2$  are shown in figure 3.3 and the snapshot of a few vibrational modes is given in figure 3.5 and 3.6 for reference. Tables 3.20 and 3.21 presents the predicted normal modes with the respective irreducible representations and the assignment of IR and Raman active modes. The  $M(N_3)_2$  has 14 atoms in primitive cell its leads to 42 normal modes. The irreducible representation of the phonon modes at the Brillouin zone center is:

Ba(N<sub>3</sub>)<sub>2</sub>: 
$$\Gamma_{acoustic} = 1A_u + 2B_u$$
  
 $\Gamma_{IR} = 6A_u + 12B_u$ 

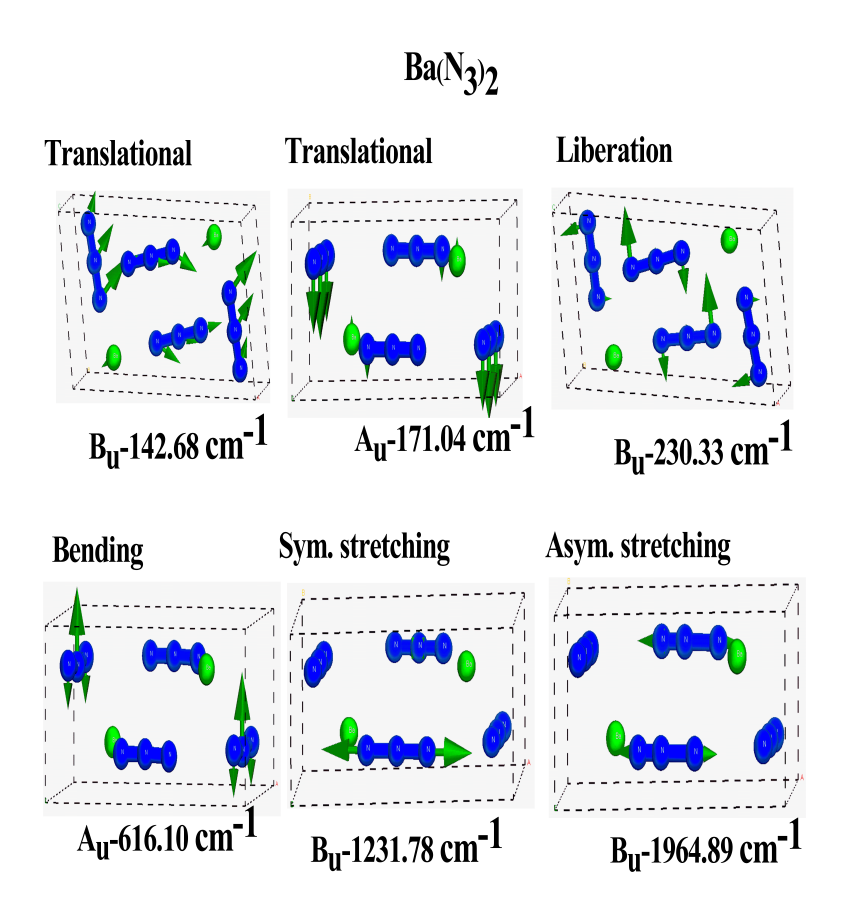


Figure 3.6: Normal modes (cm<sup>-1</sup>) behind the most intense maxima in the infrared spectra of  $Ba(N_3)_2$ .

$$\Gamma_{Raman} = 14A_g + 7B_g$$
 $Sr(N_3)_2$ :  $\Gamma_{acoustic} = B_{1u} + B_{2u} + B_{3u}$ 
 $\Gamma_{IR} = 4B_{1u} + 5B_{2u} + 5B_{3u}$ 
 $\Gamma_{Raman} = 6B_{1g} + 6B_{2g} + 5B_{3g} + 4A_g$ 
 $\Gamma_{silent} = 4A_u$ 

According to Ref. [42], IR spectrum of monoclinic Ba(N<sub>3</sub>)<sub>2</sub> is characterized by 3 absorption bands in the ranges of 0–300, 600–650 and 1200–2000 cm<sup>-1</sup>, with stretching vibration of N–N bond being located above 1200 cm<sup>-1</sup>. However, there is a reasonable agreement between the theoretical and experimental values for IR wavenumbers [42] with a small deviation. This shift in frequency could be due to the anharmonicity of the crystals.

The infrared spectrum for strontium azide presents the low frequency IR region between 0 and 300 cm<sup>-1</sup>, the most intense IR absorption peaks occur at 163 cm<sup>-1</sup>, a mode with irreducible representation  $B_{1u}$ , which is assigned to Sr and  $N_3^$ translational, the second most intense peak occurs at 141 cm<sup>-1</sup> with irreducible representation  $B_{2u}$ . The third and fourth most intense peak appears at 128  $(B_{3u})$ and 210 cm<sup>-1</sup> (B<sub>2u</sub>), corresponding to Sr and N<sub>3</sub> group lattice vibrations. For  $Ba(N_3)_2$ , IR absorption bands depicts various peaks between 0 and 300 cm<sup>-1</sup>, the most prominent maximum at 127, 142, 154, 168, 189, 230, and 268 cm<sup>-1</sup> are assigned to translational and rotational vibrations of Ba and  $N_3$  group. In the mid-frequency region, the IR spectrum of strontium azide is observed between 600 and 650 cm<sup>-1</sup>, there is only one maxima, at 608 cm<sup>-1</sup>, which is owing to outof-plane bending of the N<sub>3</sub> group. In the case of Ba(N<sub>3</sub>)<sub>2</sub> two intense IR absorption peaks occur at 616 cm<sup>-1</sup> and 623 cm<sup>-1</sup>, corresponding to an N-N-N bending movement. The high frequency region interval between 1800 and 2000 cm<sup>-1</sup> is characterized by the absence of any contribution from alkaline-earth metal atom vibrations; therefore, all the modes above 1800 cm<sup>-1</sup> originate from stretching of the N<sub>3</sub> group. The Sr(N<sub>3</sub>)<sub>2</sub> and Ba(N<sub>3</sub>)<sub>2</sub> have two maxima being observed within the 1900-2000 cm<sup>-1</sup> wavenumber range. In the case of strontium azide, the peaks at 1955 and 1941 cm<sup>-1</sup> are related to a  $B_u$  mode relative to an asymmetric stretching of the N-N bond. For barium azide the maxima at 1910.86 and 1964.89 cm<sup>-1</sup> correspond to asymmetric stretching of the N-N bond. A comparison with metal nitrate [46] results reveals that the nitrates are shifted towards the smaller wavenumbers than metal azides. Their lowest frequency absorption band was found at 1300 cm<sup>-1</sup>, and the highest absorption band at 1500 cm<sup>-1</sup>. For strontium nitrate, we have the following maxima due to stretching vibrations of N-O bond: 1310.60 cm<sup>-1</sup> and 1382 cm<sup>-1</sup>, while barium nitrate, the highest intense peak, occurs at 1300.41 cm<sup>-1</sup> (most intense) and 1357.08 cm<sup>-1</sup>. This leads to the conclusion that metal nitrates are more stable than metal azides.

### 3.3.5 Phonon dispersion and Phonon density of states

The dynamical stability of the present materials can be examined by evaluation of the lattice dynamical properties. We calculated the phonon dispersion spectra and phonon density of states for  $M(NO_3)_2$ ,  $M(N_3)_2$  (M = Sr, Ba) using DFPT [63–66]. The primitive cell of  $M(NO_3)_2$  (M = Sr, Ba) is composed of 36 atoms, yielding 108 phonon branches in total, with 3 acoustic branches and 105 optical branches. Since metal azides;  $M(N_3)_2$  (M = Sr and Ba) have 14 atoms yielding totally 42 phonon branches with 3 acoustic and 39 optical branches. The phonon dispersion curves  $M(N_3)_2$  (M = Sr and Ba) in the high symmetry directions  $X \to \Gamma \to Y \to Z \to \Gamma$ ;  $Z \to \Gamma \to Y \to A \to B \to D \to E \to C$  paths in the irreducible Brillouin zone(Figure 3.7). We could not compare our results with the experimental measurements as no study on lattice dynamics of these azides has been available so far. It is clear from the plots that the acoustic and first few optical branches for both  $M(NO_3)_2$  and  $M(N_3)_2$  are overlapping almost in the full Brillouin zone. This clearly indicates that  $M(NO_3)_2$ ,  $M(N_3)_2$  materials possess favorable conditions for thermal transport [83].

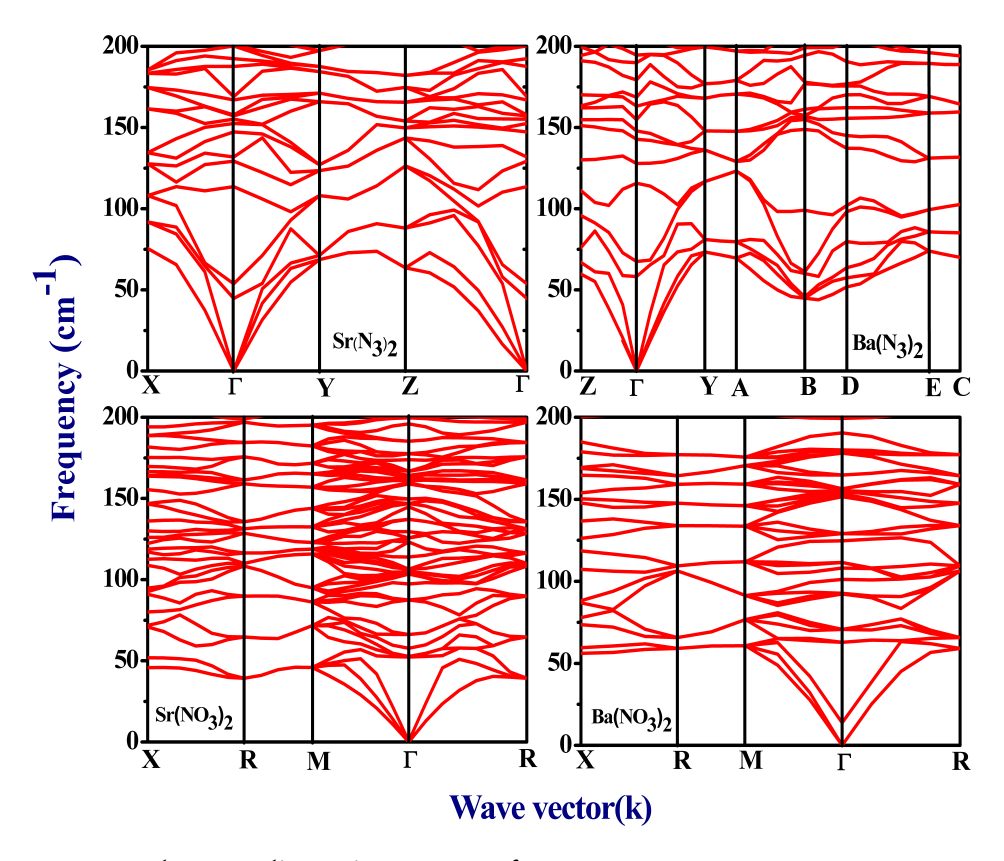


Figure 3.7: (Phonon dispersion curves for  $Sr(NO_3)_2$ ,  $Ba(NO_3)_2$ ,  $Sr(N_3)_2$  and  $Ba(N_3)_2$  wavenumber range over the  $0-200~cm^{-1}$ .

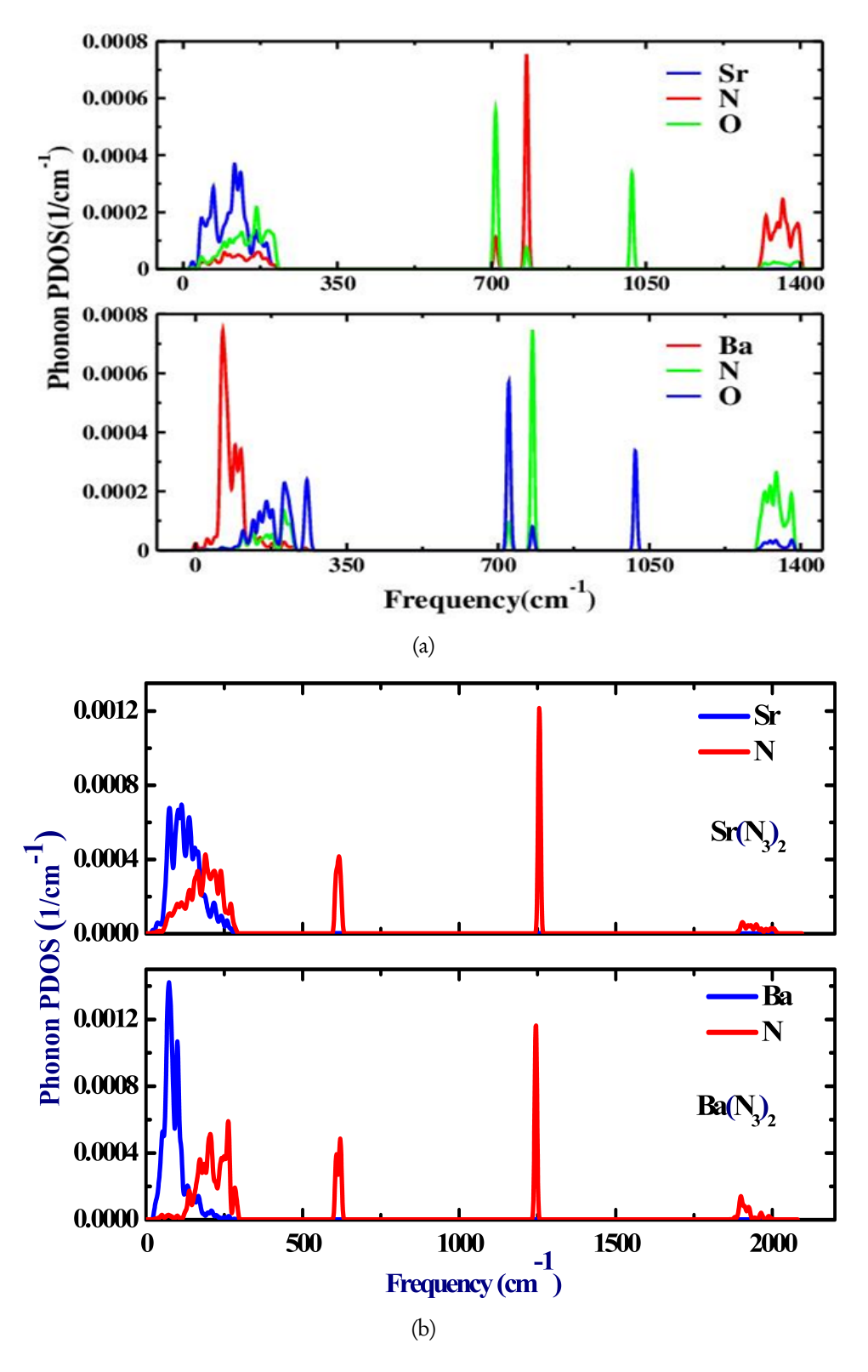


Figure 3.8: Phonon partial density of states (PDOS) for (a)  $Sr(NO_3)_2$  and  $Ba(NO_3)_2$  (b)  $Sr(N_3)_2$  and  $Ba(N_3)_2$ .

In order to know the atomic contribution in the phonon dispersion and confirm the crystal structures stability, we have plotted the partial phonon density of states (PPDOS) of M(NO<sub>3</sub>)<sub>2</sub> and M(N<sub>3</sub>)<sub>2</sub> presented in Figure 3.8. In the highfrequency region (650-1450 cm<sup>-1</sup>) PPDOS behavior is similar for Sr(NO<sub>3</sub>)<sub>2</sub> and Br(NO<sub>3</sub>)<sub>2</sub>. In this region, nitrogen and oxygen atoms have the major contribution, which is mainly due to the frequency associated with the N-O bond bending and stretching vibrations [ $\frac{46}{1}$ ]. In the low frequency region (0-300 cm<sup>-1</sup>), there are higher peaks (black) that indicate that the lattice vibrations are very strong. The highest peak (red) in the phonon partial DOS is observed at 1216.69 cm<sup>-1</sup>, 1237 cm $^{-1}$ , 691.22 cm $^{-1}$ , and 706.86 cm $^{-1}$  for  $Sr(N_3)_2$ ,  $Ba(N_3)_2$ ,  $Sr(NO_3)_2$  and Ba(NO<sub>3</sub>)<sub>2</sub>, respectively. The curves of the strong peaks in the phonon density of state diagram correspond to the smooth curves of the phonon dispersion spectra in the corresponding frequency range. It is found that in the acoustic region, the alkaline earth metal (Sr and Ba) atoms show a large contribution due to their heavier mass. The vibration of the N atom contributes to the optical branch in the high energy region for the light mass. The focus of this work was on the phonon modes, as they are directly related to the elastic moduli and heat transport of the material. Also, the calculated frequencies can be used within the quasi-harmonic approximation to evaluate thermal properties [84].

# 3.3.6 Thermodynamic properties

Thermodynamic properties are some of the most important attributes of the materials that are used in ignition [85]. Also, the thermal behavior of the present materials could play a key role in the growth of sustainable smoke compositions and in understanding the nature of chemical reactions that occur during their decomposition [86]. So we attempted to calculate the thermodynamic properties—namely, H, entropy times temperature (ST), and G—of the present materials. We applied the quasi-harmonic Debye model [87] on the lines of [88] to compute the heat capacity ( $C_V$ ), entropy ( $S_V$ ), and vibrational internal energy

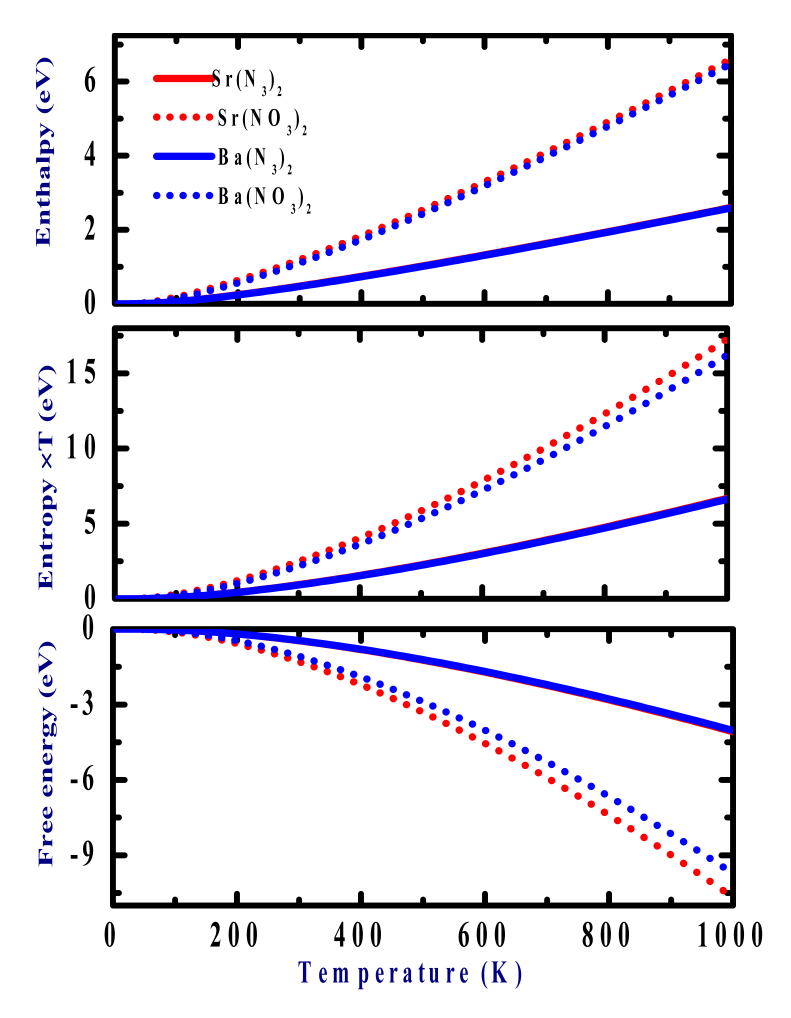


Figure 3.9: Density functional theory-calculated thermodynamic properties,  $Sr(NO_3)_2$ ,  $Ba(NO_3)_2$ ,  $Sr(N_3)_2$  and  $Ba(N_3)_2$ .

 $(U_{vib})$  [79, 80, 87]. Keeping in mind the stability of the crystal structure under high temperatures, we calculated the melting temperatures of the compounds on the lines of [89] as shown by Fine et al. [90] using the equation  $T_m = [553 \text{ K} + (5.91 \text{ K/GPa})C_{11}] \pm 300 \text{ K}$ . The calculated melting temperature of the crystals is found to be 851 K for strontium nitrate and for barium nitrate is 787 K.

For the present crystals, Figure 3.9 indicates that strontium nitrate exhibits a larger rate of increase of H and ST with temperature in comparison with barium nitrate, while the latter follows a curve just a bit below the curve of strontium

nitrate. Looking at the enthalpy curves we have, at 306 K, the following energies: 0.4956 eV (for strontium azide), 0.4956 eV (for barium azide), 1.2307 eV (for strontium nitrate), and 1.1390 eV (for barium nitrate). The enthalpy's are found to increase linearly with temperature and are higher for nitrates than azides. This could be due to the change in atomic arrangements and atomic masses of the compounds. Calculated values of ST at the temperature T = 306 K are 0.9765 eV, 0.9595 eV, 2.5786 eV, and 2.2689 eV for Sr(N<sub>3</sub>)<sub>2</sub>, Ba(N<sub>3</sub>)<sub>2</sub>, Sr(NO<sub>3</sub>)<sub>2</sub>, and Ba(NO<sub>3</sub>)<sub>2</sub> respectively. The calculated free energy for the present crystals decreases with the an increase in temperature. This behavior is due to increase in both vibrational internal energy U and entropy S, which leads to a decrease in free energy. The heat capacity of M(NO<sub>3</sub>)<sub>2</sub> displays a rapid rise between 0 and 700 K, and it increases smoothly to reach a saturation value at 750 K. Also, it is higher for strontium nitrate up to 700 K, and then for both materials Sr(NO<sub>3</sub>)<sub>2</sub> and Ba(NO<sub>3</sub>)<sub>2</sub> it behaves similarly beyond this temperature. The higher the specific heat, the higher is the phonon frequency, which is greater for the strontium compound. Our investigation confirms that the systems studied are thermodynamically stable below 750 K. In the case of azides, the heat capacity linearly increases till 150 K (faster), and after 150 K bit slower and saturate at high temperatures, it is found to be higher (almost double) for nitrates than azides in the entire studied temperature range. At 306 K , we have  $C_v$  values as follows: 58.02 cal/cell.K (for  $Ba(N_3)_2$ ), 57.66 cal/cell.K (for  $Sr(N_3)_2$ ), 139.67 cal/cell.K (for Sr(NO<sub>3</sub>)<sub>2</sub>), and 136.77 cal/cell.K (Ba(NO<sub>3</sub>)<sub>2</sub>). These observed differences in enthalpy and entropy, free energy, heat capacities clearly confirm that nitrates are more stable than azides in the studied temperature range.

The Debye temperature ( $\Theta_D$ ) is a measure of the vibrational response of a material and is the highest temperature that can be achieved as a result of a single normal mode in a solid. It is a vital parameter that correlates with many physical properties of solids, such as entropy, specific heat, and thermal expansion. The Debye temperature exhibits a strong temperature dependence for both ma-

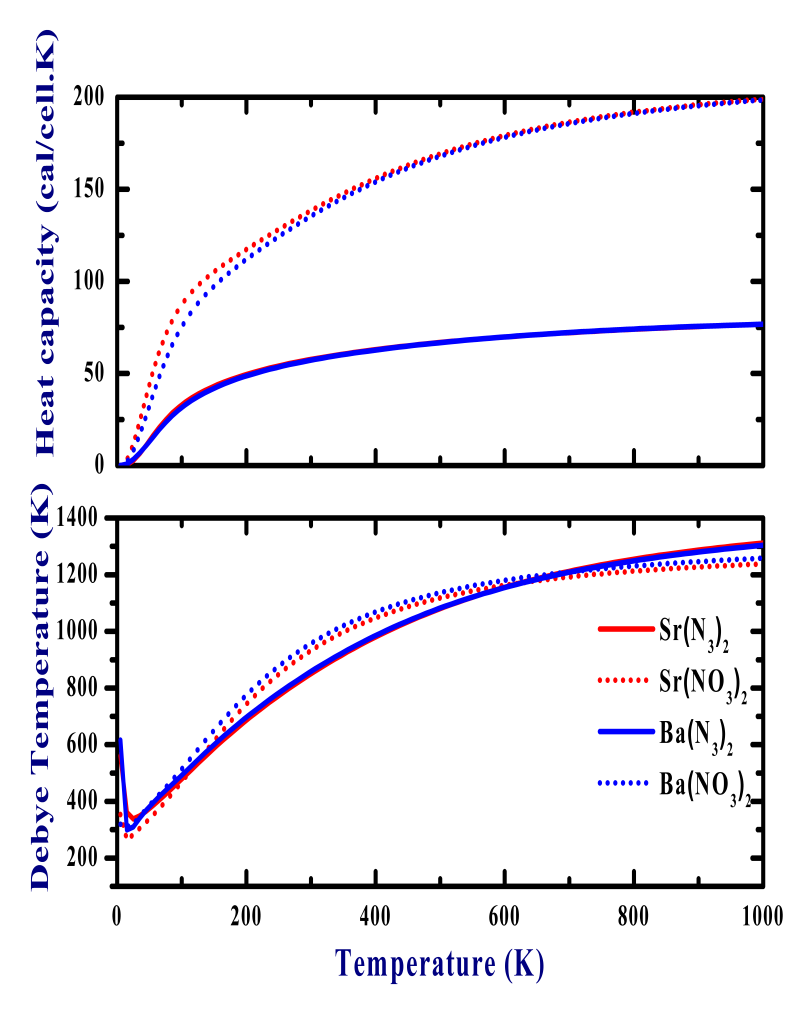


Figure 3.10: Density functional theory-calculated specific heat (top) and Debye temperature (bottom) for (a) Sr(NO<sub>3</sub>)<sub>2</sub>, Ba(NO<sub>3</sub>)<sub>2</sub>, Sr(N<sub>3</sub>)<sub>2</sub> and Ba(N<sub>3</sub>)<sub>2</sub>.

terials, so we calculated the effect of temperature up to the melting temperature range. In Figure 3.10 one can see the calculated Debye temperature (top) and the heat capacity (bottom) of each crystal as a function of temperature as obtained from the phonon density of states. The Debye temperature curves show almost similar increment behavior for all the studied compounds. The actual Debye temperature values for the studied compounds are as follows:  $Sr(N_3)_2(561.39 \text{ K})$ ,  $Ba(N_3)_2(349.06 \text{ K})$ ,  $Sr(NO_3)_2(353.71 \text{ K})$ ,  $Ba(NO_3)_2(319.22 \text{ K})$ . The higher value of  $Sr(N_3)_2$  shows high thermal conductivity [79] than other compounds. The coef-

ficient of thermal expansion was calculated with the relation  $\alpha = (\gamma C_V)/(BV)$ , where  $\gamma$ ,  $C_V$ , B, and V are the Gruneisen parameter, specific heat at constant volume, isothermal bulk modulus, and unit formula volume, which were calculated according to the rigid ion model [91].  $C_V$  and  $\alpha$  behave in a similar way with increase in temperature. The thermal expansion coefficient follows the increasing trend of specific heat owing to the  $T^{\delta}$  dependence at low temperatures, and there is a gradual linear increase at high temperatures followed by a gentler increase as 750 K is approached. At room temperature strontium nitrate has a thermal expansion coefficient of  $3.73 \times 10^{-6}/\text{K}$ , whereas for barium nitrate it is  $5.75 \times 10^{-6}/\text{K}$ . The thermal expansion coefficient decreases with increase in atomic mass from strontium nitrate to barium nitrate.

### 3.4 Conclusions

In summary, we have investigated the structural, elastic, vibrational, and thermodynamic properties of M(NO<sub>3</sub>)<sub>2</sub> and M(N<sub>3</sub>)<sub>2</sub> using an ab initio approach. We found that the van der Waals correction predicts the structural parameters, which are in fair agreement with the experimental values. The elastic constants and phonon spectra of M(NO<sub>3</sub>)<sub>2</sub> and M(N<sub>3</sub>)<sub>2</sub> confirm the mechanical and dynamical stabilities, while the calculated *B/G* ratio suggests that the materials are ductile. The phonon modes, their dispersion, and the symmetry and the IR spectra of the crystals were computed. The calculated normal mode frequencies were classified according to irreducible representations for both IR-active and Raman-active modes. IR spectra of Sr(NO<sub>3</sub>)<sub>2</sub>, Ba(NO<sub>3</sub>)<sub>2</sub>, Sr(N<sub>3</sub>)<sub>2</sub> and Ba(N<sub>3</sub>)<sub>2</sub> were analyzed in close comparison with results of lattice dynamical calculations. The zone-center low-frequency modes are different for Sr(NO<sub>3</sub>)<sub>2</sub> and Ba(NO<sub>3</sub>)<sub>2</sub>, and this was predicted for the first time. The contributions of strontium and barium are much larger than those of nitrogen and oxygen atoms in the low-frequency region whereas the high-frequency zone-center modes are relatively the same for

both materials as most of the vibrational modes here are due to the nitrate (NO<sub>3</sub>) group, owing to the covalent bonding among nitrogen and oxygen atoms. The vibrations of the azide (N<sub>3</sub>) group exhibits high intensity infrared absorption bands in the ranges of 1900-2100 cm<sup>-1</sup>. A comparison with work of metal nitrates reveal that the nitrates are shifted towards the smaller wavenumbers than metal azides. Most of the calculated vibrational modes are in satisfactory agreement with the earlier reported experimental data. It has been seen that the calculated phonon dispersion curves of M(NO<sub>3</sub>)<sub>2</sub> and M(N<sub>3</sub>)<sub>2</sub> do not show any imaginary modes, hence both the materials are dynamically stable. The acoustic and first optical branches for M(NO<sub>3</sub>)<sub>2</sub> and M(N<sub>3</sub>)<sub>2</sub> are overlapping, which clearly indicates that both materials possess favorable condition for thermal transport. Also, as the thermal behavior of these materials could play a key role in the growth of sustainable smoke compositions, the thermodynamic properties, such as entropy, Debye temperature, heat capacity, and enthalpy, at different temperatures ranging from 5 to 1000 K were described. It is inferred that strontium nitrate and barium nitrate can be reliably used in pyrotechnics as they have sufficiently low thermal conductivity. We believe that this work will pave the way to explore many more pyrotechnic-based materials of this type. The comparative study between alkaline-earth metal nitrates and alakline-earth metal azides reveals difference in energetic performance of the metal azides and metal nitrate crystals.

### References

- [1] G. Johann, T.M. Klapötke, J.J. Sabatini, RSC Adv. 54 (2018) 821-824.
- [2] G.H. Seyed, E. Abbas, J. Therm. Anal. Calorim. 101 (2010) 1111–1119.
- [3] J.A. Conkling, M. Chris, Chromatogr. Sci. Ser. 75 (2012) 79–80.
- [4] D. Juknelevicius, L. Mikoliunaite, S. Sakirzanovas, R. Kubilius, A. Ramanavicius, Z. Anorg. Allg. Chem. 640 (2014) 2560–2565.

- [5] Z. Babar, A.Q. Malik, Centr. Eur. J. Energ. Mater. 12 (2015) 579–592.
- [6] C.M. Sabaté, E. Jeanneau, J. Stierstorfer, Z. Anorg. Allg. Chem. 637 (2011) 1490–1501.
- [7] L. Wang, X. Shi, W. Wang, J. Therm. Anal. Calorim. 117 (2014) 985-992.
- [8] Z. Xiang, C. Xin, F. Minghui, Z. Zaifang, Adv. Mater. Res. 550 (2012) 27–31.
- [9] K. Yang, H. Lan, P. Li, H. Yu, S. Qian, L. Yan, N. Long, M. Shui, J. Shu, Ceram. Int. 43 (2017) 10515–10520.
- [10] L. Couture, J.P. Mathieu, Ann. Phys. 3 (1948) 521-549.
- [11] C.C. Addison, A. Walker, J. Chem. Soc. 242 (1963) 1220-1226.
- [12] M.H. Brooker, D.E. Irish, G.E. Bond, J. Chem. Phys. 53 (1970) 1083–1087.
- [13] A.M. Bon, C. Benoit, J. Giordano, Phys. Status Solidi B 78 (1976) 453–464.
- [14] A.M. Bon, C. Benoit, O. Bernard, Phys. Status Solidi B 78 (1976) 67–68.
- [15] R.A. Santos, T. Tang, W.J. Chien, S. Kwan, G.S. Harbison, J. Chem. Phys. 94 (1990) 2717-2721.
- [16] I. N. Tang, K. H. Fung, J. Chem. Phys. 106 (1997) 1653–1660.
- [17] R.J. Cooper, S. Heiles, E.R. Williams, Phys. Chem. Chem. Phys. 17 (2015) 15963–975.
- [18] L.I. Isaenko, K.E. Korzhneva, S.V. Goryainov, A.A. Goloshumova, L.A. Sheludyakova, V.L. Bekenev, O.Y. Khyzhun, Physica B 531 (2018) 149–158.

[19] P.G. Zverev, T.T. Basiev, V.V. Osiko, A.M. Kulkov, V.N. Voitsekhovskii, V.E. Yakobson, Opt. Mater. 11 (1999) 315–334.

- [20] G.K. Bichile, R.G. Kulkarni, J. Phys. C: Solid State. Phys. 8 (1975) 3988–3992.
- [21] S. Bhagavantam, R.V.G. Sundara Rao, Curr. Sci. 16 (1948) 296.
- [22] K. Sai Babu, T. Chiranjivi, J. Phys. C: Solid State. Phys. 13 (1980) L587-L589.
- [23] R. Srinivasan, Proc. Indian Acad. Sci. Sect. A 41 (1955) 49–54.
- [24] Y.N. Zhuravlev, D.V. Korabelnikov, Russ. Phys. J. 60 (2017) 149–156.
- [25] Y.N. Zhuravlev, D.V. Korabelnikov, Opt. Spektrosk. 122 (2017) 972–979.
- [26] C. Michael, Propellants Explos. Pyrotech. 37(2012) 639–646.
- [27] C. E. Hathaway, P. temple, J. Phys. Rev. B, 3 (1971) 3497–3502.
- [28] P. Gray, T. C. Waddington, Trans. Faraday Soc., 53 (1957) 901–908.
- [29] Z. Liu, S. Wei, Y. Guo, H. Sun, H. Sun, Q. Chang and Y. Sun, RSC Adv., 11 (2021) 17222–17228.
- [30] H. D. Fair, R. F. Walker, Eds. In Energetic Materials, Plenum Press, New York, 1977.
- [31] F. P. Bowden, A. D. Yoffe, Angew. Chem., 71 (1959) 752–752.
- [32] B.L. Evans, A.D. Yoffe, P. Gray, Chem. Rev., 59 (1959) 515–568.
- [33] Z. Liu, S. Wei, Y. Guo, H. Sun, H. Sun, Q. Chang, and Y. Sun, RSC Adv., 11 (2021)17222-17228.

- [34] H. Zhu, X. Han, P. Zhu, X. Wu, Y. Chen, L. Miaoran, L. Xuefeng, Q. Cui, J. Phys. Chem. C, 120 (2016) 12423–12428.
- [35] K. Ramesh Babu, G. Vaitheeswaran, Chem. Phys. Lett., 586 (2013) 44–50.
- [36] W. Zhu, J. Xiao, and H. Xiao, J. Phys. Chem. B, 110 (2006) 9856-9862.
- [37] H. A. Rafizadeh, S. Yip, J. Chem. Phys. 56 (1972) 5377–5392.
- [38] A. A. L. Michalchuk, S. Rudic, C. R. Pulham, C. A. Morrison, Phys. Chem. Chem. Phys., 20 (2018) 29061-29069.
- [39] N. Yedukondalu, V. D. Ghule, G. Vaitheeswaran, J. Phys. Chem. C 2012, 116, 16910 16917.
- [40] X. Wang, J. Li, J. Botana, M. Zhang, H. Zhu, L. Chen, H. Liu, T. Cui,M. Miao, J. Chem. Phys. 139 (2013) 164710(1-5).
- [41] K. J. Dean, G. R. Wiikinson, J Raman Spectrosc., 16 (1985) 22-26.
- [42] Z. Iqbal, C. W. Brown, S. S. Mitra, J. Chem. Phys., 52 (1970) 4867–4874.
- [43] Z. Iqbal, J. Chem. Phys., 55 (1971) 528–530.
- [44] Z. Iqbal, J. Chem. Phys. 61 (1974) 1230–1231.
- [45] W. Zhu, X. Xu, H. Xiao, J. Phys. Chem. Solids, 68 (2007) 1762–1769.
- [46] B. Adivaiah, E. Narsimha Rao, T. Atahar Parveen, G. Vaitheeswaran, J. Phys. Chem. Solids, 122 (2018) 268-277.
- [47] H. Nowotny, G. Heger, Acta Crystallogr. C 39 (1983) 952–956.
- [48] R.B. Hammond, J.O. Michael, K.J. Roberts, R.A. Jackson, M.J. Quayle, Cryst. Growth Des. 9 (2009) 2588–2594.
- [49] F. Michard, F. Plicque, A. Zarebowitch, J. Appl. Phys. 44 (1973) 572–576.

- [50] G. E. Pringle, D. E. Noakes, Acta Cryst., B24 (1968) 262–269.
- [51] C.S. Choi, Acta Cryst., B25 (1969) 2638-2644.
- [52] M.Cartwright, J. Wilkinson, Propellants Explos. Pyrotech., 35 (2010) 326–332.
- [53] S.J. Clark, M.D. Segall, C.J. Pickard, P.J. Hasnip, M.J. Probert, K. Refson, M.C. Payne, Z. Kristallogr. 220 (2005) 567–570.
- [54] I.R. Shein, V.L. Kozhevnikov, A.L. Ivanovskii, Solid State Sci., 10 (2008) 217–225.
- [55] J.P. Perdew, K. Burke, M. Ernzerhof, Phys. Rev. Lett. 77 (1996) 3865–3868.
- [56] J.P. Perdew, K. Burke, Y. Wang, Phys. Rev. B 54 (1996) 16533-16539.
- [57] M.C. Payne, M.P. Teter, D.C. Allan, T.A. Arias, J.D. Joannopoulos, Rev. Mod. Phys. 64 (1992) 1045–1097.
- [58] F. Ortmann, F. Bechstedt, W.G. Schmidt, Phys. Rev. B 73 (2006) 205101.
- [59] A. Tkatchenko, M. Scheffler, Phys. Rev. Lett., 102 (2009) 073005(1-4).
- [60] R. Fletcher, Practical Methods of Optimization, Wiley, New York, 1980.
- [61] H.J. Monkhorst, J.D. Pack, Phys. Rev. B 13 (1976) 5188-5192.
- [62] D. Hamann, M. Schluter, C. Chiang, Phys. Rev. Lett. 43 (1979) 1494–1497.
- [63] A. Togo, I. Tanaka, Scr. Mater. 108 (2015) 1–5.
- [64] S. Baroni, P. Giannozzi, A. Testa, Phys. Rev. Lett. 58 (1987) 1861–1864.
- [65] X. Gonze, J.P. Vigneron, Phys. Rev. B 39 (1989) 13120–13128.

- [66] X. Gonze, D.C. Allan, M.P. Teter, Phys. Rev. Lett. 68 (1992) 3603-3606.
- [67] L. Changyol, X. Gonze, Phys. Rev. B 51 (1955) 8610–8613.
- [68] V. Mankad, N. Rathod, S.D. Gupta, S.K. Gupta, PK Jha, Mater. Chem. Phys. 129 (2011) 816–822.
- [69] K. Ramesh Babu, G. Vaitheeswaran, Chem. Phy. Lett. 533 (2012) 35-39.
- [70] A. Roldan, D. Santos-Carballal, N.H. De Leeuw, J. Chem. Phys. 138 (2013) 204712.
- [71] S. Culas, A. Surendran and J. Samuel, Asian J. Chem. 25 (2013) 3855–3859.
- [72] K. Ramesh Babu, Ab initio study on nitrogen based energetic solids,(Ph.D) Thesis, University of hyderabad, ACRHEM, School of Physics 2013.
- [73] M. Lei, H. Ledbetter and Y. Xie, J. Appl. Phys. 76 (1994) 2738.
- [74] M. Born and K. Huang 1954 Dynamical Theory of Crystal Lattices (Oxford: Oxford University Press)
- [75] Y.Wu, W. Hu, Eur. Phys. J. B 60 (2007) 75–81.
- [76] D. Errandonea, C. Ferrer-Roca, D. Martínez-Garcia, A. Segura, O. Gomis, A. Muñoz, P. Rodríguez-Hernández, J. López-Solano, S. Alconchel, F. Sapiña, Phys. Rev. B 82 (2010) 174105(1-8).
- [77] D. Errandonea, Francisco Javier Manjón, Prog. Mater. Sci. 53 (2008) 711–773.
- [78] S. Shashi Devi, G. Rajashekhar, S. Narender Reddy, and A. Sadananda Chary, AIP Conference Proceedings 2269 (2020) 030065.

[79] E. Narsimha Rao, G. Vaitheeswaran, A. H. Reshak and S. Auluck, RSC Adv., 6 (2016) 99885–99897.

- [80] E. Moreira, J.M. Henriques, D.L. Azevedo, E.W.S. Caetano, V.N. Freire, E.L. Albuquerque, J. Solid State Chem. 184 (2011) 921–928.
- [81] S.N. Costa, V.N. Freire, E.W.S. Caetano, F.F. Maia Jr., C.A. Barboza, U.L. Fulco, and E.L. Albuquerque, J. Phys. Chem. A 120 (2016) 5752–5765.
- [82] E. Moreira, J.M. Henriques, D.L. Azevedo, E.W.S. Caetano, V.N. Freire, U.L. Fulco, and E.L. Albuquerque, J. Appl. Phys. 112 (2012) 043703(1-8).
- [83] D. Shrivastava, S.P. Sanyal, J. Alloys Compd. 784 (2019) 319-329.
- [84] N. Mounet, N. Marzari, Phys. Rev. B 71 (2005) 205214.
- [85] T.M. Klapötke, G. Steinhau ser, Angew. Chem. Int. Ed. 47 (2008) 3330-3347.
- [86] P.S. Anthony, B.S. Jason, C.P. Jay, A.M. Lauren, ACS Sustain. Chem. Eng. 4 (2016) 2309–2315.
- [87] M.A. Blanco, E. Francisco, V. Luana, Comput. Phys. Commun. 158 (2004) 57–72.
- [88] E. Moreira, C.A. Barboza, E.L. Albuquerque, U.L. Fulco, J.M. Henriques, A.I. Araújo, J. Phys. Chem. Solids 77 (2015) 85–91.
- [89] K. Ramesh Babu, G. Vaitheeswaran, Solid State Sci. 23 (2013) 17–25.
- [90] M.E. Fine, L.D. Brown, H.L. Marcus, Scr. Metall. 18 (1984) 951-956.
- [91] A. Parveen, N.K. Gaur, Physica B 407 (2012) 500-504.

# Chapter **4**

# Computational study of lattice dynamics and thermodynamic properties of energetic solid cyanuric triazide and Urea nitrate.

In this chapter, the structural, vibrational, and thermodynamic properties of the cyanuric triazide and urea nitrate crystal are investigated through density functional theory (DFT) simulations. The dispersion correction methods Grimme (DFT-D2) [1] and Tkatchenko and Scheffler (DFT-TS) [2] were used to treat the van der Waals (vdW). The norm-conserving pseudopotentials are [3] generated by utilizing the kinetic energy optimization scheme. Infrared spectra, Born effective charges are computed through the linear response method using the density functional perturbation theory (DFPT). Phonon dispersion curves and phonon density of states are obtained within the harmonic approximation. The calculated thermodynamic properties show that the Debye temperature, specific heat at constant volume, enthalpy, and entropy values increase as a function of temperature, while the free energy falls off as the temperature increases. The vibrational and thermodynamic properties reveal,  $C_3N_{12}$  is an effective initiating explosive, and urea nitrate is an improvised explosive.

**B.Adivaiah** and G. Vaitheeswaran, "Computational study of lattice dynamics and thermodynamic properties of energetic solid cyanuric triazide" **J. Phys. Chem. Solids.**, 148, 109782 (2021).

#### 4.1 Introduction

Energetic materials are considered to be quite important in propellants, pyrotechnics, explosives, and combustibles [4-6]. Organic and inorganic azides are energy-rich molecules that reveals explosive properties [7]. The series of inorganic azides such as KN<sub>3</sub>, TlN<sub>3</sub>, AgN<sub>3</sub>, CuN<sub>3</sub> plays a significant role in explosives. Unfortunately, metal azides such as silver azide, lead azide, and thallous azide suffer from instability, sensitivity, or toxicity [8]. Lead azide (Pb(N<sub>3</sub>)<sub>2</sub>) was used as a primary explosive for many years [9], but the use of Pb primaries has led to environmental pollution due to toxic Pb decomposition after detonation. One of the modern and principal trends in the development of energetic materials is to search for the so-called green primary explosives. The nitrogen-rich compounds are potential candidates for high energy density because of their high nitrogen content and good thermal stability [10]. Apart from this, these composites are environmentally safe, with molecular nitrogen as their main combustion or detonation outcomes. One of the representatives of such green primary explosives is cyanuric triazide (CTA), which has distinctive properties based on thermal decomposition reactions; they do not pose health risks to personnel and cause much less pollution to the environment, but it has no practical use because of very high sensitivity towards external stimuli [11-16]. However, efforts have been made recently addressing its use as explosive material [11]. Cyanuric triazide, is an effective initiator in explosives, synthesized and structurally characterized recently

[17], [18]. It is a quite interesting compound, since it contains only carbon and nitrogen, 3 carbon and 12 nitrogen in each molecules. The compound is highly friction sensitive; it has sharp melting point under 400 K, but it explodes upon heating above 500 K giving nitrogen and carbon in the form of graphite [12].

The decomposition reaction of cyanuric triazide has been reported previously [12]:

$$C_3N_3(N_3)_3 \rightarrow 3C + 6N_2$$
 (4.1)

By differing the chemical nature of either or both ions, an energetic material can be modified to fit specific requirements. The environmental impact and toxicity is the main in the design of energetic materials. Thus, organic nitrates are typically biodegradable and produce environmentally relatively good combustion products, which are of prime interest. Urea nitrate is one of the significant improvised explosives with a representative layered supermolecular structure [19, 20]. The urea nitrate find make use of fertilizers, and most of that urea (85%) ends up as fertilizer, with a little amount utilized for resins and plastics and a small percentage usage in cattle feed. For long time, urea nitrate has been utilized by terrorists find to make improvised explosives [21–24]. It was put in service of the bombing of the World Trade Center (February 1993) and many car bombings in Palestine [25].

The study of lattice dynamics of energetic materials is highly interesting, from which we can understand the spectroscopic and thermodynamic properties of a crystal [26–28]. Recently many researchers have reported the infrared spectra of inorganic azides using Density functional theory (DFT) [29–35]. Keeping this in mind, we have studied the vibrational and thermodynamic properties of metal azides,  $Sr(N_3)_2$  and  $Ba(N_3)_2$  using the density functional perturbation theory in our previous study [35]. For the organic azides  $(C_3N_{12})$  side, two theoretical works on the structural properties of cyanuric triazide were reported using the DFT formalism [36, 37]. The first one predicted the structural transformation of

nitrogen-rich cyanuric triazide at high pressures and temperatures [36]. In the second one, structural, elastic, and optical properties of  $C_3N_{12}$  were studied using ultra-soft potentials in which they found that  $C_3N_{12}$  has indirect band gap with 6.33 eV [37]. So far, there are no reports on vibrational and thermodynamic properties of  $C_3N_{12}$ , which helps in fundamental understanding and possible insights about atomic lattice behavior of  $C_3N_{12}$ . Similarly, in the case of urea nitrate, few experimental and theoretical [20, 21, 38–42] studies have been reported, the knowledge regarding lattice dynamics point of view is limited. This work is the first of its kind which investigates detailed understanding into lattice vibrational and thermodynamics properties of  $C_3N_{12}$  and UN.

In this work, we have presented the structural, vibrational, and thermodynamic properties of cyanuric triazide and urea nitrate crystal within the DFT formalism, using norm-conserving pseudopotential approach. The generalized gradient approximation with (GGA + G06) and Tkatchenko and Scheffler (GGA + TS) methodology to take into account the dispersion effects [1], 2]. A brief comparison with previous results (Ref. [43]) for C<sub>3</sub>N<sub>12</sub> is also included. The infrared spectra are obtained, and their normal modes are assigned. Finally, the phonon dispersion and phonon density of states are evaluated, together with its Debye temperature and specific heat. We expect that our work will further stimulate the experimentalists for the synthesis of triazine azides and improvised explosive urea nitrate crystals.

Table 4.1: Lattice parameters(Å) and unit cell volume (Å<sup>3</sup>) of the  $C_3N_{12}$  crystal unit cell as calculated at the LDA, GGA, GGA+G06 and experimental values [18] with error percentage.

Parameter	LDA	PBE	PBE + G06	Expt. <sup>a</sup>	Cal.b
a (Å)	8.74	9.74	8.95	8.75	9.00
c (Å)	5.40	6.42	5.776	8.89	5.70
$V(Å^3)$	357.06 (-8.5%)	527.32 (35%)	401.61 (2.7%)	390.44	399.44

LDA, Local density approximation; PBE, Perdew-Burke-Ernzerhof. <sup>a</sup>From [18], <sup>b</sup>From [37] using ultrasoft pseudopotentials.

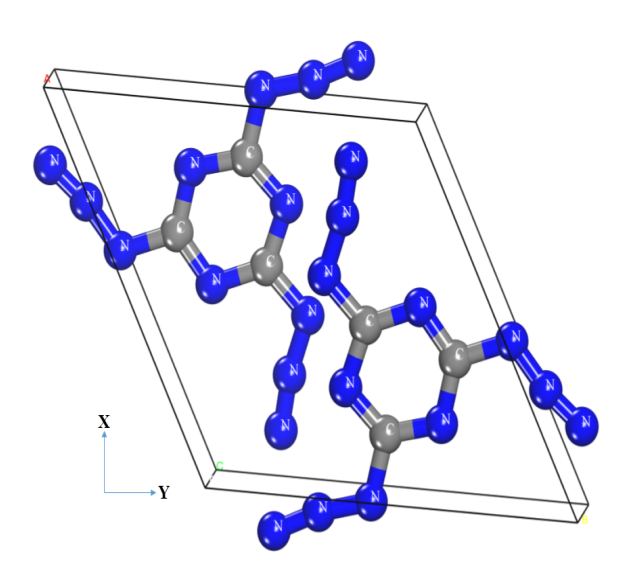


Figure 4.1: Unit cell of the cyanuric triazide crystal.

# 4.2 Computational methods

The internal atomic coordinates including lattice parameters of  $C_3N_{12}$  and UN are optimized within the density functional theory formalism by employing the plane-wave CASTEP code [44]. The generalized gradient approximation (GGA) Perdew-Burke-Ernzerhof (PBE) exchange-correlation functional [45], 46] is chosen. The dispersion correction methods Grimme (DFT-D2) [1] and Tkatchenko and Scheffler (DFT-TS) [2] were used to treat the van der Waals (vdW). The norm-conserving pseudopotentials are [3] generated by utilizing the kinetic energy optimization scheme is used to relate the ion-electron interactions (atomic nuclei and core electrons). Pseudo atomic calculations are achieved for C (2s2, 2p2) H (1s1) N (2s2, 2p3) and O (2s2, 2p4) respectively. We computed structural properties and the dynamical matrices by using the Monkhorst-Pack(MP) [47] with  $4 \times 4 \times 6$  k-grids for  $C_3N_{12}$  and  $4 \times 4 \times 5$  for UN, through high symmetry points in the Brillouin zone (BZ) integrations. The unit cell geometry optimizations of the  $C_3N_{12}$  and UN crystal are performed using the Broyden-Fletcher-Goldfarb-

Shannon (BFGS) algorithm [ $\frac{48}{1}$ ]. A plane-wave basis set with a cut-off energy of 980 eV is used for  $C_3N_{12}$  and 1100 eV is for UN, to enlarge the valance electronic wave functions. The convergence criteria for geometry optimization is as follows for both the crystals: The maximum atomic displacement should be smaller than  $0.5 \times 10^{-3}$  Å and total energy convergence should be be smaller than  $0.5 \times 10^{-5}$  eV/atom. The maximum stress component and maximum force criteria are 0.02 GPa and  $0.5 \times 10^{-2}$  eV/Å per atom, respectively.

The phonon dispersion curves and partial phonon density of states of  $C_3N_{12}$  and UN are accomplished using the density functional perturbation theory (DFPT) with linear-response method[49–52] at (GGA + G06) and (GGA + TS) level. Using the quasi-harmonic approximation [53, 54] we have calculated the Debye temperature, heat capacity and other thermodynamic properties.

Table 4.2: Lattice parameters(Å) and unit cell volume (ų) of the urea nitrate crystal unit cell as calculated at the LDA, GGA, GGA+G06 and experimental values [38] with error percentage.

Parameter	LDA	PBE	PBE + G06	PBE + TS	PW91	PW91 + OBS	Expt. <sup>a</sup>
a (Å)	9.27	9.71	9.52	9.60	9.71	9.47	9.54
b (Å)	8.07	8.32	8.23	8.28	8.30	8.20	8.20
c (Å)	7.12	8.54	7.39	7.29	8.87	7.30	7.49
$V(\text{\AA}^3)$	426.79	594.82	474.97	485.64	623.01	459.21	485.10
	(12.02%)	(35%)	(2.7%)	(-0.11%)	(28.42%)	(5.33%)	
$\beta$	126.77	120.52	125.01	123.19	119.51	125.99	124.24

LDA, Local density approximation; PBE, Perdew-Burke-Ernzerhof. <sup>a</sup>From [18], <sup>b</sup>From [37] using ultrasoft pseudopotentials.

### 4.3 Results and discussion

# 4.3.1 Crystal structure and Unit cell optimization

The  $C_3N_{12}$  molecular crystal display hexagonal structure with, space group P3 accompanied by two molecules in the unit cell (figure 4.1). The molecule is planar and the distance between the layers is 2.947 Å. The cyanuric ring has three-fold

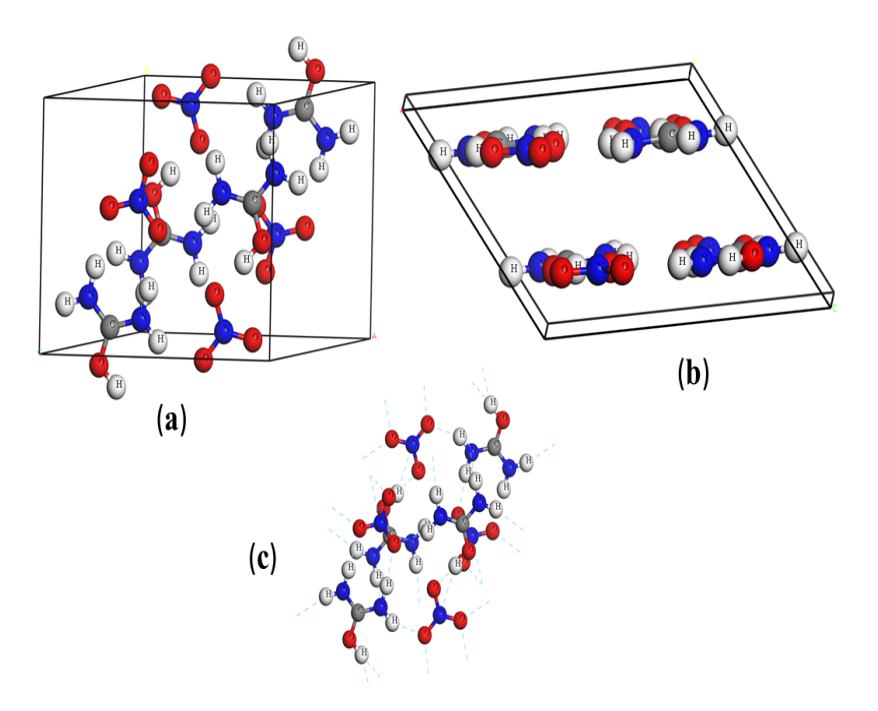


Figure 4.2: Unit cell (a), crystal structure (b), and single molecule (c) of urea nitrate.

symmetry, and contains alternate carbon and nitrogen atoms [55]. The N-N distance is 1.265 Å, and angle of the azide group (N<sub>2</sub>-N<sub>3</sub>-N<sub>4</sub>) is 172° [18]. The lattice parameters and unit cell volume are listed together with the experimental data of Elmar et al. [18] in Table 4.1. Urea nitrate crystallizes in *P2/c* symmetry and shows a simple layered supermolecular structure (figure 4.2). The N-H–O, and O-H–O hydrogen bonds hold uronium cation and nitrate anion together to form the hydrogen bond sheet[20]. The unique structure of hydrogen–bonded sheets can account for its low sensitivity to friction, shock, and electric discharge [20, 38]. The acidic proton is on the carbonyl oxygen atom with an O-H–O distance of 2.596 Å [20, 38]. Four other hydrogen bonds of the type N-H–O join the uronium and nitrate ions into a two-dimensional network. The only contacts between the layers are of the van der Waals type, and the C-O distances are 1.298, 1.311 and 1.316 Å [20, 38]. There are relatively weak NO<sub>3</sub>–NO<sub>3</sub> and NO<sub>3</sub>..π interactions

between adjacent hydrogen-bonded sheets, which are proposed to make great contributions to the stabilization of the layered structure. The calculated crystal volume using (LDA functional) is smaller than the experimental value by 8.5% for  $C_3N_{12}$ , and 12.02% for UN (table 4.2). We have used G06, TS corrections to the PBE functional. The using the PBE + G06 and PBE + TS [ $\overline{56}$ ] results obtain closer to the experiment with the deviation 2.7% and -0.11%, respectively. Further, we have used PBE + G06 and PBE + TS functionals to compute the vibrational and thermodynamic properties of  $C_3N_{12}$  and UN, respectively.

# 4.3.2 Born effective charge analysis

We have estimated the Born effective charge (BEC) tensor of each ion in hexagonal structure of  $C_3N_{12}$  and monoclinic structure UN by using DFPT [ $\overline{57}$ – $\overline{61}$ ]. Tables 4.3–4.6 presents the BEC tensor and deviations of their corresponding ionic charges (in percentage) along with  $Z_{11}$ ,  $Z_{22}$ , and  $Z_{33}$  directions. The formal valence of C, H, N, and O in  $C_3N_{12}$  and UN are +4, +1, -3 and -2, respectively. In the cyanuric triazide, the effective charge is found to be 3.26 for C and -2.54 for N, which reveals 18.48 and 15.31 % variation from the static charge, respectively. Also, we can note that the BEC ions in  $C_3N_{12}$  are significantly lower than the normal charges confirming the presence of covalent character in the structure.

The large BEC<sub>s</sub> reveal respective displacement of neighboring ions against each other, which generate considerable polarization. The C ions have a maximum of 89.78 % increase in the effective charge over its static charge, and N finds a maximum of 190.32 %, revealing the possible hybridization of C and neighboring N ions. The Born effective charge is of highly asymmetric nature for  $C_3N_{12}$  crystal  $(Z_{xx}^* \neq Z_{yy}^* \neq Z_{zz}^*)$ , it can be concluded that the C-N bond has a mixed ionic and covalent chemical nature in the studied materials [35, 62, 63]. The N atoms show larger deflections than C atoms. Also, we can observe that Born effective charges of N reveal huge antisymmetric off-diagonal elements in the Born effective charge matrix. Nevertheless, the diagonal components have a value closest to the given

Table 4.3: Calculated BEC's of  $C_3N_{12}$ . Actual ionic charges are  $C=+4,\,N=-3$ .

Atom	$Z_{11}$	$Z_{22}$	$Z_{33}$
$C_1$	2.62841	2.55777	0.40874
$C_2$	1.92571	3.26048	0.40874
$C_3$	3.22516	1.96103	0.40874
$C_4$	2.62841	2.55777	0.40874
$C_5$	1.92571	3.26048	0.40874
$C_6$	3.22516	1.96103	0.40874
$N_1$	-2.54062	-0.75530	-0.27007
$N_2$	2.71078	0.12796	0.22977
$N_3$	-1.19694	-0.02794	-0.04620
$N_4$	-2.38966	-1.11447	-0.32225
$N_5$	-0.75136	-2.54455	-0.27007
$N_6$	0.98101	1.85773	0.22977
$N_7$	-0.34035	-0.88453	-0.04620
$N_8$	-1.20692	-2.29720	-0.32225
$N_9$	-1.65189	-1.64402	-0.27007
$N_{ m 10}$	0.56632	2.27242	0.22977
$N_{11}$	-0.30004	-0.92485	-0.04620
$N_{12}$	-1.65961	-1.84451	-0.32225
$N_{13}$	-2.54062	-0.75530	-0.27007
$N_{14}$	2.71078	0.12796	0.22977
$N_{15}$	-1.19694	-0.02794	-0.04620
$N_{16}$	-2.38966	-1.11447	-0.32225
$N_{17}$	-0.75136	-2.54455	-0.27007
$N_{18}$	0.98101	1.85773	0.22977
$N_{19}$	-0.34035	-0.88453	-0.04620
$N_{20}$	-1.20692	-2.29720	-0.32225
$N_{21}$	-1.65189	-1.64402	-0.27007
$N_{22}$	0.56632	2.27242	0.22977
$N_{23}$	-0.30004	-0.92485	-0.04620
$N_{24}$	-1.65961	-1.84451	-0.32225

Table 4.4: Percentage deviations of BEC's for  $C_3N_{12}$  along the xx, yy, zz directions.

	7	7	7
Atom	$Z_{11}$	$Z_{22}$	$Z_{33}$
$C_1$	34.28	36.05	89.78
$C_2$	51.85	18.48	89.78
$C_3$	19.37	50.97	89.78
$C_4$	34.28	36.05	89.78
$C_5$	51.85	18.48	89.78
$C_6$	19.37	50.97	89.78
$N_1$	15.31	74.82	90.99
$N_2$	190.35	104.26	107.65
$N_3$	60.102	99.06	98.46
$N_4$	20.34	62.85	89.25
$N_5$	74.95	15.18	90.99
$N_6$	132.70	161.92	107.65
$N_7$	88.65	70.51	98.46
$N_8$	59.76	23.42	89.25
$N_9$	44.93	45.19	90.99
$N_{ m 10}$	118.87	175.74	107.65
$N_{11}$	89.997	69.17	98.46
$N_{12}$	44.67	38.51	89.25
$N_{13}$	15.31	74.82	90.99
$N_{14}$	190.35	104.26	107.65
$N_{15}$	60.10	99.06	98.46
$N_{16}$	20.34	62.851	89.25
$N_{17}$	74.95	15.18	90.99
$N_{18}$	132.70	161.92	107.65
$N_{19}$	88.65	70.51	98.46
$N_{20}$	59.76	23.42	89.25
$N_{21}$	44.93	45.19	90.99
$N_{22}$	118.87	175.74	107.65
$N_{23}$	89.99	69.17	98.46
$N_{24}$	44.67	38.51	89.25

charge of N(-3) that testifies the strong covalent nature of N-N bonding.

We also evaluated the BEC<sub>s</sub> of ions for UN compound and presented them in Table 4.5 and table 4.6. The maximum changes in the charges of different ions are: + 72 % for C, + 75 % for H, + 197 % for N, and 75 % for O respectively. Table 4.4 displays that the BEC<sub>s</sub> of ions in UN is remarkably higher than their nominal charges and, one can conclude that there is a notable amount of covalent character shown in the structure. Large BEC<sub>s</sub> also point into the relative displacements of neighboring ions against each other exhibit large polarization. Large BEC<sub>s</sub> of the cations compared to their nominal charges also specify that both C and H act as donors while N and O ions act as acceptors. Great extent of charges associated with the N ions also reveal about the possible hybridization of N and neighboring O ions.

Table 4.5: Calculated BEC's of UN. Actual ionic charges are C = +4, H = +1, N = -3, O = -2.

Atom	$Z_{11}$	$Z_{22}$	$Z_{33}$
$H_1$	0.79114	0.26534	0.56526
$H_2$	0.27502	1.01093	0.32911
$\overline{H_3}$	0.27320	0.88976	0.35712
$H_4$	0.80882	0.24784	0.54116
H <sub>5</sub>	0.58510	1.62756	0.46970
$H_6$	0.79114	0.26534	0.56526
$H_7$	0.27502	1.01093	0.32911
$H_8$	0.27320	0.88976	0.35712
H <sub>9</sub>	0.80882	0.24784	0.54116
$H_{10}$	0.58510	1.62756	0.46970
$H_{11}$	0.79114	0.26534	0.56526
$H_{12}$	0.27502	1.01093	0.30320
$H_{13}$	0.27320	0.88976	0.35712
П <sub>13</sub>		0.88976	
$H_{14}$	0.27320		0.35712
$H_{15}$	0.58510	1.62756	0.46970
$H_{16}$	0.79114	0.26534	0.56526
$H_{17}$	0.27502	1.01093	0.32911
$H_{18}$	0.27320	0.88976	0.35712
$H_{19}$	0.80882	0.24784	0.54116
$H_{20}$	0.58510	1.62756	0.46970
$C_1$	1.94827	2.54306	1.10188
$C_2$	1.94827	2.54306	1.10188
$C_3$	1.94827	2.54306	1.10188
$C_4$	1.94827	2.54306	1.10188
$N_1$	1.90851	2.93458	1.12585
$N_2$	-1.47578	-0.91959	-0.96783
$N_3$	-1.16903	-1.24980	-0.87389
$N_4$	1.90851	2.93458	1.12585
$N_5$	-1.47578	-0.91959	-0.96783
$N_6$	-1.16903	-1.24980	-0.87389
$N_7$	1.90851	2.93458	1.12585
$N_8$	-1.47578	-0.91959	-0.96783
$N_9$	-1.16903	-1.24980	-0.87389
$N_{10}$	1.90851	2.93458	1.12585
$N_{11}$	-1.47578	-0.91959	-0.96783
$N_{12}$	-1.16903	-1.24980	-0.87389
$O_1$	-0.64818	-2.34838	-0.48035
$O_2$	-1.45581	-0.94571	-0.90452
$O_3$	-1.11875	-1.61648	-0.71181
$O_4$	-0.72250	-2.43911	-0.55166
$O_5$	-0.64818	-2.34838	-0.48035
$O_6$	-1.45581	-0.94571	-0.90452
$O_7$	-1.11875	-1.61648	-0.71181
$O_8$	-0.72250	-2.43911	-0.55166
$O_9$	-0.64818	-2.34838	-0.48035
$O_{10}$	-1.45581	-0.94571	-0.90452
$O_{10}$	-1.11875	-1.61648	-0.71181
$O_{12}$	-0.72250	-2.43911	-0.55166
$O_{12}$ $O_{13}$	-0.72230	-2.43911	-0.33166
$O_{14}$	-1.45581	-2.34838	-0.48033
$O_{14}$ $O_{15}$	-1.43381	-1.61648	-0.71181
O <sub>15</sub>	-0.72250	-2.43911	-0.71181
O <sub>16</sub>	-0.7 2230	-2.43711	-0.55166

Table 4.6: Percentage deviations of BEC's for UN along the xx, yy, zz directions.

Atom	$Z_{11}$	$Z_{22}$	$Z_{33}$
$H_1$	20.88	73.46	43.47
$H_2$	72.49	-1.09	67.08
$H_3$	72.68	11.02	64.28
$H_4$	19.11	75.21	45.88
$H_5$	41.49	-62.75	53.03
$H_6$	20.88	73.46	43.47
$H_7$	72.49	-1.09	67.08
$H_8$	72.68	11.024	64.288
$H_9$	19.11	74.21	45.88
$H_{10}$	41.49	-62.75	53.03
$H_{11}$	20.88	73.46	43.47
$H_{12}$	72.49	-1.09	67.08
$H_{13}$	72.68	11.02	64.28
$H_{14}$	19.11	75.21	45.88
$H_{15}$	41.49	-62.75	53.03
$H_{16}$	20.88	73.46	43.47
$H_{17}$	72.49	-1.093	67.08
$H_{18}$	72.68	11.02	64.28
$H_{19}$	19.11	75.21	45.88
$H_{20}$	41.49	-62.75	53.03
$C_1$	51.29	36.42	72.45
$C_2$	51.29	36.42	72.45
$C_3$	51.29	36.42	72.45
$C_4$	51.29	36.42	72.45
$N_1$	163.61	197.81	137.52
$N_2$	50.80	69.34	67.73
$N_3$	61.03	58.34	70.87
$N_4$	163.61	197.81	137.52
$N_5$	50.80	69.34	67.73
$N_6$	61.03	58.34	70.87
$N_7$	163.61	197.81	137.52
$N_8$	50.80	69.34	67.73
$N_9$	61.03	58.34	70.87
$N_{10}$	163.61	197.81	137.52
$N_{11}$	50.80	69.34	67.73
$N_{12}$	61.03	58.34	70.87
$O_1$	67.59	-17.41	75.98
$O_2$	27.20	52.71	54.77
$O_3$	44.06	19.17	64.40
$O_4$	63.87	-21.95	72.41
$O_5$	67.59	-17.41	75.98
$O_6$	27.20	52.71	54.77
$O_7$	44.06	19.17	64.40
$O_8$	63.87	-21.95	72.41
$O_9$	67.59	-17.41	75.98
O <sub>10</sub>	27.20	52.71	54.77
$O_{11}$	44.06	19.17	64.40
$O_{12}$	63.87	-21.95	72.41
$O_{13}$	67.59	-17.41	75.98
$O_{14}$	27.20	52.71	54.77
$O_{15}$	44.06	19.17	64.40
O <sub>16</sub>	63.87	-21.95	72.41

## 4.3.3 Infrared spectra

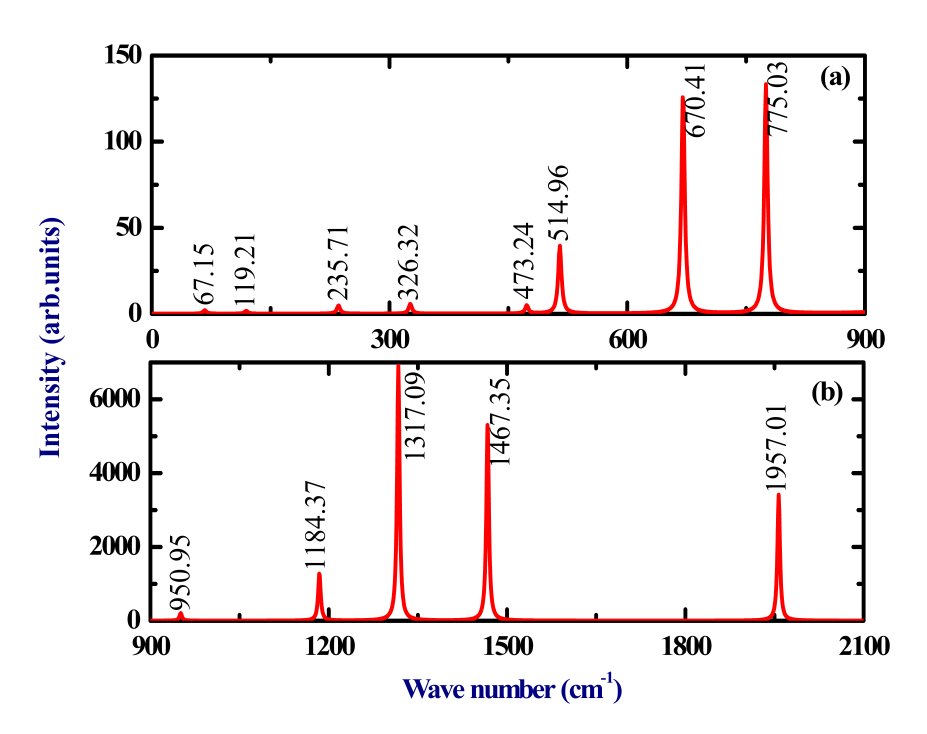


Figure 4.3: Calculated infrared spectra of  $C_3N_{12}$  at the optimized equilibrium volume in the  $0-900~\rm cm^{-1}$  range (fig(a)) and  $900-2100~\rm cm^{-1}$  (fig(b)).

We have computed the IR spectra using density functional perturbation theory (DFPT) at the center of the Brillouin zone. The unit cell of  $C_3N_{12}$  crystal contains 30 atoms, giving rise to 90 normal modes, three of them being acoustic modes and 87 optical modes. According to the irreducible representations;  $\Gamma_{acoustic} = A_u + 2E_u$ ,  $\Gamma_{IR} = 14A_u + 28E_u$ ,  $\Gamma_{Raman} = 15A_g + 30E_g$ . Among these modes,  $A_u$ ,  $A_g$  is doubly degenerate and  $E_u$ ,  $E_g$  is non-degenerate modes. The  $A_u$ ,  $E_u$  modes are IR active, and the  $A_g$ ,  $E_g$  modes are Raman active. Table 4.7 and 4.8 shows the vibrational assignments for IR modes and compare with experimental values. Figure 4.3 and 4.4 show the calculated IR spectra and selection of normal modes corresponding to the wavenumbers 67, 514, 670, 775, 1184, 1317, 1467 and 1957 cm<sup>-1</sup>.

The frequency range 0-300 cm<sup>-1</sup> corresponds to normal modes distinguished

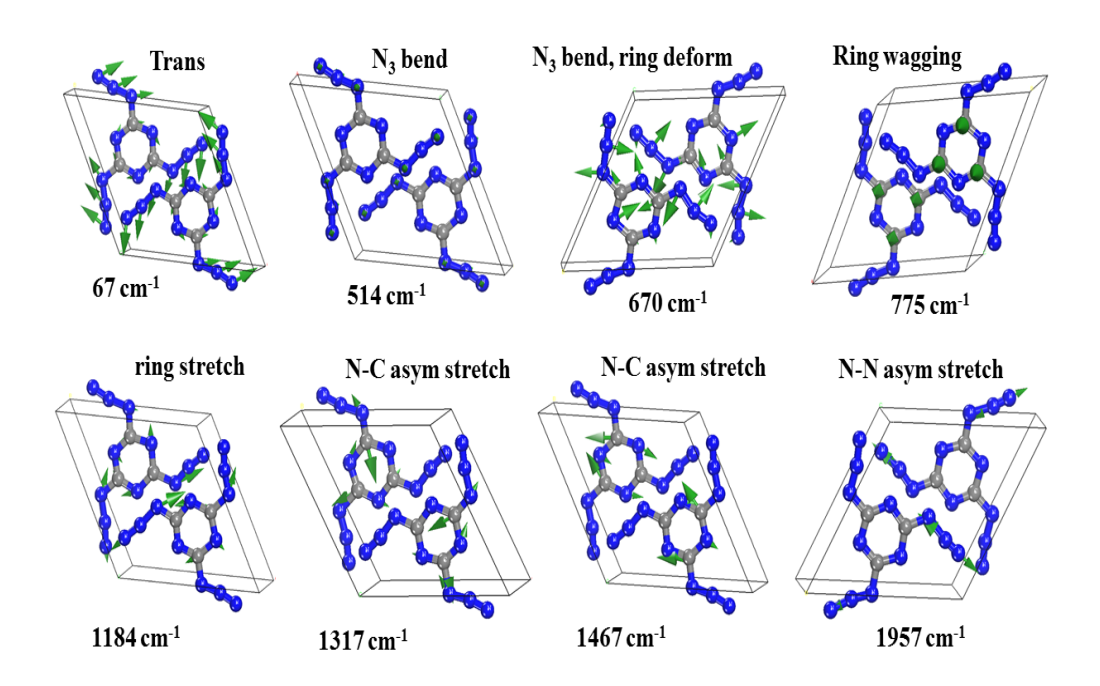


Figure 4.4: Normal modes of  $C_3N_{12}$  corresponding to the calculated IR absorption lines at 67, 514, 670, 775, 1184, 1317, 1467 and 1957 cm<sup>-1</sup> with their respective assignments.

by rotational, and translational modes over the entire molecular structure. The highest noticeable IR-active modes being at 67 cm<sup>-1</sup>, 119 cm<sup>-1</sup> and 235 cm<sup>-1</sup> which are due to C-N translational modes, N<sub>3</sub> twist, and lattice combination, respectively. Moreover, IR absorption in the wavenumbers between 320 cm<sup>-1</sup> and 900 cm<sup>-1</sup>, corresponding to the N<sub>3</sub> bend and ring deformations, respectively. In this range, the highest intense IR active modes appear at 326 cm<sup>-1</sup> (N<sub>3</sub> bend), 473 cm<sup>-1</sup> (N<sub>3</sub> bend, ring deformation), 514 cm<sup>-1</sup> (N<sub>3</sub> bend), 670 cm<sup>-1</sup> (N<sub>3</sub> bend, ring deformation), and 775 cm<sup>-1</sup> (ring twist). The infrared absorption maxima in the experiment are found at 325 cm<sup>-1</sup>, 543 cm<sup>-1</sup>, 634 cm<sup>-1</sup> and 703 cm<sup>-1</sup> [43], respectively. The IR spectra between 950 cm<sup>-1</sup> and 1350 cm<sup>-1</sup>, involve ring deformation and N<sub>3</sub> stretching, respectively. In the experimental IR spectra

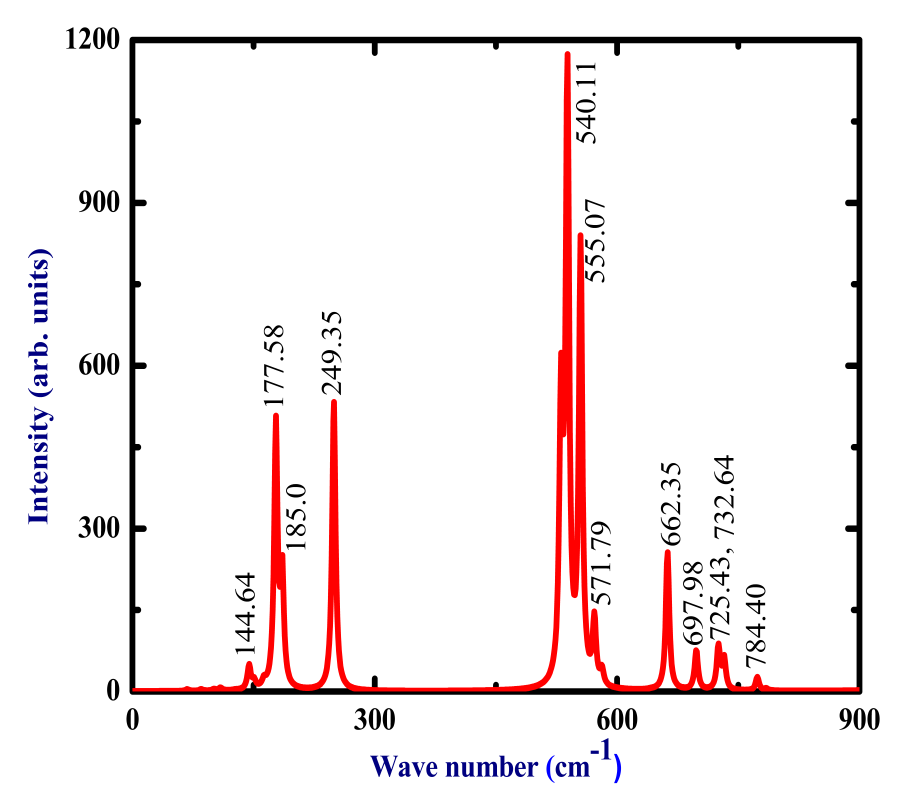


Figure 4.5: Calculated infrared spectra of Urea nitrate at the optimized equilibrium volume in the 0-900 cm<sup>-1</sup> range.

the maximum which located at 980 cm<sup>-1</sup>, 1194 cm<sup>-1</sup> and 1342 cm<sup>-1</sup> [43], which are closely associated with the theoretical spectrum with the wavelengths of 950 cm<sup>-1</sup>, 1184 cm<sup>-1</sup>, and 1317 cm<sup>-1</sup> respectively. The assigned modes are mainly due to N<sub>3</sub> symmetric stretching and ring deformation, respectively. Finally, in the highest wavenumber range between 1450 cm<sup>-1</sup> and 2000 cm<sup>-1</sup>, the modes are related to N-N bond stretching and N-C bond stretching. Two maxima are situated at 1467 cm<sup>-1</sup>, and 1957 cm<sup>-1</sup>, the first being assigned to N-C asymmetric stretching and the second one implying asymmetric stretching of N-N bond. Experimental measurements of the IR spectrum have demonstrated a sharp peak at 1410 cm<sup>-1</sup> and 2110 cm<sup>-1</sup> [43], which agrees well with the calculations.

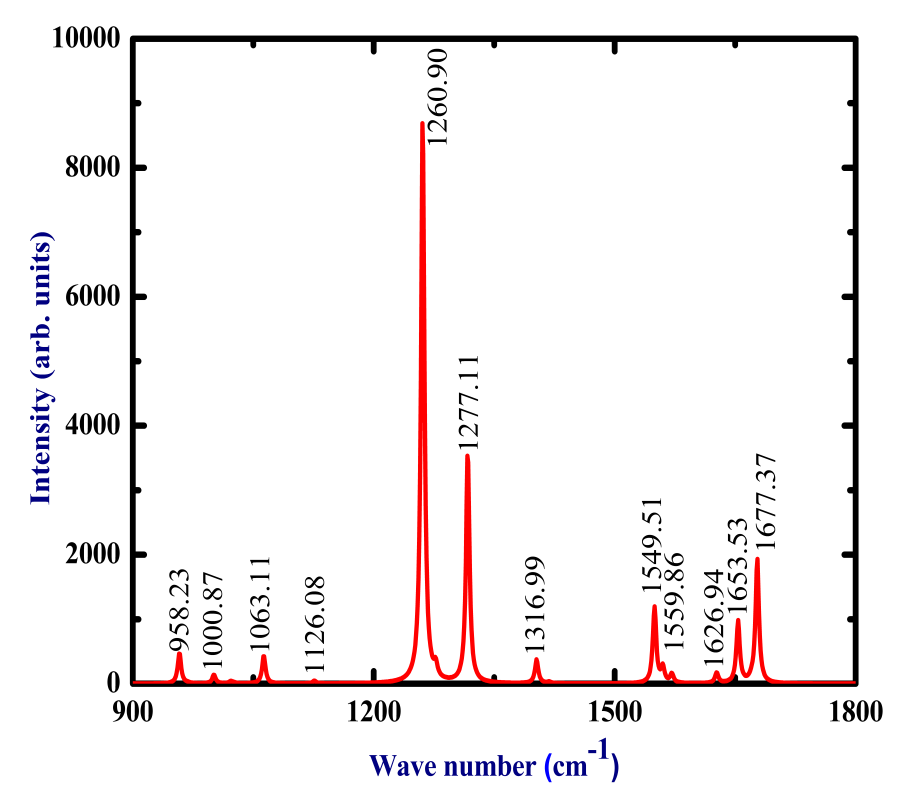


Figure 4.6: Calculated infrared spectra of Urea nitrate at the optimized equilibrium volume in the  $900-1800~\text{cm}^{-1}$  range.

Table 4.7: Calculated normal modes infrared frequencies (0-670 cm<sup>-1</sup>) with symmetry assignment for the cyanuric triazide crystal using the DFT GGA+G06 approach.

Mode number	Calculated frequency (cm <sup>-1</sup> )	Expt.[43]	Symmetry	Mode	Assignment
M4-M5	53.043		$E_g$	Raman	translational
M6-M7	53.96		$E_u$	IR	rotational
M8-M9	57.07		$E_{g}$	Raman	rotational
M10	66.19		$A_u$	IR	translational
M11	67.15		$A_u$	IR	translational
M12	85.43		$A_g$	Raman	rotational
M13	99.39		$A_g$	Raman	translational
M14-M15	107.99		$E_{\mu}$	IR	rotational
M16	113.16		$A_g$	Raman	translational
M17-M18	119.06		$E_g$	Raman	translational
M19-M20	119.21		$egin{array}{c} A_{ m g} \ E_{ m g} \ E_{ m u} \end{array}$	IR	$N_3$ twist
M21-M22	150.45		$E_{g}$	Raman	N <sub>3</sub> twist
M23	163.49		$A_g$	Raman	N₃ bend
M24	165.87		$A_{\scriptscriptstyle H}$	IR	N <sub>3</sub> bend
M25-M26	211.64		$E_{\mu}$	IR	$N_3$ twist
M27-M28	222.85		$E_{g}$	Raman	N <sub>3</sub> bend
M29	235.71		$A_u$	IR	lattice/combination
M30	260.03		$E_{u}$	IR	lattice/combination
M31-M32	324.79		$E_{g}$	Raman	lattice/combination
M33-M34	326.32	325	$E_u$	Raman	N <sub>3</sub> bend
M35	445.74		$A_u$	IR	N₃ bend
M36	446.37		$A_{g}$	Raman	$N_3$ bend
M37-M38	472.63		$E_g$	Raman	N <sub>3</sub> bend, ring deformation
M39-M40	473.24		$E_{\mu}$	IR	N <sub>3</sub> bend, ring deformation
M41-M42	513.51		$E_{u}$	IR	N₃ bend
M43-M44	513.54		$E_{g}$	Raman	$N_3$ bend
M45	513.89		$A_{g}$	Raman	N <sub>3</sub> bend
M46	514.96		$A_{u}$	IR	$N_3$ bend
M47	539.29		$A_g$	Raman	N <sub>3</sub> bend, ring deformation
M48	542.12	543	$A_u$	IR	N <sub>3</sub> bend, ring deformation
M49-M50	670.41	634	$E_{\mu}$	IR	N <sub>3</sub> bend, ring deformation
M51-M52	670.9		$E_g$	Raman	N <sub>3</sub> bend, ring deformation

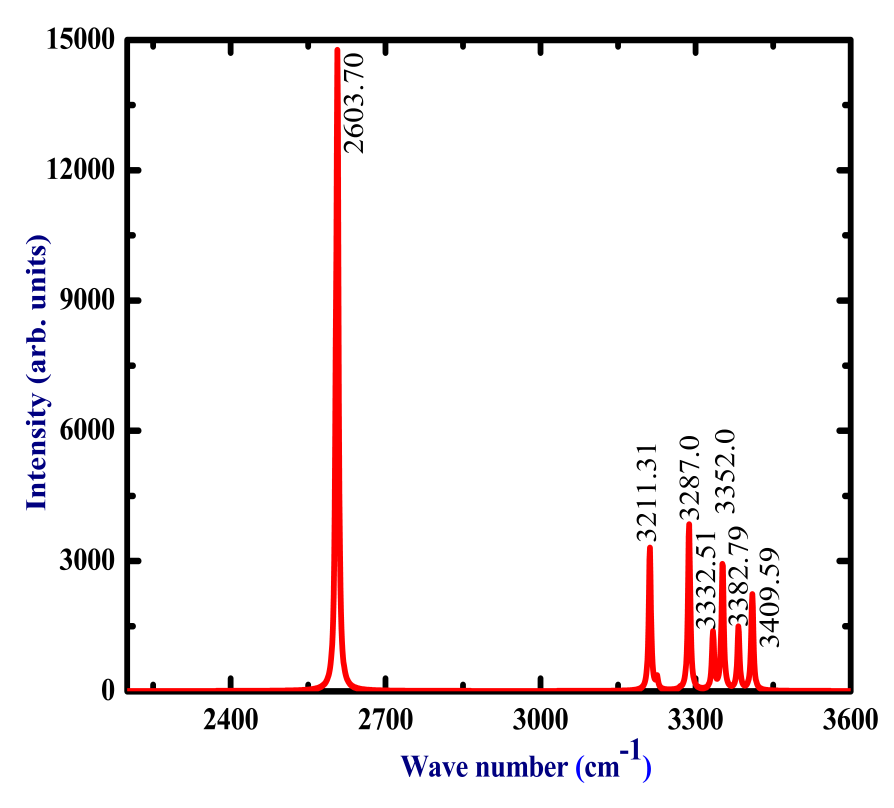


Figure 4.7: Calculated infrared spectra of Urea nitrate at the optimized equilibrium volume in the 2100-3600 cm<sup>-1</sup> range.

Table 4.8: Calculated normal modes infrared frequencies (670-2000  $\,\mathrm{cm}^{-1}$ ) with symmetry assignment for the cyanuric triazide crystal using the DFT GGA+G06 approach.

Mode number	Calculated (cm <sup>-1</sup> )	Expt. [43]	Symmetry	Mode	Assignment
M53-M54	684.81	666	$E_u$	IR	ring twist
M55-M56	687.33		$E_g$	Raman	ring twist
M57	775.03	703	$A_u$	IR	ring twist
M58	775.87		$A_g$	Raman	ring twist
M59	796.49		$A_{u}$	IR	N <sub>3</sub> bend, ring deformation
M60	800.10	804	$A_g$	Raman	N <sub>3</sub> bend, ring deformation
M61	940.56		$A_{g}$	Raman	N <sub>3</sub> stretch
M62	941.87		$A_u$	IR	N <sub>3</sub> stretch
M63-M64	950.95	980	$E_u$	IR	ring deformation
M65-M66	1017.66		$E_g$	Raman	ring deformation
M67	1120.09		$A_u$	IR	N <sub>3</sub> sym stretch, ring stretch
M68	1124.95		$A_g$	Raman	N <sub>3</sub> sym stretch, ring stretch
M69-M70	1184.37	1194	$E_u$	IR	N <sub>3</sub> sym stretch, ring stretch
M71-M72	1184.85		$E_g$	Raman	N <sub>3</sub> sym stretch, ring stretch
M73	1243.45		$A_g$	Raman	ring asym stretch
M74	1243.49	1270	$A_u$	IR	ring asym stretch
M75-M76	1309.54		$E_{g}$	Raman	ring deformation
M77-M78	1317.09	1342	$E_u$	IR	ring deformation
M79	1402.60		$A_g$	Raman	ring stretch
M80	1417.38		$A_{u}$	IR	ring stretch
M81-M82	1467.35	1480	$E_u$	IR	ring deformation N-C asym stretch
M83-M84	1473.07		$E_g$	Raman	ring deformation N-C asym stretch
M85	1946.61		$A_u$	IR	N₃ asym stretch
M86-M87	1954.96		$E_g$	Raman	N <sub>3</sub> asym stretch
M88-M89	1957.01	2110	$E_u$	IR	N <sub>3</sub> asym stretch
M90	1978.35		$A_g$	Raman	N <sub>3</sub> asym stretch

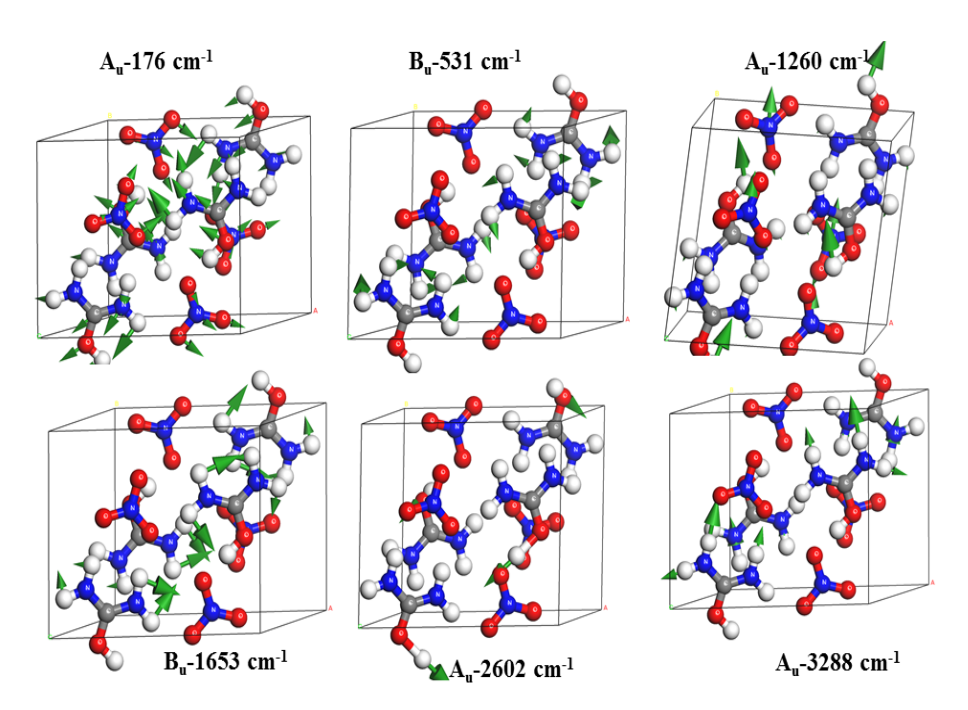


Figure 4.8: Normal modes of UN corresponding to the calculated IR absorption lines at 176, 531, 1260, 1653, 2602 and 3288 cm<sup>-1</sup> with their respective assignments.

Figures 4.5–4.7 depict the infrared spectra and normal modes of urea nitrate in the wavenumber range 0-3600 cm<sup>-1</sup>. Urea nitrate crystal contains 52 atoms in the unit cell, which leads to total of 156 vibrational modes. Figure 4.8 shows the selection of normal modes corresponding to the wavenumbers. Table 4.9–4.11 shows the vibrational assignments for IR modes. The irreducible description of this symmetry is described;

$$\Gamma_{total} = 39A_u + 39B_u + 39B_g + 39A_g$$

$$\Gamma_{acoustic} = A_u + 2B_u$$

$$\Gamma_{optical} = 38A_u + 37B_u + 39B_g + 39A_g$$

The group-theoretical analysis gives the  $A_g$ , and  $B_g$  modes are Raman-active and  $A_u$ ,  $B_u$  modes are Infrared-active. In the low-frequency region the vibrational modes at 114.64, 177.58, 185.0, and 249.35 cm<sup>-1</sup> are attributed to the external modes. The frequency region from 500 to 900 cm<sup>-1</sup> exhibits total of eight

peaks, which are come from both external modes as well as internal modes. The frequency region at 540.11 and 555.07 cm<sup>-1</sup> are mainly due to the NH<sub>2</sub> wagging vibrational modes. And the frequencies at 571.79 cm<sup>-1</sup> are associated with the NH<sub>2</sub> rocking vibrational modes. In the frequency range from 600 to 900 cm<sup>-1</sup> are assigned to the NH<sub>2</sub> and NO<sub>3</sub> vibrational modes. The frequency at 662.35 cm<sup>-1</sup> is related to the NH<sub>2</sub> wagging and frequency at 725.43 cm<sup>-1</sup> is assigned to NO<sub>3</sub> scissoring. Finally, the frequency at 784.41 cm<sup>-1</sup> is occured due to twisting NH<sub>2</sub>.

Figure 4.6 displays the infrared spectra frequency region from 900 to 1800 cm<sup>-1</sup> exhibits a set of twelve high-intensity peaks. The most intense lines at 1260.90 cm<sup>-1</sup>, 1277.11 cm<sup>-1</sup>, and 1316.99 cm<sup>-1</sup> which are assigned to wagging vibrational modes of NH<sub>2</sub> groups and NO<sub>3</sub> stretching. The vibrations at 1063.12 and 1126.08 cm<sup>-1</sup> frequencies are owing to wagging vibrational modes NH<sub>2</sub> groups. The frequencies from 1500 to 1700 cm<sup>-1</sup> (figure 4.6) originate from scissoring vibrational modes of NO<sub>3</sub> groups. The highest intense maxima were observed at 2603.70 cm<sup>-1</sup> owing to the single O-H bond stretching. The higher frequency interval between 3100 and 3600 cm<sup>-1</sup> is depicted in figure 4.7. All modes above 3100 cm<sup>-1</sup> originate from stretching vibrational modes of N-H bonds. The frequencies at 3211.31 and 3287.0 cm<sup>-1</sup> are assigned to N-H symmetric stretching, while 3332.51, 3352.0, 3382.83, and 3409.59 cm<sup>-1</sup> are related to the N-H asymmetric stretching vibrational modes.

Table 4.9: Calculated normal modes infrared frequencies (0-200 cm<sup>-1</sup>) with symmetry assignment for the UN crystal using the DFT GGA+G06 approach.

Mode number	Calculated frequency (cm <sup>-1</sup> )	Symmetry	Mode	Assignment
M4	29.38	<u> </u>	Raman	translational
M5	29.75	$B_{\rm g}$	IR	translational
		$A_{u}$		
M6	34.74	$A_{g}$	Raman	translational translational
M7	64.13	$A_g$	Raman	
M8	73.97	$B_{u}$	IR	translational
M9	76.03	$A_g$	Raman	translational
M10	78.36	$B_{\rm g}$	Raman	rotational
M11	78.94	$A_{u}$	IR	translational
M12	85.21	$A_{u}$	IR	rotational
M13	86.39	$B_{g}$	Raman	translational
M14	88.73	$B_u$	IR	translational
M15	94.06	$B_{\mathrm{g}}$	Raman	translational
M16	96.99	$A_g$	Raman	rotational
M17	101.66	$B_{u}$	IR	translational
M18	101.73	$A_u$	IR	rotational
M19	105.72	$B_{g}$	Raman	rotational
M20	107.26	$A_g$	Raman	rotational
M21	109.08	$A_u$	IR	rotational
M22	112.68	$B_{u}$	IR	NO <sub>3</sub> rotational
M23	125.28	$E_{g}$	Raman	translational
M24	127.91	$A_u$	IR	translational
M25	128.01	$B_{ m g}$	Raman	translational
M26	144.64	$B_u$	IR	rotational
M27	144.68	$B_{g}$	Raman	rotational
M28	145.86	$A_g^{\circ}$	Raman	translational
M29	149.44	$B_u^{\circ}$	IR	rotational
M30	150.74	$A_u$	IR	UN trans.
M31	155.76	$B_{\mathrm{g}}$	Raman	rotational
M32	159.04	$\mathring{A_g}$	Raman	twisting
M33	162.37	$A_u^{\circ}$	IR	twist
M34	164.08	$A_g^{"}$	Raman	Urea, NO3 lib.
M35	165.09	$B_u^{\circ}$	IR	Urea, NO <sub>3</sub> lib.
M36	166.64	$B_{\mathrm{g}}^{"}$	Raman	Urea, NO <sub>3</sub> lib.
M37	175.96	$B_{g}^{^{\circ}}$	Raman	translational
M38	176.86	$A_g^{g}$	Raman	translational
M39	177.58	$A_u^{^8}$	IR	translational
M40	177.75	$B_u$	IR	translational
M41	185.28	$B_u$	IR	translational
M42	187.73	$B_{g}$	Raman	translational
M43	217.91	$A_u$	IR	rotational
M44	218.20	$A_g$	Raman	rotational
M45	249.09	$\stackrel{I_g}{A_g}$	Raman	rotational
M46	249.35		IR	rotational
M47	260.07	$A_u$	IR IR	rotational
		$B_u$		
M48	262.78	$B_{ m g}$	Raman	rotational

### 4.3.4 Phonon dispersion

To acquire an understanding on the dynamical stability of the C<sub>3</sub>N<sub>12</sub> and UN, we have calculated the phonon dispersion curves using DFPT [49–52]. The phonon dispersion curve and the corresponding phonon density of states (PDOS) for the C<sub>3</sub>N<sub>12</sub> and UN, compounds are illustrated in figure 4.9 (a,b)-figure 4.11 (a,b) respectively. The obtained phonon dispersion spectra do not show any imaginary frequencies, indicating that C<sub>3</sub>N<sub>12</sub> and UN are dynamically stable. We can note that there is no gap between the low-lying optical modes and acoustic modes, implying that energy transfer between these modes is easy. Therefore, low-frequency optical modes will scatter acoustic modes, which carry the heat flow, consequently leading to low thermal conductivity [20, 64-66]. From this, we can conclude that because of the low thermal conductivity, cyanuric triazide is found to possess high vapor pressure and high volatility, which might lead to immensely powerful explosive behaviour [66, 67]. Further, we have calculated the partial phonon density of states to see the contribution of different atoms to the vibrational modes. Since the acoustic branches play a major contribution to heat transport, we highlight these phonon modes in the local close-up range as shown in figure 4.10 (a,b). The acoustic phonon modes are located below 200 cm<sup>-1</sup>, and optical phonon modes lie above that range. We can also find that the lowest optical modes overlap with its acoustic branches, resulting in strong acoustic-optical interactions which might result in low lattice thermal conductivity. The low-frequency region 500 cm<sup>-1</sup> arises from strong hybridization between C and N atoms, dominated by N atoms, while high-frequency regions (around 1500 cm $^{-1}$ ) are influence by the vibrations of C atoms. The sharp phonon peaks around 750, 1300 and 2100 cm<sup>-1</sup>, indicates a gap between optical-optical phonon modes.

The partial phonon density of states (PPDOS) of urea nitrate presented in figure 4.12 (a,b) shows the vibrational modes mainly appear in the 0 - 1600 cm<sup>-1</sup> and

Table 4.10: Calculated normal modes infrared frequencies (200-750 cm<sup>-1</sup>) with symmetry assignment for the UN crystal using the DFT GGA+G06 approach.

Mode number	Calculated frequency (cm <sup>-1</sup> )	Symmetry	Mode	Assignment
M49	521.78	$A_g$	Raman	NH <sub>2</sub> wag.
M50	531.16	$B_{u}$	IR	$NH_2$ rock.
M51	533.35	$A_u$	IR	$NH_2$ rock.
M52	533.50	$A_{g}$	Raman	$NH_2$ rock.
M53	533.82	$A_g$	Raman	NH <sub>2</sub> rock.
M54	537.75	$A_u$	IR	NH <sub>2</sub> twist.
M55	540.11	$B_{u}$	IR	$NH_2$ wag.
M56	555.07	$B_{u}$	IR	NH <sub>2</sub> twist.
M57	571.79	$A_{u}$	IR	NH <sub>2</sub> wag.
M58	572.12	$A_g^{"}$	Raman	NH <sub>2</sub> wag.
M59	581.16	$B_{ m g}^{\circ}$	Raman	NH <sub>2</sub> wag.
M60	581.21	$B_u^{^{8}}$	IR	NH <sub>2</sub> wag.
M61	588.08	$B_g$	Raman	NH <sub>2</sub> twist.
M62	597.96	$\stackrel{\mathcal{L}_g}{A_g}$	Raman	NH <sub>2</sub> twist.
M63	619.72	$A_u$	IR	NH <sub>2</sub> wag.
M64	624.03		Raman	NH <sub>2</sub> twist.
M65	641.90	$B_{g}$	IR	NH <sub>2</sub> wag.
		$A_{u}$	IR	
M66	662.35	$B_{u}$	_	NH <sub>2</sub> twist.
M67	669.26	$A_g$	Raman	NH <sub>2</sub> twist.
M68	674.02	$B_{\rm g}$	Raman	NH <sub>2</sub> wag.
M69	697.63	$A_{g}$	Raman	NO <sub>3</sub> Sciss.
M70	697.98	$A_u$	IR	NO <sub>3</sub> Sciss.
M71	701.10	$A_{u}$	IR	NO <sub>3</sub> Sciss.
M72	701.70	$B_{ m g}$	Raman	NO <sub>3</sub> Sciss.
M73	724.82	$A_g$	Raman	NO <sub>3</sub> Sciss.
M74	725.07	$A_{u}$	IR	NO <sub>3</sub> Sciss.
M75	725.43	$A_u$	IR	NH <sub>2</sub> wag., NO <sub>3</sub> Sciss.
M76	726.13	$B_{u}$	IR	NO <sub>3</sub> Sciss.
M77	726.31	$B_{g}$	Raman	NO <sub>3</sub> Sciss.
M78	730.50	$B_{g}$	Raman	$NH_2$ wag.
M79	730.83	$A_{g}$	Raman	NH <sub>2</sub> wag.
M80	732.64	$B_u$	IR	$NH_2$ wag.
M81	772.27	$A_{u}$	IR	NO <sub>3</sub> bend., NH <sub>2</sub> twist.
M82	773.52	$B_{u}$	IR	NO <sub>3</sub> bend., NH <sub>2</sub> twist.
M83	774.17	$B_{ m g}$	Raman	NO <sub>3</sub> bend., NH <sub>2</sub> twist.
M84	774.18	$\mathring{A_g}$	Raman	NO <sub>3</sub> bend., NH <sub>2</sub> twist.
M85	784.40	$A_g^{\circ}$	Raman	NO <sub>3</sub> bend., NH <sub>2</sub> twist.
M86	788.79	$B_{\rm g}^{^{\rm g}}$	Raman	NO <sub>3</sub> bend., NH <sub>2</sub> twist.
M87	789.73	$A_u^g$	IR	NO <sub>3</sub> bend., NH <sub>2</sub> twist.
M88	805.62	$A_g$	Raman	NH <sub>2</sub> twist.
M89	954.80	$A_g$	Raman	OH wag.
M90	958.23	$B_u$	IR	OH wag.
M91	963.77		Raman	OH wag.
M92	968.29	$egin{aligned} B_{ m g} \ A_{\it u} \end{aligned}$	IR	OH wag., NH <sub>2</sub> twist.
			IR	
M93	1000.87	$B_u$		C-N, C-O sym. stretch.
M94	1001.33	$A_g$	Raman	C-N, C-O sym. stretch.
M95	1001.39	$A_{u}$	IR	C-N, C-O sym. stretch.
M96	1002.16	$B_{\rm g}$	Raman	C-N, C-O sym. stretch.
M97	1022.13	$B_{u}$	IR	NO <sub>3</sub> sym. stretch., NH <sub>2</sub> roc
M98	1022.37	$B_{g}$	Raman	NO <sub>3</sub> sym. stretch., NH <sub>2</sub> roc
M99	1025.90	$A_{u}$	IR	NO <sub>3</sub> , C-N sym. stretch.
M100	1026.23	$A_{g}$	Raman	NO <sub>3</sub> , C-N sym. stretch.

Table 4.11: Calculated normal modes infrared frequencies (1250-3450  $\,\mathrm{cm}^{-1}$ ) with symmetry assignment for the UN crystal using the DFT GGA+G06 approach.

de number (	Calculated frequency (cm <sup>-1</sup> )	Symmetry	Mode	Assignment
M101	1061.72	$A_{g}$	Raman	NH <sub>2</sub> wag.
M102	1062.94	$\mathring{A_u}$	IR	$NH_2$ wag.
M103	1063.11	$B_u$	IR	NH <sub>2</sub> wag.
M104	1063.14	$B_g$	Raman	$NH_2$ wag.
M105	1118.98	$B_g^{\epsilon}$	Raman	NH <sub>2</sub> wag.
M106	1119.77	$B_u^{g}$	IR	NH <sub>2</sub> wag.
M107	1126.08	$A_u$	IR	$NH_2$ wag.
M108	1126.11	$A_g$	Raman	$NH_2$ wag.
M109	1260.90	$A_u$	IR	NO <sub>3</sub> asym. stretch., O-H bend.
M110	1261.44	$A_g$	Raman	NO <sub>3</sub> asym. stretch., O-H bend.
M111	1277.11	$B_u$	Raman	NO <sub>3</sub> asym. stretch., O-H bend.
M112	1302.76	$B_g$	Raman	NO <sub>3</sub> asym. stretch., O-H bend.
M113	1316.99	$B_u$	IR	NO <sub>3</sub> asym. stretch., O-H bend.
M114	1322.83	$A_u$	IR	NO <sub>3</sub> asym. stretch., O-H, NH <sub>2</sub> bend.
M115	1330.80		Raman	NO <sub>3</sub> asym. stretch., O-H, NH <sub>2</sub> bend.
		$B_{\rm g}$	Raman	
M116	1336.28	$A_g$		NO <sub>3</sub> asym. stretch., O-H, NH <sub>2</sub> bend.
M117	1396.14	$B_{g}$	Raman IR	NO <sub>3</sub> asym. stretch., O-H, NH <sub>2</sub> bend.
M118	1336.28	$A_{u}$		NO <sub>3</sub> , O-H bend.
M119	1404.57	$A_g$	Raman	NO <sub>3</sub> , N-C-N asym. stretch., O-H bend.
M120	1418.42	$A_g$	Raman	NO <sub>3</sub> , N-C-N asym. stretch., O-H bend.
M121	1547.95	$B_{g}$	Raman	NH <sub>2</sub> scis., N-C-O asym. stretch.
M122	1549.51	$A_{u}$	IR	NH <sub>2</sub> scis., N-C-O asym. stretch.
M123	1557.05	$A_g$	Raman	NH <sub>2</sub> scis., N-C-O asym. stretch.
M124	1559.86	$A_u$	IR	NH <sub>2</sub> scis., N-C-O asym. stretch.
M125	1569.20	$A_g$	Raman	NH <sub>2</sub> scis., N-C-O asym. stretch.
M126	1570.88	$B_{u}$	IR	NH <sub>2</sub> scis., N-C-O asym. stretch.
M127	1571.45	$A_u$	IR	NH <sub>2</sub> scis., N-C-O asym. stretch.
M128	1574.68	$B_{g}$	Raman	NH <sub>2</sub> scis., N-C-O asym. stretch.
M129	1625.38	$A_g$	Raman	NH <sub>2</sub> scis.
M130	1626.94	$A_u$	IR	NH <sub>2</sub> scis.
M131	1645.51	$B_{ m g}$	Raman	NH <sub>2</sub> scis.
M132	1653.53	$B_{u}$	IR	NH <sub>2</sub> scis.
M133	1669.86	$A_u$	IR	NH <sub>2</sub> scis., N-C-N asym. stretch.
M134	1675.63	$A_g$	Raman	NH <sub>2</sub> scis., N-C-N asym. stretch., O-H bend
M135	1677.37	$B_{u}$	IR	NH <sub>2</sub> scis., N-C-N asym. stretch., O-H bend
M136	1683.24	$B_{g}$	Raman	NH <sub>2</sub> scis., N-C-N asym. stretch., O-H bend
M137	2603.70	$B_u$	IR	O-H stretch.
M138	2606.84	$A_u$	IR	O-H stretch.
M139	2609.14	$A_{g}$	Raman	O-H stretch.
M140	2622.36	$B_{g}^{\circ}$	Raman	O-H stretch.
M141	3211.31	$B_u^{\circ}$	IR	N-H sym. stretch.
M142	3211.84	$B_{g}$	Raman	N-H sym. stretch.
M143	3224.42	$\mathring{A_g}$	Raman	N-H sym. stretch.
M144	3225.23	$A_u^{\circ}$	IR	N-H sym. stretch.
M145	3269.97	$B_{u}$	IR	N-H sym. stretch.
M146	3271.31	$B_g$	Raman	N-H sym. stretch.
M147	3286.93	$\stackrel{-g}{A_g}$	Raman	N-H sym. stretch.
M148	3287.32	$A_u$	IR	N-H sym. stretch.
M149	3332.80	$A_g$	Raman	N-H asym. stretch.
		_		
M150 M151 M152 M153 M154 M155 M156	3333.51 3333.51 3353.56 3382.74 3382.79 3409.59 3410.90	$A_u$ $A_u$ $B_g$ $A_g$ $A_u$ $B_u$ $B_u$	IR IR Raman Raman IR IR Raman	N-H asym. stretch.

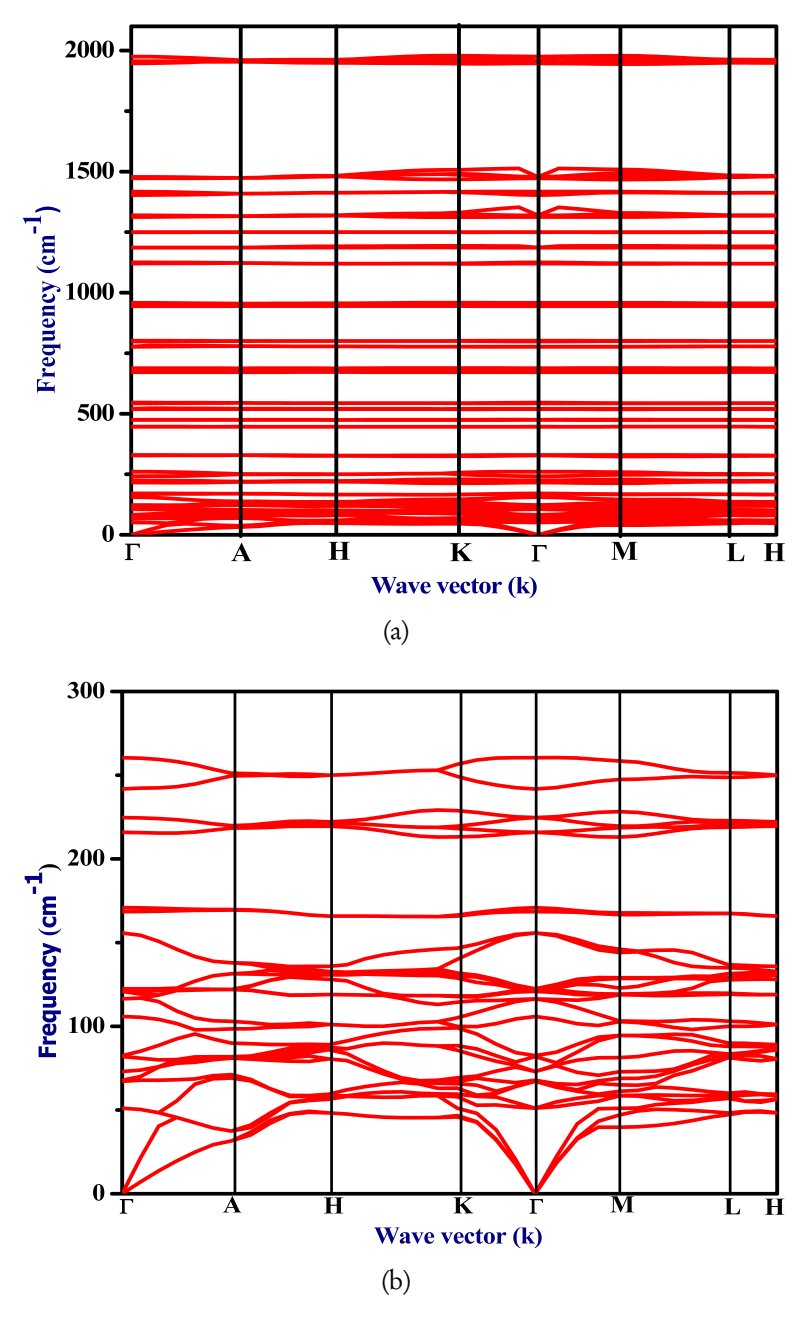


Figure 4.9: Phonon dispersion curves for  $C_3N_{12}$  crystal (a) 0-2100 cm<sup>-1</sup> (b) Close-up showing the 0-300 cm<sup>-1</sup> wavenumber range.

3100 - 3400 cm<sup>-1</sup> range. In the low-frequency region, around 300 cm<sup>-1</sup> comes from C-N, O-N-O, urea group, and C-H bonds, while oxygen atoms contributes

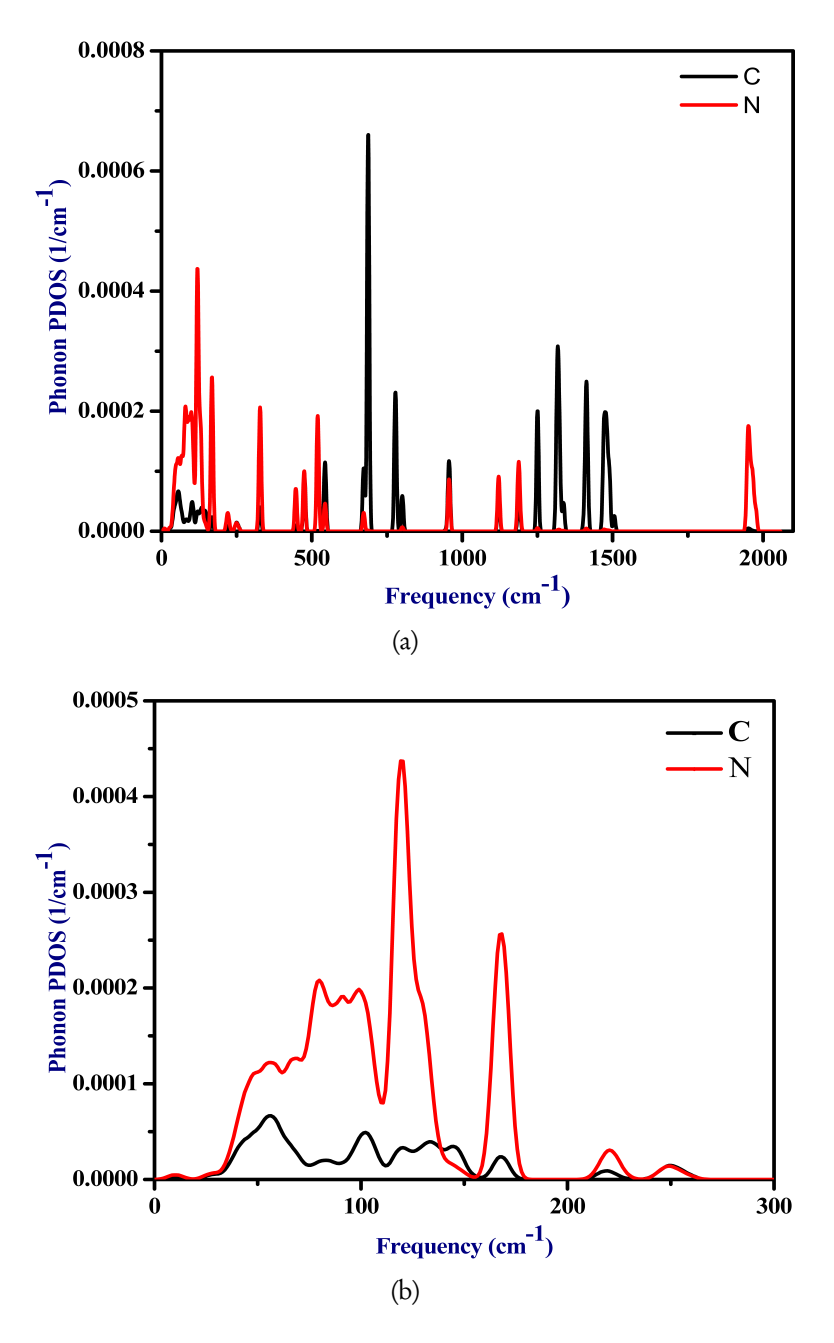


Figure 4.10: Phonon partial density of states (PDOS) for the  $C_3N_{12}$  crystal (a) (a) 0-2100 cm $^{-1}$  (b) Close-up showing the 0-300 cm $^{-1}$  wavenumber range.

in the high-frequency region. The low frequency region, the NO<sub>3</sub> groups, are the larger contribution than other selected bonds (C-N and C-H). This concludes

that the probability of energy flow from nitro groups to the urea ring.

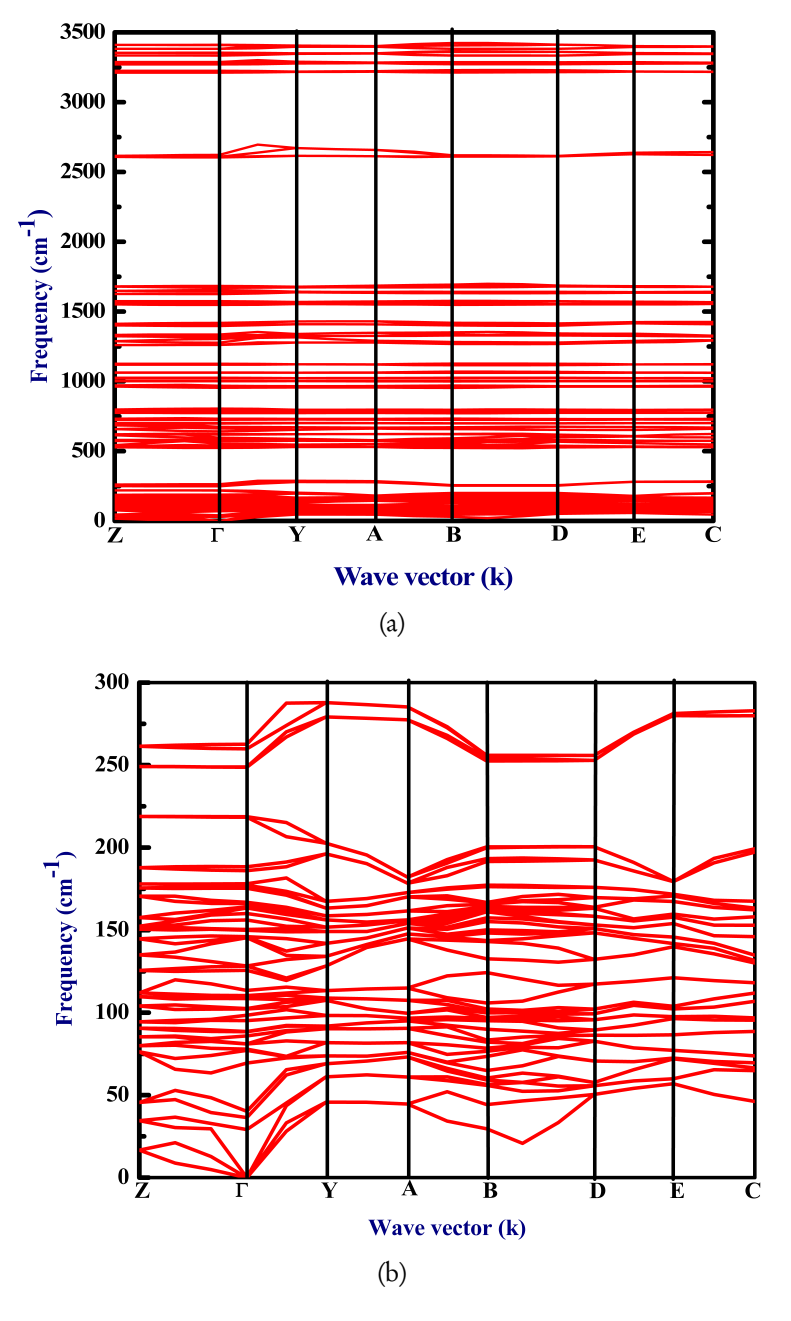


Figure 4.11: Phonon dispersion curves for Urea nitrate crystal (a)  $0-3600 \text{ cm}^{-1}$  (b) Close-up showing the  $0-300 \text{ cm}^{-1}$  wavenumber range.

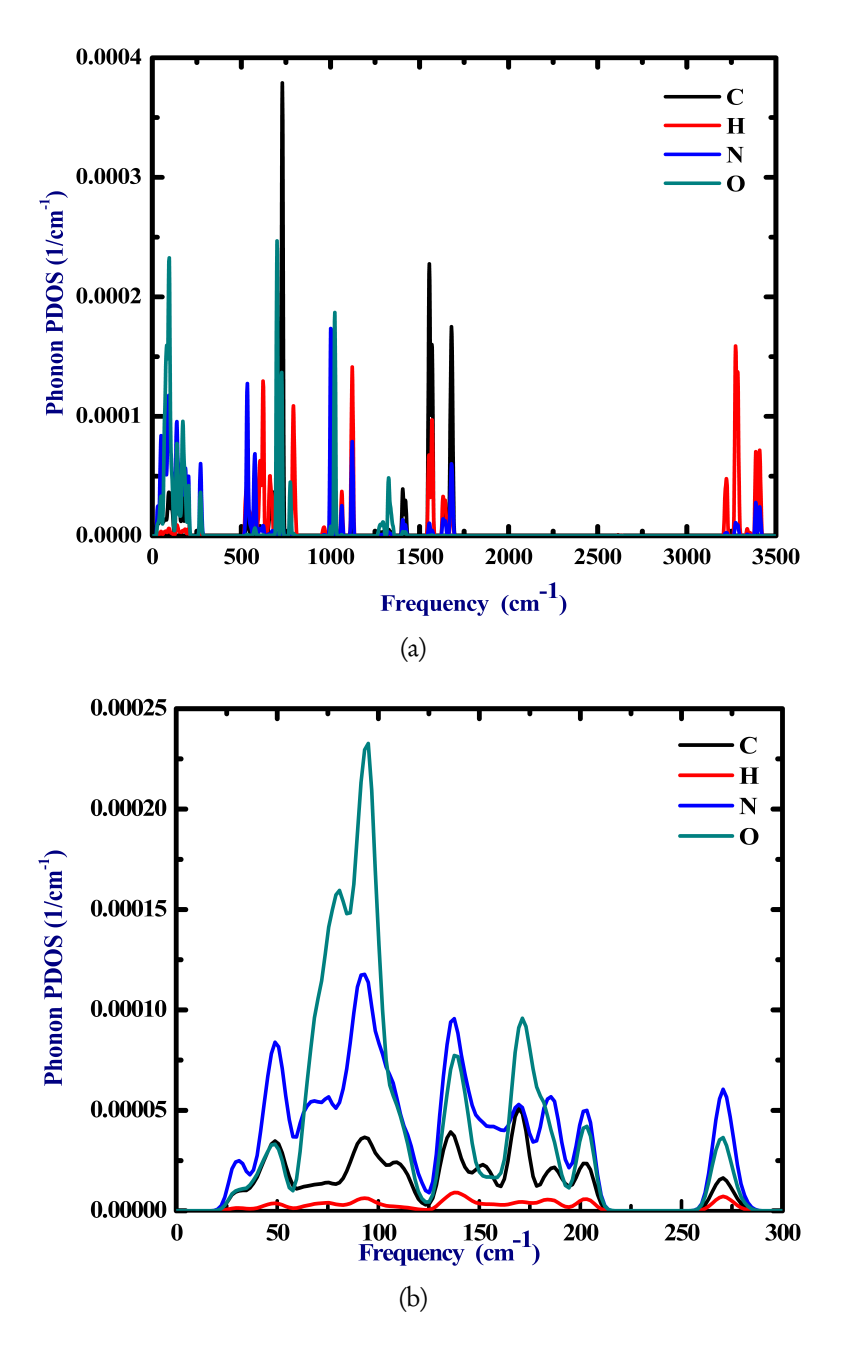


Figure 4.12: Phonon partial density of states (PDOS) for the Urea nitrate crystal (a) 0–3600 cm<sup>-1</sup> (b) Close-up showing the 0-300 cm<sup>-1</sup> wavenumber range.

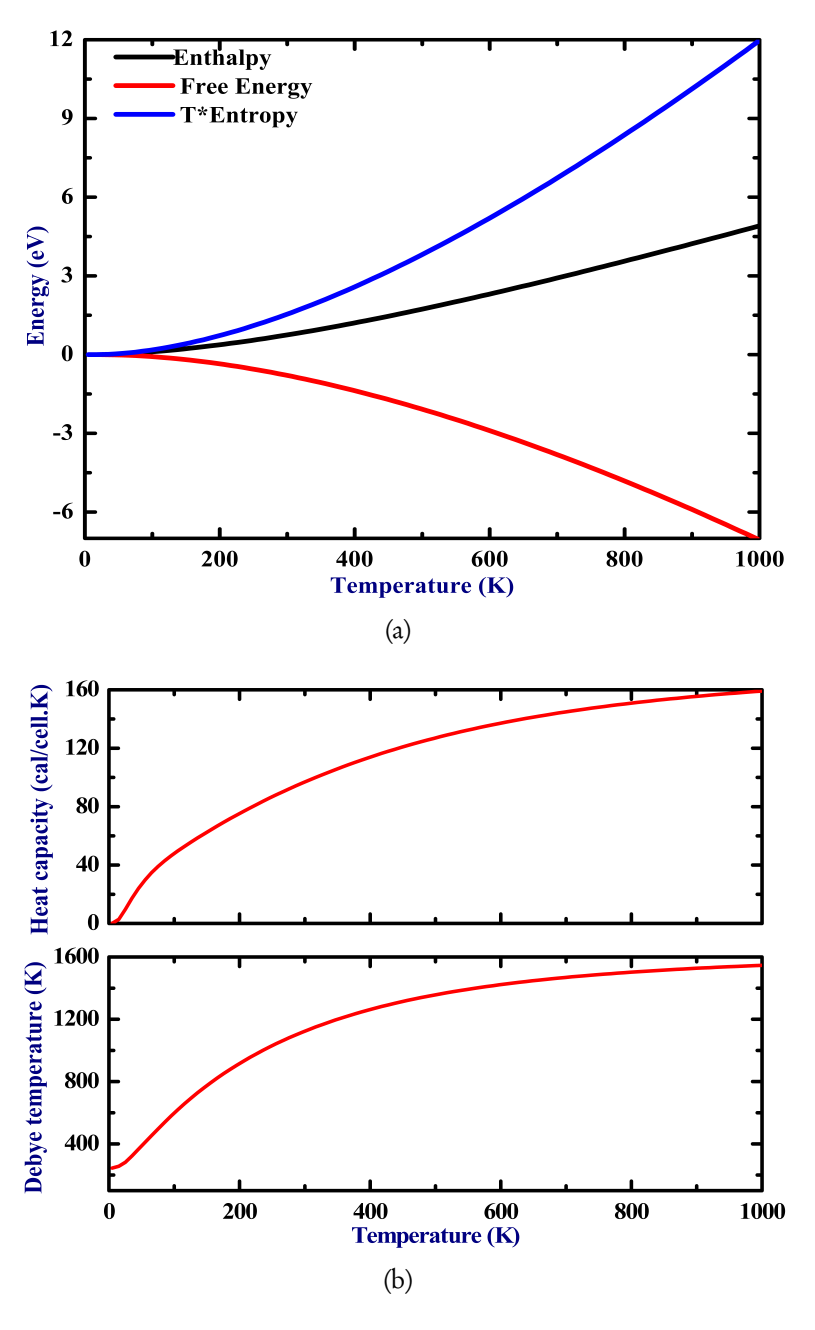


Figure 4.13: Calculated (a) temperature times entropy, enthalpy, and free energy of the cyanuric triazide crystal for temperature of up to 1000 K and (b) Heat capacity curves for the cyanuric triazide crystal.

### 4.3.5 Thermodynamic properties

The understanding of the thermal behavior of a material is most considerable in order to correlate the explosive initiation of  $C_3N_{12}$ . So we attempted to calculate basic thermodynamic properties, such as lattice Heat capacity ( $C_V$ ), entropy (S) enthalpy (E), free energy (F), and the Debye temperature ( $\Theta_D$ ) [68, 69]. Figure 4.13(a) presents the enthalpy (H), Entropy (S), and Free energy for the  $C_3N_{12}$  crystal. The enthalpy and entropy values increases monotonically as a function of temperature, with the latter displaying the most linear behavior, and the free energy decreasing as the temperature increase. The most common type of initiating event is some sort of a heat impulse (heat, flame, spark, etc.), and it is, therefore important to determine the thermal stability of explosives. In order to predict the thermal behavior of energetic material, the specific heat capacity is a fundamental property to access with respect to temperature [70, 71].

The specific heat ( $C_V$ ) of the  $C_3N_{12}$  as a function of temperature acquired from the phonon calculations within the quasi–harmonic approximation scheme is displayed in Figure 4.13 and 4.14 for a temperature in the range of 0–1000 K. The heat capacity  $C_V$  of UN is slightly larger than that of  $C_3N_{12}$ , while both compounds increase with temperature. At higher temperatures  $C_V$  is almost constant for both systems, reaching the Dulong-Petit limit at around 380 K, being 98.13 cal/cell.K for  $C_3N_{12}$  and 139.47 cal/cell.K for UN. The Debye temperature is a significant thermodynamic parameter, which is associated with elastic constants, specific heat, thermal conductivity, and melting temperature. Figure 4.13 (b) exhibits a jumps from T=0 to 10 K, afterward increasing almost linearly, reaching 400 K. The Debye temperature of  $C_3N_{12}$  is found to be 244.64 K, which is closely related to elastic Debye temperature 269.43 K [ $\overline{37}$ ]. The Debye temperature of UN is found to be 292.91 K at 15 K. These results will be helpful in the investigation of heat conductivity and structural stability for  $C_3N_{12}$ .

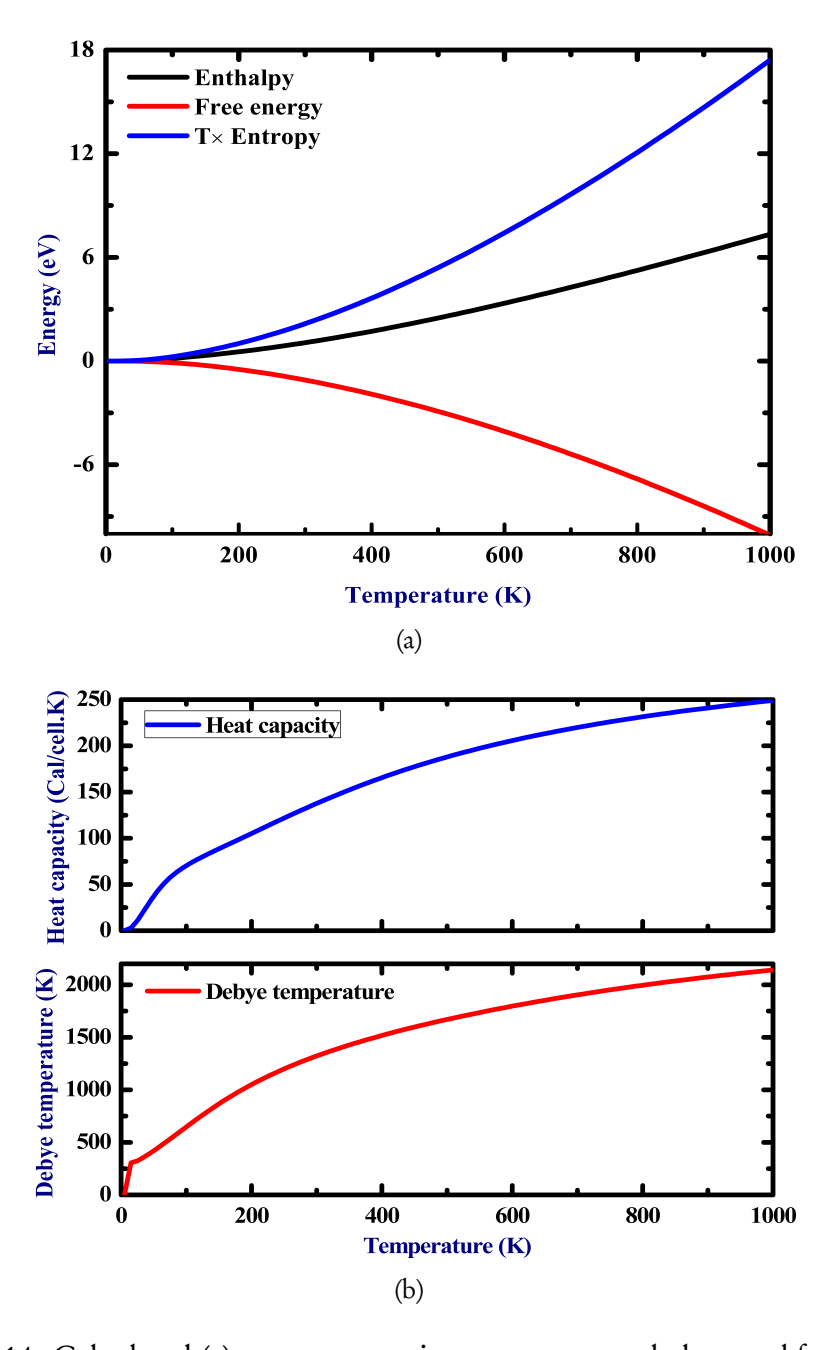


Figure 4.14: Calculated (a) temperature times entropy, enthalpy, and free energy of the urea nitrate crystal for temperature of up to 1000 K and (b) Heat capacity curves for the cyanuric triazide crystal.

## 4.4 Conclusions

To conclude, we have performed the structural, vibrational, and thermodynamic properties of the cyanuric triazide and urea nitrate crystals under ambient conditions using first-principles calculations. The structural relaxation is achieved using GGA-PBE exchange-correlation functional, together with dispersion correction (PBE + G06) and (PBE + TS) considering van der Waals interactions for C<sub>3</sub>N<sub>12</sub> and UN, respectively. The unit cell lattice parameters showed a good agreement with experimental data. The infrared spectra of the C<sub>3</sub>N<sub>12</sub> is obtained and compared with measurements from the experimental in the 0-2100 cm<sup>-1</sup> region. However, the calculated vibrational modes are in good agreement with experimental results. We note that the N<sub>3</sub> group involves high-intensity infrared absorption lines in the range of 1200-1500 cm<sup>-1</sup>. This vibration confirms to the frequency position at 1317 cm<sup>-1</sup> with irreducible representation  $E_{\mu}$ , which is allocated to an asymmetric ring stretching. Similarly, we calculated infrared spectra for urea nitrate in the range of 0-3600 cm<sup>-1</sup>; the results reveal most of the vibrational modes comes from NO<sub>3</sub> group in the low-frequency region (around 500 cm<sup>-1</sup>). The mid-frequency range from 900 to 1700 cm<sup>-1</sup> involves scissoring vibrational modes of NO<sub>3</sub> groups, and high-frequency range (2100-3100 cm<sup>-1</sup>) dominated by N-H stretching vibrational modes. The highest intense maxima being observed at 2603.70 cm<sup>-1</sup> is owing to the single O-H bond stretching vibrational mode. The absence of negative frequency in the phonon dispersion curves confirms the dynamical stability of both systems. We found that there is no gap between the low-lying optical modes and acoustic modes, which leads to low-thermal conductivity of the cyanuric triazide and urea nitrate. The phonon partial density of states results reveals the contribution of particular atoms in respected frequencies. For C<sub>3</sub>N<sub>12</sub> the low-frequency region 500 cm<sup>-1</sup> arises from strong hybridization between C and N atoms, dominated by N atoms, while high-frequency regions (around 1500 cm<sup>-1</sup>) are influenced by the vibrations of C atoms. In the case of UN, the low frequency region around 300 cm<sup>-1</sup>, contributed by lattice modes of the C-N, O-N-O, urea group, and C-H bonds, wherein the vibrations of oxygen atoms (nitro group) are located in greatest. The calculated thermodynamic properties show that the Debye temperature, constant volume–specific heat, enthalpy, and entropy values increase as a function of temperature, while the free energy falls off as the temperature increases. It can be concluded that, C<sub>3</sub>N<sub>12</sub> is an effective initiating explosive as they have low-thermal conductivity, and urea nitrate is an improvised explosive. We expect this work will encourage experimental attempts to reveal the rich role of crystallized azide in the structural, vibrational, and thermodynamic properties of other triazine azide complex and organic nitrates salts in the solid–state.

## 4.5 References

# References

- [1] M.C. Payne, M.P. Teter, D.C. Allan, T.A. Arias, J.D. Joannopoulos, Rev. Mod. Phys., 64 (1992) 1045–1097.
- [2] A. Tkatchenko, M. Scheffler, Phys. Rev. Lett., 102 (2009) 073005(1-4).
- [3] D. Hamann, M. Schluter, C. Chiang, Phys. Rev. Lett., 43 (1979) 1494–1497.
- [4] C. Mailhiot, L. Yang, A. McMahan, Phys. Rev. B, 46 (1992) 14419–14435.
- [5] J.A. Ciezak, B.M. Rice, Polymeric Nitrogen: The Ultimate, Green High Performing Energetic Material, U.S. Army Research Laboratory, 2006.
- [6] C. Sun, C. Zhang, C. Jiang, Nat. Commun., 9 (2018) 1269(1-7).
- [7] A. Katritzky, E. Scriven, J. Am. Chem. Soc., 132 (2010) 12156-12156.

120 REFERENCES

[8] M. V. Huynh, M.D. Coburn, T.J. Meyer, M. Wetzler, Proc. Natl. Acad. Sci. U S A, 103 (2006) 10322–10327.

- [9] H.D. Fair, R.F. Walker, Energetic materials: Physics and Chemistry of the Inorganic azides, Plenum Press, New York, 1977.
- [10] D. Kumar, A.J. Elias, Resonance, 24 (2019) 1253-1271.
- [11] L.M. Foroughi, R.A. Wiscons, D.R. Du Bois, A.J. Matzger, Chem. Commun., 56 (2020) 2111-2114.
- [12] G.G. Edward, Chem. Mater., 12 (2000) 3906-3912.
- [13] E. Kroke, M. Schwarz, Adv. Mater., 11 (1999) 158-161.
- [14] R. Meyer, Explosives, VCH, New York, (1987) 70.
- [15] D. Laniel, L.E. Downie, J.S. Smith, D. Savard, M. Murugesu, S. Desgreniers, J. Chem. Phys., 141 (2014) 234506(1–10).
- [16] L.E. Downie, Pathways to Recovering Single-Bonded Nitrogen at Ambient Conditions: High Pressure Studies of Molecular and Ionic Azides, Canada, 2010.
- [17] E. Ott, E. Ohse, E. Ber, Dtsch. Chem. Ges., 54 (1921) 179.
- [18] E. Kessenich, T.M. Klapötke, J. Knizek, H. Noth, A. Schulz, Eur. J. Inorg. Chem., 1998 (1998) 2013–2016.
- [19] T.P. Forbes, S.T. Krauss, G. Gillen, Trends Anal. Chem., 131 (2020) 116023.
- [20] S. Li, Q. Li, K.Wang, M.Zhou, X. Huang, J. Liu, Ke. Yang, B. Liu, T. Cui, G. Zou, Bo. Zou, J. Phys. Chem. C, 117 (2013) 152-–159.

- [21] R. I. Hiyoshi and J. Nakamura, "Explosion Properties of Urea Nitrate and its Analysis", Proc. 6th Int. Symp. Anal. Det. Expl. Prague, CZ, 1998, paper 15.
- [22] R. I. Hiyoshi and J. Nakamura, "Explosion Properties of Urea Nitrate", Kayaku Gakkaishi, 61 (2000) 120–123.
- [23] R.I. Hiyoshi, T.B. Brill, Y. Kohno, O. Takahashi, K. Saito, "Experimental and Computational Study of the Thermal Decomposition of Uronium Nitrate (Urea Nitrate)" 12th Int.Detonation Symp. (2002)11-16.
- [24] J. C. Oxley, J. L. Smith, V. Sravanthi, A.C. Brown, G. Zhang, D.S. Swanson, J. Canino, Propellants Explos. Pyrotech., 38 (2013) 335–344.
- [25] D. Price, "Contrasting Patterns in the Behavior of High Explosives", Eleventh Symp. (Int) Combustion, The Combustion Institute, Pittsburgh, PA, pp. 693-702, 1967.
- [26] Z. Wu, K. Rajiv K., N. Aiichiro, P. Vashishta, J.Chem.Phy., 134 (2011) 204509(1-10).
- [27] J.J. Haycraft, L.L. Stevens, C.J. Eckhardta, J.Appl.Phys., 100 (2006) 053508(1-9).
- [28] Z. Sheng-Hai, Q. Han, Z. Wei, C. Ying-Meng, J. Xu-Yang, W. Yu-Hang, L. Fu-Sheng, T. Bin, L. Qi-Jun, J. Mol. Model, 25 (2019) 182(1–16).
- [29] K. Ramesh Babu, G. Vaitheeswaran, Chem. Phys. Lett., 533 (2012) 35–39.
- [30] K. Ramesh Babu, G. Vaitheeswaran, Chem. Phys. Lett., 586 (2013) 44–50.
- [31] G. Vaitheeswaran, K. Ramesh Babu, J. Chem. Sci., 124 (2012) 1391–1398.
- [32] N. Yedukondalu, G. Vaitheeswaran, P. Anees, M.C. Valasakumar, Phy. Chem. Chem. Phys., 17 (2015) 29210–29225.

122 REFERENCES

[33] D. Li, P. Zhu, J. Jiang, D. Xu, R. Liu, X. Wang, Q. Cui, H. Zhu, J.Phys. Commun., 1 (2017) 025002(0–8).

- [34] J. Xuehai, X. Heming, J. Guangfu, Sci. Bull., 47 (2002) 1180-1183.
- [35] B. Adivaiah, E. Narsimha Rao, G. Vaitheeswaran, J. Phys. Condens. Matter, 31 (2019) 475402(1–14).
- [36] A. Hu, F. Zhang. J. Phys. Condens. Matter, 22 (2010) 505402(1-5)
- [37] S. Appalakondaiah, G. Vaitheeswaran, S. Lebegue, Chem. Phy. Lett., 605 (2014) 10–15.
- [38] J.E. Worsham, W.R. BUSING, Acta Cryst., B25 (1969) 572.
- [39] V.A. Kulakov, R.G. Zhbankov, V.M. Yurchenko, L.S. Galbraikh, J. Appl. Spectrosc., 47 (1987) 797–801.
- [40] J.C. Oxley, J.L. Smith, S. naik, J. Moran, J. Energ. Mater., 27 (2009) 17-39.
- [41] I.V. Tokmakov, S. Alavi, D.L. Thompson, J. Phys. Chem. A, 110 (2006) 2759–2770.
- [42] Y. Kohno, O. Takahashi, R.I. Hiyoshi, J. Nakamura, and K. Saito, J. Phys. Chem. A, 33 (2003) 6444–6450.
- [43] S. J. Shear, G. C. Turrell, J. I. Bryant, R. L. Brooks, J. Chem. Phys., 48 (1968) 1138–1144.
- [44] S.J. Clark, M.D. Segall, C.J. Pickard, P.J. Hasnip, M.J. Probert, K. Refson, M.C. Payne, Z. Kristallogr., 220 (2005) 567–570.
- [45] J.P. Perdew, K. Burke, M. Ernzerhof, Phys. Rev. Lett., 77 (1996) 3865–3868.
- [46] J.P. Perdew, K. Burke, Y. Wang, Phys. Rev., B 54 (1996) 16533–16539.

- [47] H.J. Monkhorst, J.D. Pack, Phys. Rev. B, 13 (1976) 5188-5192.
- [48] R. Fletcher, Practical Methods of Optimization, Wiley, New York, 1980.
- [49] A. Togo, I. Tanaka, Scr. Mater., 108 (2015) 1-5.
- [50] S. Baroni, P. Giannozzi, A. Testa, Phys. Rev. Lett., 58 (1987) 1861-1864.
- [51] X. Gonze, J.P. Vigneron, Phys. Rev. B 39 (1989) 13120-13128.
- [52] X. Gonze, D.C. Allan, M.P. Teter, Phys. Rev. Lett., 68 (1992) 3603–3606.
- [53] L. Changyol, X. Gonze, Phys. Rev. B, 51 (1955) 8610–8613.
- [54] V. Mankad, N. Rathod, S.D. Gupta, S.K. Gupta, P.K Jha, Mater. Chem. Phys., 129 (2011) 816–822.
- [55] E. Knaggs, Nature 135 (1935) 268.
- [56] I.R. Shein, V.L. Kozhevnikov, A.L. Ivanovskii, Solid State Sci., 10 (2008) 217–225.
- [57] P. Giannozzi, S. Gironcoli Phys. Rev. B, 43 (1991) 7231–7242.
- [58] X. Gonze, Phys. Rev. A, 52 (1995) 1086–1094.
- [59] X. Gonze, C. Lee. Phys. Rev. B, 55 (1997) 10355–10368.
- [60] S. Baroni, S. Gironcoli, A. Corso, Rev. Mod. Phys., 73 (2001) 515–561.
- [61] F. Ortmann, F. Bechstedt, W.G. Schmidt, Phys. Rev. B, 73 (2006) 205101(1-10).
- [62] E. Narsimha Rao and G. Vaitheeswaran, J. Phys. Chem. C, 123 (2019) 10034–10050.
- [63] E. Narsimha Rao, G. Vaitheeswaran, A. H. Reshak and S. Auluck, RSC Adv., 6 (2016) 99885–99897.

124 REFERENCES

- [64] E. Deligoz, U. F. Ozyar, H. B. Ozisik, Philos. Mag., 96 (2016) 1712-1723.
- [65] N.L. Lethole, P.E. Ngoepe, H.R. Chauke, Comput. Cond. Matt., 22 (2020) 00437(1-8)
- [66] R. Matya, J. Pachman, Primary Explosives Springer Heidelberg, New York Dordrecht London, 2017.
- [67] Z.D. Lawless, M.L. Hobbs, M.J. Kaneshige J. Energ. Mater., 38 (2020) 214–239.
- [68] B. Adivaiah, E. Narsimha Rao, T. Atahar Parveen, G. Vaitheeswaran, J. Phys. Chem. Solids, 122 (2018) 268–277.
- [69] N. Mounet, N. Marzari, Phys. Rev. B, 71 (2005) 205214 (1-14).
- [70] S. Vyazovkin, K. Chrissafis, M.L. Di Lorenzo, N. Koga, M. Pijolat, B. Roduit, N. Sbirrazzuoli, J.J. Suñol, Thermochimica Acta, 590 (2014) 1—23.
- [71] Y. Zhang, H. Wu, K. Xu, F. Zhao, J. Therm. Anal. Calorim., 116 (2014) 817–823.

Chapter **2** 

# DFT calculations on structural and vibrational properties of dihydroxylammonium 5,5'-bis(3-nitro-1,2,4-triazolate-1 N-oxide) (MAD-XI).

In this chapter, the vibrational and thermodynamic properties of MAD-XI crystal are presented by using density functional theory within the GGA-PW91 + OBS approximation. The calculated lattice parameters are compared with the experimental values. The vibrational mode assignments are described in a detailed way. The high-frequency region shows symmetric and asymmetric stretching of N-H, O-H bonds. We have presented the phonon dispersion and partial phonon density of states for MAD-XI crystalline solid by using DFPT. The absence of imaginary phonon frequencies in the Brillouin zone reveals the dynamical stability of MAD-XI crystalline solid. The individual atomic contribution in the vibrational modes is displayed in the partial phonon density of states. The thermodynamic properties such as enthalpy (E), entropy (S), free energy (F), heat capacity ( $C_V$ ), and the Debye temperature ( $\Theta_D$ ) were presented in detail. We believe that this work will encourage an experimental attempts to reveal the behavior of bis 1,2,4-triazoles and N-oxide derivatives.

### 5.1 Introduction

Energetic materials (explosives, propellants, and pyrotechnics) are utilized broadly for both civilian and military applications [1-3]; therefore, it is necessary to explore and understand the behavior of these materials. Insensitive high explosives (IHE) have high detonation properties, which means that they have high density, high detonation velocity, and excellent security properties. The last aspect also ensures that the response to external exigencies such as friction, shock, impact, heat, etc. [1, 2, 4] are met with amiable responses. This makes insensitive high explosives (IHE), which are highly favored for research. The Nitrogen-rich azole derivatives show great interest to making use in newer primary and secondary explosives considering their high heats of formation, high density, improved thermal stability, and low sensitivities toward external stimuli [5–10]. Recently, various favorable high nitrogen-containing energetic materials have been synthesized that show great applications as insensitive high-performance explosives, such as 4amino-3,5-dinitropyrazole (ADNP), 2,6-diamino-3,5-dinitropyrazine-N-oxide (LLM-105), dihydroxylammonium 5,5'-bistetrazole-1,1'-diolate (TKX-50), and 5,5'-dinitro-2H,2H'-3,3'-bi-1,2,4-triazole (DNBT) and dihydroxylammonium 5,5'-bis(3-nitro-1,2,4-triazolate-1 N-oxide) (MAD-XI)[5, 11–13].

The energetic material MAD-XI is one of the most widely used military explosives and thus has been subject to a large number of studies [12–14]. The earlier reports from Fischer. et al. [7] suggested that MAD-XI has the lowest sensitivities and has higher density, detonation pressure, and detonation velocity than TNT and RDX.

The compound crystallizes in the monoclinic space group *P21/c* with two molecules in the unit cell. The MAD-XI has different inter-/intramolecular interactions, including strong hydrogen bonds (N-H···N, N-H···O, O-H···N, and O H···O) between close by molecules of the N-oxide anion and the hydroxylammonium cations [15].

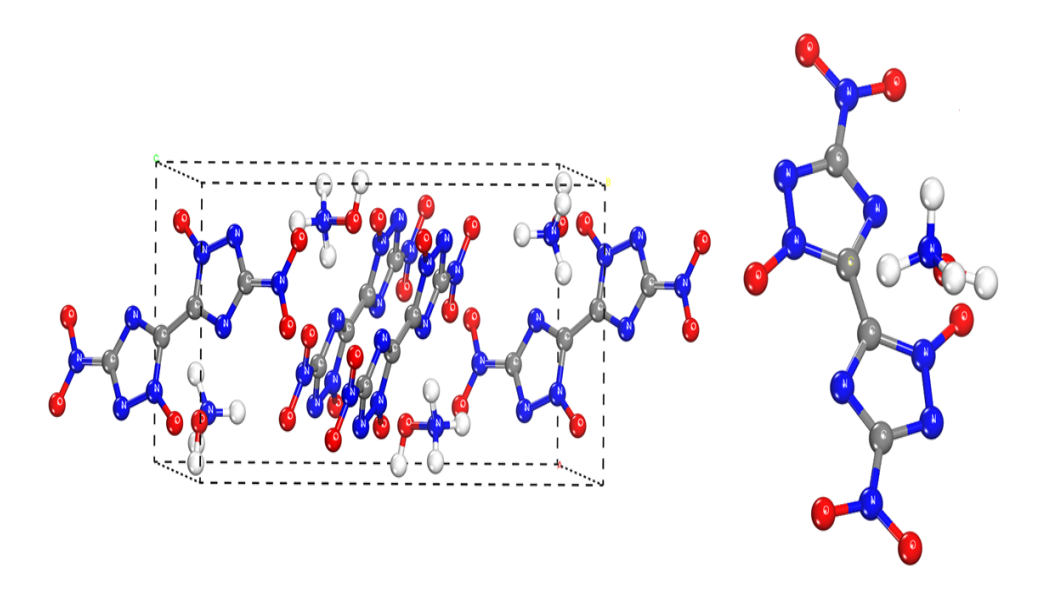


Figure 5.1: Unit cell and single molecule of the MAD-XI crystal. Here, Blue color represents N atoms, red color O atoms, white color H atoms, and gray represents C atoms.

The previous experimental reports suggest MAD-X1 material could serve as an insensitive RDX replacement in energetic formulations [12]. Thermodynamically stable up to 513 K and thermally decomposed by 533 K at ambient pressure, and the melting point is 607–634 K [16, 17]. So far, there are no experimental and theoretical studies on vibrational and thermodynamic properties of MAD-XI. Hence, in this study, we attempt, for the first time the structural, vibrational, and thermodynamic properties of newly synthesized material MAD-X1 crystal from a theoretical point of view on the lines of [16, 18, 19]. The vibrational modes and their corresponding peak frequencies of infrared spectra are critically analyzed, and thermodynamic properties MAD-X1 crystal were calculated within the harmonic approximation.

### 5.2 Materials and methods

#### 5.2.1 Crystal structure

The MAD-XI molecule contains two ammonium hydroxide groups, two nitro groups, and one pyrazine ring. The MAD-XI crystal under the space group *P21/c* has monoclinic structure with two molecules in the unit cell. The crystal structure is presented in figure 5.1, and it is obvious that there is a twisting angle between the nitro group and chemical C-NO<sub>2</sub> in the axis. The unit cell has mixed inter-/intramolecular interactions, including strong hydrogen bonds (N-H···N, N-H···O, O-H···N, and O-H···O) between close by molecules of the N-oxide anion and the hydroxylammonium cations [20].

As presented in Table 5.1, the lattice parameters of MAD-XI are compared with experimental analyses. In the case of LDA functional, the unit cell volume is 8.57% which is lower than the observed value. Taking the pure GGA functional, the obtained unit cell volume is larger by 32.01%. These differences can be minimized by the incorporation of dispersion corrections[21]. The PW91+ Ortmann Bechstedt and Schmidt (OBS) [21] approximation is found close to the experimental results with 3.59% deviation. Hence, we have used PW91 + OBS functional to compute the vibrational and thermodynamic properties of MAD-XI crystal.

# 5.2.2 Computational details

Ab initio calculations were employed by using the density functional theory [22]. The Perdew-Burke-Ernerho(PBE) within generalized gradient approximation (GGA) [23, 24] was used. The parameter-free dispersion correction GGA-PW91+OBS [25] method were used to describe long-range van der Waals interactions. The Norm-conserving pseudo-potentials [26] were performed to describe the ion-electron interactions for C (2s2 2p2), H (1s1), N (2s2 2p3) and O (2s2 2p4). Integrations in the Brillouin zone are achieved using special k points generated

Table 5.1: Lattice parameters(Å) and unit cell volume (Å<sup>3</sup>) of the MAD-XI crystal calculated at the LDA, GGA, GGA + OBS and experimental values [12] with error percentage.

Parameter	LDA	PW91	PW91 + OBS	Expt. <sup>a</sup>
a (Å)	7.091	7.367	7.229	7.307
b (Å)	5.354	5.269	5.338	5.243
c (Å)	13.283	16.039	14.036	14.403
$V(Å^3)$	357.06 (-8.5%)	527.32 (32.01%)	390.44 (3.59%)	399.44

LDA, Local density approximation; PBE, Perdew-Burke-Ernzerhof.

<sup>a</sup>Ref. [12]

with  $5 \times 6 \times 2$  mankhorst-pack meshes [27]. The plane-wave basis set with an energy cutoff of 1100 eV is used for MAD-XI, to expand the valence electronic wave functions. The self-consistent convergence of the total energy was used at,  $0.5 \times 10^{-6}$  eV/atom. The geometry optimizations of the MAD-XI unit cell were carried out by using the Broyden - Fletcher- Goldfarb-Shanno algorithm (BFGS) [28].

The phonon dispersion curves and partial phonon density of states of MAD-XI are accomplished using the Density Functional Perturbation Theory (DFPT) within the linear-response method[29–32] at (GGA + OBS) level. Using the quasi-harmonic approximation[33, 34] we have calculated the Debye temperature, heat capacity, and other thermodynamic properties.

## 5.3 Results and discussion

# 5.3.1 Zone center IR spectra

The MAD-XI primitive crystal structure (space group: P21/c) contains 60 atoms which, leads to 180 normal modes, Among 3 acoustic modes and 177 optical modes. From which 90 ( $A_u$ ,  $B_u$ ) modes IR active, 90 ( $A_g$ ,  $B_g$ ) are Raman active. The zone-center normal modes are distributed over irreducible symmetry representations as follows:  $\Gamma_{total} = 45B_u + 45 A_u + 45 B_g + 45 A_g$ . The calculated

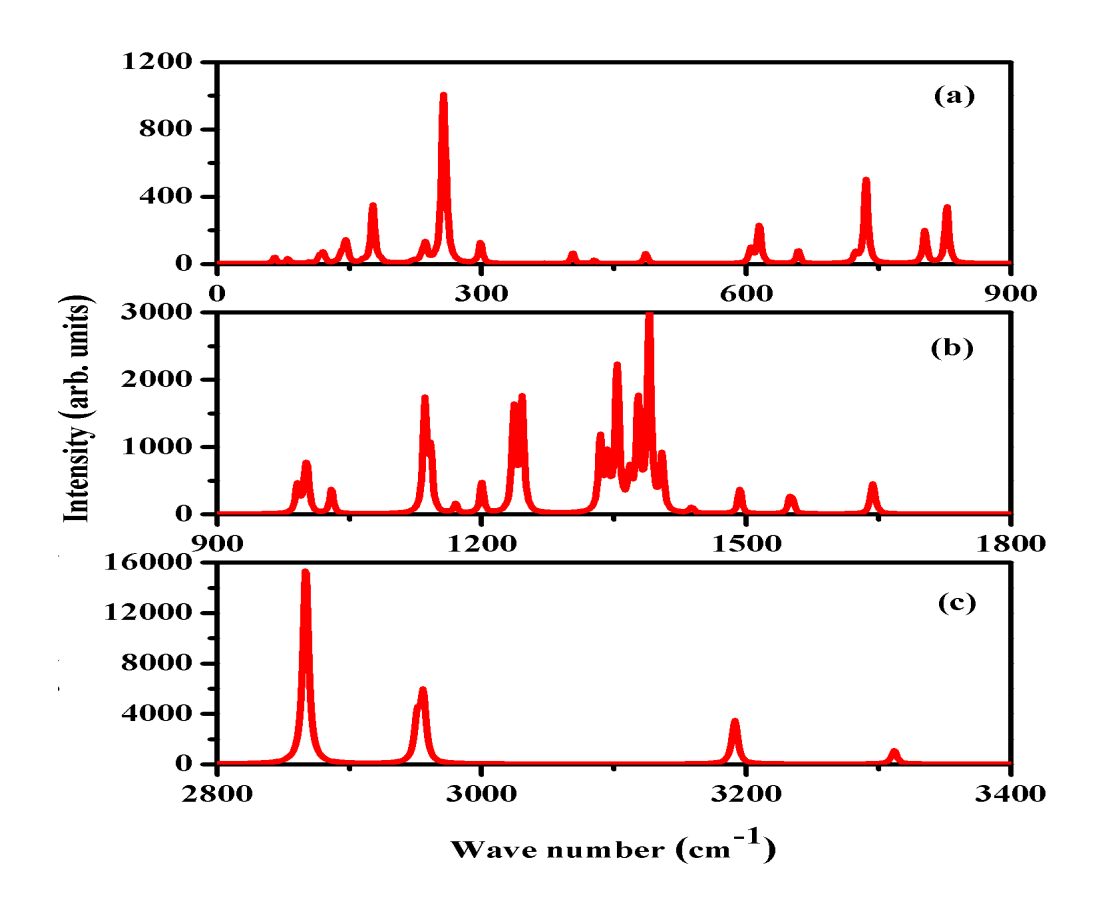


Figure 5.2: Calculated infrared spectra of MAD-XI at the optimized equilibrium volume in the  $0-900~\rm cm^{-1}$  range (fig(a)),  $900-1800~\rm cm^{-1}$  (fig(b)), and  $2800-3400~\rm cm^{-1}$  ((fig(c)).

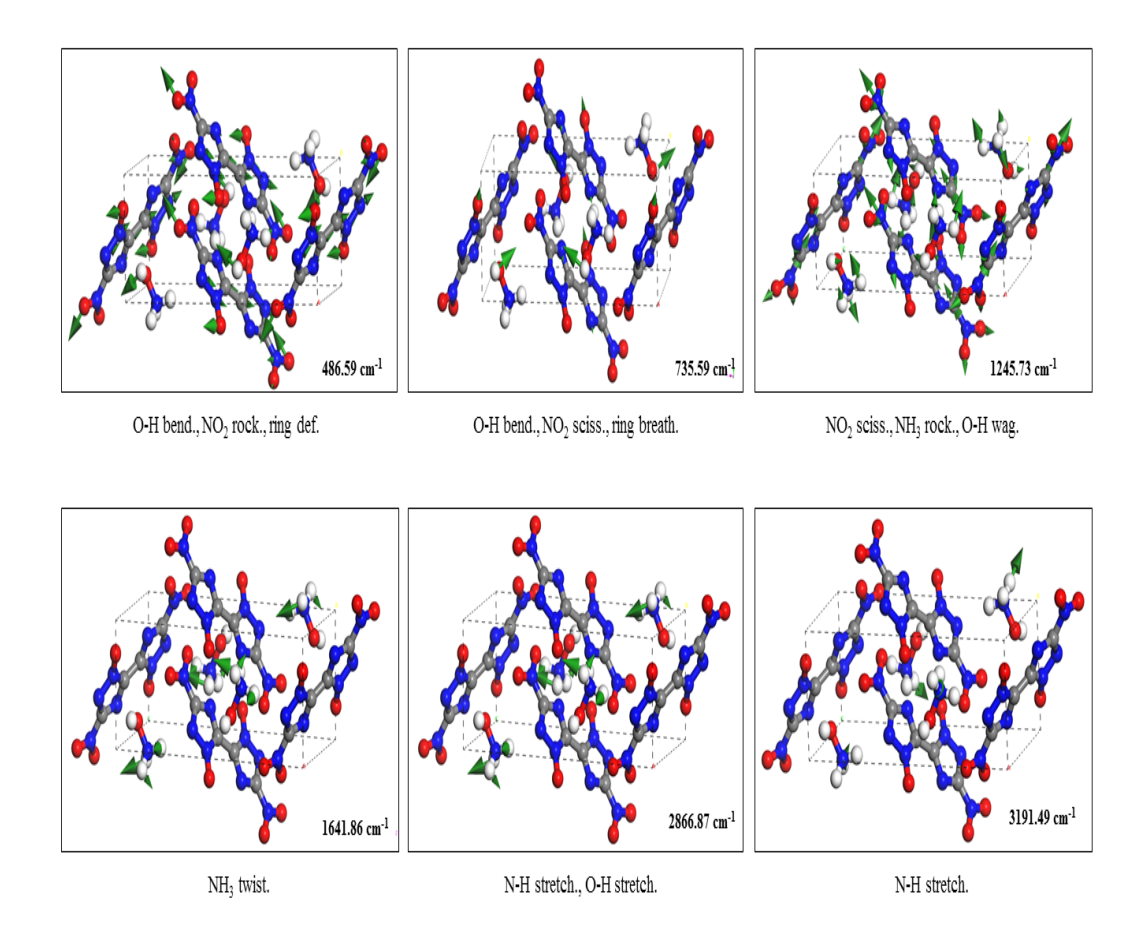


Figure 5.3: Normal modes of MAD-XI corresponding to the calculated IR absorption lines at 486.59, 735.59, 1245.73, 1641.86, 2866.87, and 3191.49 cm<sup>-1</sup> with their respective assignments..

Table 5.2: Calculated normal modes infrared frequencies (0-400  $\rm cm^{-1}$ ) with symmetry assignment for the MAD-XI crystal using the DFT GGA + OBS approach.

M5         55.67         B <sub>E</sub> Raman rotational rotational rotational mortal rotational mortal rotational mortal rotational mortal mor	Mode number	Calculated frequency (cm <sup>-1</sup> )	Symmetry	Mode	Assignment
M7         65.15 $A_u$ IR         translational           M9         78.43 $B_g$ Raman         rotational           M10         78.87 $A_g$ Raman         rotational           M11         80.43 $B_g$ IR         translational           M12         83.89 $B_g$ Raman         rotational           M13         87.37 $A_u$ IR         rotational           M14         103.80 $B_g$ Raman         rotational           M15         106.41 $A_g$ Raman         translational           M16         115.21 $A_u$ IR         translational           M17         116.35 $B_g$ IR         translational           M18         120.29 $A_u$ IR         translational           M19         121.67 $A_g$ Raman         translational           M20         123.09 $B_g$ Raman         translational           M21         129.40 $A_g$ Raman         translational           M22         129.89 $B_g$ IR         t		41.55	$A_u$	IR	rotational
M7         65.15 $A_w$ IR         translational           M9         78.43 $B_z$ Raman         rotational           M10         78.87 $A_z$ Raman         rotational           M11         80.43 $B_u$ IR         translational           M12         83.89 $B_z$ Raman         rotational           M13         87.37 $A_u$ IR         translational           M14         103.80 $B_u$ IR         rotational           M15         106.41 $A_z$ Raman         translational           M16         115.21 $A_u$ IR         translational           M17         116.35 $B_y$ IR         translational           M18         120.29 $A_u$ IR         translational           M19         121.67 $A_z$ Raman         translational           M20         123.09 $B_z$ Raman         translational           M21         129.40 $A_z$ Raman         translational           M22         129.89 $B_u$ IR         t		55.67	$B_{g}$	Raman	rotational
M7         65.15 $A_w$ IR         translational           M9         78.43 $B_z$ Raman         rotational           M10         78.87 $A_z$ Raman         rotational           M11         80.43 $B_u$ IR         translational           M12         83.89 $B_z$ Raman         rotational           M13         87.37 $A_u$ IR         translational           M14         103.80 $B_u$ IR         rotational           M15         106.41 $A_z$ Raman         translational           M16         115.21 $A_u$ IR         translational           M17         116.35 $B_y$ IR         translational           M18         120.29 $A_u$ IR         translational           M19         121.67 $A_z$ Raman         translational           M20         123.09 $B_z$ Raman         translational           M21         129.40 $A_z$ Raman         translational           M22         129.89 $B_u$ IR         t	M6		$A_g$	Raman	rotational
$ \begin{array}{c ccccccccccccccccccccccccccccccccccc$		65.15	$A_u$	IR	translational
M10         78.87         Ag         Raman         rotational           M11         80.43         Bg         Raman         rotational           M12         83.89         Bg         Raman         rotational           M13         87.37         Au         IR         rotational           M14         103.80         Bg         IR         rotational           M15         106.41         Ag         Raman         translational           M16         115.21         Ag         IR         translational           M17         116.35         Bg         IR         translational           M18         120.29         Ag         IR         translational           M19         121.67         Ag         Raman         translational           M20         123.09         Bg         Raman         translational           M21         129.40         Ag         Raman         translational           M22         129.89         Bg         IR         translational           M23         130.72         Bg         Raman         translational           M24         133.87         Bg         Raman         translational	M8	66.25			translational
M10         78.87         Ag         Raman         rotational           M11         80.43         Bg         Raman         rotational           M12         83.89         Bg         Raman         rotational           M13         87.37         Au         IR         rotational           M14         103.80         Bg         IR         rotational           M15         106.41         Ag         Raman         translational           M16         115.21         Ag         IR         translational           M17         116.35         Bg         IR         translational           M18         120.29         Ag         IR         translational           M19         121.67         Ag         Raman         translational           M20         123.09         Bg         Raman         translational           M21         129.40         Ag         Raman         translational           M22         129.89         Bg         IR         translational           M23         130.72         Bg         Raman         translational           M24         133.87         Bg         Raman         translational		78.43	$B_{g}$	Raman	
M12         83.89         B <sub>E</sub> Raman rotational NII           M13         87.37         A <sub>H</sub> IR rotational IR rotational IR rotational IR rotational IR IR rotational IR IR rotational III           M15         106.41         A <sub>E</sub> Raman translational translational IR Tr	M10	78.87	$A_g$	Raman	rotational
M13         87.37 $A_n$ IR         rotational           M14         103.80 $B_n$ IR         rotational           M15         106.41 $A_g$ Raman         ranslational           M16         115.21 $A_n$ IR         translational           M17         116.35 $B_n$ IR         translational           M18         120.29 $A_n$ IR         translational           M19         121.67 $A_g$ Raman         translational           M20         123.09 $B_g$ Raman         translational           M21         129.40 $A_g$ Raman         translational           M22         129.89 $B_n$ IR         translational           M23         130.72 $B_g$ Raman         translational           M24         133.87 $B_n$ IR	M11			IR	translational
$\begin{array}{c ccccccccccccccccccccccccccccccccccc$					rotational
M15         106.41 $A_g$ Raman IT translational M16         I15.21 $A_u$ IR translational IT transla					
M16         115.21 $A_u$ IR         translational           M17         116.55 $B_u$ IR         translational           M18         120.29 $A_u$ IR         translational           M19         121.67 $A_g$ Raman         translational           M20         123.09 $B_g$ Raman         translational           M21         129.40 $A_g$ Raman         translational           M22         129.89 $B_u$ IR         translational           M23         130.72 $B_g$ Raman         translational           M24         133.87 $B_u$ IR         translational           M25         140.60 $A_u$ IR         translational           M25         140.60 $A_u$ IR         translational           M27         145.10 $A_u$ IR         translational           M27         145.10 $A_u$ IR         translational           M29         146.97 $B_u$ IR         translational           M31         169.33 $A_g$ Raman					
M17         116.35 $B_u$ IR         translational           M18         120.29 $A_u$ IR         translational           M19         121.67 $A_g$ Raman         translational           M20         123.09 $B_g$ Raman         translational           M21         129.40 $A_g$ Raman         translational           M22         129.89 $B_u$ IR         translational           M23         130.72 $B_g$ Raman         translational           M24         133.87 $B_u$ IR         translational           M25         140.60 $A_u$ IR         translational           M26         142.07 $A_g$ Raman         translational           M27         145.10 $A_g$ Raman         translational           M28         145.85 $B_g$ Rama					
M18         120.29         A <sub>u</sub> IR         translational translational translational translational           M20         123.09         B <sub>g</sub> Raman translational           M21         129.40         A <sub>g</sub> Raman translational           M22         129.89         B <sub>u</sub> IR         translational           M24         133.87         B <sub>u</sub> IR         translational           M25         140.60         A <sub>u</sub> IR         translational           M26         142.07         A <sub>g</sub> Raman         translational           M27         145.10         A <sub>u</sub> IR         translational           M28         145.85         B <sub>g</sub> Raman <t< td=""><td></td><td></td><td></td><td></td><td></td></t<>					
M19         121.67 $A_g$ Raman translational translational M20         123.09 $B_g$ Raman translational translational translational translational M21         M21         129.40 $A_g$ Raman translational translational translational translational M22         129.89 $B_g$ Raman translational translational translational M23         M23         130.72 $B_g$ Raman translational translational translational M24         133.87 $B_g$ IR         translational translational translational M25         140.60 $A_n$ IR         translational translational translational M26         142.07 $A_g$ Raman translational translational M27         M45.10 $A_n$ IR         translational translational M28         145.85 $B_g$ Raman translational translational M29         146.97 $B_n$ IR         translational translational Translational M30         165.11 $B_g$ IR         translational Translational Translational M31         169.33 $A_g$ Raman translational Translational Translational M33         177.90 $B_g$ Raman translational Translational Translational Translational M34         178.18 $A_g$ Raman rotational Translational Translational M35         181.41 $A_g$ Raman rotational Translational Translational M36         185.20 $A_n$ IR <td></td> <td></td> <td></td> <td></td> <td></td>					
M20         123.09 $B_g$ Raman translational translational translational translational translational translational M22         129.89 $B_u$ IR translational translational translational translational M23         130.72 $B_g$ Raman translational translational translational M24         133.87 $B_u$ IR translational translational translational translational translational M26         142.07 $A_g$ Raman translational translational M27         145.10 $A_u$ IR translational translational translational M28         145.85 $B_g$ Raman translational M29         146.97 $B_u$ IR translational translational M30         165.11 $B_u$ IR translational translational M31         169.33 $A_g$ Raman translational translational translational M32         176.96 $B_u$ IR translational translational translational Translational M34         178.18 $A_g$ Raman translational translational Translational M35         181.41 $A_g$ Raman translational Translational Translational M36         185.20 $A_u$ IR translational Translational M38         194.20 $A_g$ Raman rotational Translational M39         197.39 $B_g$ Raman rotational Translational M41         M41         219.16 $A_u$ IR rotational RM41         M42         223.08 $B_g$ Raman rotational RM42         M43         232.27 $A_u$ IR rotational RM44         M44         236.06 $B_g$ IR rotational RM49         M45         256.45 $B_u$ IR Raman rotational RM49         <					
M21         129.40 $A_g^g$ Raman translational translational M22         129.89 $B_g$ IR translational translational translational translational translational translational M24         133.87 $B_g$ IR translational translational translational translational M25         140.60 $A_u$ IR translational translational translational M26         142.07 $A_g$ Raman translational translational translational M27         145.10 $A_u$ IR translational translational translational M28         145.85 $B_g$ Raman translational translational translational M29         146.97 $B_u$ IR translational translational translational M30         165.11 $B_u$ IR translational translational translational translational M31 $A_g$ Raman translational translational translational M32 $A_g$ Raman translational translational translational M33 $A_g$ Raman rotational Translational Translational M35 $A_g$ Raman rotational Translational Translational M35 $A_g$ Raman rotational Translational Translational M36 $A_g$ Raman rotational Raman rotational Raman rotational M37 $A_g$ Raman rotational Raman rotational Raman rotational Raman Ram			$A_g$		
M22         129.89 $B_u$ IR         translational           M23         130.72 $B_g$ Raman         translational           M24         133.87 $B_u$ IR         translational           M25         140.60 $A_u$ IR         translational           M26         142.07 $A_g$ Raman         translational           M27         145.10 $A_u$ IR         translational           M28         145.85 $B_g$ Raman         translational           M29         146.97 $B_u$ IR         translational           M30         165.11 $B_u$ IR         translational           M31         169.33 $A_g$ Raman         translational           M32         176.96 $B_u$ IR         translational           M33         177.90 $B_g$ Raman         translational           M34         178.18 $A_g$ Raman         rotational           M35         181.41 $A_g$ Raman         rotational           M36         185.20 $A_u$ IR			$B_{g}$		
M23         130.72 $B_g$ Raman translational translational M24         133.87 $B_u$ IR translational translational translational translational M25         140.60 $A_u$ IR translational translational translational M26         142.07 $A_g$ Raman translational translational Translational M27 $A_u$ IR translational translational translational M28 $A_u$					
M24         133.87 $B_u$ IR         translational           M25         140.60 $A_u$ IR         translational           M26         142.07 $A_g$ Raman         translational           M27         145.10 $A_u$ IR         translational           M28         145.85 $B_g$ Raman         translational           M29         146.97 $B_u$ IR         translational           M30         165.11 $B_u$ IR         translational           M31         169.33 $A_g$ Raman         translational           M32         176.96 $B_u$ IR         translational           M33         177.90 $B_g$ Raman         translational           M34         178.18 $A_g$ Raman         translational           M35         181.41 $A_g$ Raman         rotational           M36         185.20 $A_u$ IR         translational           M37         187.68 $B_g$ Raman         rotational           M38         194.20 $A_g$ Raman </td <td></td> <td></td> <td></td> <td></td> <td></td>					
M25140.60 $A_u$ IRtranslationalM26142.07 $A_g$ RamantranslationalM27145.10 $A_u$ IRtranslationalM28145.85 $B_g$ RamantranslationalM29146.97 $B_u$ IRtranslationalM30165.11 $B_u$ IRtranslationalM31169.33 $A_g$ RamantranslationalM32176.96 $B_u$ IRtranslationalM33177.90 $B_g$ RamantranslationalM34178.18 $A_g$ RamantranslationalM35181.41 $A_g$ RamanrotationalM36185.20 $A_u$ IRtranslationalM37187.68 $B_g$ RamanrotationalM38194.20 $A_g$ RamanrotationalM39197.39 $B_g$ RamanrotationalM40202.56 $B_g$ RamanrotationalM41219.16 $A_u$ IRtranslationalM42223.08 $B_u$ IRtranslationalM43232.27 $A_u$ IRrotationalM44236.06 $B_u$ IRrotationalM45256.45 $B_u$ IRrotationalM46259.81 $A_u$ IRrotationalM47260.49 $B_g$ RamanrotationalM50294.63 $B_g$ RamanrotationalM51296.39 $A_g$ </td <td></td> <td></td> <td></td> <td></td> <td></td>					
M26142.07 $A_g$ RamantranslationalM27145.10 $A_u$ IRtranslationalM28145.85 $B_g$ RamantranslationalM29146.97 $B_u$ IRtranslationalM30165.11 $B_u$ IRtranslationalM31169.33 $A_g$ RamantranslationalM32176.96 $B_u$ IRtranslationalM33177.90 $B_g$ RamantranslationalM34178.18 $A_g$ RamantranslationalM35181.41 $A_g$ RamanrotationalM36185.20 $A_u$ IRtranslationalM37187.68 $B_g$ RamanrotationalM38194.20 $A_g$ RamanrotationalM39197.39 $B_g$ RamanrotationalM40202.56 $B_g$ RamanrotationalM41219.16 $A_u$ IRtranslationalM42223.08 $B_u$ IRtranslationalM43232.27 $A_u$ IRrotationalM44236.06 $B_u$ IRrotationalM45256.45 $B_u$ IRrotationalM46259.81 $A_u$ IRrotationalM47260.49 $B_g$ RamanrotationalM50294.63 $B_g$ RamanrotationalM51296.39 $A_g$ RamanrotationalM52298.46 $B_u$ </td <td></td> <td></td> <td></td> <td></td> <td></td>					
M27145.10 $A_u$ IRtranslationalM28145.85 $B_g$ RamantranslationalM29146.97 $B_u$ IRtranslationalM30165.11 $B_u$ IRtranslationalM31169.33 $A_g$ RamantranslationalM32176.96 $B_u$ IRtranslationalM33177.90 $B_g$ RamantranslationalM34178.18 $A_g$ RamantranslationalM35181.41 $A_g$ RamanrotationalM36185.20 $A_u$ IRtranslationalM37187.68 $B_g$ RamanrotationalM38194.20 $A_g$ RamanrotationalM39197.39 $B_g$ RamanrotationalM40202.56 $B_g$ RamanrotationalM41219.16 $A_u$ IRtranslationalM42223.08 $B_u$ IRtranslationalM43232.27 $A_u$ IRrotationalM44236.06 $B_u$ IRrotationalM45256.45 $B_u$ IRrotationalM46259.81 $A_u$ IRrotationalM47260.49 $B_g$ RamanrotationalM50294.63 $B_g$ RamanrotationalM51296.39 $A_g$ RamanrotationalM52298.46 $B_u$ IRrotationalM53299.17 $A_u$ <td< td=""><td></td><td></td><td></td><td></td><td></td></td<>					
M28 $145.85$ $B_g$ RamantranslationalM29 $146.97$ $B_u$ IRtranslationalM30 $165.11$ $B_u$ IRtranslationalM31 $169.33$ $A_g$ RamantranslationalM32 $176.96$ $B_u$ IRtranslationalM33 $177.90$ $B_g$ RamantranslationalM34 $178.18$ $A_g$ RamantranslationalM35 $181.41$ $A_g$ RamanrotationalM36 $185.20$ $A_u$ IRtranslationalM37 $187.68$ $B_g$ RamanrotationalM38 $194.20$ $A_g$ RamanrotationalM39 $197.39$ $B_g$ RamanrotationalM40 $202.56$ $B_g$ RamanrotationalM41 $219.16$ $A_u$ IRtranslationalM42 $223.08$ $B_u$ IRtranslationalM43 $232.27$ $A_u$ IRrotationalM44 $236.06$ $B_u$ IRrotationalM45 $256.45$ $B_u$ IRrotationalM46 $259.81$ $A_u$ IRrotationalM47 $260.49$ $B_g$ RamanrotationalM48 $265.04$ $A_g$ RamanrotationalM50 $294.63$ $B_g$ RamanrotationalM51 $296.39$ $A_g$ RamanrotationalM52 $298.46$ $B_u$ IRrotational					
M29 $146.97$ $B_u$ IRtranslationalM30 $165.11$ $B_u$ IRtranslationalM31 $169.33$ $A_g$ RamantranslationalM32 $176.96$ $B_u$ IRtranslationalM33 $177.90$ $B_g$ RamantranslationalM34 $178.18$ $A_g$ RamantranslationalM35 $181.41$ $A_g$ RamanrotationalM36 $185.20$ $A_u$ IRtranslationalM37 $187.68$ $B_g$ RamanrotationalM38 $194.20$ $A_g$ RamanrotationalM39 $197.39$ $B_g$ RamanrotationalM40 $202.56$ $B_g$ RamanrotationalM41 $219.16$ $A_u$ IRtranslationalM42 $223.08$ $B_u$ IRtranslationalM43 $232.27$ $A_u$ IRrotationalM44 $236.06$ $B_u$ IRrotationalM45 $256.45$ $B_u$ IRrotationalM46 $259.81$ $A_u$ IRrotationalM47 $260.49$ $B_g$ RamanrotationalM48 $265.04$ $A_g$ RamanrotationalM50 $294.63$ $B_g$ RamanrotationalM51 $296.39$ $A_g$ RamanrotationalM52 $298.46$ $B_u$ IRrotationalM53 $399.75$ $A_g$ Ramanrotational <tr< td=""><td></td><td></td><td></td><td></td><td></td></tr<>					
M30 $165.11$ $B_u$ IRtranslationalM31 $169.33$ $A_g$ RamantranslationalM32 $176.96$ $B_u$ IRtranslationalM33 $177.90$ $B_g$ RamantranslationalM34 $178.18$ $A_g$ RamantranslationalM35 $181.41$ $A_g$ RamanrotationalM36 $185.20$ $A_u$ IRtranslationalM37 $187.68$ $B_g$ RamanrotationalM38 $194.20$ $A_g$ RamanrotationalM39 $197.39$ $B_g$ RamanrotationalM40 $202.56$ $B_g$ RamanrotationalM41 $219.16$ $A_u$ IRtranslationalM42 $223.08$ $B_u$ IRtranslationalM43 $232.27$ $A_u$ IRrotationalM44 $236.06$ $B_u$ IRrotationalM44 $236.06$ $B_u$ IRrotationalM45 $256.45$ $B_u$ IRrotationalM46 $259.81$ $A_u$ IRrotationalM47 $260.49$ $B_g$ RamanrotationalM48 $265.04$ $A_g$ RamanrotationalM50 $294.63$ $B_g$ RamanrotationalM51 $296.39$ $A_g$ RamanrotationalM52 $298.46$ $B_u$ IRrotationalM53 $299.17$ $A_u$ IRrotationalM					
$\begin{array}{cccccccccccccccccccccccccccccccccccc$					
M32 $176.96$ $B_u$ IR         translational           M33 $177.90$ $B_g$ Raman         translational           M34 $178.18$ $A_g$ Raman         translational           M35 $181.41$ $A_g$ Raman         rotational           M36 $185.20$ $A_u$ IR         translational           M37 $187.68$ $B_g$ Raman         rotational           M38 $194.20$ $A_g$ Raman         rotational           M39 $197.39$ $B_g$ Raman         rotational           M40 $202.56$ $B_g$ Raman         rotational           M40 $202.56$ $B_g$ Raman         rotational           M41 $219.16$ $A_u$ IR         rotational           M41 $219.16$ $A_u$ IR         rotational           M42 $223.08$ $B_u$ IR         translational           M43 $232.27$ $A_u$ IR         rotational           M44 $236.06$ $B_u$					
M33         177.90 $B_g$ Raman translational           M34         178.18 $A_g$ Raman translational           M35         181.41 $A_g$ Raman rotational           M36         185.20 $A_u$ IR translational           M37         187.68 $B_g$ Raman rotational           M38         194.20 $A_g$ Raman rotational           M39         197.39 $B_g$ Raman rotational           M40         202.56 $B_g$ Raman rotational           M41         219.16 $A_u$ IR rotational           M42         223.08 $B_u$ IR translational           M43         232.27 $A_u$ IR rotational           M44         236.06 $B_u$ IR rotational           M44         236.06 $B_u$ IR rotational           M45         256.45 $B_u$ IR rotational           M46         259.81 $A_u$ IR rotational           M47         260.49 $B_g$ Raman rotational           M48         265.04 $A_g$ Raman rotational <td></td> <td></td> <td></td> <td></td> <td></td>					
M34       178.18 $A_g$ Raman       translational         M35       181.41 $A_g$ Raman       rotational         M36       185.20 $A_u$ IR       translational         M37       187.68 $B_g$ Raman       rotational         M38       194.20 $A_g$ Raman       rotational         M39       197.39 $B_g$ Raman       rotational         M40       202.56 $B_g$ Raman       rotational         M41       219.16 $A_u$ IR       rotational         M41       219.16 $A_u$ IR       rotational         M42       223.08 $B_u$ IR       rotational         M42       223.08 $B_u$ IR       rotational         M43       232.27 $A_u$ IR       rotational         M44       236.06 $B_u$ IR       rotational         M44       236.06 $B_u$ IR       rotational         M45       256.45 $B_u$ IR       rotational         M46       259.81 $A_u$ IR       rotational					
M35       181.41 $A_g$ Raman       rotational         M36       185.20 $A_u$ IR       translational         M37       187.68 $B_g$ Raman       rotational         M38       194.20 $A_g$ Raman       rotational         M39       197.39 $B_g$ Raman       rotational         M40       202.56 $B_g$ Raman       rotational         M41       219.16 $A_u$ IR       rotational         M41       219.16 $A_u$ IR       rotational         M42       223.08 $B_u$ IR       translational         M42       223.08 $B_u$ IR       rotational         M43       232.27 $A_u$ IR       rotational         M44       236.06 $B_u$ IR       rotational         M44       236.06 $B_u$ IR       rotational         M45       256.45 $B_u$ IR       rotational         M46       259.81 $A_u$ IR       rotational         M47       260.49 $B_g$ Raman       rotational			$B_{g}$		
M36       185.20 $A_u$ IR       translational         M37       187.68 $B_g$ Raman       rotational         M38       194.20 $A_g$ Raman       rotational         M39       197.39 $B_g$ Raman       rotational         M40       202.56 $B_g$ Raman       rotational         M41       219.16 $A_u$ IR       rotational         M42       223.08 $B_u$ IR       translational         M43       232.27 $A_u$ IR       rotational         M44       236.06 $B_u$ IR       rotational         M44       236.06 $B_u$ IR       rotational         M44       236.06 $B_u$ IR       rotational         M45       256.45 $B_u$ IR       rotational         M46       259.81 $A_u$ IR       rotational         M47       260.49 $B_g$ Raman       rotational         M48       265.04 $A_g$ Raman       rotational         M50       294.63 $B_g$ Raman       rotational <t< td=""><td></td><td></td><td><math>A_g</math></td><td></td><td></td></t<>			$A_g$		
M37       187.68 $B_g$ Raman       rotational         M38       194.20 $A_g$ Raman       rotational         M39       197.39 $B_g$ Raman       rotational         M40       202.56 $B_g$ Raman       rotational         M41       219.16 $A_u$ IR       rotational         M42       223.08 $B_u$ IR       translational         M43       232.27 $A_u$ IR       rotational         M44       236.06 $B_u$ IR       rotational         M44       236.06 $B_u$ IR       rotational         M45       256.45 $B_u$ IR       rotational         M46       259.81 $A_u$ IR       rotational         M47       260.49 $B_g$ Raman       rotational         M48       265.04 $A_g$ Raman       rotational         M49       291.75 $A_g$ Raman       rotational         M50       294.63 $B_g$ Raman       rotational         M51       296.39 $A_g$ Raman       rotational					
M38 $194.20$ $A_g$ Raman rotationalM39 $197.39$ $B_g$ Raman rotationalM40 $202.56$ $B_g$ Raman rotationalM41 $219.16$ $A_u$ IR rotationalM42 $223.08$ $B_u$ IR translationalM43 $232.27$ $A_u$ IR rotationalM44 $236.06$ $B_u$ IR rotationalM45 $256.45$ $B_u$ IR rotationalM46 $259.81$ $A_u$ IR rotationalM47 $260.49$ $B_g$ Raman rotationalM48 $265.04$ $A_g$ Raman rotationalM49 $291.75$ $A_g$ Raman rotationalM50 $294.63$ $B_g$ Raman rotationalM51 $296.39$ $A_g$ Raman rotationalM52 $298.46$ $B_u$ IR rotationalM53 $299.17$ $A_u$ IR rotationalM54 $300.23$ $B_g$ Raman rotationalM55 $357.51$ $B_g$ Raman rotationalM56 $358.31$ $A_g$ Raman rotationalM57 $369.47$ $A_u$ IR rotationalM58 $371.67$ $B_u$ IR rotationalM59 $392.70$ $A_g$ Raman NH4 rotational					
M39       197.39 $B_g$ Raman       rotational         M40       202.56 $B_g$ Raman       rotational         M41       219.16 $A_u$ IR       rotational         M42       223.08 $B_u$ IR       rotational         M43       232.27 $A_u$ IR       rotational         M44       236.06 $B_u$ IR       rotational         M44       236.06 $B_u$ IR       rotational         M45       256.45 $B_u$ IR       rotational         M45       256.45 $B_u$ IR       rotational         M46       259.81 $A_u$ IR       rotational         M47       260.49 $B_g$ Raman       rotational         M48       265.04 $A_g$ Raman       rotational         M49       291.75 $A_g$ Raman       rotational         M50       294.63 $B_g$ Raman       rotational         M51       296.39 $A_g$ Raman       rotational         M52       298.46 $B_u$ IR       rotational					
M40       202.56 $B_g$ Raman       rotational         M41       219.16 $A_u$ IR       rotational         M42       223.08 $B_u$ IR       rotational         M43       232.27 $A_u$ IR       rotational         M44       236.06 $B_u$ IR       rotational         M44       236.06 $B_u$ IR       rotational         M45       256.45 $B_u$ IR       rotational         M46       259.81 $A_u$ IR       rotational         M47       260.49 $B_g$ Raman       rotational         M47       260.49 $B_g$ Raman       rotational         M48       265.04 $A_g$ Raman       rotational         M49       291.75 $A_g$ Raman       rotational         M50       294.63 $B_g$ Raman       rotational         M51       296.39 $A_g$ Raman       rotational         M52       298.46 $B_u$ IR       rotational         M53       299.17 $A_u$ IR       rotational			$A_g$		
M41219.16 $A_u$ IRrotationalM42223.08 $B_u$ IRtranslationalM43232.27 $A_u$ IRrotationalM44236.06 $B_u$ IRrotationalM45256.45 $B_u$ IRrotationalM46259.81 $A_u$ IRrotationalM47260.49 $B_g$ RamanrotationalM48265.04 $A_g$ RamanrotationalM49291.75 $A_g$ RamanrotationalM50294.63 $B_g$ RamanrotationalM51296.39 $A_g$ RamanrotationalM52298.46 $B_u$ IRrotationalM53299.17 $A_u$ IRrotationalM54300.23 $B_g$ RamanrotationalM55357.51 $B_g$ RamanrotationalM56358.31 $A_g$ RamanrotationalM57369.47 $A_u$ IRrotationalM58371.67 $B_u$ IRrotationalM59392.70 $A_g$ RamanNH4 rotational			$D_g$		
M42         223.08 $B_u$ IR translational           M43         232.27 $A_u$ IR rotational           M44         236.06 $B_u$ IR rotational           M45         256.45 $B_u$ IR rotational           M46         259.81 $A_u$ IR rotational           M47         260.49 $B_g$ Raman rotational           M48         265.04 $A_g$ Raman rotational           M49         291.75 $A_g$ Raman rotational           M50         294.63 $B_g$ Raman rotational           M51         296.39 $A_g$ Raman rotational           M52         298.46 $B_u$ IR rotational           M53         299.17 $A_u$ IR rotational           M54         300.23 $B_g$ Raman rotational           M55         357.51 $B_g$ Raman rotational           M56         358.31 $A_g$ Raman rotational           M57         369.47 $A_u$ IR rotational           M58         371.67 $B_u$ IR rotational			$D_g$		
M43       232.27 $A_u$ IR       rotational         M44       236.06 $B_u$ IR       rotational         M45       256.45 $B_u$ IR       rotational         M46       259.81 $A_u$ IR       rotational         M47       260.49 $B_g$ Raman       rotational         M48       265.04 $A_g$ Raman       rotational         M49       291.75 $A_g$ Raman       rotational         M50       294.63 $B_g$ Raman       rotational         M51       296.39 $A_g$ Raman       rotational         M52       298.46 $B_u$ IR       rotational         M53       299.17 $A_u$ IR       rotational         M54       300.23 $B_g$ Raman       rotational         M55       357.51 $B_g$ Raman       rotational         M56       358.31 $A_g$ Raman       rotational         M57       369.47 $A_u$ IR       rotational         M58       371.67 $B_u$ IR       rotational					
M44       236.06 $B_{\mu}$ IR       rotational         M45       256.45 $B_{\mu}$ IR       rotational         M46       259.81 $A_{\mu}$ IR       rotational         M47       260.49 $B_{g}$ Raman       rotational         M47       260.49 $B_{g}$ Raman       rotational         M48       265.04 $A_{g}$ Raman       rotational         M49       291.75 $A_{g}$ Raman       rotational         M50       294.63 $B_{g}$ Raman       rotational         M51       296.39 $A_{g}$ Raman       rotational         M52       298.46 $B_{u}$ IR       rotational         M53       299.17 $A_{u}$ IR       rotational         M54       300.23 $B_{g}$ Raman       rotational         M55       357.51 $B_{g}$ Raman       rotational         M56       358.31 $A_{g}$ Raman       rotational         M57       369.47 $A_{u}$ IR       rotational         M58       371.67 $B_{u}$ IR					
M45 $256.45$ $B_u$ IR         rotational           M46 $259.81$ $A_u$ IR         rotational           M47 $260.49$ $B_g$ Raman         rotational           M48 $265.04$ $A_g$ Raman         rotational           M49 $291.75$ $A_g$ Raman         rotational           M50 $294.63$ $B_g$ Raman         rotational           M51 $296.39$ $A_g$ Raman         rotational           M52 $298.46$ $B_u$ IR         rotational           M53 $299.17$ $A_u$ IR         rotational           M54 $300.23$ $B_g$ Raman         rotational           M55 $357.51$ $B_g$ Raman         rotational           M56 $358.31$ $A_g$ Raman         rotational           M57 $369.47$ $A_u$ IR         rotational           M58 $371.67$ $B_u$ IR         rotational           M59 $392.70$ $A_g$ Raman					
M46       259.81 $A_u$ IR       rotational         M47       260.49 $B_g$ Raman       rotational         M48       265.04 $A_g$ Raman       rotational         M49       291.75 $A_g$ Raman       rotational         M50       294.63 $B_g$ Raman       rotational         M51       296.39 $A_g$ Raman       rotational         M52       298.46 $B_u$ IR       rotational         M53       299.17 $A_u$ IR       rotational         M54       300.23 $B_g$ Raman       rotational         M55       357.51 $B_g$ Raman       rotational         M56       358.31 $A_g$ Raman       rotational         M57       369.47 $A_u$ IR       rotational         M58       371.67 $B_u$ IR       rotational         M59       392.70 $A_g$ Raman       NH4 rotational					
M47 $260.49$ $B_g$ Raman       rotational         M48 $265.04$ $A_g$ Raman       rotational         M49 $291.75$ $A_g$ Raman       rotational         M50 $294.63$ $B_g$ Raman       rotational         M51 $296.39$ $A_g$ Raman       rotational         M52 $298.46$ $B_u$ IR       rotational         M53 $299.17$ $A_u$ IR       rotational         M54 $300.23$ $B_g$ Raman       rotational         M55 $357.51$ $B_g$ Raman       rotational         M56 $358.31$ $A_g$ Raman       rotational         M57 $369.47$ $A_u$ IR       rotational         M58 $371.67$ $B_u$ IR       rotational         M59 $392.70$ $A_g$ Raman       NH4 rotational					
M48       265.04 $A_g$ Raman       rotational         M49       291.75 $A_g$ Raman       rotational         M50       294.63 $B_g$ Raman       rotational         M51       296.39 $A_g$ Raman       rotational         M52       298.46 $B_u$ IR       rotational         M53       299.17 $A_u$ IR       rotational         M54       300.23 $B_g$ Raman       rotational         M55       357.51 $B_g$ Raman       rotational         M56       358.31 $A_g$ Raman       rotational         M57       369.47 $A_u$ IR       rotational         M58       371.67 $B_u$ IR       rotational         M59       392.70 $A_g$ Raman       NH4 rotational					
M49       291.75 $A_g$ Raman       rotational         M50       294.63 $B_g$ Raman       rotational         M51       296.39 $A_g$ Raman       rotational         M52       298.46 $B_u$ IR       rotational         M53       299.17 $A_u$ IR       rotational         M54       300.23 $B_g$ Raman       rotational         M55       357.51 $B_g$ Raman       rotational         M56       358.31 $A_g$ Raman       rotational         M57       369.47 $A_u$ IR       rotational         M58       371.67 $B_u$ IR       rotational         M59       392.70 $A_g$ Raman       NH4 rotational					
M50       294.63 $B_g$ Raman       rotational         M51       296.39 $A_g$ Raman       rotational         M52       298.46 $B_u$ IR       rotational         M53       299.17 $A_u$ IR       rotational         M54       300.23 $B_g$ Raman       rotational         M55       357.51 $B_g$ Raman       rotational         M56       358.31 $A_g$ Raman       rotational         M57       369.47 $A_u$ IR       rotational         M58       371.67 $B_u$ IR       rotational         M59       392.70 $A_g$ Raman       NH4 rotational					
M51       296.39 $A_g$ Raman       rotational         M52       298.46 $B_u$ IR       rotational         M53       299.17 $A_u$ IR       rotational         M54       300.23 $B_g$ Raman       rotational         M55       357.51 $B_g$ Raman       rotational         M56       358.31 $A_g$ Raman       rotational         M57       369.47 $A_u$ IR       rotational         M58       371.67 $B_u$ IR       rotational         M59       392.70 $A_g$ Raman       NH4 rotational					
M52       298.46 $B_u^s$ IR       rotational         M53       299.17 $A_u$ IR       rotational         M54       300.23 $B_g$ Raman       rotational         M55       357.51 $B_g$ Raman       rotational         M56       358.31 $A_g$ Raman       rotational         M57       369.47 $A_u$ IR       rotational         M58       371.67 $B_u$ IR       rotational         M59       392.70 $A_g$ Raman       NH4 rotational					
M53299.17 $A_u$ IRrotationalM54300.23 $B_g$ RamanrotationalM55357.51 $B_g$ RamanrotationalM56358.31 $A_g$ RamanrotationalM57369.47 $A_u$ IRrotationalM58371.67 $B_u$ IRrotationalM59392.70 $A_g$ RamanNH4 rotational					
M54300.23 $B_g$ Raman rotationalM55357.51 $B_g$ Raman rotationalM56358.31 $A_g$ Raman rotationalM57369.47 $A_u$ IR rotationalM58371.67 $B_u$ IR rotationalM59392.70 $A_g$ Raman NH4 rotational					
M55357.51 $B_g$ RamanrotationalM56358.31 $A_g$ RamanrotationalM57369.47 $A_u$ IRrotationalM58371.67 $B_u$ IRrotationalM59392.70 $A_g$ RamanNH4 rotational					
M56358.31 $A_g$ Raman rotationalM57369.47 $A_u$ IR rotationalM58371.67 $B_u$ IR rotationalM59392.70 $A_g$ Raman NH4 rotational					
M57 $369.47$ $A_u$ IR rotationalM58 $371.67$ $B_u$ IR rotationalM59 $392.70$ $A_g$ Raman NH4 rotational					
M58 371.67 $B_u$ IR rotational M59 392.70 $A_g$ Raman NH <sub>4</sub> rotational					
M59 392.70 $A_g$ Raman NH <sub>4</sub> rotational					
			$B_{g}$	Raman	NH <sub>4</sub> rotational

Table 5.3: Calculated normal modes infrared frequencies (400-1200  $\,\mathrm{cm}^{-1}$ ) with symmetry assignment for the MAD-XI crystal using the DFT GGA + OBS approach.

Mode number	Cal. frequency (cm <sup>-1</sup> )	Symmetry	Mode	Assignment
M61	400.82	$A_{u}$	IR	NH <sub>4</sub> Rot.
M62	403.29	$B_{u}$	IR	NH <sub>4</sub> Rot.
M63	427.64	$A_{u}$	IR	Rot.
M64	429.84	$B_u$	IR	Ring Trans., NH₄ Rot.
M65	454.88	$A_{g}$	Raman	Ring Trans., NH4 Rot.
M66	455.75	$B_{g}$	Raman	Ring Trans., NH4 Rot.
M67	458.24	$A_{\sigma}$	Raman	Ring Trans., NH <sub>4</sub> Rot.
M68	459.80	$B_{g}^{\circ}$	Raman	Ring Trans., O-H bend.
M69	485.44	$A_{u}^{\circ}$	IR	Ring Trans., O-H bend.
M70	486.58	$B_{u}$	IR	Trans., N-O-H torsion
M71	556.86	$A_g$	Raman	Trans., N-O-H torsion
M72	557.43	$B_g^{\circ}$	Raman	Trans., N-O-H torsion
M73	605.02	$B_{u}$	IR	Ring def., O-H bend, NO2 rock.
M74	606.70	$A_{\mu}$	IR	Ring def., O-H bend., NO2 rock.
M75	614.50	$A_{u}^{"}$	IR	Ring def., O-H bend., NO2 rock.
M76	615.29	$B_{u}^{"}$	IR	Ring def., O-H bend., NO2 rock.
M77	621.18	$A_g$	Raman	Ring def.
M78	622.78	$B_{\rm g}$	Raman	Ring def.
M79	658.86	$B_{u}^{g}$	IR	Ring def.
M80	659.29	$B_u$	IR	Ring def.
M81	691.40	$B_g$	Raman	Ring def., O-H bend.
M82	692.22	$A_g$	Raman	Ring def., O-H bend.
M83	703.70	$A_g$	Raman	Ring def.
M84	703.78	R R	Raman	Ring def.
M85	723.69	$B_{g}$	IR	NO <sub>2</sub> def.
M86	724.12	$A_{u}$ $R$	IR	NO <sub>2</sub> def.
M87	724.77	$B_u$	IR	
		$B_{u}$		NO <sub>2</sub> def.
M88	725.16	$A_g$	Raman	NO <sub>2</sub> def.,
M89	735.59	$A_{\mu}$	IR	Ring breath., NO <sub>2</sub> sci., O-H bend.
M90	736.41	$B_{u}$	IR	Ring breath., NO <sub>2</sub> sci., O-H bend.
M91	766.77	$A_g$	Raman	Ring breath., NO <sub>2</sub> sci., O-H bend.
M92	770.17	$B_g$	Raman	Ring breath., NO <sub>2</sub> sci., O-H bend.
M93	802.24	$B_{u}$	IR	Ring breath.,NO <sub>2</sub> sci., O-H bend.
M94	803.66	$A_{\mu}$	IR	Ring breath., NO <sub>2</sub> sci., O-H bend.
M95	827.35	$B_u$	IR	Ring breath., NO <sub>2</sub> sym stretch., O-H bend.
M96	828.20	$A_g$	Raman	Ring breath., NO <sub>2</sub> sym stretch., O-H bend.
M97	828.87	$A_{u}$	IR	Ring breath., NO <sub>2</sub> sym stretch., O-H bend.
M98	829.46	$B_{g}$	Raman	Ring breath., NO <sub>2</sub> sci., O-H bend.
M99	861.49	$A_{g}$	Raman	Ring breath., NO <sub>2</sub> sym stretch., O-H bend.
M100	861.95	$B_{\rm g}$	Raman	Ring breath., NO <sub>2</sub> sym stretch., O-H bend.
M101	990.85	$B_{\mu}$	IR	Ring breath., NO <sub>2</sub> sym stretch., O-H bend.
M102	992.02	$A_{g}$	Raman	Ring breath., NO <sub>2</sub> sym stretch., O-H bend.
M103	992.35	$A_{u}$	IR	Ring breath., O-H bend.
M104	994.22	$B_g$	Raman	ring breath, N-H wag, NO2 sym stretch.
M105	1000.09	$A_{\mu}$	IR	ring breath, N-H wag, NO2 sym stretch.
M106	1002.50	$A_{u}$	IR	N-O stretch.(hydroxy), N-H wag.
M107	1029.22	$B_{u}$	IR	N-O stretch.(hydroxy), N-H wag.
M108	1029.80	$A_{u}$	IR	N-O stretch.(hydroxy), N-H wag.
M109	1141.91	$A_g$	Raman	N-O stretch.(hydroxy), N-H wag.
M110	1029.22	$B_{g}^{s}$	Raman	N-O stretch.(hydroxy), N-H wag.
M111	1085.02	$A_g^s$	Raman	C-N stretch., O-H bend.
M112	1086.04	$B_g$	Raman	C-N stretch., O-H bend.
M113	1135.40	$B_u$	IR	Ring stretch., O-H bend., N-O stretch.
M114	1141.91	$A_u$	IR	Ring stretch., N-H wag., O-H bend., N-O stretch.
M115	1170.11	$A_u$	IR	O-H bend, N-H wag.
M116	1170.11		IR	
M117		$B_u$ <sub>A</sub>		O-H bend, N-H wag.
	1171.65	$A_g$	Raman Raman	O-H bend, N-H wag.
M118 M119	1172.78 1171.13	$B_g B_u$	IR	O-H bend, N-H wag. O-H bend, N-H wag.

Table 5.4: Calculated normal modes infrared frequencies (1200-3400  $\,\mathrm{cm^{-1}}$ ) with symmetry assignment for the MAD-XI crystal using the DFT GGA + OBS approach.

Mode number	Cal. frequency (cm <sup>-1</sup> )	Symmetry	Mode	Assignment
M121	1200.01	$B_{u}$	IR	O-H bend., NH3 rock.
M122	1200.16	$B_{g}$	Raman	O-H bend., NH3 rock.
M123	1236.32	$B_u^{\circ}$	IR	ring stretch., O-H bend., NO2 sym stretch., NH3 rock.
M124	1238.07	$A_g$	Raman	ring stretch., O-H bend., NO <sub>2</sub> sym stretch., NH <sub>3</sub> rock.
M125	1245.71	$A_u^g$	IR	ring stretch., O-H bend., NO <sub>2</sub> sym stretch., NH <sub>3</sub> rock.
M126	1246.31	$B_g$	Raman	ring stretch., O-H bend., NO <sub>2</sub> sym stretch., NH <sub>3</sub> rock.
M127	1263.32	$A_g$	Raman	ring stretch., O-H bend., NO <sub>2</sub> sym stretch., NH <sub>3</sub> rock.
M128	1264.33	$B_g$	Raman	ring stretch., O-H bend., NO <sub>2</sub> sym stretch., NH <sub>3</sub> rock.
M129	1334.38	$B_u$	IR	ring stretch., O-H bend., NO <sub>2</sub> sym stretch., NH <sub>3</sub> rock.
M130	1342.70	$A_g$	IR	ring stretch., O-H bend., NO <sub>2</sub> sym stretch., NH <sub>3</sub> rock.
M131	1345.11		Raman	C-N stretch., O-H bend., NO <sub>2</sub> sym stretch., NH <sub>3</sub> rock.
M132	1349.67	$A_{\mathrm{g}} B_{\mathrm{g}}$	Raman	C-N stretch., O-H bend., NO <sub>2</sub> sym stretch., NH <sub>3</sub> rock.
M133	1353.04	$B_u$	IR	C-C rock., O-H bend., NO <sub>2</sub> sym stretch., NH <sub>3</sub> rock.
M134	1354.28	$B_u$	IR	C-C rock., O-H bend., NO <sub>2</sub> sym stretch., NH <sub>3</sub> rock.
M135	1367.61		IR	C-N stretch., O-H bend., NO <sub>2</sub> sym stretch., NH <sub>3</sub> rock.
M136	1377.21	$A_u$	IR	C-N stretch., O-H bend.
			IR	
M137	1389.86	$B_{\nu}$		Ring stretch., N-H wag., O-H bend., NO stretch.
M138	1390.88	$B_{\rm g}$	Raman	Ring stretch., N-H wag., O-H bend., NO stretch.
M139	1394.30	$A_g$	Raman	Ring stretch., N-H wag., O-H bend., NO stretch.
M140	1396.56	$B_{\rm g}$	Raman	Ring stretch., NH sci., O-H bend., NO stretch.
M141	1404.24	$A_{\scriptscriptstyle H}$	IR	Ring stretch., NH sci., O-H bend., NO stretch.
M142	1407.65	$A_g^{"}$	Raman	Ring stretch., NH sci., O-H bend., NO stretch.
M143	1436.83	$B_{\mu}$	IR	Ring stretch, NO <sub>2</sub> asym stretch., N-H wag.
M144	1437.26	$B_g$	Raman	Ring stretch, NO <sub>2</sub> asym stretch., N-H wag.
M145	1439.21	$A_{\mu}$	IR	NO <sub>2</sub> stretch., ring stretch., NH <sub>3</sub> sci.
M146	1439.32	$A_g$	Raman	NO <sub>2</sub> stretch., ring stretch., NH <sub>3</sub> sci.
M147	1492.17	$B_{\mu}$	IR	NO <sub>2</sub> stretch., ring stretch., NH <sub>3</sub> wag.
M148	1493.26	$A_{u}$	IR	N-O stretch., ring stretch., NH <sub>3</sub> wag.
M149	1499.70	$A_g$	Raman	NO <sub>2</sub> asm stretch., ring stretch., NH <sub>3</sub> wag.
M150	1499.92	$B_{\rm g}$	Raman	NO <sub>2</sub> asm stretch., ring stretch., NH <sub>3</sub> wag.
M151	1547.43	$A_g$	Raman	NH <sub>3</sub> wag.
M152	1549.09	$A_{u}$	IR	NH <sub>3</sub> wag.
M153	1551.15	$B_{g}^{"}$	Raman	NH <sub>3</sub> wag.
M154	1552.65	$B_{u}^{g}$	IR	NH <sub>3</sub> wag.
M155	1574.98	$A_g$	Raman	C-C stretch., N-H wag.
M156	1576.24	$B_g$	Raman	C-C stretch., N-H wag.
M157	1640.00	$B_g$	Raman	N-H sci.
M158	1641.83	$B_{u}$	IR	N-H sci.
M159	1643.29	$A_{u}$	IR	N-H sci.
M160	1643.30	$A_g$	Raman	N-H sci.
M161	1644.03	$B_{u}$	IR	N-H sci.
M162	1644.03	$B_u$	IR	N-H sci.
M163	1644.03	$B_u$	IR	N-H sci.
M164	1650.13	$A_{u}$	IR	N-H sci.
M165	2866.80	$B_u$	IR	N-H sym stretch., O-H sym stretch.
M166	2867.14	$A_{u}$	IR	N-H sym stretch., O-H sym stretch.
M167	2867.15	$A_{g}$	Raman	N-H sym stretch., O-H sym stretch.
M168	2867.71	$B_g$	Raman	N-H sym stretch., O-H sym stretch.
M169	2943.72	$A_g$	Raman	N-H asym stretch., O-H asym stretch.
M170	2951.11	$B_g$	Raman	N-H asym stretch., O-H asym stretch.
M171	2951.16	$A_u$	IR	N-H asym stretch., O-H asym stretch.
M172	2955.66	$B_u$	IR	N-H asym stretch., O-H asym stretch.
M173	3187.38	$A_g$	Raman	N-H asym stretch., O-H asym stretch.
M174	3189.24	$A_u$	IR	N-H asym stretch., O-H asym stretch.
M175	3190.12	$B_g$	Raman	N-H asym stretch., O-H asym stretch.
M176	3191.44	$B_u$	IR	N-H asym stretch., O-H asym stretch.
M177	3310.06	$A_g$	Raman	N-H asym stretch., O-H asym stretch.
M178	3310.19	$A_u^{g}$	IR	N-H asym stretch., O-H asym stretch.
M179	3311.87	$B_u$	IR	N-H asym stretch., O-H asym stretch.
M180	3315.73	$B_g$	Raman	N-H asym stretch., O-H asym stretch.
1,1100	55.55.5	y		1 wo j in octoberin, O 11 wo j in octoberin

vibrational mode assignments are depicted in table 5.2 to table 5.5. The Infrared spectra in the frequency region from 0 to 3400 cm<sup>-1</sup> of MAD-XI crystal displayed in figure 5.2. The corresponding frequency regions are distributed with respect to different vibrational modes (figure 2a).

The lower frequency region from 41.55 cm<sup>-1</sup> to 449.80 cm<sup>-1</sup> are occurred due to external and internal vibrational modes. The frequency region from 485.44 cm<sup>-1</sup> and 725.16 cm<sup>-1</sup> are mainly involves the O-H bending, ring deformation and NO<sub>2</sub> rocking. The frequencies between 735.59 cm<sup>-1</sup> and 1000.09 cm<sup>-1</sup> are mainly allocated to the ring breathing, N-O scissoring, O-H bending. The frequency region from 1002.50 cm<sup>-1</sup> to 1200.16 cm<sup>-1</sup> is associated NH<sub>3</sub> rocking and N-O stretching (hydroxy), N-H wagging. The frequency region from 1236.32 cm<sup>-1</sup> to 1439.32 cm<sup>-1</sup> are belonged to scissoring of NH<sub>2</sub> vibration. The frequencies region from 1492.17 cm<sup>-1</sup> and 1650.13 cm<sup>-1</sup> are due to the C-NO<sub>2</sub> stretching vibrational mode. The higher frequency regions 2866.80–2867.71 cm<sup>-1</sup>, 2940.72–3315.73 cm<sup>-1</sup>, are related to the NH<sub>3</sub>, OH symmetric and NH<sub>2</sub>, OH antisymmetric stretching vibrational modes, respectively.

#### 5.3.2 Phonon dispersion

The density functional perturbation theory[29–32] was used to calculate the phonon dispersion curve along with the high symmetry directions ( $Z \to \Gamma \to Y \to A \to B \to D \to E \to C$ ) of MAD-X1 crystal. Figure 5.3 (a) shows that there are no imaginary frequencies in the phonon dispersion, revealing that the MAD-XI compound is dynamically stable.

In addition, We have analyzed the partial phonon density of states (PPDOS) in order to see individual atomic contributions in the whole region of phonon spectra. The Figure 5.3 (b) show the low-frequency region (41 cm<sup>-1</sup> -449.80 cm<sup>-1</sup>), PPDOS contribution comes from triozole ring, NH<sub>4</sub>OH, and NO<sub>2</sub> and is mainly dominated by O atom. In the frequency region from 500 cm<sup>-1</sup> to 1400 cm<sup>-1</sup>, the PPDOS is contributed by C and H atoms, which are mainly due to the frequency

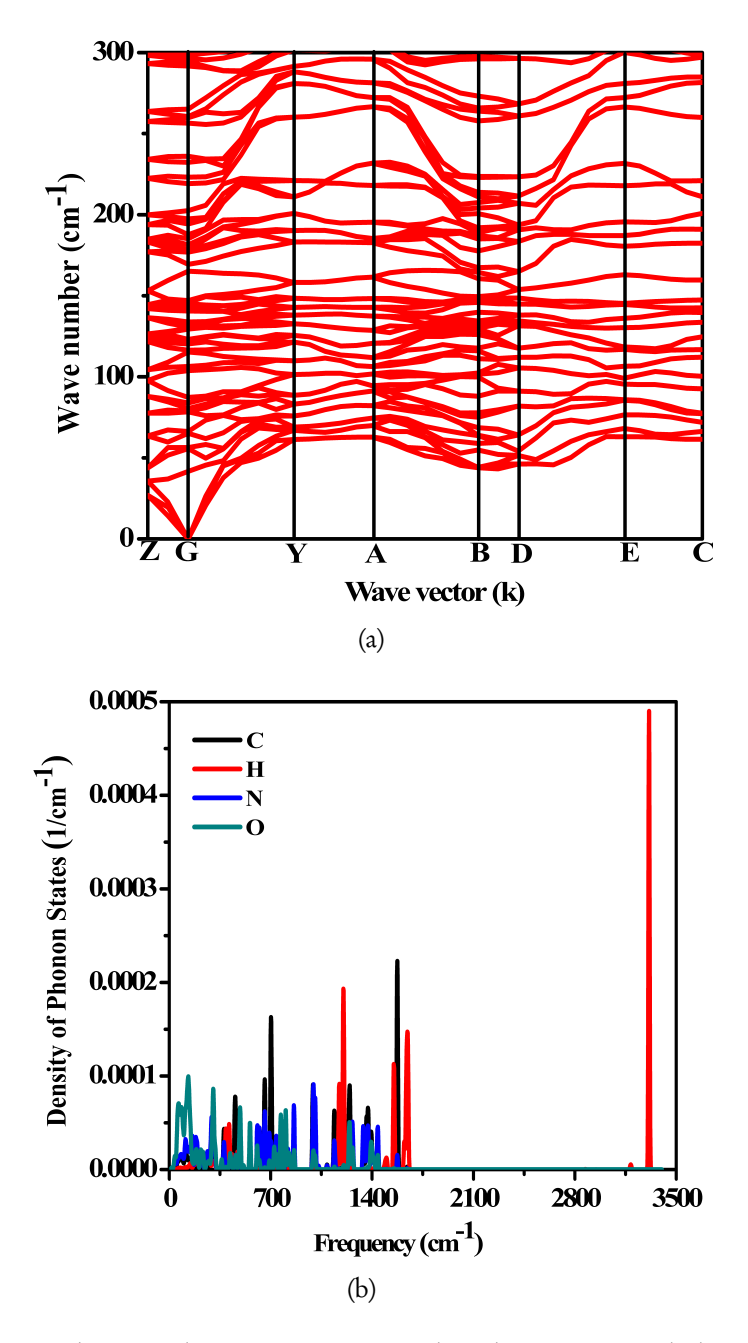


Figure 5.4: (a) Phonon dispersion curves, (b) Phonon partial density of states (PDOS) for the MAD-X1 crystal.

associated with the triozole ring. The PPDOS in the high-frequency regions from 2866.80 to 3315.73 cm<sup>-1</sup>) is completely dominated by H atom, which is mainly due to the frequency related to the NH<sub>4</sub>OH group.

#### 5.3.3 Thermodynamic properties

In the harmonic approximation, the vibration of crystal is considered as a combination of numerous normal modes namely lattice waves. Usually, the language of normal modes is replaced by an equivalent corpuscular description, which is analogous to the terminology used in the quantum theory of electromagnetic theory. Here, the allowed energies of normal mode are discrete, which are given by  $(n_q + 1/2) \hbar w_q$  (k), where  $w_q$  is the frequency of the mode,  $n_q$  is the number of particles with energy  $w_q$  (k). These quasi-particles are called "phonons" and obey Bose-Einstein statistics. Phonon is a typical elementary excitation. In this way the vibrational state of the crystal is described by giving the number of phonons of each type present in the crystal. Thus, we can describe the excitation number  $n_q$  of the normal mode with wave vector k in branch q by  $E_{nq} = (n_q + 1/2) \hbar w_q$  (k), one says that there are  $n_q$  phonons of type q with wave vector k present in the crystal.

The thermodynamic properties such as entropy (S), enthalpy (E), free energy (F), heat capacity ( $C_V$ ), and the Debye temperature ( $\Theta_D$ ) were calculated by using PPDOS [ $\overline{35}$ ,  $\overline{36}$ ]. Figure 5.4 (a) is displayed E, F, and S with respect to temperature within the range of 0–1000 K. The enthalpy (H) and temperature\*entropy (T × S) increases, and free energy (F) gradually shows downfall as temperature increases. The heat capacity ( $C_V$ ) (shown in figure 5.4 (b)) of MAD-XI increases with temperature, reaching the Dulong-Petit limit at around 380 K, being 160.90 cal/cell.K at T = 306 K. The Debye temperature with the temperature increasing under lower temperature, and the slow-change curve of Debye temperature with the temperature increasing at higher temperature. This is because that the heat capacity is contributed by lattice vibration and thermal vibration of the elec-

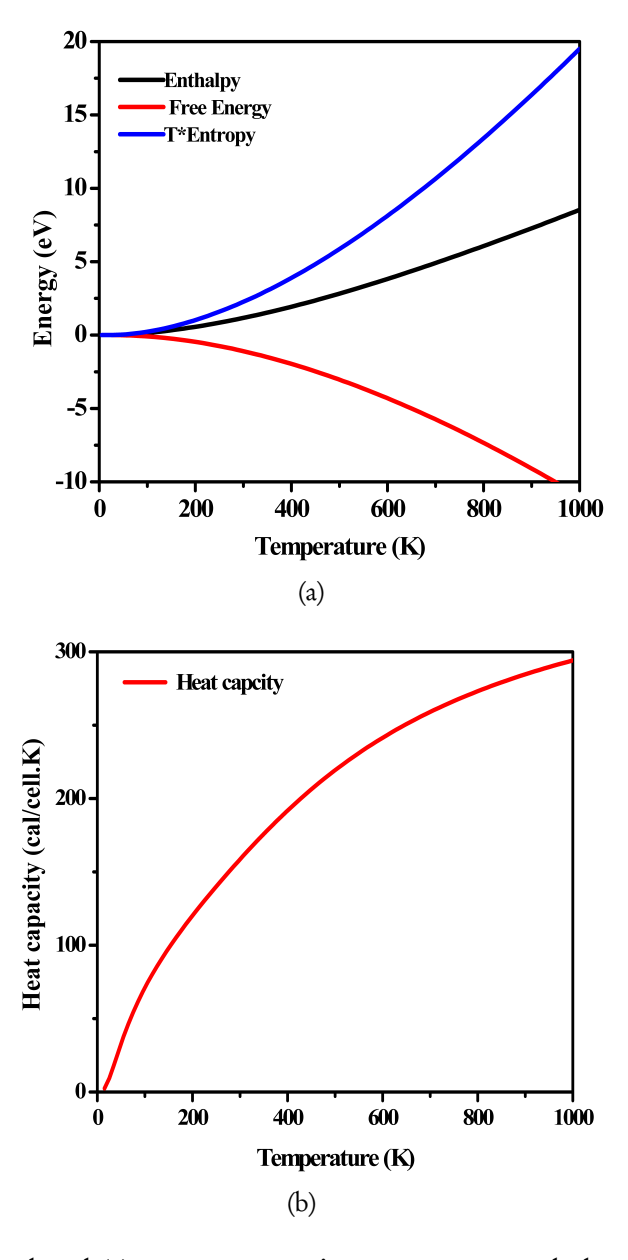


Figure 5.5: Calculated (a) temperature times entropy, enthalpy, and free energy (b) Heat capacity of the MAD-XI crystal for temperature of up to 1000 K for the MAD-XI crystal).

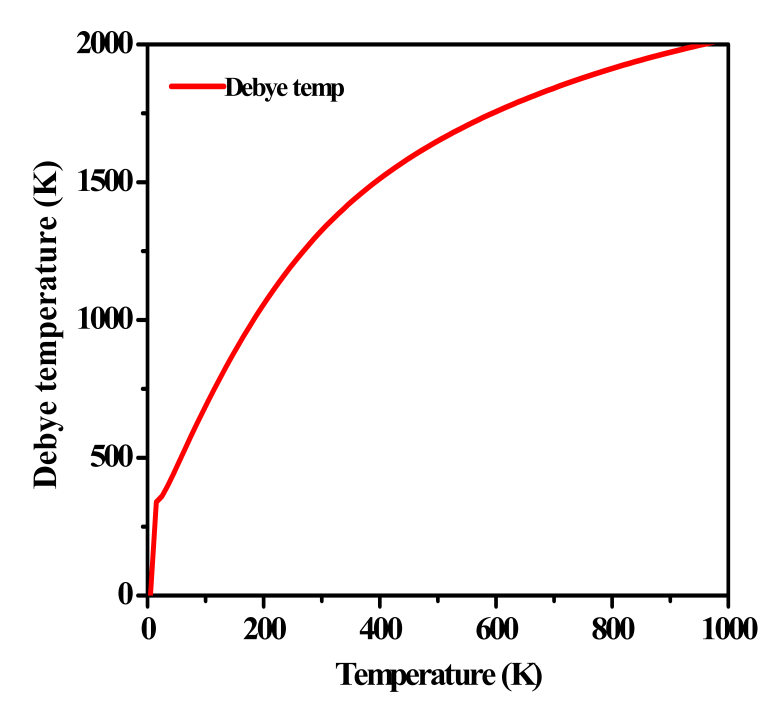


Figure 5.6: Calculated Debye temperature curves of the MAD-XI crystal for temperature of up to 1000 K for the MAD-XI crystal.

trons at lower temperature, and effect of the energy of the thermal motion of the electrons on the heat capacity can be negligible with a higher temperature. The Debye temperature of MAD-XI displayed in figure 5.5 reveals that it increases under lower temperatures, and its curve changes slowly at a higher temperature. The Debye temperature of MAD-XI is found to be 338.88 K at 15 K.

#### 5.4 Conclusions

In conclusion, the generalized gradient approximation (GGA) with PW91 and Ortmann, Bechstedt, and Schmidt (OBS) method were employed to describe the van der Waals interactions. The obtained lattice parameters and unit cell volume show well agreement with experimental results. The vibrational frequencies of MAD-XI crystal are computed by utilizing density functional perturbation theory. The calculated infrared spectra reveal higher frequency regions (2866.80-2867.71 cm<sup>-1</sup>) are corresponding to NH<sub>3</sub>, OH symmetric stretching. The frequencies 2940.72-3315.73 cm<sup>-1</sup>, are associated to antisymmetric stretching of NH<sub>2</sub>, OH vibrational modes. The absence of imaginary frequencies in the phonon dispersion curve displays the MAD-XI compound is dynamically stable. It has been found that thermodynamic properties such as heat capacity  $(C_V)$ , entropy (S) enthalpy (E), free energy (F), and the Debye temperature ( $\Theta_D$ ) are analyzed in detail. The Debye temperature increases under lower temperature, and its curve changes slowly at a higher temperature. The Debye temperature of MAD-XI is found to be 338.88 K, at temperature 15 K. As a consequence of our systematic review, we hope our results will help by providing guidelines for future research on triazole materials.

#### References

[1] J.P. Agrawal, Prog. Energy Combust. Sci., 29 (1998) 1–30.

- [2] J. Akhavan, The chemistry of explosives. Gmbridge, UK: R. Soc. Chem., 2011.
- [3] D. Bedrova, G.D. Smith, and T.D. Sewell. 2000, J. Chem. Phys., 112 (2000) 7203–7208.
- [4] P. Pagoria, Propellants, Explosives, Pyrotechnics, 2016 Wiley Online Library.
- [5] A.A. Dippold, T.M. Klapötke, Chem. Eur. J., 18 (2012) 16742–16753.
- [6] T.M. Klapötke and C.M. Sabaté, Chem. Mater., 20 (2008) 1750–1763.
- [7] N. Fischer, T.M. Klapötke, M. Reymann and J. Stierstorfer, Eur. J. Inorg. Chem., 12 (2013) 2167–2180.
- [8] M. Dachs, A.A. Dippold, J. Gaar, M. Holler, T.M. Klapötke, Z. Anorg. Allg. Chem., 639 (2013) 2171–2180.
- [9] Y. Zhang, D. A. Parrish, J.M. Shreeve, J. Mater. Chem. A, 1 (2013) 585-593.
- [10] T. M. Klapötke, D. G. Piercey, Stierstorfer, Eur. J. Inorg. Chem, 9 (2013) 1509–1517.
- [11] R.P. Singh, R.D. Verma, D. T. Meshri, J.M. Shreeve, Angew. Chem., Int. Ed., 45 (2006) 3584–3601.
- [12] J.C. Bennion, J.A. Ciezak-Jenkins, T.A. Jenkins, Propellants Explos. Pyrotech., 44 (2019) 1263–1269.
- [13] N. Fischer, D. Fischer, T. M. Klapötke, D.G. Piercey, J. Stierstorfer, J. Mater. Chem., 22 (2012) 20418–20422.
- [14] A. A. Dippold, T.M. Klapötke, J. Am. Chem. Soc., 135 (2013) 9931–9938.

142 REFERENCES

- [15] S. J. Sabatini, K.D. Oyler, Crystals, 6 (2015) 1-22.
- [16] W.S. Yuan, Y.D. Gan, C.L. Jiang, S.H. Zhu, M.J. Zhang, F.S. Liu, B. Tang, D. Hong, Q. JunLiu, Chemical Physics 548 (2021) 111232 (1–11).
- [17] B. Yuan, Z. Yu, and E. R. Bernstein, J. Phys. Chem. A, 119 (2015) 2965-2981.
- [18] H. Qin, W. Zeng, F. Liua, Y. Gan, B. Tang, S. Zhu, and Q. Liua, J. Energ. Mater. 39 (2021) 125–169.
- [19] W. Perger, AIP Conference Proceedings, 1426 (2012) 571.
- [20] I.E. Knaggs, Nature 135 (1935) 268.
- [21] I.R. Shein, V.L. Kozhevnikov, A.L. Ivanovskii, Solid State Sci. 10 (2008) 217–225.
- [22] S.J. Clark, M.D. Segall, C.J. Pickard, P.J. Hasnip, M.J. Probert, K. Refson, M.C. Payne, Z. Kristallogr. 220 (2005) 567–570.
- [23] J.P. Perdew, K. Burke, M. Ernzerhof, Phys. Rev. Lett. 77 (1996) 3865–3868.
- [24] J.P. Perdew, K. Burke, Y. Wang, Phys. Rev. B 54 (1996) 16533–16539.
- [25] F. Ortmann, F. Bechstedt, W.G. Schmidt, Phys. Rev. B, 73 (2006) 205101.
- [26] D. Hamann, M. Schluter, C. Chiang, Phys. Rev. Lett. 43 (1979) 1494–1497.
- [27] H.J. Monkhorst, J.D. Pack, Phys. Rev. B 13 (1976) 5188-5192.
- [28] R. Fletcher, Practical Methods of Optimization, Wiley, New York, 1980.
- [29] A. Togo, I. Tanaka, Scr. Mater. 108 (2015) 1–5.

- [30] S. Baroni, P. Giannozzi, A. Testa, Phys. Rev. Lett. 58 (1987) 1861-1864.
- [31] X. Gonze, J.P. Vigneron, Phys. Rev. B 39 (1989) 13120–13128.
- [32] X. Gonze, D.C. Allan, M.P. Teter, Phys. Rev. Lett. 68 (1992) 3603-3606.
- [33] L. Changyol, X. Gonze, Phys. Rev. B 51 (1955) 8610–8613.
- [34] V. Mankad, N. Rathod, S.D. Gupta, S.K. Gupta, P.K Jha, Mater. Chem. Phys. 129 (2011) 816–822.
- [35] B. Adivaiah, E. Narsimha Rao, T. Atahar Parveen, G. Vaitheeswaran, J. Phys. Chem. Solids 122 (2018) 268–277.
- [36] N. Mounet, N. Marzari, Phys. Rev. B 71 (2005) 205214 (1-14).
- [37] B. Adivaiah, E. Narsimha Rao, G. Vaitheeswaran, J. Phys. Condens. Matter 31 (2019) 475402(1–14).
- [38] K. Ramesh Babu, G. Vaitheeswaran, Chem. Phys. Lett. 533 (2012) 35–39.
- [39] K. Ramesh Babu, G. Vaitheeswaran, Chem. Phys. Lett. 586 (2013) 44–50.
- [40] G. Vaitheeswaran, K. Ramesh Babu, J. Chem. Sci. 124 (2012) 1391–1398.
- [41] N. Yedukondalu, G. Vaitheeswaran, P. Anees, M.C. Valasakumar, Phy. Chem. Chem. Phys. 17 (2015) 29210–29225.
- [42] S. J. Shear, G. C. Turrell, J. I. Bryant, R. L. Brooks, J. Chem. Phys. 48 (1968) 1138-1144.
- [43] P. Giannozzi, S. Gironcoli Phys. Rev. B 43 (1991) 7231–7242.
- [44] H.V. Brand, R. L. Rabie, D.J. Funk, I. Diaz-Acosta, P. Pulay, and T. K. Lippert, J. Phys. Chem. B, 106 (2002) 10594–10604.
- [45] E. Kessenich, T.M. Klapötke, J. Knizek, H. Noth, A. Schulz, Eur. J. Inorg. Chem. 1998 (1998) 2013–2016.

# Chapter 9

### Conclusions

The study of lattice dynamics and thermodynamic properties of energetic materials are extremely important, from which we can understand spectroscopic and thermodynamic properties of a crystal. Density functional theory (DFT) calculations were used to investigate the structural, elastic, vibrational, and thermodynamic properties for several energetic materials at ambient conditions. The vibrational normal modes, as well as infrared spectra, were obtained and assigned. The vibrational nature of bonds in solid crystals was further explored by obtaining a fundamental understanding of their thermodynamic behavior. This thesis mainly focus on a brief comparison with results for Sr(NO<sub>3</sub>)<sub>2</sub>, Ba(NO<sub>3</sub>)<sub>2</sub>, Sr(N<sub>3</sub>)<sub>2</sub>, Ba(N<sub>3</sub>)<sub>2</sub>, C<sub>3</sub>N<sub>12</sub>, UN, and MAD-XI crystals are accompanied in order to understand the difference in energetic performances of the organic azides and organic nitrates crystals when compared to inorganic azides and inorganic nitrates crystals. Similarly, vibrational, and thermodynamic properties of C<sub>3</sub>N<sub>12</sub>, and UN crystals were explored in order to understand the energetic performances of organic azides and organic nitrates crystals. Finally, the high-performance insensitive energetic material MAD-XI crystal were studied, which is replacement for well-known energetic material 1,3,5-trinitro-1,3,5-triazacyclohexane (RDX). The results presented in this work could open a way to understand the lattice dynamics of materials of this type and could provide necessary input from the explosive applicability point of view, which would help experimental researchers in the future.

146 6.1. SUMMARY

#### 6.1 Summary

In summary, a series of energetic materials, namely  $Sr(NO_3)_2$ ,  $Ba(NO_3)_2$ ,  $Sr(N_3)_2$ ,  $Ba(N_3)_2$ ,  $C_3N_{12}$ , UN, and MAD-X1 were thoroughly investigated to understand the structure-property-performance interrelationship.

We have investigated the structural, elastic, vibrational, and thermodynamic properties of a series of energetic materials, namely Sr(NO<sub>3</sub>)<sub>2</sub>, Ba(NO<sub>3</sub>)<sub>2</sub>, Sr(N<sub>3</sub>)<sub>2</sub>, and Ba(N<sub>3</sub>)<sub>2</sub>, using an ab initio approach. We found that the van der Waals correction predicts the structural parameters, which are in fair agreement with the experimental values. The elastic constants and phonon spectra of M(NO<sub>3</sub>)<sub>2</sub> and M(N<sub>3</sub>)<sub>2</sub> confirm the mechanical and dynamical stabilities, while the calculated B/G ratio suggests that the materials are ductile. The phonon modes, their dispersion, and symmetry and the IR spectra of the crystals were computed. The calculated normal mode frequencies were classified according to irreducible representations for both IR-active and Raman-active modes. IR spectra of Sr(NO<sub>3</sub>)<sub>2</sub>,  $Ba(NO_3)_2$ ,  $Sr(N_3)_2$ , and  $Ba(N_3)_2$  were analyzed in close comparison with results of lattice dynamical calculations. The zone-center low-frequency modes are different for Sr(NO<sub>3</sub>)<sub>2</sub> and Ba(NO<sub>3</sub>)<sub>2</sub>, and this was predicted for the first time. The contributions of strontium and barium are much larger than those of nitrogen and oxygen atoms in the low-frequency region, whereas the high-frequency zone-center modes are relatively the same for both materials as most of the vibrational modes here are due to the nitrate (NO<sub>3</sub>) group, owing to the covalent bonding among nitrogen and oxygen atoms. The vibrations of the azide (N<sub>3</sub>) group exhibit high-intensity infrared absorption bands in the ranges of 1900-2100 cm<sup>-1</sup>. A comparison with the work of metal nitrates reveals that the nitrates are shifted towards the smaller wavenumbers than metal azides. Most of the calculated vibrational modes are in satisfactory agreement with the earlier reported experimental data. It has been seen that the calculated phonon dispersion curves of M(NO<sub>3</sub>)<sub>2</sub> and M(N<sub>3</sub>)<sub>2</sub> do not show any imaginary modes hence both the materials are dynamically stable. Also, as the thermal behavior of these materials could play a key role in the growth of sustainable smoke compositions, the thermodynamic properties, such as entropy, Debye temperature, heat capacity, and enthalpy, at different temperatures ranging from 5 to 1000 K were described. It is inferred that strontium nitrate and barium nitrate can be reliably used in pyrotechnics as they have sufficiently low thermal conductivity. We believe that this work will pave the way to explore many more pyrotechnic-based materials of this type. The comparative study between alkaline-earth metal nitrates and alkaline-earth metal azides reveals difference in energetic performance of the metal azides and metal nitrate crystals.

The structural, vibrational, and thermodynamic properties of the cyanuric triazide and urea nitrate crystals were performed under ambient conditions using first-principles calculations. The structural relaxation is achieved using GGA-PBE exchange-correlation functional, together with dispersion correction (PBE + G06) and (PBE + TS) considering van der Waals interactions for C<sub>3</sub>N<sub>12</sub> and UN, respectively. The unit cell lattice parameters showed a good agreement with experimental data. The infrared spectra of the  $C_3N_{12}$  are obtained and compared with measurements from the experimental in the 0-2100 cm<sup>-1</sup> region. However, the calculated vibrational modes are in good agreement with experimental results. We note that the N<sub>3</sub> group involves high–intensity infrared absorption lines in the range of 1200-1500 cm<sup>-1</sup>. This vibration confirms the frequency position at 1317 cm $^{-1}$  with irreducible representation  $E_{\nu}$ , which is allocated to an asymmetric ring stretching. Similarly, we calculated infrared spectra for urea nitrate in the range of 0-3600 cm<sup>-1</sup>; the results reveal most of the vibrational modes come from NO<sub>3</sub> group in the low frequency region (around 500 cm<sup>-1</sup>). The mid-frequency range from 900 to 1700 cm<sup>-1</sup> involves scissoring vibrational modes of NO<sub>3</sub> groups, and high-frequency range (2100-3100 cm<sup>-1</sup>) is dominated by N-H stretching vibrational modes. The highest intense maxima were observed at 2603.70 cm<sup>-1</sup> due to the single O-H bond stretching vibrational mode. The absence of negative frequency in the phonon dispersion curves confirms the dynamical stability of both systems. We found that there is no gap between the low-lying optical modes and acoustic modes, which leads to low-thermal conductivity of the cyanuric triazide and urea nitrate. The partial phonon density of states results reveals the contribution of particular atoms in respected frequencies. For C<sub>3</sub>N<sub>12</sub> the low-frequency region 500 cm<sup>-1</sup> arises from strong hybridization between C and N atoms, dominated by N atoms, while high-frequency regions (around 1500 cm<sup>-1</sup>) are influ148 6.1. SUMMARY

ence by the vibrations of C atoms. In the case of UN, the low frequency region 300 cm<sup>-1</sup>, the energy of lattice modes was contributed by the C-N, O-N-O, urea group, and C-H bonds, wherein the vibrations of oxygen atoms on the nitro groups are the greatest. The calculated thermodynamic properties show that the Debye temperature, constant–volume specific heat, enthalpy, and entropy values increase as a function of temperature, while the free energy falls off as the temperature increases. It can be concluded that, C<sub>3</sub>N<sub>12</sub> is an effective initiating explosive as they have low thermal conductivity, and urea nitrate is an improvised explosive. We expect this work will encourage experimental attempts to reveal the rich role of crystallized azide in the structural, vibrational, and thermodynamic properties of other triazine azide complex and organic nitrates salts in the solid state.

Finally, the vibrational and thermodynamic properties of MAD-XI crystal presented by using density functional theory within the GGA-PW91 + OBS approximation. The calculated lattice parameters are compared with the experimental values. The vibrational modes assignments are described in a detailed way The infrared spectra show that the higher frequency regions 2866.80-2867.71 cm<sup>-1</sup>, 2940.72-3315.73 cm<sup>-1</sup>, are corresponding to NH<sub>3</sub>, OH symmetric stretching and NH<sub>2</sub>, OH antisymmetric stretching vibrational modes respectively. The phonon dispersion curve concludes the compound is dynamically stable. The thermodynamic properties such as heat capacity  $(C_V)$ , entropy (S), enthalpy (E), free energy (F), and the Debye temperature ( $\Theta_D$ ) are analyzed in detail. The Debye temperature increases under lower temperature, and its curve changes slowly at higher temperature. The Debye temperature of MAD-X1 is found to be 338.88 K at 15 K. These results propose that MAD-XI material can develop into an insensitive RDX replacement in energetic formulations. We believe that this work will encourage experimental attempts to reveal the behavior of bis 1,2,4-triazoles and N-oxide derivatives [1].

#### 6.2 Future scope

In this thesis, as we have mainly focused on nitrate and azide-based materials, we can carry forward this work with other advance energetic materials such as green-pyrotechnic based, Nickel Hydrazine Nitrate (NHN) compounds, ect. NHN is known as the potential replacement for toxic lead azide [2]. Especially in the case of energetic solids, further computational study on many more green pyrotechnic-based compounds is tremendous challenging in terms of spectroscopic nature and thermal behavior, which provides deep insights about different properties of this class of materials. To extend the present work, Time-Dependent Density Functional Theory (TD-DFT) can be used to find the Anharmonic vibrational contribution.

#### References

- [1] J. C. Bennion, J. A. Ciezak-Jenkins, T. A. Jenkins, Propellants Explos. Pyrotech., 44 (2019) 1263–1269.
- [2] Z. Shunguan, W. Youchen, Z. Wenyi, M. Jingyan, Propellants Explos. Pyrotech., 22 (1997) 317-320.

#### List of Publications

#### Publications included in the thesis

- [1] **B. Adivaiah**, E. Narsimha Rao, T. Atahar Parveen, G. Vaitheeswaran, "Lattice dynamics and thermodynamic properties of alkaline earth metal nitrates M (NO<sub>3</sub>)<sub>2</sub> (M = Sr, Ba): A first principles study", *J. Phy. Chem. Solids*, 122 (2018) 268.
- [2] **Bushnagar Adivaiah**, Elaprolu Narsimha Rao, G. Vaitheeswaran, "Structure-property correlation studies of alkaline-earth metal—azides M (N<sub>3</sub>)<sub>2</sub> (M = Sr, Ba)", *J. Phys.: Condens. Matter* 31 (2019) 475402.
- [3] **B. Adivaiah**, G. Vaitheeswaran, "Computational study of lattice dynamics and thermodynamic properties of energetic solid cyanuric triazide", *J. Phy. Chem. Solids*, 148 (2021) 109782.

#### Publications not included in the thesis

- [1] T. Atahar Parveen, E. Narsimha Rao, **B. Adivaiah**, G. Vaitheeswaran, "Correction: Topological behaviour of ternary non-symmorphic crystals KZnX (X = P, As, Sb) under pressure and strain: a first principles study" *Phys. Chem. Chem. Phys.*, 20 (2018)5084.
- [2] B. Moses Abraham, **B. Adivaiah**, G. Vaitheeswaran, "Microscopic origin of pressure-induced phase-transitions in urea: a detailed investigation through first principles calculations", *Phys. Chem. Chem. Phys.*, 21 (2019) 884.
- [3] T Atahar Parveen, E Narsimha Rao, **B. Adivaiah**, G Vaitheeswaran, Conference proceeding, 7th Annual International Conference on Emerging Research Areas (AICERA), (2018) 20.

- [4] **B.** Adivaiah and G. Vaitheeswaran, "A Computational study of lattice dynamics and thermodynamic properties of an improvised explosive urea nitrate", *To be communicated*.
- [5] **B. Adivaiah**, N Yeduondalu and G. Vaitheeswaran, "DFT calculations of the structural, elastic and vibrational properties of dihydroxylammonium 5,5'-bis(3-nitro-1,2,4-triazolate-1 N-oxide) (MAD-X1)", *To be communicated*.

#### Scientific Activities

## Conference/Symposium/Workshop/Poster presentations

- Lattice dynamics and Thermodynamic response of cubic alkaline-earth metal nitrates M (NO<sub>3</sub>)<sub>2</sub> (M = Sr, Ba): A First principle study, "11th International High Energy Materials conference and Exhibits", Pune, November (2017)
- Structural, Electronic and Vibrational Properties of Alkaline-earth metal Nitrates,
  - "15th Indian Theoretical Chemistry Symposium (TCS-2016)", Hyderabad, December (2016)
- Structural, Electronic and Vibrational Properties of Alkaline-earth metal Nitrates,
  - "15th Indian Theoretical Chemistry Symposium (TCS-2016)", Hyderabad, December (2016)
- Participated in the "10th International High Energy Materials conference and Exhibits, Hyderabad", February (2016)
- Workshop on "Functional Magnetic Materials" organized by UGC Networking Resource Centre, School of Physics, University of Hyderabad during 26th February 3rd March, 2018.

# Vibrational and thermodynamic properties of Energetic Materials: A Density functional theory study

by Bushnagar Adivaiah

Dr. G.S. Vaitheeswaran Associate Professor

G. Vaithees war

School of Physics University of Hyderabad Hyderabad-500 046. (TS) INDIA

Submission date: 21-Jan-2022 04:31PM (UTC+0530)

Submission ID: 1745343780

File name: Bushnagar\_Adivaiah.pdf (14.91M)

Word count: 34195

Character count: 160865

#### Vibrational and thermodynamic properties of Energetic Materials: A Density functional theory study

ORIGINALITY REPORT

SIMILARITY INDEX

INTERNET SOURCES

**PUBLICATIONS** STUDENT PAPERS

**PRIMARY SOURCES** 

- B. Adivaiah, E. Narsimha Rao, T. Atahar Parveen, G. Vaitheeswaran. "Lattice dynamics and thermodynamic properties of alkaline earth metal nitrates M(NO 3) 2 (M = Sr, Ba): A first principles study", Journal of Physics and author paper which is include Chemistry of Solids, 2018 Dr. G.S. Vaitheeswaran Publication
- School of Physics 146 (TS) INDIA Ganapathy Vaitheeswaran. "Structure-This paper metal - azides  $M(N_3)_2$  (M = Sr, Ba)", Journal of Student's first Physics: Condensed Matter as  $M(N_3)_2$  (M = Sr, Ba)", Journal of Student's first Physics: Condensed Matter as  $M(N_3)_2$  (M) Physics: Condensed Matter, 2019 author paper which is included in Publication Chapter-3 G. Voitherstran
- Dr. G.S. Vaitheeswaran Associate Professor School of Privsig B. Adivaiah, G. Vaitheeswaran. "Computational study of lattice dynamics - School of Hyder University of Hyder (T thermodynamic properties of energetic solid Chemistry of Solids, 2021 first author paper which is included Publication

- B. Adivaiah, G. Vaitheeswaran. "Computational study of lattice dynamics and thermodynamic properties of energetic solid This paper belong cyanuric triazide", Journal of Physics and to Shudent's first author paper which is included in chapter -4 G. Vaithean Chemistry of Solids, 2020 Publication
- Submitted to University of Hyderabad, Hyderabad

Dr. G.S. Vaitheeswaran Associate Professor School of Filesson
School of Filesson
University of Hydeo had
Hyderabad-500 046 (TS) INDIA

Student Paper

Bushnagar Adivaiah, Elaprolu Narsimha Rao, G Vaitheeswaran. " Structure-property correlation studies of alkaline-earth metal azides M(N) (M = Sr, Ba) ", Journal of Physics: culther paper which is viched i Condensed Matter, 2019 chapter -4

Dr. G.S. Vaitheeswaran Associate Professor School of Physics
University of Hyderabad
Hyderabad-500 (460//TS) INDIA

%

Sevegney, M.S.. "Vibrational spectroscopic investigation of stereoregularity effects on syndiotactic polypropylene structure and morphology", Vibrational Spectroscopy, 20060317

Publication

Publication

E. Moreira, C.A. Barboza, E.L. Albuquerque, U.L. Fulco, J.M. Henriques, A.I. Araújo. "Vibrational and thermodynamic properties of orthorhombic CaSnO3 from DFT and DFPT calculations", Journal of Physics and Chemistry of Solids, 2015

Publication

Exclude quotes On Exclude matches < 14 words

Exclude bibliography On